

Structural and Biochemical Analyses of Human and Sheep Xanthine Oxidoreductase

Dissertation presented to the Faculty of Medicine and Surgery in part fulfilment of the requirements for the degree of Doctor in Philosophy at the University of Malta



Supervisor: Prof Thérèse Hunter
Co-Supervisor: Prof Arwen Pearson, University of Hamburg, Germany

Brandon Charles Seychell
2019



L-Università
ta' Malta

University of Malta Library – Electronic Thesis & Dissertations (ETD) Repository

The copyright of this thesis/dissertation belongs to the author. The author's rights in respect of this work are as defined by the Copyright Act (Chapter 415) of the Laws of Malta or as modified by any successive legislation.

Users may access this full-text thesis/dissertation and can make use of the information contained in accordance with the Copyright Act provided that the author must be properly acknowledged. Further distribution or reproduction in any format is prohibited without the prior permission of the copyright holder.

DECLARATION OF AUTHENTICITY

I, the undersigned, BRANDON CHARLES SEYCHELL, declare that this dissertation is my original work, gathered and utilised only to fulfil the objectives of this study.

Mr. Brandon Charles Seychell

ETHICS DECLARATION

This research is in conformity with the University of Malta's research code of practice and research ethics review procedures. It has been approved by FREC, UNIQUE FORM ID: 190:26.11.2018

Mr. Brandon Charles Seychell

ABSTRACT

Human recombinant xanthine oxidoreductase (hXOR) and ovine XOR were purified to homogeneity and characterised using various biophysical techniques. XOR catalyses the last two steps of purine degradation to produce uric acid using either NAD^+ or oxygen as the electron acceptor. When oxygen is used, the reactive oxygen species (ROS) hydrogen peroxide and superoxide are produced. Various studies have shown that ROS are implicated in a number of pathological conditions including cardiovascular diseases.

Transmission electron microscopy of both hXOR and ovine XOR revealed that these proteins form soluble filaments under physiological conditions and that the majority of these filaments are composed of two interacting dimers. A hypothesis is proposed which describes the assembly of the filaments in relation to their catalytic function. This may be verified by further analysis of the cryo electron microscopy (cryoEM) data of both the dimer and filamentous hXOR that has already been collected. The structure of hXOR, determined by X-ray crystallography, yielded a resolution of 3.95 Å with a space group of P 31 2 1.

The optimised expression system was used to analyse the activity of three clinical-relevant hXOR mutants (G172R, A932T, N1109T), which have been implicated in hypertension. Only hXOR[A932T] exhibited altered activity, increasing three-fold with respect to the wild type. *In silico* structural studies indicate that this may be due to the additional interactions that T932 forms with neighbouring residues, absent in the wild type. T932 was found to be in a helix connected to the molybdenum active site and the mutation itself might shift the amino acids in the catalytic site, resulting into this increase in activity. Moreover, the inhibitory action of two recently published XOR inhibitors, 4-[(Z)-(6-hydroxy-3-oxo-1-benzofuran-2(3H)-ylidene)methyl]benzoic acid (inhibitor A) and (2E)-1-(2,4-dihydroxyphenyl)-3-(4-hydroxyphenyl)prop-2-en-1-one (inhibitor B) was evaluated with IC_{50} values of 0.648 μM and 45.5 μM respectively. The mode of interaction of these inhibitors to hXOR was determined via docking experiments that showed that both inhibitors blocked the solvent funnel leading to the molybdenum centre. Inhibitor A, which had better inhibitory properties and had some structural homogeneity to purines, also formed stronger interactions with neighbouring residues.

The formation of hXOR filaments poses new questions regarding the mechanism of XOR in the cell, whether this is a resting state or a hyperactive of the enzyme or whether the filaments are favoured in the presence of substrate or product. This study also

demonstrated how an efficient expression system might be used to study clinically relevant mutations as well as conduct inhibition studies on the human enzyme. The structure obtained from X-ray crystallography and cryoEM data may be employed for the design of novel inhibitors that target the human enzyme.

ACKNOWLEDGEMENTS



The research work disclosed in this publication is partially funded by the Endeavour Scholarship Scheme (Malta). This Scholarship is part-financed by the European Union - European Social Fund (ESF) under Operational Programme II – Cohesion Policy 2014-2020, “Investing in human capital to create more opportunities and promote the well being of society”.



European Union- European Structural and Investment
Funds Operational Programme II – Cohesion Policy 2014-2020
*Investing in human capital to create more opportunities and
promote the well being of society*



Scholarship part-financed by the European Union
European Social Fund (ESF)

Co-financing rate: 80% EU Funds; 20% National Funds

Investing in your future

ACKNOWLEDGEMENTS

This project was carried out at the Laboratory of Biochemistry and Protein Science at the University of Malta, the Centre of Free-Electron Laser Science (CFEL, Germany), the Astbury Centre for Structural Molecular Biology (University of Leeds, UK), the European Synchrotron Radiation Facility (ESRF, France), and the Deutsches Elektronen-Synchrotron (DESY, Germany).

Firstly, I would like to express my sincere gratitude to my supervisor, Prof. Thérèse Hunter for the support, guidance, constructive criticism and patience throughout these four years. I would like to extend my gratitude to Prof. Gary Hunter for his patience in explaining multiple laboratory techniques, guidance and discussions during my project. Moreover, I am grateful to Ms Marita Vella for supporting me both morally and academically and for having endless discussions during these past four years.

I am also grateful to my co-supervisor, Prof. Arwen Pearson, for hosting me at her laboratory in Hamburg, for teaching me crystallography and for her guidance. I would like to extend my appreciation to her staff and students, past and present, for their help. Special thanks go to Dr Marta Sans Valls for her help in organic synthesis and support, Ms Maria Kokkinidou for the discussions on crystallography and motivation, and Ms Susanne Meier for her support in the laboratory. I am also thankful to Dr. Iosifina Sarrou for hosting me during my stay in Hamburg and aiding me during my project and to Ms Dana Komadina for assisting me. Without the moral support of these people, my stay in Hamburg could not be possible.

Special thanks go to Dr. Chi Trinh for hosting me in his laboratory at the Astbury Centre and for the long discussions in crystallisation, Dr. Rebecca Thompson for her help in negative staining and cryoEM, Prof. Tracy Palmer for providing me a source of TP1000 cells, Dr. Francisco Javier Chichon Garcia for the preliminary negative staining and Dr. Jiří Nováček for the cryoEM data collection.

Finally, I wish to thank my family and friends, especially Donatella and Malcolm, for their moral support and encouragement during the course of this project.

TABLE OF CONTENTS

TITLE PAGE	i
DECLARATION OF AUTHENTICITY	ii
ETHICS DECLARATION	iii
ABSTRACT	iv
ACKNOWLEDGEMENTS	vi
TABLE OF CONTENTS	viii
LIST OF TABLES	xiii
LIST OF FIGURES	xv
LIST OF ABBREVIATIONS	xx
AMINO ACID CHAIN ABBREVIATIONS	xxii
Chapter 1 Introduction	1
1.1. Molybdenum and Molybdenum containing enzymes	1
1.1.1. The sulfite oxidase family	2
1.1.2. The DMSO reductase family	3
1.2. The Xanthine Oxidase Family	3
1.2.1. Xanthine Oxidoreductase	3
1.2.2. Aldehyde oxidase	4
1.2.3. Carbon monoxide dehydrogenase	4
1.3. Species distribution of Xanthine Oxidoreductase	4
1.4. Mammalian Xanthine Oxidoreductase	7
1.4.1. Human Xanthine Oxidoreductase	8
1.5. Xanthine Oxidoreductase amino acid sequence alignment	9
1.6. Structure of Bovine Xanthine Oxidoreductase	13
1.7. Reaction mechanism of xanthine to uric acid	15
1.8. Mechanism of XDH to XO conversion	17

1.8.1.	Ovine Xanthine Oxidoreductase	21
1.9.	Role of Xanthine Oxidoreductase in human health	21
1.9.1.	Health conditions related directly to Xanthine Oxidoreductase ..	21
1.9.2.	Mutations of Xanthine Oxidoreductase	22
1.9.3.	Xanthine Oxidoreductase and reactive oxygen species	23
1.9.4.	Xanthine Oxidoreductase and nitrate(III)	26
1.9.5.	Reactive nitrogen species	27
1.9.6.	Xanthine Oxidoreductase-based Therapeutics	28
1.10.	Objectives of the thesis	31
Chapter 2	Methodology	32
2.1.	Materials	32
2.1.1.	General chemicals	32
2.1.2.	<i>E. coli</i> bacterial strains	32
2.1.3.	2xTY bacterial media and agar plates	33
2.1.4.	Preparation of calcium competent cells	33
2.1.5.	Bacterial transformation	33
2.2.	Recombinant DNA methodology	34
2.2.1.	Isolation of plasmid DNA	34
2.2.2.	Agarose gel electrophoresis	34
2.2.3.	Lambda DNA preparation	34
2.2.4.	Restriction digest of plasmid DNA	35
2.2.5.	Ethanol precipitation of DNA	35
2.2.6.	DNA Oligonucleotides	35
2.2.7.	Generation of 6xHis-Tagged pTrc99a-hXOR clone	37
2.2.8.	<i>In-vitro</i> site-directed mutagenesis	38
2.3.	Protein analysis methodology	39
2.3.1.	SDS-polyacrylamide gel electrophoresis (SDS-PAGE)	39

2.3.2.	Native-PAGE	40
2.3.3.	Blue native-PAGE.....	41
2.3.4.	Western blotting	41
2.4.	Human XOR Expression and Purification	42
2.4.1.	Optimisation of expression of recombinant hXOR.....	42
2.4.2.	Expression of recombinant hXOR under optimised conditions...	42
2.4.3.	Protein extraction and purification.....	43
2.5.	Extraction of ovine XOR from milk	45
2.6.	Protein Characterisation	46
2.6.1.	Circular dichroism.....	46
2.6.2.	Thermal shift assay	46
2.6.3.	Matrix-assisted laser desorption/ionisation-time of flight (MALDI-TOF) mass spectroscopy	47
2.6.4.	In-gel trypsin digest mass spectrometry.....	47
2.6.5.	Estimation of FAD content of purified hXOR.....	48
2.6.6.	Element analysis.....	48
2.7.	Protein Crystallisation	48
2.8.	Electron Microscopy	49
2.8.1.	Negative staining.....	49
2.8.2.	Grid preparation for cryoEM	49
2.9.	Synthesis of XOR inhibitors	50
2.9.1.	Synthesis of inhibitor A	51
2.9.2.	Synthesis of inhibitor B.....	51
2.10.	Enzymatic Assays	54
2.10.1.	Uric acid activity assay	54
2.10.2.	Thermal inactivation analysis using zymography	54
Chapter 3 Results		55

3.1.	pTrc-hXOR	55
3.1.1.	Plasmid Map.....	55
3.1.2.	Sanger sequencing of pTrc-hXOR.....	56
3.2.	pTrcHis-hXOR	57
3.2.1.	Plasmid Map.....	57
3.2.2.	Generation of the pTrcHis-hXOR clone	58
3.2.3.	Sanger DNA sequencing of pTrcHis-hXOR.....	60
3.3.	<i>In-vitro</i> site-directed mutagenesis	62
3.4.	Expression of hXOR	63
3.5.	Purification of hXOR	67
3.6.	Expression of His-hXOR	74
3.7.	Purification of His-hXOR	76
3.8.	Extraction of ovine XOR from milk	79
3.9.	Protein characterisation	83
3.9.1.	Circular dichroism.....	83
3.9.2.	Thermal shift assays.....	86
3.9.3.	MALDI-TOF mass spectroscopy.....	91
3.9.4.	In-gel trypsin digest.....	92
3.9.5.	Element analysis.....	95
3.9.6.	Estimation of FAD content of purified hXOR.....	96
3.10.	Inhibitor synthesis	97
3.10.1.	Inhibitor A.....	97
3.10.2.	Inhibitor B	101
3.11.	Protein Crystallisation and Crystallography	111
3.11.1.	Crystallisation and X-ray data collection.....	111
3.11.2.	Crystallographic analysis of hXOR	114
3.11.3.	Molecular modelling of the hXOR mutants.....	132

3.11.4.	Molecular docking	135
3.12.	Electron microscopy	139
3.12.1.	Preliminary negative staining: tomography electron microscopy	139
3.12.2.	Negative staining at different conditions	143
3.12.3.	Grid preparation for cryoEM	148
3.13.	Enzymatic assays	150
3.13.1.	Specific activity of hXOR.....	150
3.13.2.	Activity of hXOR at different temperatures.....	152
3.13.3.	Thermal inactivation analysis of hXOR.....	153
3.13.4.	Activity of hXOR in different buffers.....	155
3.13.5.	Inhibition studies of hXOR	158
3.13.6.	Activity assays of hXOR mutants	160
3.13.7.	Specific activity of ovine XOR.....	160
3.13.8.	Thermal inactivation analysis of ovine XOR.....	162
Chapter 4	Discussion	163
4.1.	Protein Purification	163
4.2.	Thermal shift assays	165
4.3.	Specific Activity of XOR	166
4.4.	Protein Crystallisation and Crystallography	166
4.5.	Inhibition studies	168
4.6.	<i>In-vitro</i> site directed mutagenesis	170
4.7.	Electron Microscopy	171
4.8.	Conclusions	175
4.9.	Suggestions for future work	176
References		178

LIST OF TABLES

Chapter 1 Introduction

Table 1.1: Deposited structures of xanthine oxidoreductase	5
Table 1.2: Molecular mass of XOR in different mammalian species.....	7
Table 1.3: Percent identity and divergence of the different domains and the whole sequences of XOR.	12
Table 1.4: Half-reactions at the XOR active sites	14
Table 1.5: List of mutations of human XOR.	23
Table 1.6: Chemical structures of approved XOR inhibitor drugs.....	29
Table 1.7: Urate-lowering therapy medications..	30

Chapter 2 Methodology

Table 2.1: Primers.....	36
Table 2.2: Components of the polymerase chain reaction.....	37
Table 2.3: PCR cycling parameters	37
Table 2.4: Components of the blunt-end ligation reaction	38
Table 2.5: Components of the <i>in-vitro</i> site-directed mutagenesis reaction	38
Table 2.6: QuikChange XL cycling parameters	39
Table 2.7: SDS-PAGE Gel Composition.....	40
Table 2.8: Native-PAGE Gel Composition	41

Chapter 3 Results

Table 3.1: Expression conditions tested for hXOR.	63
Table 3.2: Purification table of the hXOR purification.	74
Table 3.3: Expression conditions tested for hXOR.	74
Table 3.4: Purification table of the His-hXOR purification.	78
Table 3.5: Absorbances after purification steps.....	81
Table 3.6: Secondary structure estimation from CD data using the CDSSTR method ..	85
Table 3.7: Secondary structure content from PDB using the DSSP method.....	85
Table 3.8: Experimental and theoretical molecular mass	92
Table 3.9: In-gel trypsin digest analysis	94
Table 3.10: Element analysis of His-hXOR.	95
Table 3.11: Proposed different metallation combinations of His-hXOR.	95

Table 3.12: Amount and yield of intermediates Br1 and Br2.....	104
Table 3.13: Amount and yield of intermediate Br3.	106
Table 3.14: Amount and yield of intermediate Br3.	108
Table 3.15: Statistics for data collection and refinement.....	118
Table 3.16: Dimer interface interaction residues according to the SPPIDER server. ..	122
Table 3.17: Abundance of hXOR dimers in 50 mM HEPES pH 8.0	141
Table 3.18: Abundance of hXOR across different pH.....	147
Table 3.19: Activities of hXOR at different temperatures.....	152
Table 3.20: Thermal Inactivation constant and half-time of hXOR.....	154

LIST OF FIGURES

Chapter 1 Introduction

Figure 1.1: MPT structure.....	1
Figure 1.2: Formation of Moco.....	2
Figure 1.3: The different Moco structures in three families of Mo-containing enzymes. 2	
Figure 1.4: The general reaction catalysed by XOR.....	4
Figure 1.5: Human, ovine and bovine XOR alignment.	11
Figure 1.6: Crystal structure of the bovine XOR, PDB 1FO4 with a resolution up to 2.1 Å.....	14
Figure 1.7: Reaction mechanism of XOR with xanthine as a substrate.	15
Figure 1.8: XOR catalysed reactions.	16
Figure 1.9: General transfer of electrons in XOR.....	17
Figure 1.10: Mechanism of the conversion of XDH to XO.....	19
Figure 1.11: Representation of the electrostatic environment around the FAD domain.20	
Figure 1.12: Sequences alignment of XOR obtained from the NCBI.	21
Figure 1.13: Adenosine pathway of extracellular ATP catabolism.	24
Figure 1.14: Ischaemia-reperfusion effects on XOR action.	24
Figure 1.15: Effects of overproduction of ROS on human health.	26
Figure 1.16: The uric acid pathway and site of urate lowering therapy drugs.	30

Chapter 2 Methodology

Figure 2.1: Aldol condensation of 6-hydroxy-1-benzofuran-3(2 <i>H</i>)-one (1) with 4-formylbenzoic acid (2) to produce 4-[(<i>Z</i>)-(6-hydroxy-3-oxo-1-benzofuran-2(3 <i>H</i>)-ylidene)methyl]benzoic acid (Inhibitor A).	51
Figure 2.2: General reaction scheme of inhibitor B synthesis.	52

Chapter 3 Results

Figure 3.1: pTrc-hXOR plasmid map.	55
Figure 3.2: Agarose gel (0.7% w/v) of linearised pTrc-hXOR DNA.....	56
Figure 3.3: Sequencing strategy for pTrc-hXOR.....	57
Figure 3.4: The multiple cloning site of pTrc99a vector.	57
Figure 3.5: pTrcHis-hXOR plasmid map..	58
Figure 3.6: PCR of pTrc-hXOR to introduce a 6xHis-tag.....	59

Figure 3.7: Agarose gel (0.7%, w/v) of the PCR product.....	60
Figure 3.8: Sequencing results of pTrc99a-His-hXOR DNA	61
Figure 3.9: Plasmid maps indicating the position of the His-tag.....	61
Figure 3.10: Sites for <i>in-vitro</i> mutagenesis.....	62
Figure 3.11: Sequencing results confirming the mutations in the pTrc-hXOR clone. ...	62
Figure 3.12: SDS-PAGE gel (8%) of the optimisation conditions 1-10.	64
Figure 3.13: SDS-PAGE gel (8%) after lysis and clarification.	65
Figure 3.14: SDS-PAGE gel (8%) of the optimisation conditions 12-21.....	66
Figure 3.15: SDS-PAGE gel (8%) after lysis.	66
Figure 3.16: SDS-PAGE gel (8%) of the ammonium sulfate precipitation optimisations.	67
Figure 3.17: Heparin affinity chromatography purification.	69
Figure 3.18: Anion exchange chromatography purification.	71
Figure 3.19: Western blot of purified hXOR.....	72
Figure 3.20: Native-PAGE gel (4%) of hXOR.....	73
Figure 3.21: SDS-PAGE gel (8%) of the hXOR purification.....	73
Figure 3.22: SDS-PAGE gel (8%) of the expression optimisation conditions.	75
Figure 3.23: IMAC chromatography purification.....	76
Figure 3.24: Western blot of purified His-hXOR.....	77
Figure 3.25: Blue-native-PAGE 4-16% gradient gel.....	78
Figure 3.26: Typical plot of hXOR.....	79
Figure 3.27: SDS-PAGE gel (8%) of the ovine XOR purification.....	80
Figure 3.28: Western blot of purified ovine XOR.	81
Figure 3.29: Native-PAGE gel (4%) of sXOR.	82
Figure 3.30: Far-UV CD spectrum of 0.2 mg.mL ⁻¹ His-hXOR.....	84
Figure 3.31: Far-UV CD spectrum of 0.88 mg.mL ⁻¹ ovine XOR.....	84
Figure 3.32: Top ten buffers which yielded the highest T _M	87
Figure 3.33: Least favourable buffers which yielded the lowest T _M	88
Figure 3.34: Nano-DSF plots of ovine XOR.	90
Figure 3.35: Top ten buffers which yielded the highest T _M	90
Figure 3.36: MALDI-TOF spectrum of His-hXOR.....	91
Figure 3.37: SDS-PAGE gel (8%) sent to EMBL (Heidelberg) for in-gel trypsin digestion.....	93
Figure 3.38: FAD standard curve.	96

Figure 3.39: Mechanism of the aldol condensation between 6-hydroxy-1-benzofuran-3(2 <i>H</i>)-one (a) and 4-formylbenzoic acid (b) to form inhibitor A.....	98
Figure 3.40: ¹ H NMR (400 MHz, DMSO) of inhibitor A.	99
Figure 3.41: Inhibitor A with ¹ H chemical shift annotations.....	100
Figure 3.42: ¹³ C NMR (100 MHz, DMSO) of inhibitor A.	100
Figure 3.43: Inhibitor A with ¹³ C chemical shift annotations.....	101
Figure 3.44: Protection of the hydroxyl group by the addition of a benzyl group.	102
Figure 3.45: TLC for Br1 using 4:1, hexane:ethyl acetate.	103
Figure 3.46: TLC for Br2 using 4:1, hexane:ethyl acetate.	104
Figure 3.47: Mechanism (summarised) of the aldol condensation between Br1 and Br2 to form Br3.....	105
Figure 3.48: TLC for Br3.....	106
Figure 3.49: Removal of the benzyl group by boron tribromide.	107
Figure 3.50: TLC for inhibitor B.	108
Figure 3.51: ¹ H NMR (400 MHz, DMSO) of inhibitor B.	109
Figure 3.52: Inhibitor B with ¹ H chemical shifts.....	109
Figure 3.53: ¹³ C NMR (101 MHz, DMSO) of inhibitor B.	110
Figure 3.54: Inhibitor B with ¹³ C chemical shifts.....	110
Figure 3.55: Drop with yellow crystal needles formed.	111
Figure 3.56: Drop with yellow crystal needles.	112
Figure 3.57: Collected crystals for analysis.....	113
Figure 3.58: Crystals formed at 12 mg.mL ⁻¹	114
Figure 3.59: Ramachandran plots of hXDH.	117
Figure 3.60: hXDH asymmetric unit.	119
Figure 3.61: Biological hXDH dimeric unit.	120
Figure 3.62: Vacuum electrostatics of the dimer unit.....	121
Figure 3.63: Dimer unit with measurements.	122
Figure 3.64: Electrostatic protein-protein interface interaction representation of the dimeric unit.....	123
Figure 3.65: Relative overall B-factors of the dimeric unit.....	124
Figure 3.66: Structural based alignment of hXDH (green) with bovine XDH (cyan)..	125
Figure 3.67: The Moco centre.....	126
Figure 3.68: Alignment of bovine XDH (3UNC) and hXDH at the Moco.	127
Figure 3.69: The two [2Fe-2S] domains in hXDH.	128

Figure 3.70: Vacuum electrostatics around the FAD molecule.....	129
Figure 3.71: Interactions of the Gln ⁴²³ -Lys ⁴³³ loop.	130
Figure 3.72: Interactions of the FAD molecule with the surrounding residues.....	131
Figure 3.73: Wild type and A932T mutant hXDH aligned..	132
Figure 3.74: Vacuum electrostatics around the residue 932.	133
Figure 3.75: Interactions of the residue 932 with the surrounding residues.....	133
Figure 3.76: Wild type and mutant N1109T hXDH aligned.	134
Figure 3.77: Vacuum electrostatics around the residue 1109.....	134
Figure 3.78: Interactions of the residue 1109 with the surrounding residues.	135
Figure 3.79: Docking experiment against crystallographic experiment.	136
Figure 3.80: Interactions of Inhibitor A with hXDH.	137
Figure 3.81 Interactions of Inhibitor B with hXDH.	138
Figure 3.82: Transition electron microscopy (TEM) images of 1:100 hXOR in 50 mM HEPES buffer pH 8.0.....	140
Figure 3.83: Distribution of hXOR dimers in 50 mM HEPES pH 8.0.	141
Figure 3.84: Transition electron microscopy (TEM) images of 1:100 ovine XOR in 50 mM HEPES buffer pH 8.0.....	142
Figure 3.85: TEM images of hXOR in 50 mM HEPES pH 8.0 at different concentrations.	143
Figure 3.86: TEM images of hXOR in different buffers.	145
Figure 3.87: Distribution of hXOR filaments across different pH.	146
Figure 3.88: Different morphologies hXOR dimers and filaments.	147
Figure 3.89: Hydrated cryoEM image of 0.1 mg.mL ⁻¹ hXOR.	148
Figure 3.90: Hydrated cryoEM image of 0.5 mg.mL ⁻¹ hXOR.	149
Figure 3.91: hXO activity assay.	151
Figure 3.92: hXOR activity assay.....	151
Figure 3.93: Activity of hXOR at 25, 30 and 37°C.	152
Figure 3.94: Activity of hXOR after incubation for 10 minutes at different temperatures.	153
Figure 3.95: Thermal inactivation of hXOR.....	154
Figure 3.96: First-order thermal inactivation of hXOR.....	155
Figure 3.97: Activity of hXOR in different buffer systems.....	156
Figure 3.98: Peak formation at A ₂₃₀ produced by hXOR with sodium acetate.	157
Figure 3.99: Absorbance increase over time at 230 nm.	157

Figure 3.100: Enzymatic activity with (red) and without (blue) allopurinol.....	158
Figure 3.101: Enzyme activity against the logarithm of the concentration of inhibitor A.	159
Figure 3.102: Enzyme activity against the logarithm of the concentration of inhibitor B.	159
Figure 3.103: Activities of hXOR and mutants.	160
Figure 3.104: Ovine XO activity assay.....	161
Figure 3.105: Ovine XOR activity assay.	161
Figure 3.106: Activity of ovine XOR after incubation for 10 minutes at different temperatures.....	162

Chapter 4 Discussion

Figure 4.1: Tryptophan and tyrosine residues in hXOR and possible interaction.....	172
Figure 4.2: Proposed areas of interaction between the two hXOR dimers to form the filaments.....	173
Figure 4.3: Hypothesis 1.....	174
Figure 4.4: Hypothesis 2.....	174

LIST OF ABBREVIATIONS

The following abbreviations have been used within this dissertation:

[2Fe-2S]	Iron-sulfur cluster
¹³ C-NMR	Carbon nuclear magnetic resonance
¹ H-NMR	Proton nuclear magnetic resonance
AO	Aldehyde oxidase
ASA	Accessible surface area
BN-PAGE	Blue native PAGE
CD	Circular dichroism
COD	Carbon monoxide dehydrogenase
cPMP	Cyclopyranoperin monophosphate
DMSO	Dimethyl sulfoxide
DTT	Dithiothreitol
EDTA	Ethylenediaminetetraacetic acid
EM	Electron microscopy
FAD	Flavin adenine dinucleotide
GAGs	Glycosaminoglycans
GTP	Guanosine triphosphate
hXDH	Human xanthine dehydrogenase
hXO	Human xanthine oxidase
IMAC	Immobilised metal affinity chromatography
IPTG	Isopropyl-β-D-thiogalactopyranoside
MALDI-TOF	Matrix-assisted laser desorption ionisation-time of flight
MCSU	Moco sulfurase
Moco	Molybdenum cofactor
MPT	Molybdopterin
NAD ⁺	Oxidised nicotinamide adenine dinucleotide
NADH	Reduced nicotinamide adenine dinucleotide
nanoDSF	Nano-differential scanning fluorimetry
NBT	Nitroblue tetrazolium
NCBI	National centre of biotechnology information
NO [•]	Nitric oxide
O ₂ ^{•-}	Superoxide

OH [•]	Hydroxyl radicals
ONOO ⁻	Peroxynitrite
PCR	Polymerase chain reaction
PEG	Polyethylene glycol
PMSF	Phenylmethylsulfonyl fluoride
RNS	Reactive nitrogen species
ROS	Reactive oxygen species
RSA	Residue solvent accessibility
SDS	Sodium dodecyl sulfate
SVD	Singular value decomposition
TB	Terrific broth
TCEP	Tris(2-carboxyethyl)phosphine hydrochloride
TEM	Transmission electron microscopy
TEMED	Tetramethylethylenediamine
TLC	Thin layer chromatography
XDH	Xanthine dehydrogenase
XO	Xanthine oxidase
XOI	Xanthine oxidase inhibitor
XOR	Xanthine oxidoreductase

AMINO ACID SIDE CHAIN ABBREVIATIONS

Group	Donor	Acceptor
Main Chain	NH	CO
Arg (R)	NE, NH1, NH2	
Asn (N)	ND2	OD1
Asp (D)		OD1, OD2
Cys (C)	SG	
Gln (Q)	NE2	OE1
Glu (E)		OE1, OE2
His (H)	ND1, NE2	ND1
Met (M)		SD
Ser (S)	OG	OG
Thr (T)	OG1	OG1
Trp (W)	NE1	
Tyr (Y)	OH	OH

Chapter 1 Introduction

Xanthine oxidoreductase is a molybdoflavin enzyme which occurs in two forms; the reduced form known as xanthine dehydrogenase (XDH, EC 1.17.1.4) and the oxidised form known as xanthine oxidase (XO, EC 1.17.3.2). In humans, it is a 293 kDa homodimer which catalyses consecutive hydroxylation steps of purine degradation. The oxidised form of the enzyme produces hydrogen peroxide and superoxide ($O_2^{\cdot-}$), both of which are reactive oxygen species which can interact with a number of biomolecules producing adverse reactions. Xanthine oxidoreductase can also produce nitric oxide, a cardiovascular protective molecule. Overproduction of nitric oxide results in the formation of the highly reactive peroxyxynitrite radical. Due to the presence of xanthine oxidase in patients suffering from cardiovascular disease, the enzyme is now considered to be a reliable biomarker for this pathological condition.

1.1. Molybdenum and Molybdenum containing enzymes

Molybdenum is the only second-row transition metal found in living organisms and is present in over fifty enzymes (Hille, Hall and Basu, 2014). In all characterised Mo-containing enzymes, the Mo is incorporated in an organic cofactor known as pyranopterin or molybdopterin (MPT) (Chan *et al.*, 1995).

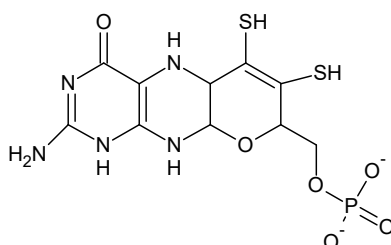


Figure 1.1: MPT structure. Structure drawn using ACD/Chemsketch (version 2018.1).

When Mo is present in MPT, the organic structure is referred to as molybdenum cofactor (Moco). The general biosynthesis of Moco involves three steps: (a) formation of cyclopyranoperin monophosphate (cPMP) intermediate from the cyclization of guanosine triphosphate (GTP); (b) formation of MPT by the sulfuration of cPMP; (c) and the incorporation of molybdate to the enedithiolate moiety (Leimkühler, Wuebbens and Rajagopalan, 2011).

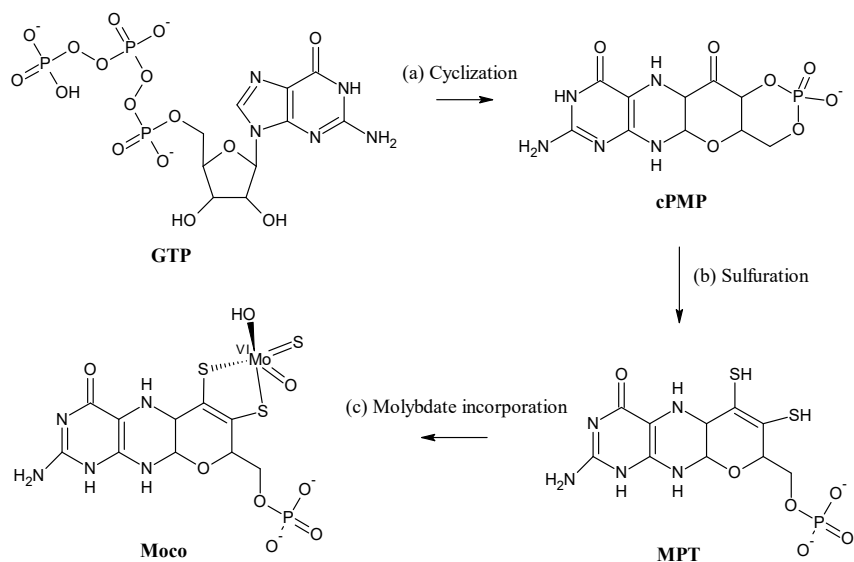
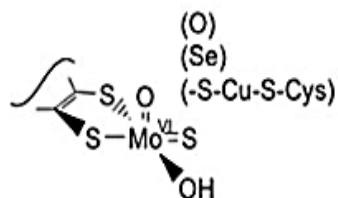


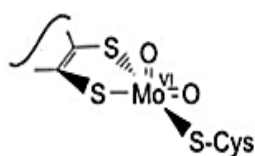
Figure 1.2: Formation of Moco. Structures drawn using ACD/Chemsketch (version 2018.1).

All Mo-containing enzymes except for nitrogenase can be divided into three families: xanthine oxidase family, sulfite oxidase family, and dimethyl sulfoxide (DMSO) reductase family (Hille, 1996). The three classes differ in their Moco structure as shown in Figure 1.3 below.

xanthine oxidase family



sulfite oxidase family



DMSO reductase family

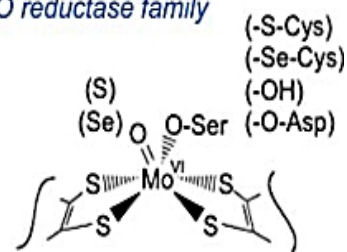


Figure 1.3: The different Moco structures in three families of Mo-containing enzymes (Hille, Hall and Basu, 2014).

1.1.1. The sulfite oxidase family

The sulfite oxidase family consists of sulfite oxidase, sulfite dehydrogenase and assimilatory nitrate reductase. Enzymes in this family are considered as true oxygen atom transferases with the oxidised LMo^{VI}O₂(S-Cys) as the oxygen atom donor and the reduced LMo^{IV}O(OH-Cys) as the oxygen atom acceptor, where L is a bidentate enedithiolate ligand. The most studied enzyme in this family is chicken sulfite oxidase (Hille, Hall and Basu, 2014). Mammalian sulfite oxidase is present in the mitochondrion intermembrane space and contains two domains: a Moco and a haem domain. Sulfite oxidase is involved

in the sulfite oxidation to sulfate in the decomposition of methionine, cysteine, and other sulfur containing substrates. Deficiencies or mutations in this enzyme cause severe neurological disorders which are fatal to infants and developing foetuses (Hänsch *et al.*, 2007).

1.1.2. The DMSO reductase family

The enzymes in this family are present only in prokaryotes and are the most catalytically and structurally diverse of the Mo-containing families. The first structurally characterised protein in this group was DMSO reductase from *Rhodobacter sphaeroides*. DMSO reductase acts as a terminal electron acceptor during anaerobic growth in the presence of DMSO (McEwan *et al.*, 2002; Hille, Hall and Basu, 2014).

1.2. The Xanthine Oxidase Family

Enzymes in the xanthine oxidase family catalyse the oxidative hydroxylation of aldehydes or aromatic heterocycles. Enzymes forming the xanthine oxidase family include xanthine oxidoreductase (XOR), aldehyde oxidase and carbon monoxide dehydrogenase (Hille, Hall and Basu, 2014). The longest studied enzyme in this family is bovine xanthine oxidase which was first purified in 1924 (Dixon and Thurlow, 1924). All the enzymes in this family have three redox centres: a molybdenum cofactor (Moco), a ferredoxin-like iron-sulfur cluster denoted as [2Fe-2S] and a flavin adenine dinucleotide (FAD). These centres exhibit very high degree of structural similarity in known xanthine oxidase proteins (Santiago *et al.*, 1999).

1.2.1. Xanthine Oxidoreductase

Xanthine oxidoreductase (XOR) occurs in the reduced and oxidised forms: xanthine dehydrogenase (XDH) and xanthine oxidase (XO) respectively. Since both forms are expressed by the same gene, this enzyme is referred to XOR. Although XO and XDH have been identified in mammals, only XDH is observed in other organisms. (Montero-Moran *et al.*, 2007). XOR primarily catalyses consecutive hydroxylation steps in the pathway of purine degradation that converts hypoxanthine into xanthine and xanthine to uric acid (Bray, 1977).

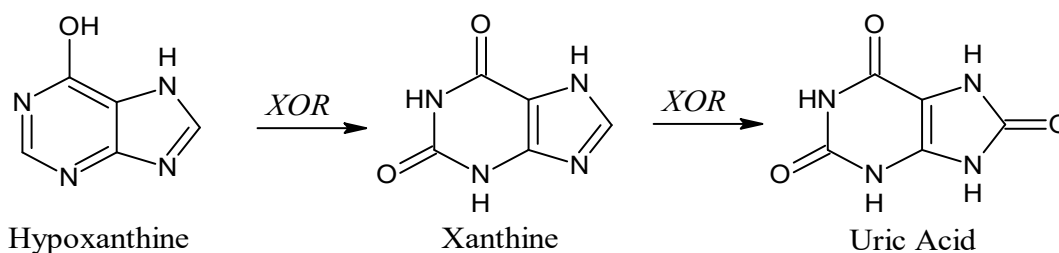


Figure 1.4: The general reaction catalysed by XOR. Structures drawn using ACD/Chemsketch (version 2018.1).

1.2.2. Aldehyde oxidase

Aldehyde oxidase (AO) catalyses the oxidation of aldehydes and the hydroxylation of heterocycles. AO exhibits high amino acid sequence homology with XOR, with similar protein structure and properties. However, in contrast to XOR, AO is only present as the oxidase form where the sole electron acceptor is molecular oxygen. In general, AO has a wider, less specific, substrate specificity than XOR (Terao *et al.*, 2016). However, even though the physiological functions of XOR are widely recognized, the physiological and biochemical relevance of AO is not fully understood (Kitamura, Sugihara and Ohta, 2006).

1.2.3. Carbon monoxide dehydrogenase

Carbon monoxide dehydrogenase (COD) catalyses the oxidation of carbon monoxide into carbon dioxide without the cleavage of any carbon-hydrogen bond (in contrast to XOR and AO). The active site of Mo-containing COD contains a dinuclear heterometal cluster composed of a copper atom bridged to a molybdenum atom via a μ -sulfido ligand [CuSMoO₂] (Brondino *et al.*, 2006). COD in aerobic and anaerobic bacteria and archaea is an essential part of the biogeochemical cycle of atmospheric carbon monoxide. Organisms with COD are thus extremely important to the environment as they keep carbon monoxide levels at sub-hazardous levels (Dobbek *et al.*, 2002).

1.3. Species distribution of Xanthine Oxidoreductase

XOR is ubiquitous amongst different organisms. Only the XDH form is present in bacteria, insects and birds. In fact, XDH is normally isolated from *Gallus gallus* (Rajagopalan and Handler, 1967; Kanda *et al.*, 1972). A search of XOR genes in the National Centre for Biotechnology Information (NCBI) database yielded a total of 67,961 genes. The majority of these were identified from different bacterial species and strains

(62,073, 91.4%). A comparison of XOR amino acid sequences from various organisms shows that eukaryotic XORs share the highest similarity and identity between them and that from all the domains, the [2Fe-2S] domain is the most conserved while the FAD domain is the least conserved (Wang, Zhang and Xing, 2016).

Both eukaryotic and bacterial XOR proteins have been studied. The bovine XOR was first characterised in 1939 (Corran *et al.*, 1939). Later, in 1960, Bradshaw and Barker characterised the first bacterial XOR which was isolated from *Clostridium cylindrosporium* (Bradshaw and Barker, 1960).

The current Protein Data Bank (PDB) accessible (May, 2019) XOR crystal structures are the *Bos taurus* XOR (PDB code: 3UNC), *Rattus norvegicus* XOR (PDB code: 4YRW), *Rhodobacter capsulatus* XOR (PDB code: 1JRO), *Bacillus halodurans* XOR (PDB code: 3ON5) and *Homo sapiens* XOR (PDB code: 2CKJ) (PDB codes given are of the wild type with no substrates bound). All the deposited xanthine oxidoreductase structures are listed in Table 1.1 below (Berman *et al.*, 2000).

Table 1.1: Deposited structures of xanthine oxidoreductase

Species	Form	PDB Code	Resolution/Å	Ligand
<i>Bacillus halodurans</i>	Dehydrogenase	3ON5	2.8	
<i>Bos taurus</i>	Dehydrogenase	3UNC	1.65	
<i>Bos taurus</i>	Dehydrogenase	1FO4	2.1	
<i>Bos taurus</i>	Dehydrogenase	3SR6	2.1	Arsenite
<i>Bos taurus</i>	Dehydrogenase	1V97	1.94	FYX-051
<i>Bos taurus</i>	Dehydrogenase	3UNA	1.9	NAD
<i>Bos taurus</i>	Dehydrogenase	3UNI	2.2	NADH
<i>Bos taurus</i>	Dehydrogenase	3BDJ	2.0	Oxypurinol inhibitor
<i>Bos taurus</i>	Dehydrogenase	1N5X	2.8	TEI-6720
<i>Bos taurus</i>	Dehydrogenase	3AM9	2.17	Trihydroxy FYX-051
<i>Bos taurus</i>	Dehydrogenase	3AMZ	2.1	Urate
<i>Bos taurus</i>	Dehydrogenase	1VDV	1.98	Y-700
<i>Bos taurus</i>	Oxidase Protease cleaved	3AX9	2.3	
<i>Bos taurus</i>	Oxidase	1FIQ	2.5	
<i>Bos taurus</i>	Oxidase	3B9J	2.3	2-hydroxy-6-methylpurine

<i>Bos taurus</i>	Oxidase	3NS1	2.6	6-mercaptapurine
<i>Bos taurus</i>	Oxidase	3NVV	1.82	Arsenite
<i>Bos taurus</i>	Oxidase	3NVW	1.6	Guanine
<i>Bos taurus</i>	Oxidase	3NRZ	1.8	Hypoxanthine
<i>Bos taurus</i>	Oxidase	3NVZ	1.6	Indole-3-aldehyde
<i>Bos taurus</i>	Oxidase	3ETR	2.2	Lumazine
<i>Bos taurus</i>	Oxidase	3NVY	2.0	Quercetin
<i>Bos taurus</i>	Oxidase Desulfo form	3EUB	2.6	Xanthine
<i>Homo sapiens</i>	Dehydrogenase G803V mutant	2E1Q	2.6	
<i>Homo sapiens</i>	Dehydrogenase	2CKJ	3.59	
<i>Rattus norvegicus</i>	Dehydrogenase C-terminal deletion	4YRW	1.99	
<i>Rattus norvegicus</i>	Dehydrogenase W335A F336L mutant	2E3T	2.28	
<i>Rattus norvegicus</i>	Dehydrogenase C535A C992R C1324S mutant	1WYG	2.6	
<i>Rattus norvegicus</i>	Dehydrogenase C-terminal deletion	4YSW	1.99	NADH
<i>Rattus norvegicus</i>	Dehydrogenase C535A C992R C1324S mutant	4YTY	2.2	NADH
<i>Rattus norvegicus</i>	Dehydrogenase D428A mutant	3AN1	1.73	Urate
<i>Rattus norvegicus</i>	Oxidase	4YTZ	2.3	
<i>Rhodobacter capsulatus</i>	Dehydrogenase Desulfo form	2W3S	2.6	
<i>Rhodobacter capsulatus</i>	Dehydrogenase	1JRO	2.7	
<i>Rhodobacter capsulatus</i>	Dehydrogenase	1JRP	3.0	Alloxanthine
<i>Rhodobacter capsulatus</i>	Dehydrogenase Desulfo form	2W3R	2.9	Hypoxanthine

<i>Rhodobacter capsulatus</i>	Dehydrogenase E232Q mutant	2W55	3.4	Hypoxanthine
<i>Rhodobacter capsulatus</i>	Dehydrogenase	2W54	3.3	Pterin-6- aldehyde

Full list of deposited XOR structures. Form describes whether it is XDH (dehydrogenase) or XO (oxidase) and if relevant, if it has other modifications like mutations, deletions, cleavages, or present in desulfo form. PDB code is the code given by the Protein Data Bank repository. Ligand describes if there is a substrate or an inhibitor bound to the XOR in crystal structure. Ligand is left blank for structures without substrates or inhibitors.

1.4. Mammalian Xanthine Oxidoreductase

Mammalian XOR occurs as a homodimer of a molecular weight of approximately 300 kDa. Although XOR is found in both XO and XDH forms, under normal physiological conditions, the predominant form is the reduced XDH form. The XO form is normally isolated from milk since XDH is converted to XO during purification via reversible oxidation of the cysteine residues forming a disulfide bond or via irreversible proteolysis (Nakamura and Yamazaki, 1982; Hille, Nishino and Bittner, 2011).

Table 1.2: Molecular mass of XOR in different mammalian species.

Species	XOR Molecular Mass/Da
<i>Bos taurus</i>	293,580
<i>Homo sapiens</i>	292,848
<i>Mus musculus</i>	293,124
<i>Ovis aries</i>	292,992
<i>Rattus norvegicus</i>	292,486

XOR is widely spread in mammalian tissues, with intestine and liver tissue having the highest levels. However, the tissue distribution of XOR varies amongst species. For instance, in bovines, XOR levels are high in mammary glands compared to other mammals. In addition to acting as a catalyst for the hydroxylation of hypoxanthine and xanthine, XOR functions as an NADH oxidase (Sanders, Eisenthal and Harrison, 1997) as well as catalysing the hydroxylation of a variety of aldehydes (Veskoukis, Kouretas and Panoutsopoulos, 2006) and N-heterocyclic compounds (Beedham, 1987). Inactive forms of XOR have also been reported in mammalian tissues. For instance, Ventom, Deistung and Bray showed that 60% of purified bovine milk XOR was in fact inactive towards xanthine (Ventom, Deistung and Bray, 1988). These inactive forms include demolybdo XOR, which is the enzyme without Mo and possibly the whole MPT cofactor,

or desulfo XOR, which is XOR with a Mo=O instead of Mo=S in the Moco. Deflavo (XOR without FAD) has not been reported *in vivo* (Harrison, 2002).

1.4.1. Human Xanthine Oxidoreductase

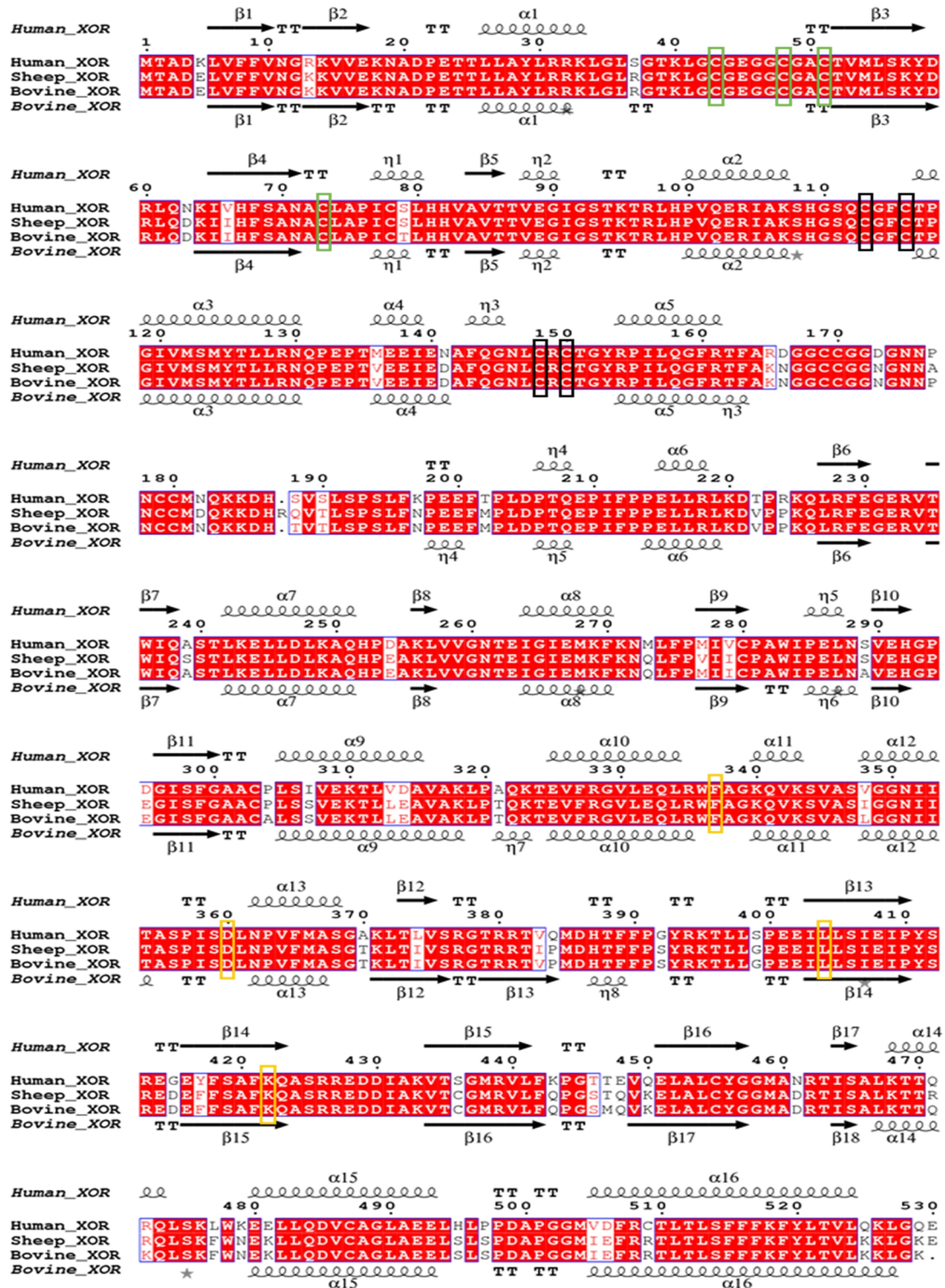
In humans, XOR activity was found to be low in tissues other than liver and intestine. Using human anti-XOR antibodies, Jarasch *et al.* observed that XOR is also present in the epithelial and capillary endothelial cells of mammary glands. The existing data regarding XOR tissue distribution is not conclusive as the studies do not take into account the inactive forms (demolybdo and desulfo) of XOR and the possible cross-reactivity of anti-XOR antibodies with aldehyde oxidase (Jarasch *et al.*, 1981; Harrison, 2002).

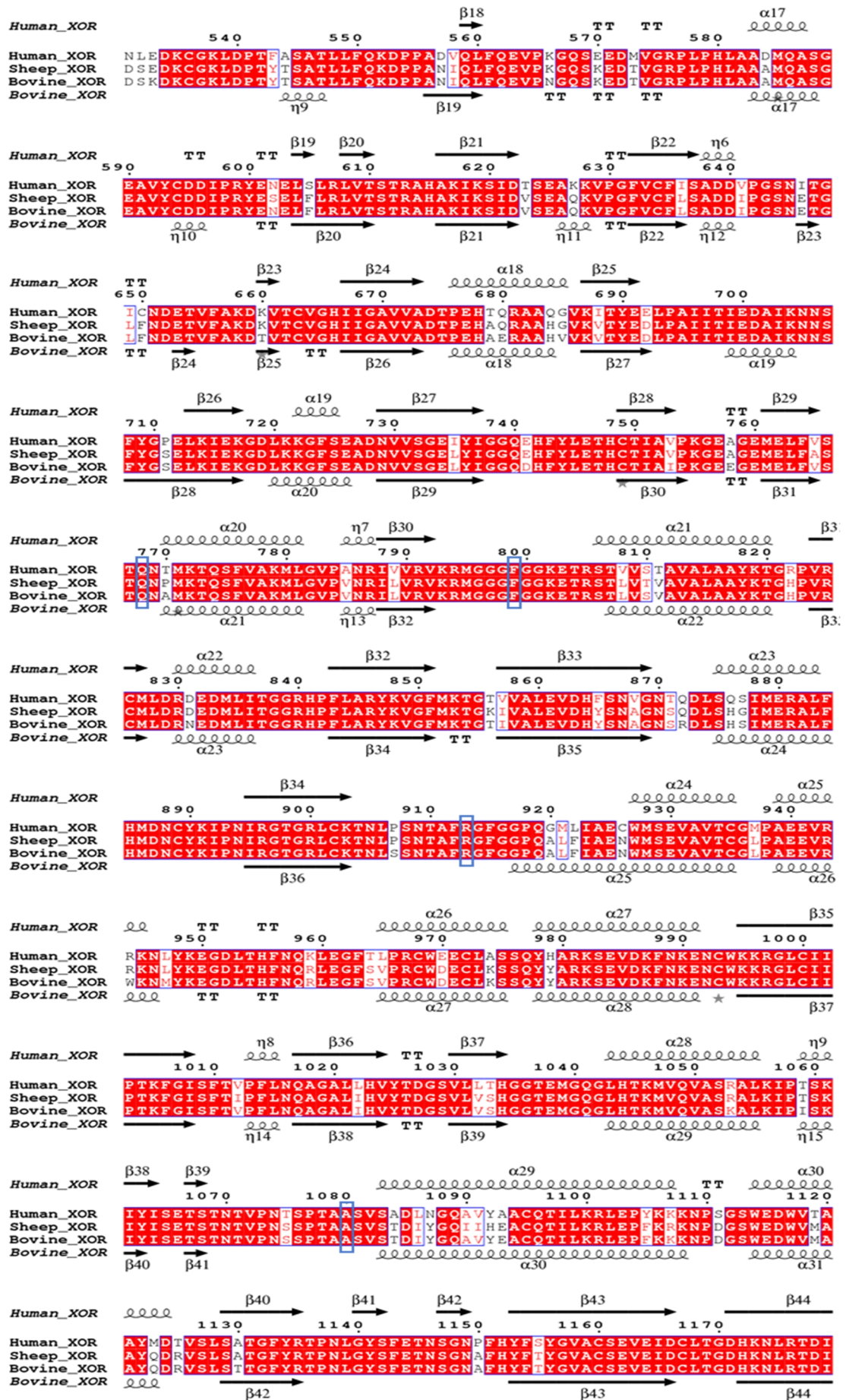
XOR was shown to be a source of reactive oxygen species (ROS) and reactive nitrogen species (RNS) in vasculature and digestive tract. In an inflammatory response, it was deduced that XOR provides protection against infection by generating ROS and RNS and thus was classified as an agent of innate immunity (Martin *et al.*, 2004). In the gastrointestinal tract, XOR is concentrated in surface epithelial cells where the reactive species it generates provides antimicrobial defence (Van Den Munckhof *et al.*, 1995). Milk XOR was also shown to have bactericidal properties and provides immunity in the neonatal gut where other immune responses are not yet developed (Harrison, 2006). In the liver, XOR is able to catalyse the oxidation of various metabolites, including purines, pyrimidines, heterocyclic compounds and aldehydes (Krenitsky *et al.*, 1972) and can catalyse different xenobiotics including anti-cancer agents. As a result, XOR contributes to liver detoxification (Pritsos, 2000).

Human XOR has been purified from liver tissue (Krenitsky, Spector and Hall, 1986) and breast milk (Godber *et al.*, 2005), and has been recombinantly expressed in bacteria (Yamaguchi *et al.*, 2007). The measured activity of human liver and milk XO was only 5% the activity of the bovine milk. This was consistent with the measurement of the molybdenum content that showed that human milk XOR was 96% in the demolybdo form (Bray *et al.*, 1999) while bovine milk XOR was between 30 to 40% (Ventom, Deistung and Bray, 1988). XOR activity was found to be the highest in the liver. In general, though, the specific activity of human XOR was observed to be low when compared to other mammals such as *Bos taurus* (Ventom, Deistung and Bray, 1988), *Ovis aries* (Benboubetra *et al.*, 2004) and *Capra aegagrus* (Atmani, Benboubetra and Harrison, 2004).

1.5. Xanthine Oxidoreductase amino acid sequence alignment

Human, sheep and bovine XOR sequences were aligned using ESPrpt 3.0. (Robert and Gouet, 2014).





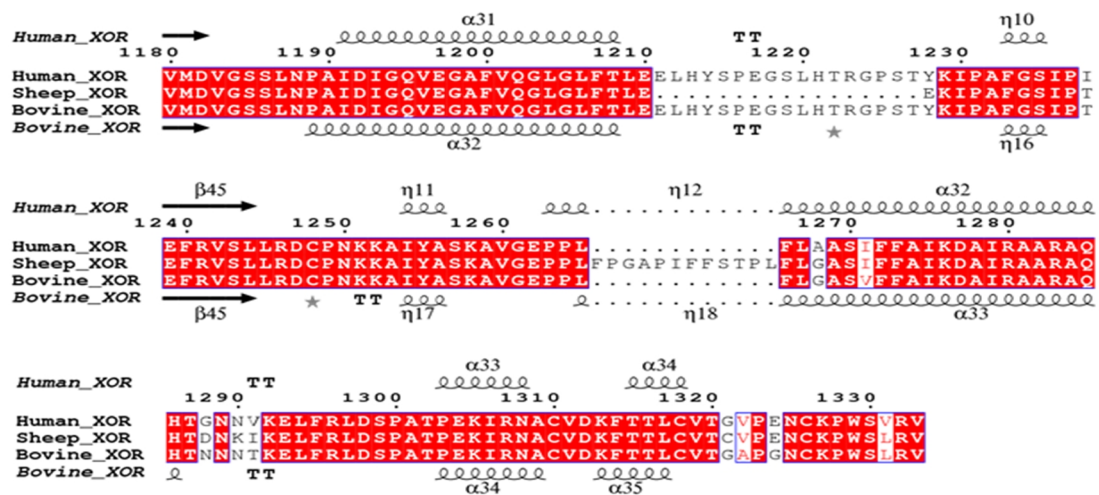


Figure 1.5: Human, ovine and bovine XOR alignment. Amino acids in red boxes represent conserved amino acids; amino acids in red font colour represent amino acids that have similar properties; the other amino acids have different properties. The amino acids in: green boxes represent the first iron-sulfur binding site; in black boxes represent the second iron-sulfur binding site; in yellow boxes represent the FAD binding site; blue boxes represent the Moco binding site. The structural information for the human XOR was extracted from PDB 2CKJ while that of the bovine XOR was given by PDB 3UNC. The amino acid numbering represents the human enzyme. Alignment was done using ESPrpt 3.0 (Robert and Gouet, 2014).

Table 1.3: Percent identity and divergence of the different domains and the whole sequences of XOR. In the amino acids, the iron-sulfur domains correspond to the 1-166 fragment; the FAD domain corresponds to the 228-542 fragment of human XOR, the 228-543 fragment of sheep XOR, and the 228-541 fragment of bovine XOR; the Moco domain corresponds to the 557-1333 fragment of human XOR, the 558-1329 fragment of sheep XOR, and the 556-1329 fragment of bovine XOR.

Iron-Sulfur domains				
	<i>Percent Identity</i>			
		Human XOR	Sheep XOR	Bovine XOR
<i>Divergence</i>	Human XOR		94.6	94.0
	Sheep XOR	5.6		99.4
	Bovine XOR	6.3	0.6	
FAD domain				
	<i>Percent Identity</i>			
		Human XOR	Sheep XOR	Bovine XOR
<i>Divergence</i>	Human XOR		88.0	87.6
	Sheep XOR	13.1		96.8
	Bovine XOR	13.6	3.2	
Moco domain				
	<i>Percent Identity</i>			
		Human XOR	Sheep XOR	Bovine XOR
<i>Divergence</i>	Human XOR		90.3	89.8
	Sheep XOR	10.4		95.5
	Bovine XOR	10.9	4.6	
Whole Sequence				
	<i>Percent Identity</i>			
		Human XOR	Sheep XOR	Bovine XOR
<i>Divergence</i>	Human XOR		88.0	89.7
	Sheep XOR	10.8		94.1
	Bovine XOR	11.1	3.7	

The iron-sulfur domains show the highest percent identity for the three species compared. The FAD domain of the human XOR shows the lowest percent identity with both sheep and bovine XOR. The sheep and bovine XOR share the highest whole

sequence percent identity with 94.1% identity while the human and sheep XOR share the lowest whole sequence percent identity with 88.0% identity. All amino acid numbering given in this section are according to the human XOR, unless otherwise stated.

All three XOR proteins have iron-sulfur clusters coordinated to cysteine residues, specifically residues Cys⁴³, Cys⁴⁸, Cys⁵¹, Cys⁷³ for the first iron-sulfur cluster (green boxes in alignment) and Cys¹¹³, Cys¹¹⁶, Cys¹⁴⁸ and Cys¹⁵⁰ for the second iron-sulfur cluster (black boxes in alignment). Also, the amino acids for the FAD binding site (amino acids Phe³³⁷, Asp³⁶⁰, Leu⁴⁰⁴, Lys⁴²²) (yellow boxes in alignment) and for the Moco binding site (amino acids Gln⁷⁶⁸, Phe⁷⁹⁹, Arg⁹¹³, Ala¹⁰⁸⁰) (blue boxes in alignment) are conserved in the three proteins.

The amino acid cluster responsible for the conversion of XDH to XO (amino acids Arg³³⁵, Trp³³⁶, Arg⁴²⁷, and Phe⁵⁴⁹) is conserved in all three species. The loop that blocks NAD⁺ binding once XDH converts to XO (amino acid Gln⁴²³ to Lys⁴³³) is conserved. The NAD⁺ binding loop (amino acid Glu⁴⁹³ to Gly⁵⁰³) is conserved with the exception of amino acids 495 and 497 (bovine and sheep XOR have Ser⁴⁹⁴ and Ser⁴⁹⁶ while human XOR has His⁴⁹⁵ and Pro⁴⁹⁷). Serine is a polar charged amino acid while histidine is a positively charged amino acid and proline is a nonpolar aliphatic amino acid. Due to these difference in charges, the shape of both loops may be affected.

All the amino acids, Glu⁸⁰³, Arg⁸⁸¹, Thr¹⁰¹¹, Glu¹²⁶², at the active site of the Moco, are conserved in all three species.

1.6. Structure of Bovine Xanthine Oxidoreductase

The first X-ray crystal structures of both forms of XOR, isolated from bovine milk, were determined by Eger and co-workers (Eger *et al.*, 2000). From the crystal structure, it was determined that bovine XOR is a homodimer where each monomer contains five domains, from the C-terminus: two large domains that together form the binding site of the molybdenum domain (the Moco), an FAD domain, and two [2Fe-2S] domains at the N-terminus. The two monomers are bound via the Mo binding portion forming the homodimer. The Mo centres are 52 Å apart and there is no electron transfer between the two monomers. The transfer of electrons within each monomer is an almost linear pathway starting from the Moco where the oxidative half-reaction occurs, continuing through the two [2Fe-2S] domains and finishing at the FAD domain where the reductive half-reaction occurs (Enroth *et al.*, 2000). Half-reactions are shown in Table 1.4.

Table 1.4: Half-reactions at the XOR active sites

$\text{RH} + \text{H}_2\text{O} \rightarrow \text{ROH} + 2\text{H}^+ + 2\text{e}^-$	<i>General oxidative half-reaction at Moco</i>
$\text{C}_5\text{H}_5\text{N}_4\text{O} \text{ (hypoxanthine)} + \text{H}_2\text{O} \rightarrow \text{C}_5\text{H}_4\text{N}_4\text{O}_2 \text{ (xanthine)} + 2\text{H}^+ + 2\text{e}^-$	<i>Hypoxanthine oxidative half-reaction at Moco</i>
$\text{C}_5\text{H}_4\text{N}_4\text{O}_2 \text{ (xanthine)} + \text{H}_2\text{O} \rightarrow \text{C}_5\text{H}_4\text{N}_4\text{O}_3 \text{ (uric acid)} + 2\text{H}^+ + 2\text{e}^-$	<i>Xanthine oxidative half-reaction at Moco</i>
$2\text{O}_2 + 2\text{H}_2\text{O} + \text{e}^- \rightarrow 2\text{H}_2\text{O}_2 + \text{O}_2^-$	<i>Reductive half-reaction at FAD for XO</i>
$\text{NAD}^+ + \text{H}^+ + 2\text{e}^- \rightarrow \text{NADH}$	<i>Reductive half-reaction at FAD for XDH</i>

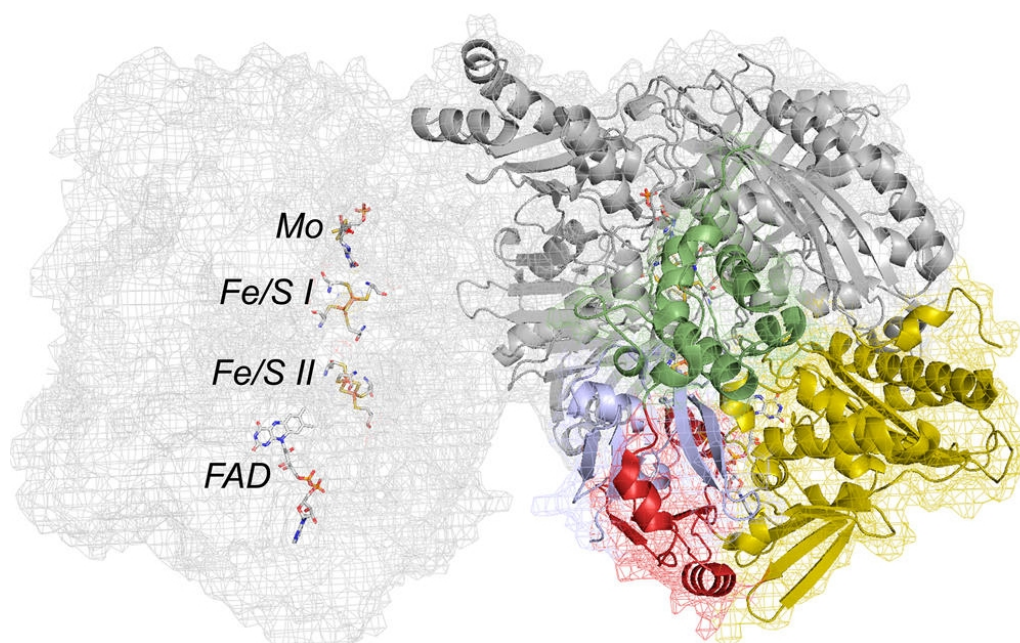


Figure 1.6: Crystal structure of the bovine XOR, PDB 1FO4 with a resolution up to 2.1 Å. On the right-hand side, from the C-terminus: grey represents the Moco domain, yellow represents the FAD domain and the green and blue represent the [2Fe-2S] I and [2Fe-2S] II domains respectively at the N-terminus. The red represents the link portion between the [2Fe-2S] II domain and the FAD domain. On the left hand side, the electron transfer from Moco to FAD is shown (Enroth *et al.*, 2000; Hille, Hall and Basu, 2014).

1.7. Reaction mechanism of xanthine to uric acid

The overall mechanism by which XOR converts xanthine to uric acid is depicted in Figure 1.7 (Hille, 1996; Xia, Dempski and Hille, 1999). The ultimate oxygen donor is water which at the end of the reaction donates its hydroxide ion to the Mo (Murray, Watson and Chaykin, 1966). The mechanism starts with a proton extraction from the hydroxide (OH) bound to the Mo at the Moco site by Glu¹²⁶¹ in the active site of bovine XOR. This is followed by a nucleophilic attack by the deprotonated Mo-O⁻, which is nucleophilic enough to attack the hydrogen on the to-be hydroxylated carbon (xanthine, carbon 6). The hydride removed from this carbon is transferred to the Mo=S group which changes the valency of the Mo from (VI) to (IV). The subsequent reactions are dependent on the reaction conditions and substrate. If the electron transfer from the Mo centre to the sulfur precedes the product displacement, Path B (Figure 1.7) will happen. In this case, an Mo(V) species will form which, ‘very rapidly’ (according to EPR signal terms (Xia, Dempski and Hille, 1999)), will displace the product and form the Mo(VI) species via hydrolysis. Path B was shown to occur at high substrate concentration (Morpeh, 1983; Xia, Dempski and Hille, 1999), high pH where the accumulation of the Mo(V) intermediate increased from pH 8.3 to 10 (Mcwhirter and Hille, 1991), and with slow substrates such as 2-hydroxy-6-methylpurine (Mcwhirter and Hille, 1991). However, the Mo(V) intermediate is skipped in most conditions and the product dissociation occurs first (Path A, Figure 1.7) (Xia, Dempski and Hille, 1999; Hille, Hall and Basu, 2014).

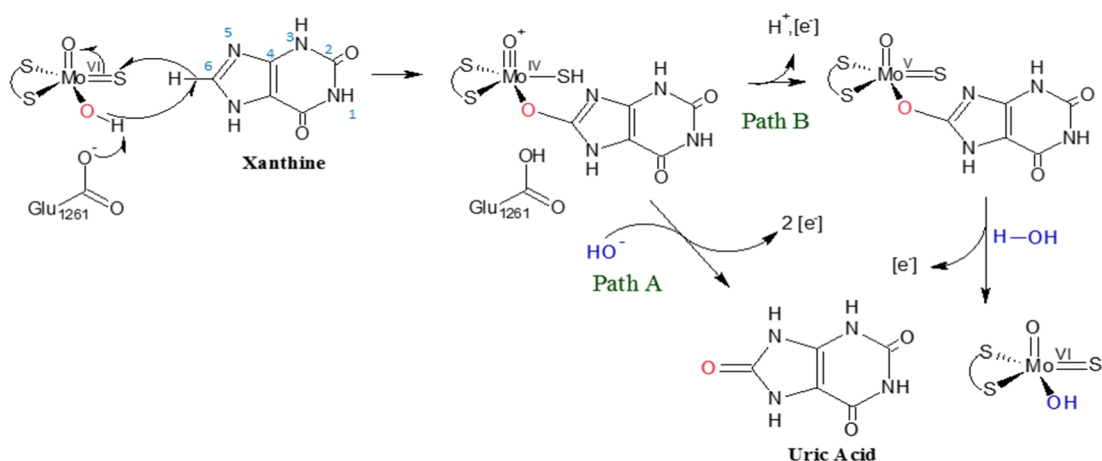


Figure 1.7: Reaction mechanism of XOR with xanthine as a substrate. From the first intermediate, two paths can occur. Which pathway takes place is dependent on the reaction conditions; at pH's lower than 8.3, Path A occurs whereas at high pH, high substrate concentration, and slow substrates, Path B occurs. Structures drawn using ACD/Chemsketch (version 2018.1).

Both forms of XOR carry out the reaction mechanism described. However, the electron acceptor at the end of reaction differs depending on the form of XOR; XDH favours oxidized nicotinamide adenine dinucleotide (NAD^+), converting it to reduced nicotinamide adenine dinucleotide (NADH) while XO is specific for oxygen (O_2), reducing it to hydrogen peroxide (H_2O_2) and superoxide ($\text{O}_2^{\bullet-}$) (Nishino, 1994; R Hille and Nishino, 1995). The reactions that are catalysed by XOR are shown in Figure 1.8.

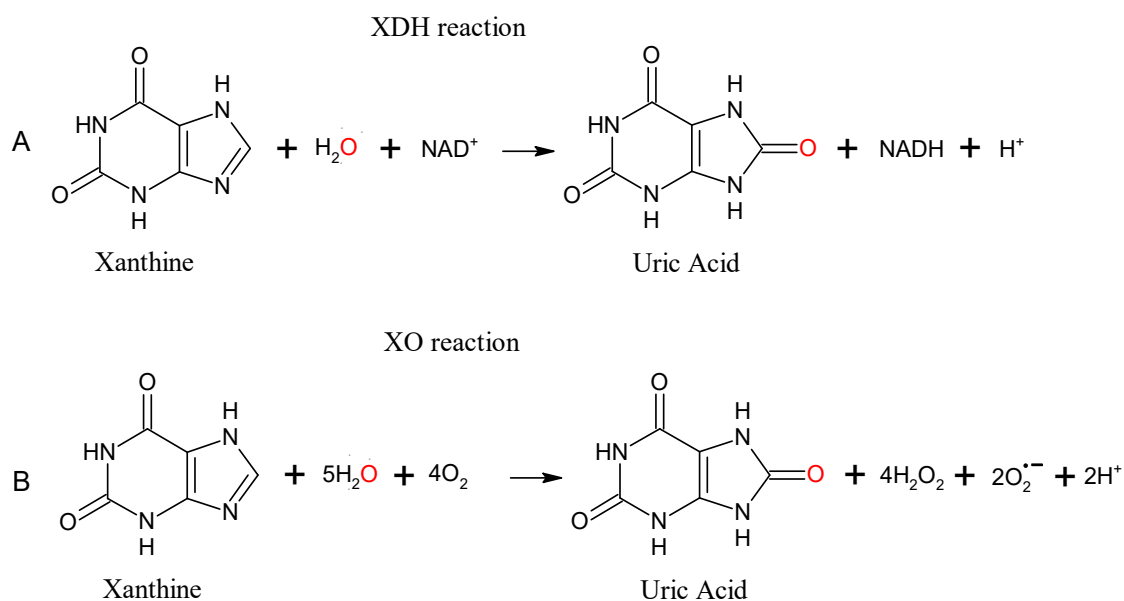


Figure 1.8: XOR catalysed reactions. A – XDH reaction with NAD^+ . B – XO reaction with O_2 . Structures drawn using ACD/Chemsketch (version 2018.1).

Figure 1.9 summarises the general transfer of electrons in XOR. Xanthine donates its electrons at the Moco domain where they are transferred to two $[2\text{Fe-2S}]$ domains and ultimately to the FAD domain where the electrons are accepted either by NAD^+ or O_2 .

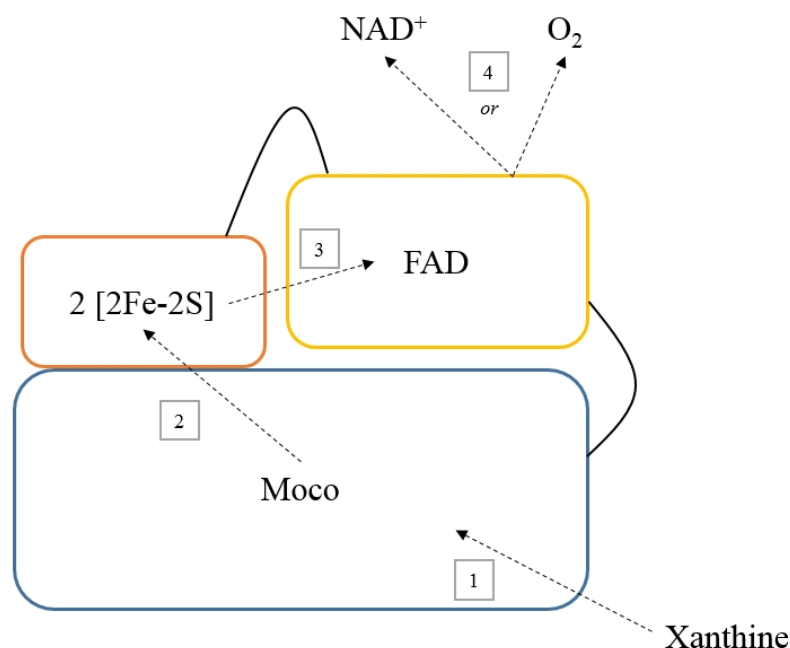


Figure 1.9: General transfer of electrons in XOR. The arrows represent the electron transfer. Xanthine donates a pair of electrons at the Moco domain which subsequently propagate to the two [2Fe-2S] clusters to the FAD domain. The electrons are then accepted by either oxygen or NAD⁺, depending if the enzyme is in the oxidised or reduced state respectively. Figure adapted from Hille, R. and Nishino, T. (Russ Hille and Nishino, 1995).

1.8. Mechanism of XDH to XO conversion

XDH can be converted to XO via oxidation or limited irreversible proteolysis. Limited irreversible proteolysis occurs due to proteases such as chymotrypsin, trypsin after Lys⁵⁵¹ (Stirpe and Della Corte, 1969; Enroth *et al.*, 2000), mitochondrial proteases (Saksela, Lapatto and Raivio, 1999) or pancreatin cleavage after Leu²¹⁹ and Lys⁵⁶⁹ (Enroth *et al.*, 2000) (bovine XOR numbering). The conversion mechanism of XDH to XO is of particular interest in humans where XO was attributed to a number of disorders due to its ability of producing oxygen radicals (Enroth *et al.*, 2000). To elucidate this conversion, bovine XOR and rat XOR were studied (Enroth *et al.*, 2000). It was found that although there are 36 cysteines residues in rat XOR, only four are modified by disulfide bonds during this oxidation step (Saito, Nishino and Massey, 1989). On comparing the *Rattus norvegicus* XOR, which is found in both XO and XDH forms, with the *Gallus gallus* XDH, which is found only as XDH, Nishino *et al.* demonstrated that two pairs of cysteine, Cys⁵³⁵ and Cys⁹⁹², and Cys¹³¹⁶ and Cys¹³²⁴ (rat XOR numbering)

appeared to be involved in the conversion of XDH to XO (Nishino *et al.*, 2005). In the bovine XOR crystal structure, the Cys⁹⁹² is situated on the molecule surface whereas Cys⁵³⁵ is located on a linker peptide (Lys⁵³² – Ser⁵⁸⁹) between the Moco and FAD that is not resolved in the crystal structure. Through reversible oxidation and site-directed mutagenesis Kuwabara *et al.* determined that the amino acid cluster of Phe⁵⁴⁹, Arg³³⁵, Trp³³⁶, and Arg⁴²⁷ (bovine XOR numbering) form a π -cation interaction that is important for holding the active site loop Gln⁴²² – Lys⁴³². The disruption of this amino acid cluster displaces the active site loop Gln⁴²² – Lys⁴³² during the conversion of XDH to XO (Kuwabara *et al.*, 2003). The displacement of this active loop determines the preference of XDH for NAD⁺ and XO for O₂ as electron acceptors/substrates respectively (Enroth *et al.*, 2000).

The proposed mechanism of the conversion of XDH to XO is summarised in Figure 1.11. In the XDH form, the linker peptide is stabilised by the π -cation interactions of the amino acid cluster. The oxidation of the cysteine residues and the formation of a disulfide bridge between Cys⁵³⁵ and Cys⁹⁹², disrupts this linker peptide, opening a solvent gate. This disruption produces a conformational change on the active site loop Gln⁴²² – Lys⁴³² which blocks the NAD⁺ approach, lowering NAD⁺ activity and changes the electrostatic environment of the FAD. Both the solvent gate opening and the change in the electrostatics increase the reactivity towards O₂. The oxidation and disulfide bond formation at Cys¹³¹⁶ and Cys¹³²⁴ obstruct the insertion of the C-terminus into the NAD⁺ binding cavity. This insertion was observed to be important for the NAD⁺ binding in the bovine structure. This further lowers NAD⁺ binding, favouring O₂ binding and thus XO activity (Nishino *et al.*, 2005).

From the X-ray structures (Figure 1.11) of the bovine XDH and XO, Enroth *et al.* demonstrated that on conversion of the XDH to XO, a conformational change masks the FAD active site and changes the electrostatic potential around the FAD, resulting into a change in substrate specificity (Enroth *et al.*, 2000).

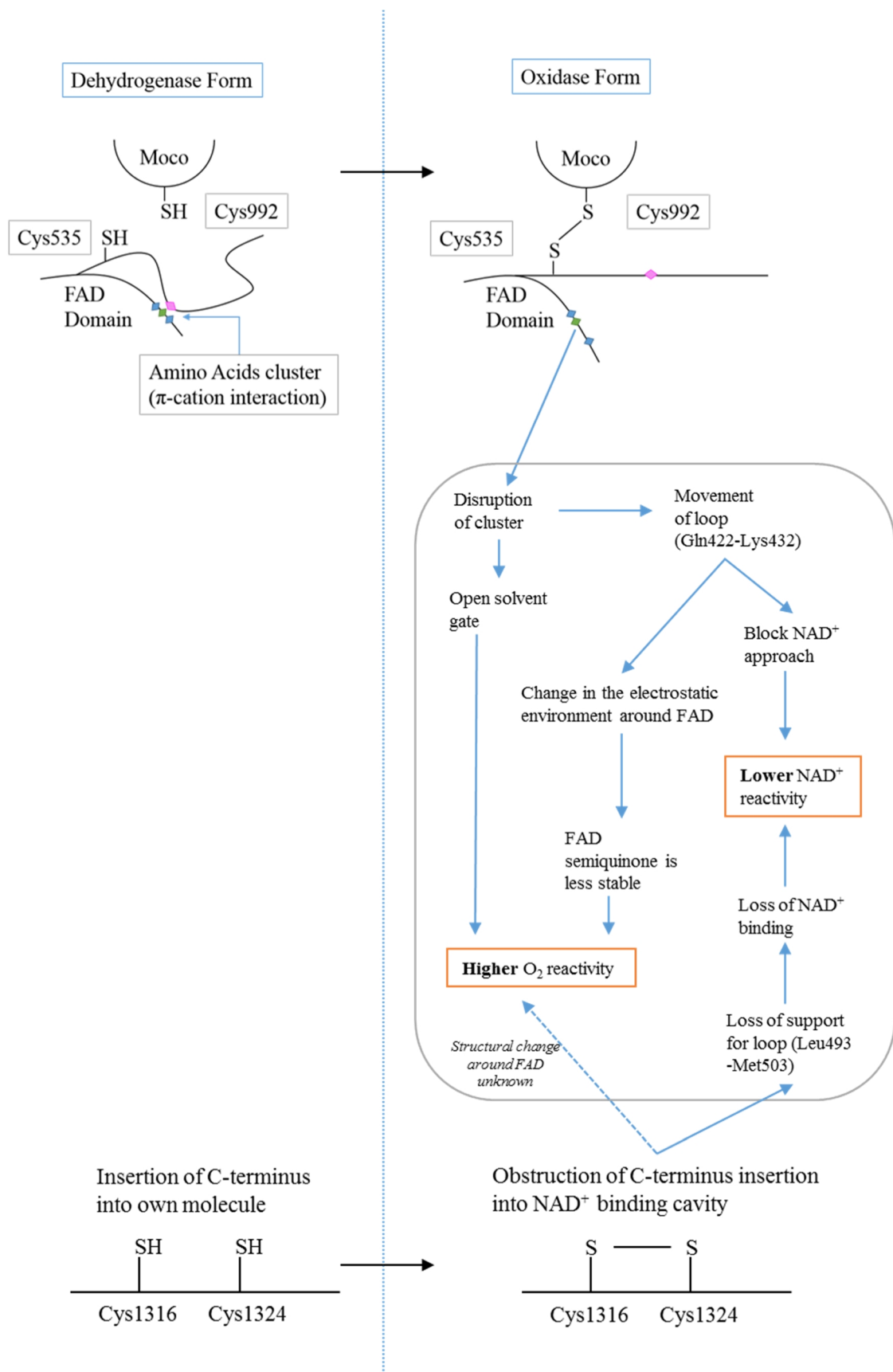


Figure 1.10: Mechanism of the conversion of XDH to XO. Reproduced from Nishino, T. *et al.* (Nishino *et al.*, 2005).

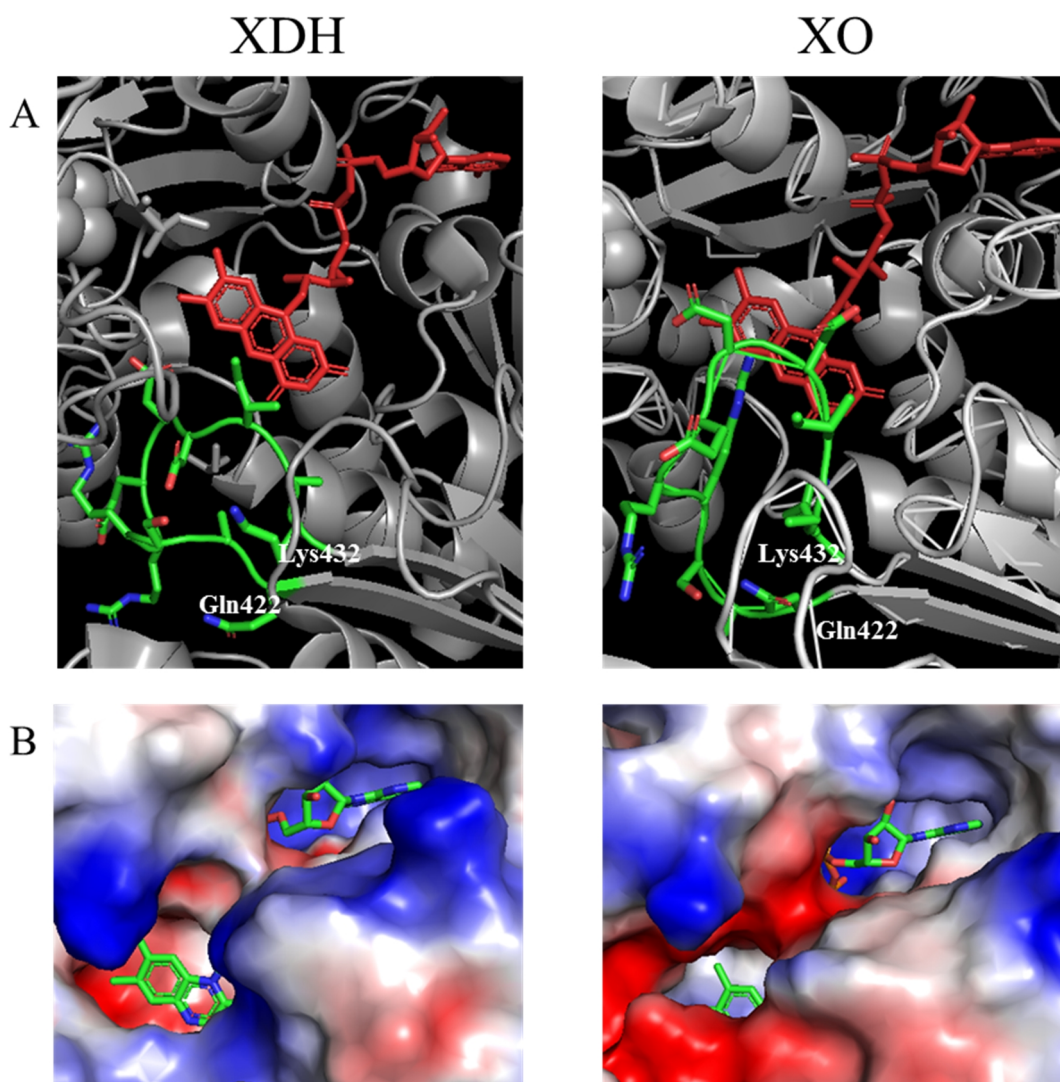


Figure 1.11: Representation of the electrostatic environment around the FAD domain. A: The Gln422-Lys432 loop (green) with respect to the FAD (red). In XO the loop obstructs the FAD. B: Electrostatic surface around the FAD (green) where the red and blue regions represent electronegative regions and electropositive regions respectively. XDH has more electropositive regions around the FAD and bigger pores for the active site. XO has more electronegative regions around the FAD and smaller pores, blocking NAD^+ approach. XDH was generated from PDB code 3UNC while XO was generated from 1FIQ. Figure generated by PyMOL Molecular Graphics System (Schrodinger, 2019).

1.8.1. Ovine Xanthine Oxidoreductase

Ovine XOR was first purified from sheep milk in 2004 by M. Benboubetra *et al.* using the method described for bovine milk XOR (Benboubetra *et al.*, 2004). The majority of the XOR in sheep milk was demolybdo XOR (80%). Ovine XOR lacks the strong affinity to heparin that is characteristic of both bovine and caprine XOR (Benboubetra *et al.*, 2004). A comparison of the amino acid sequences of XOR reveals a deletion of 17 amino acids at position 1200 and an insertion of 12 amino acids at position 1266 (bovine numbering) in the ovine protein (Figure 1.12). It has been postulated that the weak heparin binding of ovine XOR may be due to the lack of surface arginine and lysine residues (Vella *et al.*, 2014).

Human	VQGLGLFTLEELHYSPEGSLHTRGPSTYKIPAFGSIHTEFRVSLLRDCPNKKAIYASKAVGEPPLF.....LAASIFFFAIKDAIRARAQH
Bovine	VQGLGLFTLEELHYSPEGSLHTRGPSTYKIPAFGSIHTEFRVSLLRDCPNKKAIYASKAVGEPPLF.....LGASVFFFAIKDAIRARAQH
Ovine	VQGLGLFTLEE.....KIPAFGSIHTEFRVSLLRDCPNKKAIYASKAVGEPPLFPGAPIFFSTPLFLGASVFFFAIKDAIRARAQH

Figure 1.12: Sequences alignment of XOR obtained from the NCBI. Blue and red coloured amino acid residues represent positively and negatively charged residues respectively. Boxes highlight the differences in the amino acids. The ellipses highlight the deletion and insertion parts of the ovine XOR. Figure adapted from M. Vella *et al.* (Vella *et al.*, 2014).

1.9. Role of Xanthine Oxidoreductase in human health

1.9.1. Health conditions related directly to Xanthine Oxidoreductase

XOR catalyses the last two steps of purine degradation that include the sequential oxidation of hypoxanthine to xanthine, and xanthine to uric acid. Humans, together with other primates like the New World monkeys, experienced a mutational loss during evolution resulting in the lack the enzyme uricase. Subsequently, XOR became the final catalyst in purine degradation. As a consequence, the end product of purine degradation is uric acid which is not broken down into the more soluble allantoin.

Deficiency of XOR activity might result in xanthinuria. There are two types of xanthinuria: xanthinuria type I and xanthinuria type II. In xanthinuria type I, mutations cause a loss of activity of XOR, leading to the accumulation of xanthine and hypoxanthine in urine. Patients with xanthinuria type I are at risk of developing acute renal failure, urinary tract calculi and myositis. In these patients, xanthine concentrations are higher

than those of hypoxanthine, suggesting that hypoxanthine was salvaged. Since XOR can hydroxylate purines analogues, polymorphisms in the XOR gene might also elevate the toxicity of drugs like 6-mercaptopurine. In xanthinuria type II, mutations in the Moco sulfurase (MCSU) gene, the gene responsible for the sulfuration of the Moco moiety, cause loss of function to both XOR and aldehyde oxidase. Even though both types of xanthinuria have similar risks, xanthinuria type II patients lack the ability to metabolize allopurinol, a competitive inhibitor which can be metabolized by both XOR and aldehyde oxidase to produce oxypurinol. Xanthinuria type II is also associated with behavioural symptoms, autism, mental delay, osteopenia, and hair and teeth defects and it is considered as one of the metabolic disorders that may contribute to complex neuropsychiatric disorder development (Schwarz and Belaidi, 2013).

In contrast to xanthinuria, an increased XOR activity leads to secondary hyperuricemia. Hyperuricemia is a condition involving an increase in the levels of uric acid that results in increased urinary excretion. If hyperuricemia is not monitored, this condition could lead to gout which is a rheumatic disease involving the precipitation of urate crystals in periarticular structures and joints. This leads to inflammation and possible destruction of tissues surrounding the urate crystals. With about 4% of males being affected, gout is the commonest inflammatory arthropathy in the western world. Both types of xanthinuria and hyperuricemia were associated with cardiovascular diseases where studies showed that rheumatic conditions increase the probability of having a cardiovascular disease. Allopurinol is the current treatment protocol for these conditions, however, novel structure-based drugs are being developed (Shah and Keenan, 2010; Schwarz and Belaidi, 2013).

Uric acid may facilitate vascular damage by inducing the production of tumour necrosis factor- α , a potent inflammatory mediator. This proinflammatory action of uric acid may contribute to endothelial damage. Moreover, uric acid can cause vascular occlusion and ischaemia by inducing proliferation of vascular endothelial cells by increasing levels of endothelin-1 (Shah and Keenan, 2010).

1.9.2. Mutations of Xanthine Oxidoreductase

The gene coding for human XOR is located on chromosome 2p23. Presently, a total of 18 mutations have been identified. Conditions related to these mutations were described (Yang *et al.*, 2008; Stiburkova *et al.*, 2012).

Table 1.5: List of mutations of human XOR. (Yang *et al.*, 2008; Stiburkova *et al.*, 2012).

Associated with disease	Low XOR activity	High XOR activity	Associated with hypertension
p.R149C	p.P555S	p.I703V	p.G172R
p.R228X	p.R607Q	p.H1221R	p.A932T
p.K722X	p.T623I		p.N1109T
p.T910K	p.N909K		
p.T910M	p.R1150P		
c.2567del1	p.C1318Y		
c.1664dup1			

Details on Table 1.5: p. – Protein. c. – coding DNA. del – Deletion. dup – Duplication.

Yang *et al.* screened 48 Japanese patients with either hypertension or renal failure or both and found three mutations that give rise to single nucleotide polymorphism. These mutations are present in conserved residues amongst different species. The G172R is not present in any of XOR active site domains whereas both A932T and N1109T are present in the Moco domain. As a result, Yang *et al.* suggest that A932T and N1109T might have a role in hypertension and that more *in vivo* and *in vitro* studies are required (Yang *et al.*, 2008).

1.9.3. Xanthine Oxidoreductase and reactive oxygen species

In humans, XOR is transcribed as XDH. XDH may then be oxidized or auto-protolysed to XO. This conversion may occur during an ischaemia-reperfusion injury. Ischaemia is a state of limited oxygen levels, known as hypoxia, due to blood supply restriction while reperfusion is the return of blood supply (and thus oxygen) to the tissue. During ischaemia, oxygen-starved cells experience an increase in calcium that activates calpain, a calcium-dependent protease. Calpain converts XDH irreversibly to XO via limited proteolysis (Robert and Robert, 2014). Furthermore, during ischaemic conditions, ATP is released into the extracellular space where a set of membrane bound enzymes convert ATP into adenosine. Adenosine is further catabolised to produce hypoxanthine as the final product (Barsotti and Ipata, 2004).

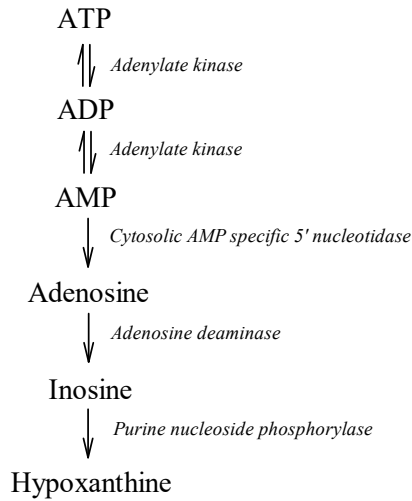


Figure 1.13: Adenosine pathway of extracellular ATP catabolism.

Ischaemic/hypoxic conditions also lead to the binding of XO to glycosaminoglycans (GAGs) on the surface of the endothelial cells. This binding causes localised amplification of the XO levels and an increase in XO activity (Kelley, 2015). During reperfusion, an oxidizing environment develops in the cells that, in turn further oxidizes XDH into XO. Moreover, in the presence of oxygen, hypoxanthine can act as a substrate for XO to produce H_2O_2 and $O_2^{\cdot-}$ as shown in Figure 1.14.

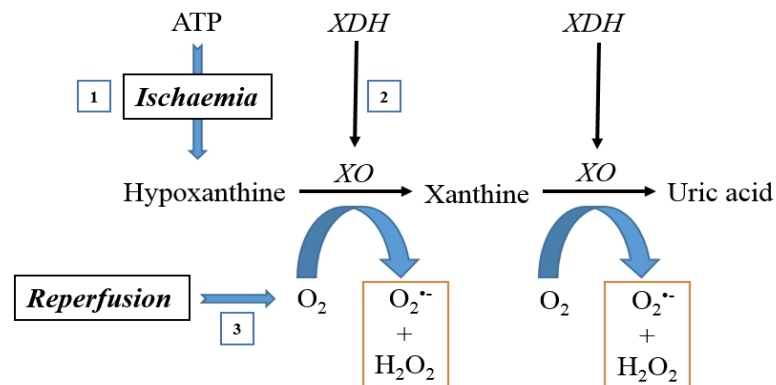


Figure 1.14: Ischaemia-reperfusion effects on XOR action. 1. During ischaemia ATP is catabolised to hypoxanthine. 2. XDH is converted to XO due to limited proteolysis during ischaemia or oxidation during reperfusion. 3. Oxygen supply is back during reperfusion which can act as an electron acceptor producing reactive oxygen species marked in red.

Hypoxia and various inflammatory cytokines lead to the induction of XOR expression in arterial endothelial cells (Kelley *et al.*, 2006). Once expressed, XOR is secreted and transported by the circulatory system (Zhou *et al.*, 2005; Kelley *et al.*, 2006). Even though oxygen is not the preferred substrate of XDH, oxygen may be reduced by XDH when NAD^+ concentrations are low enough. This can also happen during the state of ischaemia/hypoxia, where oxidation of NADH by the mitochondria is decreased, leading to a reduction in NAD^+ concentration (Zhou *et al.*, 2005).

Both H_2O_2 and $\text{O}_2^{\cdot-}$ are reactive oxygen species (ROS). ROS are oxygen radicals such as $\text{O}_2^{\cdot-}$ or compounds like H_2O_2 that form oxygen radicals (Droge, 2002). Although it is not a very powerful ROS, H_2O_2 can react with $\text{O}_2^{\cdot-}$ to form the more reactive hydroxyl radicals (OH^{\cdot}) via the Fenton reaction using iron or copper as catalysts (Walling, 1975). Alternatively, $\text{O}_2^{\cdot-}$ can react with nitric oxide (NO^{\cdot}) to produce peroxynitrite (ONOO^-). ONOO^- is a very strong oxidizing agent which can cause damage to a number of biomolecules such as aconitase (Hausladen and Fridovichs, 1994), Hsp90 (Franco *et al.*, 2013), and mitochondrial membrane components (Szabó, Ischiropoulos and Radi, 2007).

Excess ROS appear to promote vascular leakage during inflammation and participate in the cellular response to injury. These cellular responses include vascular smooth muscle cell apoptosis and monocyte adhesion. Moreover, ROS increase the degree of activation of nuclear factor- κB , a potent inflammation regulator and pro-atherogenic agent that facilitates oncogenesis due to its role in cell proliferation and survival (Shah and Keenan, 2010).

It is important to note that ROS bring about cellular damage only when the concentration of ROS exceeds the physiological set point (Kovac, Dinkova-Kostova and Abramov, 2005). In fact, ROS, together with reactive nitrogen species (RNS), have a fundamental role in signal transduction and antimicrobial activity. Moderate concentrations of these species are important for processes such as cell proliferation, neurotransmission and phagocyte activation (Fang, 2004). However, the target moieties for ROS and RNS are not only present in microorganisms and thus they may damage host tissues when levels are high. When this limit is exceeded, ROS may cause oxidative DNA damage, resulting in the stimulation of repair enzymes, depletion of ATP and the stimulation of cell death cascades (Fang, 2004).

ROS can lead to lipid peroxidation. Polyunsaturated lipids react with ROS to form reactive compounds such as lipid peroxy radicals and 4-hydroxyononanal (Barrera, Pizzimenti and Dianzani, 2008) which in turn can react with DNA and membrane proteins

(Esterbauer, Schaur and Zollner, 1991). Lipid peroxidation thus leads to changes in fluidity and permeability of the lipid bilayer (Dix and Aikens, 1993). Involvement of ROS has been associated with neurodegenerative disorders and acute neurological diseases such as strokes and epilepsy (Kovac, Dinkova-Kostova and Abramov, 2005; Abramov, Scorziello and Duchen, 2007). This may be due to the formation of OH^\bullet radicals by the Fenton reaction as the brain is an organ rich in iron and copper. In fact, studies show that XO has a role in brain injury and stroke (Abramov, Scorziello and Duchen, 2007).

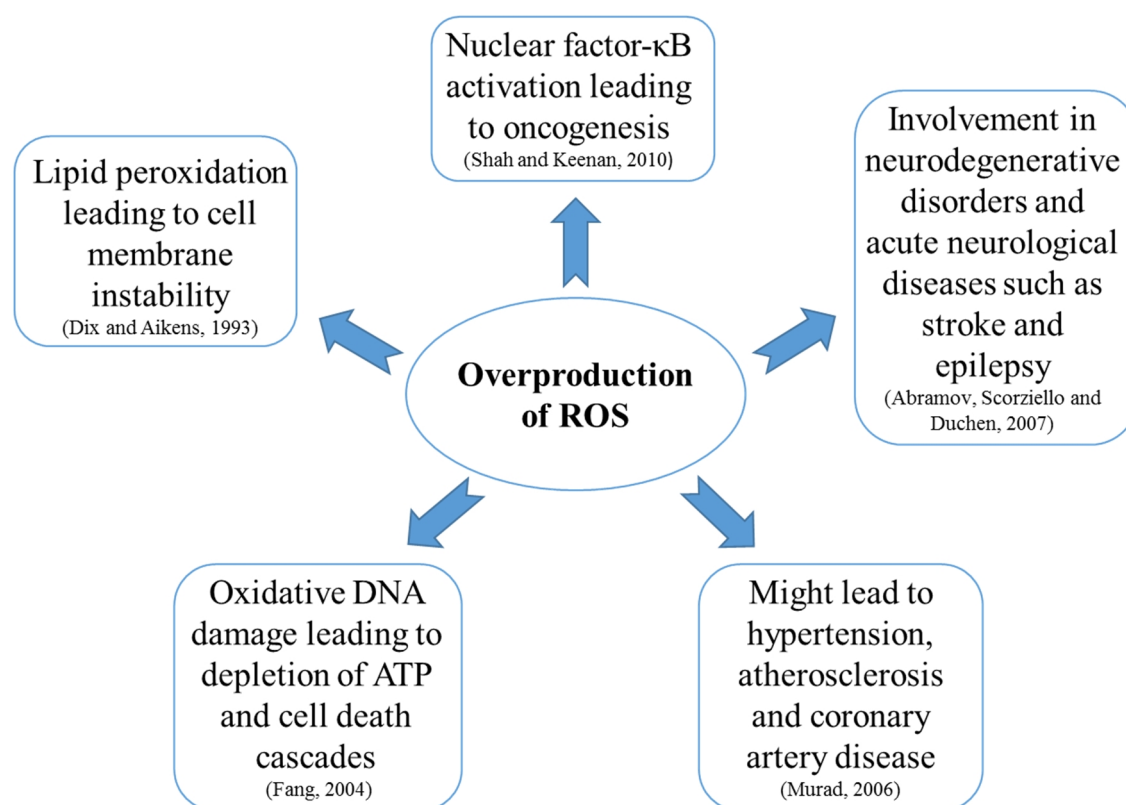


Figure 1.15: Effects of overproduction of ROS on human health.

1.9.4. Xanthine Oxidoreductase and nitrate(III)

XOR is capable of producing beneficial NO^\bullet under hypoxic conditions via a nitrate(III) reductase activity. This involves the reduction of NO_2^- to NO^\bullet at the Moco site using either NADH or xanthine as the electron donor (Godber *et al.*, 2000; Maia and Moura, 2011). However, the site of electron donation differs with the electron donor; NADH donates its electrons to the FAD site while xanthine donates its electrons directly to the Moco site (Li *et al.*, 2008). Under normal physiological conditions, the preferential use of xanthine as an electron acceptor to produce uric acid inhibits the nitric oxide formation. Hence, it is hypothesised that it is the NADH that acts as the primary electron

donor to produce nitric oxide, which indicates that XDH, not XO, is the favoured catalyst under hypoxic conditions (Li *et al.*, 2001). The presence of oxygen, in fact, leads to a lower production of NO[•] due to the oxidation of the Moco site. Consequently, NO[•] forms under hypoxic conditions. The formation of NO[•] is also an acid catalysed reaction and it only forms under acidic pH, for example during inflammation or intracellular acidosis under ischaemic conditions where pH values fall to 6.0 or below (Zweier, Samouilov and Kuppusamy, 1999).

NO[•] acts as a vasodilator and a cardiovascular protective molecule. The risk factor of cardiovascular disease is inversely proportional to the concentration of plasma nitrite (Bolli, 2001). As a vasodilator, nitric oxide decreases the mean blood pressure and thus controls hypertension and protect against cardiovascular disease (Ghosh *et al.*, 2013). When rats were administered allopurinol, a Moco XOR inhibitor, the decrease in blood pressure by nitrites was reduced, suggesting that XOR has a key role in NO[•] production from nitrites. Other cardiovascular diseases in which NO[•] plays an important protective role are peripheral artery disease, myocardial infarction and cardiac arrest (Omar and Webb, 2014). Further research is required to identify the possible impact of XOR-mediated NO[•] formation on therapeutic approaches to address vascular disease (Kelley, 2015).

1.9.5. Reactive nitrogen species

Reactive nitrogen species (RNS) are a series of nitrogen compounds that act as reactive free radicals. These include peroxynitrite (ONOO⁻), nitrogen dioxide and dinitrogen trioxide. The formation of ONOO⁻ by the reaction of NO[•] and O₂^{-•}, which can both be produced by XOR (Nishino, 1994; Godber *et al.*, 2000), results in a rapid depletion of NO[•]. ONOO⁻ is therefore a secondary product of XOR. As NO[•] is a cardiovascular protective molecule, its deficiency may contribute to cardiovascular disease such as hypertension, atherosclerosis and coronary artery disease (Murad, 2006).

The formation of ONOO⁻ is associated with the site of O₂^{-•} generation. This is due to the fact that O₂^{-•} has a shorter half-life and has diffusion restriction when compared to NO[•]. Once formed, ONOO⁻ has a very short half-life of about 10 ms at physiological pH. Despite this, the ONOO⁻ can cross cell membranes and react with molecules in the surrounding cells (Marla, Lee and Groves, 1997). In fact, ONOO⁻ can exert its effect within 20 μm from its source of formation (Szabó, Ischiropoulos and Radi, 2007).

A number of adverse reactions occur when ONOO^- reacts with other biomolecules. For instance, ONOO^- inactivates antioxidant enzymes such as manganese superoxide dismutase, causing mitochondrial injury (Crowt, Kerby and Beckmantt, 1996); oxidises cysteine and nitrates tyrosine residues in membrane channels such as calcium pumps, thereby impairing cellular ionic balance (Bartesaghi *et al.*, 2006); causes DNA double-strand breakages which result in cell death (Salgo *et al.*, 1995); and deplete antioxidants such as cysteine, thus increases free-radical damage (Quijano *et al.*, 1997).

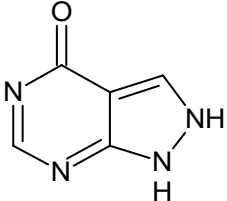
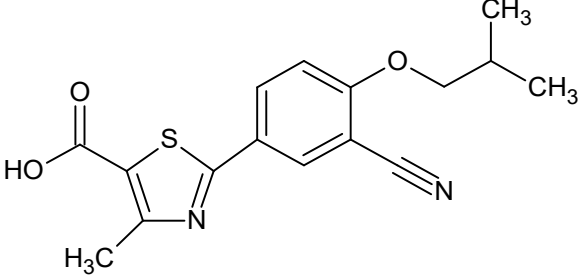
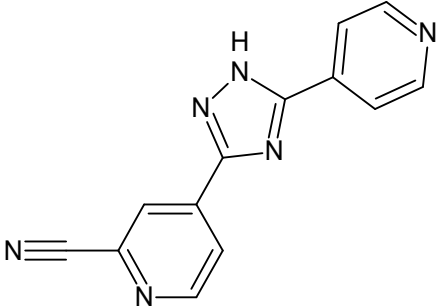
1.9.6. Xanthine Oxidoreductase-based Therapeutics

The level of XO in blood can be used as an indication of disease and can act as a biomarker for a number of conditions including oxidative stress that is attributed to neurodegenerative diseases. A biomarker has to have the potential to give an indication of the severity of the disease, be able to identify patients with complication risks and can monitor treatment response (Phillips *et al.*, 2004).

The first line of treatment of high urate levels is the use of xanthine oxidase inhibitors (XOI). The current available drugs are administered when the serum urate concentration is equal to or higher than 6.8 mg/dl (Choi, Mount and Reginato, 2005). Allopurinol is the predominant XOI used for clinical applications, acting as a uric acid lowering drug. Allopurinol is used to treat gout and to prevent high uric acid levels in cancer patients receiving chemotherapy. Uric acid levels in cancer patients increase due to tumour lysis syndrome which may result in rapid cell death. Allopurinol has a high efficacy and is relatively inexpensive. It is a nonspecific competitive and a suicide inhibitor of XOR. XOR oxidises allopurinol to oxypurinol which in turn binds to the Mo(IV) at the Moco site. This binding prevents the enzyme from functioning any further. Since the half-life of the complex formed is 300 min ($t_{1/2} = 300$ min at 25 °C), allopurinol has to be administered trice a day (Okamoto *et al.*, 2003). Several side effects are attributed to the use of allopurinol, including nephropathy, hepatitis, Steven-Johnson's syndrome and allopurinol hypersensitivity syndrome (Arellano and Sacristan, 1993). Febuxostat is another XOI, acting as a non-purine specific inhibitor. Febuxostat acts by binding tightly to the Moco site of both forms of XOR. It was observed that febuxostat has a higher serum urate lowering effect than allopurinol (Sattui and Gaffo, 2016). The most common side effects of febuxostat are diarrhoea, nausea and elevation of liver enzymes levels (Becker *et al.*, 2005). The main disadvantage of febuxostat is cost and as a result, febuxostat remains a second choice after allopurinol. Topiroxostat is a selective

XOI that initially behaves as a competitive inhibitor by binding to the XOR active site and then binds covalently with the molybdenum, blocking the Moco site. The dissociation of topiroxostat from the Moco site has a long halftime of 20 h (Matsumoto *et al.*, 2011; Diaz-Torné, Perez-Herrero and Perez-Ruiz, 2015). While allopurinol and febuxostat are approved in the United States of America, European Union and Japan, topiroxostat is only approved in Japan.

Table 1.6: Chemical structures of approved XOR inhibitor drugs. Structures drawn using ACD/Chemsketch (version 2018.1).

Approved XOR inhibitor drugs	Chemical structure
Allopurinol	
Febuxostat	
Topiroxostat	

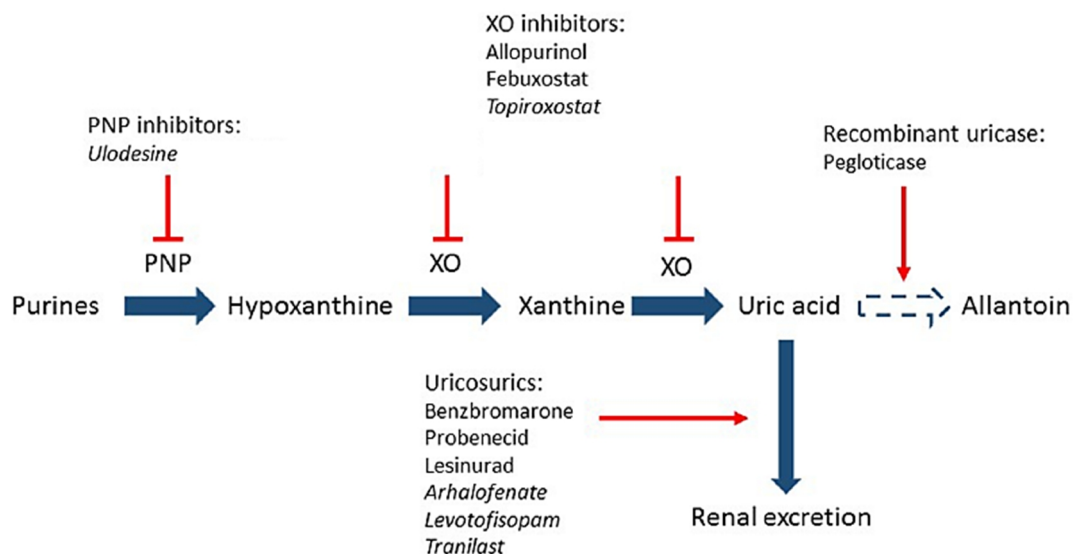


Figure 1.16: The uric acid pathway and site of urate lowering therapy drugs. PNP – purine nucleoside phosphorylase; XO – xanthine oxidase; dashed arrow – lack of metabolic pathway in humans. Figure adapted from Sattui S. et al (Sattui and Gaffo, 2016).

Table 1.7: Urate-lowering therapy medications. Table adapted from Sattui S. *et al.* and Diaz-Torné C. *et al.* (Diaz-Torné, Perez-Herrero and Perez-Ruiz, 2015; Sattui and Gaffo, 2016).

Generic Name	Trade Name	Target	Clinical development	Approved
Allopurinol	Zyloprim® Caplenal® Others	XOR	Complete	FDA(1966) WHO EML
Febuxostat	Uloric® Adenuric® Others	XOR	Complete	EMA(2008) FDA(2009) PMDA(2011)
Topiroxostat	Topiloric® Uriadec®	XOR	Complete	PMDA(2013)
Lesinurad	Zurampic®	URAT OAT	Complete	FDA(2015) EMA(2016)
Lesinurad/allopurinol combination	Duzallo®	URAT OAT XOR	Complete	FDA(2017)
Ulodesine	/	PNP	Phase II	No
Arhalofenate	/	URAT OAT	Phase II	No

FDA – Food and Drug Administration (United States of America); WHO EML - WHO Model List of Essential Medicines; EMA – European Medicines Agency (European Union); PMDA – Pharmaceutical and Medical Devices Agency (Japan); URAT – Uric Acid Renal Transporter; OAT – Organic Acid Transporter; PNP – Purine Nucleotide Phosphorylase; / - not available

1.10.Objectives of the thesis

In the human body, XOR is associated with the production of superoxide, hydrogen peroxide, nitric oxide and uric acid. Due to the presence of xanthine oxidase in patients suffering from cardiovascular disease, the enzyme is now considered as a reliable biomarker for this pathological condition. The main aim of this study is to elucidate the structure of the recombinant hXOR produced in a prokaryotic expression system and draw comparisons with the ovine XOR extracted from source. The focus of the study is to design a reproducible protocol for the purification of the human enzyme and investigate the biochemical and structural properties of human and ovine XOR. This may expand the current understanding of the physiological roles of hXOR. To this end, the objectives of this study are:

- To establish a reproducible purification protocol of hXOR and extract the ovine enzyme from source.
- To investigate the biochemical properties of hXOR and ovine XOR using several techniques including thermal shift assays and enzymatic assays.
- To synthesise inhibitors and evaluate their effect on the human enzyme using enzymatic assays and docking experiments.
- To introduce clinically-relevant mutations on hXOR and compare their activity with the wild type and propose their effects on the enzyme.
- To employ X-ray crystallography or otherwise to elucidate the structure of hXOR

Chapter 2 Methodology

2.1. Materials

2.1.1. General chemicals

Acetic acid, acrylamide, ammonium persulfate, bisacrylamide, bromophenol blue, Coomassie Brilliant Blue R250, cupric acetate, Ficoll 400, glycine, isopropyl alcohol, methanol, sodium hydroxide were purchased from VWR chemicals. Agarose, 1,4-dithiothreitol, ethylenediaminetetraacetic acid (EDTA), glycerol, nitroblue tetrazolium chloride, tris base, xanthine and xylene cyanol were bought from Sigma Aldrich/Merck. Bromophenol blue, calcium chloride, sodium chloride, sodium dodecyl sulfate (SDS), tetramethylethylenediamine (TEMED) were Fluka molecular biology grade. Bacterial agar, tryptone and yeast extract were bought from Oxoid. Bovine XOR used for SDS-gels was purified previously in the lab. Chemicals not listed here were from Sigma Aldrich/Merck unless otherwise stated.

2.1.2. *E. coli* bacterial strains

2.1.2.1. XL-1 Blue cells

XL-1 Blue cells (Agilent) lack the endonuclease and recombination genes (denoted by *endA1* and *recA1* respectively) and are recommended for the extraction of plasmid DNA. Competent XL-1 cells were transformed with plasmid DNA for miniprep DNA extraction.

Genotype: *recA1 endA1 gyrA96 thi-1 hsdR17 supE44 relA1 lac* [F' *proAB lacI^f ZΔM15 Tn10* (Tet^r)].

2.1.2.2. NEB 5-alpha cells

NEB 5-alpha cells (high efficiency, New England Biolabs) are derived from the parental strain of K12 cells. NEB 5-alpha cells have an *hsdR17* mutation that eliminates endonuclease activity and thus can be used for efficient transformation of unmethylated DNA derived from polymerase chain reaction (PCR). These cells are also engineered to deliver plasmid preparation of the highest quality and thus were used for transformation with ligated DNA products.

Genotype: *fhuA2 (argF-lacZ)U169 phoA glnV44 80 (lacZ)M15 gyrA96 recA1 relA1 endA1 thi-1 hsdR17*

2.1.2.3. TP1000 cells

TP1000 cells (kindly provided by Professor Tracy Palmer, University of Dundee) are derived from the parental strain of MC4100 cells in which the *mobA* and *B* genes were replaced by a kanamycin resistant gene (denoted by $\Delta mobAB::Kan$ in the genotype). This mutation prevents the conversion of molybdopterin to molybdopterin guanine dinucleotide, allowing molybdopterin to be incorporated in the protein. TP1000 cells were the cells of choice for the expression of recombinant hXOR.

Genotype: $\Delta mobAB::Kan$ [F' *araD139*]B/r, *Del(argF-lac)169*, *lambda-*, *e14-*, *flhD5301*, $\Delta(fruK-yeiR)725(fruA25)$, *relA1*, *rpsL150(strR)*, *rbsR22*, *Del(fimB-fimE)632(::IS1)*, *deoC1*]

2.1.3. 2xTY bacterial media and agar plates

All bacterial cultures were grown in 2xTY media composed of 16 g/L tryptone, 10 g/L yeast extract and 5 g/L NaCl. Agar plates contained 20 g/L bacterial agar in 2xTY media. All solutions were sterilised by autoclaving at 121 °C and 15 Psi for 20 minutes.

2.1.4. Preparation of calcium competent cells

All cells were made competent by the calcium method using a modified version of the protocol described by Sambrook *et al.* (Sambrook *et al.*, 2012). A single colony of the appropriate *E. coli* cells was used to inoculate 10 mL 2xTY medium supplemented with the appropriate antibiotic and grown overnight at 37°C at 200 rpm. The overnight culture was used to inoculate 500 mL 2xTY medium (1:100 ratio), which was grown at 37°C at 200 rpm until an OD₆₀₀ of 0.4 was reached. The culture was divided into two 250 mL prechilled centrifuge bottles and incubated on ice for 10 minutes. The cells were centrifuged for 7 minutes at 6,000 x g, 4°C. The supernatant was poured off and each pellet was resuspended in 30 mL ice-cold 100 mM CaCl₂ solution. The cell were transferred to four pre-chilled 30 mL Corex® tubes and left on ice for 30 minutes followed by centrifugation for 7 minutes at 6,000 x g at 4°C. The supernatant was discarded and the pellets were resuspended in 2 mL ice-cold 100 mM CaCl₂ solution containing 10% (v/v) glycerol. The competent cell suspensions were stored as 300 µL aliquots at -80°C.

2.1.5. Bacterial transformation

Competent cells were thawed on ice for 5-10 minutes. Once thawed, 1 ng DNA was added to 100 µL of cells and left on ice for 45 minutes. The cells were heat shocked

for 3 minutes in a heat block at 42°C. After the addition of 400 µL of 2xTY, the cells were incubated at 37°C for 1 hour. The transformed cells were spread on an agar plate containing the appropriate antibiotic and left overnight at 37°C.

2.2. Recombinant DNA methodology

2.2.1. Isolation of plasmid DNA

Plasmid DNA was isolated using the ZR Plasmid Miniprep™-Classic (Zymo Research) according to manufacturer's instruction. The protocol was modified with the addition of 100 µg/mL RNase A to the resuspension buffer. The quality of purified DNA was assessed via agarose gel electrophoresis. The concentration of the DNA was quantified by measuring the A_{260} and calculated using Equation 1 (Sambrook *et al.*, 2012).

$$[DNA] = 50 \times df \times A_{260} \quad \text{Equation 1}$$

Where:

[DNA] is the concentration of DNA in $\text{ng}\cdot\mu\text{L}^{-1}$

50 is the double stranded DNA concentration in µg at an A_{260} of 1

df is the dilution factor

A_{260} is the absorbance at 260 nm

2.2.2. Agarose gel electrophoresis

The agarose gel was prepared by adding 0.7 g of agarose in 100 mL of TAE buffer (20 mM Tris base, 1.14 % (v/v) glacial acetic acid, 10 mM EDTA) (Sambrook *et al.*, 2012). The mixture was boiled, allowed to cool to approximately 50°C and poured into a casting tray with a well comb. Once solidified, the tray was filled with TAE buffer and the DNA samples were loaded with a 10x loading dye (20% (w/v) Ficoll 400, 1% (v/v) SDS, 20% (v/v) 0.5 M EDTA, 0.25% (w/v) bromophenol blue, 0.25% (w/v) xylene cyanol) (Sambrook *et al.*, 2012). Electrophoresis was carried out at a constant voltage of 75 V until the dye front reached two-thirds of the gel. The agarose gel was stained in dilute ethidium bromide, destained in water and visualised on a UV trans-illuminator.

2.2.3. Lambda DNA preparation

To 1 µg of lambda (λ) DNA (*cI857ind1 Sam 7*, Roche), 1 U of *Hind*III restriction enzyme (Roche) in SuRE/Cut™ Buffer B was added and left for 2 hours at 37°C. The

digested fragments were used as molecular weight standards for agarose gel electrophoresis.

2.2.4. Restriction digest of plasmid DNA

Plasmid DNA was linearised by using *NcoI* restriction enzyme (Merck) for 2 hours at 37°C in SuRE/Cut™ Buffer B.

2.2.5. Ethanol precipitation of DNA

To the DNA, 1/10 volume of 3M sodium acetate pH 5.2 and 3 volumes of ice cold ethanol were added. The sample was mixed, incubated at -20°C for 1 h and centrifuged at 16,000 x g at 4°C for 1 h. The supernatant was pipetted out carefully and the DNA pellet was left to dry at room temperature for 15 min. The DNA was resuspended in TE buffer (10 mM Tris-HCl pH 8.0, 1 mM EDTA) (Sambrook *et al.*, 2012).

2.2.6. DNA Oligonucleotides

The pTrc99a-hXOR clone was kindly provided by Prof Pearson (Universität Hamburg, Germany). Lasergene SeqBuilder (DNASTAR) was used to design the sequencing and PCR primers.

The internal sequencing primers of hXOR (4002 bp) were designed to sequence consecutive 700-nucleotide fragments. The primers at the 5' and the 3' end of the cDNA were designed complementary to pTrc99a (listed as pK-PRO and pK-TERM respectively in Table 2-1). The mutagenesis primers were designed according to the instructions of the QuikChange II XL site-directed mutagenesis kit (Agilent Technologies). The 6xHis-tag primers include a Factor Xa cleavage site and were designed to the 5' end of the XOR DNA. The synthesis of the primers and DNA sequencing were conducted by Bioneer (South Korea). The sequences of the primers are listed in Table 2.1.

Table 2.1: Primers

Primer Name	Primer Sequence (5' → 3')	N	GC ratio/ %	T _M / °C
Sequencing primers				
XOR701	TTCACGCCCTGGATCCAACC	21	61.9	63.7
XOR1401	CAAGACCACTCAGAGGCAGC	20	60.0	59.7
XOR2101	GATGCTATAAAGAACAACCTCC	21	38.1	51.1
XOR2801	CCTGTGGGATGCCTGCAGAGG	21	66.7	64.1
XOR3501	CCTAACAGGAGATCATAAGAACC	23	43.5	54.9
pK-PRO	TGTGTGGAATTGTGAGC	17	47.1	51.1
pK-TERM	GGCTGAAAATCTTCTCT	17	41.2	47.1
Mutagenesis primers				
hXOR_G172R-F	CAGGGATGGTGGATGCTGTGGA A GAGATGGG AATAATCCAAATTG	45	46.7	72.1
hXOR_G172R-R	CAATTTGGATTATTCCCATCTC T TCCACAGCAT CCACCATCCCTG	45	46.7	72.1
hXOR_A932T-F	GCTGGATGAGTGAAGTT A CAGTGACCTGTGGG ATG	35	51.4	69.6
hXOR_A932T-R	CATCCCACAGGTCAGT T AACTTCACTCATCCA GC	35	51.4	69.6
hXOR_N1109T-F	GGAACCCTACAAGAAGAAG A CTCCAGTGGCT CCTGGGAAG	41	56.1	74.0
hXOR_N1109T-R	CTTCCCAGGAGCCACTGGGA G TCTTCTTCTTGT AGGGTTCC	41	56.1	74.0
6xHis-tag primers				
hisXOR-F	<u>CACGTGATCGAAGGTAGGACCGCAGACAAATT</u> GGTT	36	50.0	71.1
hisXOR-R	<u>GTGGTGGTGGTGGTGCATGTCTGTTTCCTGTGT</u>	33	54.6	71.9

Red nucleotides represent the mutated nucleotides. Underlined nucleotides represent the introduced nucleotides not present in the original DNA template. N represents the number of bases.

The melting temperatures were calculated using the Bioneer T_M calculator calculated by the nearest-neighbour method with 1 nM oligo concentration and 50 mM salt concentration (Breslauert *et al.*, 1986).

2.2.7. Generation of 6xHis-Tagged pTrc99a-hXOR clone

The 6-histidine tag was introduced in the pTrc99a-hXOR DNA using the Invitrogen™ Platinum™ SuperFi™ Green DNA polymerase kit (ThermoFisher Scientific). The pTrc99a-hXOR clone was used as the template. The reaction mixture was prepared as shown in Table 2.2. The PCR parameters are described in Table 2.3.

Table 2.2: Components of the polymerase chain reaction

Reagent	Amount
Sterile AnalaR® water (VWR)	Top up to 50 μ L
5x SuperFi Green Buffer	10 μ L
10 mM dNTP mix	1 μ L
Forward primer (hisXOR-F)	0.5 μ M
Reverse primer (hisXOR-R)	0.5 μ M
DNA template	20 ng
Platinum™ SuperFi™ DNA polymerase	1 U

Table 2.3: PCR cycling parameters

Segment	Cycles	Temperature/°C	Time
1	1	98	2 min
2*	35	98	10 s
		1 st 10 cycles – 58 2 nd 25 cycles – 68	10 s
		72	15-30 s/kb of plasmid
3	1	72	5 min

* - The annealing temperature was calculated using the ThermoFisher Scientific T_M calculator (Allawi and Santalucia, 1997; ThermoFisher Scientific, 2019)

The PCR products were analysed by agarose gel electrophoresis and the band of interest was excised using a clean scalpel blade. The DNA in the excised band was purified using the GenElute™ PCR Clean-up kit (Merck). The eluted DNA was further

purified via an ethanol precipitation (Section 2.2.3). The purified PCR product was then blunt-end ligated using T4 DNA ligase (ThermoFisher Scientific). The ligation reaction mixture was prepared as shown in Table 2.4 and was incubated for 2 hours at room temperature.

Table 2.4: Components of the blunt-end ligation reaction

Reagent	Amount
DNA	100 ng
10x T4 DNA Ligase Buffer (ThermoFisher Scientific)	2 μ L
50% (w/v) PEG 4000 solution (ThermoFisher Scientific)	2 μ L
T4 DNA Ligase (ThermoFisher Scientific)	5 U
Sterile AnalaR [®] water (VWR)	Top up to 20 μ L

The ligated plasmid DNA was used to transform competent NEB 5-alpha cells. The transformants were cultured for plasmid extraction.

2.2.8. *In-vitro* site-directed mutagenesis

In-vitro site-directed mutagenesis was performed using the QuikChange II XL Site-Directed Mutagenesis Kit (Agilent Technologies). The pTrc99a-hXOR clone was used as the template for site-directed mutagenesis. The reaction mixture was prepared as shown in Table 2.5. The PCR parameters are described in Table 2.6.

Table 2.5: Components of the *in-vitro* site-directed mutagenesis reaction

Reagent	Amount
10x reaction buffer	5 μ L
DNA template	10 ng
Forward primer	125 ng
Reverse primer	125 ng
dNTP mix	1 μ L
QuikSolution	3 μ L
Sterile AnalaR [®] water (VWR)	Top up to 50 μ L
2.5 U/ μ L <i>PfuUltra</i> high fidelity DNA polymerase	1 μ L

Table 2.6: QuikChange XL cycling parameters

Segment	Cycles	Temperature/°C	Time
1	1	95	1 min
2	18	95	50 s
		60	50 s
		68	1 min/kb of plasmid
3	1	68	7 min

Once the amplification reaction was complete, 10 U of *Dpn* I added and aspirated gently. The reaction mixture was centrifuged for 1 minute and incubated at 37°C for 2 hours. From the reaction mixture, 2 µL were removed and used to transform competent NEB 5-alpha cells. The transformants were then cultured for subsequent plasmid DNA extraction and DNA sequencing.

2.3. Protein analysis methodology

2.3.1. SDS-polyacrylamide gel electrophoresis (SDS-PAGE)

Protein samples were separated by SDS-PAGE (Laemmli, 1970; Sambrook *et al.*, 2012). An 8% resolving gel was prepared and poured between two glass plates. The resolver was layered with 500 µL of water-equilibrated butanol to prevent oxygen from interfering with the polymerisation of the gel. The gel was allowed to polymerise at room temperature for approximately 20 minutes and the butanol was removed. A 5% stacking gel was then prepared and poured over the resolver gel. A comb was inserted and the gel was left for an additional 20 minutes.

Table 2.7: SDS-PAGE Gel Composition

8% Resolver Gel		5% Stacking Gel	
Chemical	Volume/mL	Chemical	Volume/mL
MilliQ Water	4.6	MilliQ Water	2.7
1.5 M Tris pH 8.8	2.5	1.0 M Tris pH 6.8	0.5
30% _t , 3.3% _c Acrylamide/Bisacrylamide [29:1]	2.7	30% _t , 3.3% _c Acrylamide/Bisacrylamide [29:1]	0.67
10% (w/v) SDS	0.1	10% (w/v) SDS	0.04
10% (w/v) APS	0.1	10% (w/v) APS	0.04
TEMED	0.01	TEMED	0.004

The protein samples were prepared by adding 2x SDS loading dye (50 mM Tris-HCl pH 6.8, 10% (v/v) glycerol, 0.1% (w/v) bromophenol blue, and 2% (w/v) SDS) and 250 mM DTT. The resultant solution was added in a 1:1 ratio to the protein samples and boiled for 10 minutes. The samples were then loaded on the gel and electrophoresis was carried out at 200 V using 1x Tris-Glycine SDS buffer (25 mM tris, 250 mM glycine, 0.1% (w/v) SDS). After electrophoresis, the gel was stained overnight with Coomassie Brilliant Blue stain solution (40% (v/v) methanol, 10% (v/v) acetic acid, 0.2% (w/v) Coomassie Brilliant Blue R250, 0.2% (w/v) cupric acetate). Excess stain was removed using a destain solution consisting of 20% (v/v) isopropyl alcohol and 10% (v/v) acetic acid (Sambrook *et al.*, 2012).

2.3.2. Native-PAGE

A 4% native gel was prepared as shown in Table 2.8 (Sambrook *et al.*, 2012). The gel was then poured between two plates and a comb was inserted to form the wells. The gel was left for about 30 minutes to polymerise.

Table 2.8: Native-PAGE Gel Composition

4% Native Gel	
Chemical	Volume/mL
MilliQ Water	6.1
1.5 M Tris pH 8.8	2.5
30%t, , 3.3%c Acrylamide/Bisacrylamide [29:1]	1.3
10% (w/v) APS	0.1
TEMED	0.01

The samples were prepared by adding 6x native dye (consisting of 20% (v/v) 1.5M Tris pH 8.8, 60% (v/v) glycerol and 0.6% (w/v) bromophenol blue) in a 5:1 ratio. The samples were loaded and electrophoresis was carried out at a constant voltage of 150 V using 1x Tris-Glycine buffer. After electrophoresis, the gel was either stained using Coomassie Brilliant Blue stain solution or a XOR activity stain consisting of 10 mM xanthine, 25 mM NaOH and 15 μ M NBT for 15 minutes at 37°C (Fried, 1966).

2.3.3. Blue native-PAGE

The NativePAGE™ Novex® Bis-Tris Gel system (ThermoFisher Scientific) was assembled according to the manufacturer's instructions using an XCell SureLock® Mini-Cell chamber (ThermoFisher Scientific). The samples were loaded and the electrophoresis was conducted carried out at a constant voltage of 150 V for 120 min at room temperature. After electrophoresis, the gels were stained overnight with Coomassie Brilliant Blue stain solution and destained using the destain solution as described in Section 2.3.1.

2.3.4. Western blotting

Protein samples were separated by SDS-PAGE as described in Section 2.3.1. Once run, the upper stacker gel was cut off and the dimensions of the resolver gel were taken. The dimensions were used to cut six filter papers and one nitrocellulose membrane. The nitrocellulose membrane (Hybond, GE Healthcare) was then equilibrated for 10 minutes in water and 10 minutes in transfer buffer (39 mM glycine, 48 mM tris base, 0.037% (w/v) SDS, 20% (v/v) methanol) (Sambrook *et al.*, 2012) while the resolver gel was equilibrated for 20 minutes in the transfer buffer. A Semi-dry transfer was then carried out on a 2117-250 NOVABLOT Electrophoretic Transfer Kit (LKB). Three filter papers were soaked in the transfer buffer and carefully placed on top of each other on the

anode, ensuring that there were no air bubbles. The nitrocellulose membrane, the resolver gel and the remaining soaked filter papers were layered sequentially on top of the filter papers. The graphite cathode was placed on top of the filter papers. The current used for the transfer was calculated by multiplying the area by 0.8 mA/cm^2 and the transfer was performed for 1.5 h at the calculated current. After transfer, the nitrocellulose membrane was removed and soaked in Pierce™ Fast Blocking Buffer overnight at 4°C with constant shaking.

The nitrocellulose membrane was removed from the blocking reagent and washed trice with fresh changes of phosphate buffered saline solution containing TWEEN® 20 (PBS-T, 137 mM NaCl, 2.7 mM KCl, 10 mM Na_2HPO_4 , 1.8 mM KH_2PO_4 , 0.1% (v/v) TWEEN® 20) (Sambrook *et al.*, 2012). The primary antibody (for XOR detection, xanthine oxidase antibody from rabbit host, Novus Biologicals was used; for His-tag detection, anti-His tag primary antibody from mouse host, Aviva Systems Biology was used) was diluted in PBS in a 1:1000 ratio. The nitrocellulose membrane was placed in the primary antibody solution for 1 h at constant shaking. Subsequently, the membrane was washed as previously described and incubated with the secondary antibody solution (1:10,000 dilution of goat anti-rabbit IRdye @800CW in PBS or anti-mouse IRDye® 800CW in PBS (LI-COR) for XOR and His-tag detection respectively) in the dark for 1 h with constant shaking. Analysis of the western blot was performed using LI-COR Odyssey Model 9120 (LI-COR Biosciences).

2.4. Human XOR Expression and Purification

2.4.1. Optimisation of expression of recombinant hXOR

Competent TP1000 cells were transformed with either pTrc-hXOR or pTrcHis-hXOR DNA. The transformants were grown under various expression conditions to optimise the production of hXOR and His-hXOR in bacterial system. These included: optimal OD_{600} for induction, optimal IPTG concentration, optimal time of harvest, optimal temperature for protein expression, and optimal media. The resultant expression patterns were then analysed by SDS-PAGE.

2.4.2. Expression of recombinant hXOR under optimised conditions

Competent TP1000 cells were transformed with the pTrc-hXOR or pTrcHis-hXOR plasmid before every expression experiment. A starting culture was inoculated

with a colony from freshly prepared transformants and grown overnight at 37°C with aeration in 2xTY media containing 200 µg/mL ampicillin sodium salt. The starting culture was then used to inoculate 500 mL of 2xTY media supplemented with ampicillin. This culture was incubated at 37°C until an OD₆₀₀ between 0.4 – 0.6 was reached and then induced with 20 µM isopropyl-β-D-thiogalactopyranoside (IPTG). Sodium molybdate (1 mM) was added to the culture and the cells were grown at 20°C (for hXOR) or 30°C (for His-hXOR) for 20 h. The overnight cultures were harvested for 10 minutes at 10,000 x g and the pellets were frozen at -80°C until required.

2.4.3. Protein extraction and purification.

2.4.3.1. Cell Lysis

The frozen cell pellet was resuspended in 40 mL start buffer (buffer A for hXOR or buffer C for His-hXOR) containing 10 mM phenylmethylsulfonyl fluoride (PMSF). The cell suspension was lysed using a French® Pressure Cell Press (SLM instruments, Inc.) at 1,000 PSIG and sonicated at 15 Amplitude microns using a Soniprep 150 (MSE) for 5 cycles of 10 seconds on/50 seconds off. The lysed cells were centrifuged for 30 minutes at 33,000 x g. The supernatant was collected and filtered using a 0.45 µm cellulose acetate Whatman™ filter (GE Healthcare Life Sciences).

2.4.3.2. Ammonium sulfate precipitation

Aliquots of clarified lysate (1 mL) were pipetted in tubes and different amounts of ammonium sulfate were slowly added to the tubes at 4°C. The percentage ammonium sulfate saturation was calculated using Equation 2 (Sambrook *et al.*, 2012) using an ammonium sulfate calculator (EnCor Biotechnology, 2019).

$$g = \frac{G_{\text{sat}}(S_2 - S_1)}{M_{\text{sat}} - (V_{\text{sp}}/1000 \times 132.14 \times M_{\text{sat}} \times S_2)} \quad \text{Equation 2}$$

Where:

g is the amount of ammonium sulfate in grams

G_{sat} is the amount of ammonium sulfate contained in 1 L of saturated solution

S₁ is the starting % ammonium sulfate saturation

S₂ is the final % ammonium sulfate saturation

M_{sat} is the concentration of a saturated solution of ammonium sulfate in M

V_{sp} is the specific volume of ammonium sulfate in mL

132.14 is the relative molecular weight of ammonium sulfate

G_{sat} , M_{sat} and V_{sp} vary with temperature

The tubes were left on a roller at 4°C for 1 hour and centrifuged at 10,000 x g for 30 min at 4°C. The supernatant was removed and the pellets were drained. The pellets were resuspended in 1 volume of 25 mM sodium phosphate pH 7.4 buffer and both the supernatant and the resuspended pellets were analysed by SDS-PAGE. The maximum percentage ammonium sulfate saturation that did not precipitate the protein and the minimum percentage ammonium sulfate saturation that precipitated the protein were then selected for the purification protocol.

2.4.3.3. Polyethylene glycol precipitation

A 50% (w/v) polyethylene glycol 4000 (PEG4000) solution was prepared and different amounts of PEG4000 were added to 1 mL protein aliquots. The aliquots were left on a roller at 4°C for 1 hour and centrifuged at 10,000 x g for 30 min at 4°C. The supernatant was removed and the pellets were resuspended in 1 volume of 25 mM sodium phosphate pH 7.4 buffer. Both the supernatant and the resuspended pellets were analysed by SDS-PAGE.

2.4.3.4. Heparin affinity chromatography

A HiTrapTM Heparin HP column (GE Healthcare Life Sciences) was washed with 5 column volumes of buffer A (25 mM sodium phosphate pH 7.4, 50 mM NaCl, 0.5 mM EDTA, 1 mM sodium salicylate, 10 mM DTT). The protein sample was loaded on the column and a stepwise NaCl gradient from 50 mM to 500 mM was applied. The A_{280} was monitored during the gradient. The protein fractions collected were analysed via SDS-PAGE. The hXOR fractions were pooled together and desalted for further purification.

2.4.3.5. Anion exchange chromatography

A HiTrapTM Q HP column (GE Healthcare Life Sciences) was washed with 5 column volumes of buffer B (50 mM 4-(2-hydroxyethyl)-1-piperazineethanesulfonic acid (HEPES) pH 8.0, 0.5 mM EDTA, 1 mM sodium salicylate, 10 mM DTT). The protein sample was loaded and a continuous NaCl gradient from 50 mM to 500 mM was applied using an ÄKTAprime plus (GE healthcare Life Sciences). The protein fractions collected

were analysed via SDS-PAGE. The hXOR fractions were pooled together, buffer exchanged and stored at -80°C.

2.4.3.6. Immobilised metal affinity chromatography

A HiTrap™ Chelating HP column (GE Healthcare Life Sciences) was charged with 0.1 M nickel (II) sulfate. The column was then washed with 5 column volumes of distilled water and equilibrated with 5 column volumes of buffer C (50 mM HEPES pH 8.0, 500 mM NaCl, 1 mM Tris(2-carboxyethyl)phosphine hydrochloride (TCEP)). The protein sample was loaded and a stepwise imidazole gradient from 20 mM to 500 mM was applied. The protein fractions collected were analysed via SDS-PAGE. The His-hXOR fractions were pooled together, desalted and stored at -80°C.

2.4.3.7. Buffer exchange and protein concentration

Purified protein samples were buffer exchanged to the storage buffer (50 mM HEPES pH 8.0, 100 mM NaCl, 0.5 mM EDTA, 1 mM sodium salicylate and 1 mM TCEP) and concentrated using an Amicon® Ultra-15 Centrifugal Filter with a molecular cut-off of 100 kDa. The samples were stored at -80°C as 1 mL aliquots.

The concentration of the purified enzyme was determined by measuring the absorbance of the FAD at 450 nm using an extinction coefficient of 35.8 mM⁻¹cm⁻¹ (Johnson *et al.*, 1974) and the purity was assessed by using SDS-PAGE gels and determining the A₂₈₀:A₄₅₀ ratio.

2.5. Extraction of ovine XOR from milk

Fresh ovine milk was kindly provided by the Government Farm Ghammieri, Marsa, Malta. The ovine milk was stirred and a final concentration of 1 mM EDTA was added. The ovine milk was centrifuged at 3,000 x g for 30 minutes at 4°C on a swinging bucket rotor. The upper cream layer was collected, resuspended in 0.2 M K₂HPO₄ containing 1 mM EDTA and left stirring for 2 hours at 4°C. The solution was centrifuged at 3,000 x g for 30 minutes at 4°C on a fixed angle rotor. The supernatant was filtered through glass wool and 15% v/v ice-cold n-butanol was added to the resulting volume whilst stirring. To the supernatant, 15% w/v ammonium sulfate was slowly added whilst stirring at 4°C for 1 hour. The solution was centrifuged at 10,000 x g for 30 minutes at 4°C on a fixed angle rotor. The supernatant was filtered again through glass wool and 20%

w/v ammonium sulfate was added slowly whilst stirring at 4°C. The mixture was left to stir for 1 hour and centrifuged at 10,000 x g for 30 minutes at 4°C (Benboubetra *et al.*, 2004). The formed 'skin' was collected and resuspended 2 volumes of 25 mM sodium phosphate pH 7.4 with 10 mM DTT. This was then dialysed against 25 mM sodium phosphate pH 7.4 and 1 mM DTT once for 1 h, and twice for 2 h each at 4°C. The dialysed protein solution was purified via a HiTrap Heparin HP column using a 50 mM NaCl wash and a 300 mM NaCl elution. The eluate was diluted in 25 mM sodium phosphate pH 7.4, 50 mM NaCl and passed through a HiTrap Q HP column. The flow-through (containing the ovine XOR) was collected and analysed by SDS-PAGE. The protein was aliquoted and stored at -80°C until required.

2.6. Protein Characterisation

2.6.1. Circular dichroism

Circular dichroism (CD) was performed on a ChirascanTM CD spectrophotometer (Applied Photophysics) at EMBL, Hamburg and at the Astbury Centre for Structural Molecular Biology, University of Leeds. The protein was buffer exchanged to 10 mM potassium phosphate buffer pH 7.4 with 25 mM sodium sulfate and 0.1 mM TCEP and concentrated to 5 µM. The spectrophotometer was purged with nitrogen and a background scan of air (empty quartz cuvette) was taken. The buffer was used as a blank and the far-UV (180 – 260 nm) CD spectrum of the protein was recorded at 20°C with a bandwidth of 2.0 nm.

2.6.2. Thermal shift assay

Thermal denaturation assays were performed at the European Molecular Biology Laboratory (EMBL), Hamburg using a thermofluor technique (Semisotnov *et al.*, 1991) for hXOR and a nano-Differential Scanning Fluorimetry (nanoDSF) (Gihaz *et al.*, 2016) for ovine XOR. RUBIC buffer screen (Molecular Dimensions) was used to identify the conditions that enhance protein stability.

For the thermofluor technique, a PCR microplate containing 21 µL of the RUBIC buffer screen was thawed on ice and spun down at 1600 x g for 30 s at 4°C. The protein was centrifuged for 5 minutes at 16,000 x g at 4°C to remove any precipitation. To each well, 2 µL of 20 µM protein and 2 µL of 62X SYPRO Orange solution were dispensed using a repeater pipette. The PCR microplate was sealed with a ClearVue sheet

(Molecular Dimensions) and centrifuged again at 1600 x g for 30 s at 4°C. The PCR microplate was then placed in an iQTM5 real-time PCR detection system (Bio-Rad) pre-equilibrated at 5°C. A temperature gradient of 1°C.min⁻¹ from 5°C to 95°C was then carried out and the signal was collected.

For the nanoDSF technique, the RUBIC buffer screen PCR microtitre plate was centrifuged as mentioned previously. To a new PCR microplate, 9 µL of the RUBIC buffer screen was pipetted and 1 µL of 20 µM protein was dispensed to each well using a repeater pipette. The PCR microplate was centrifuged at 1600 x g for 30 s at 4°C. The buffer-protein mixture was introduced into Prometheus NT.48 nanoDSF grade capillary tubes (NanoTemper) by capillary action and placed in a Prometheus NT.48 system (NanoTemper). A temperature gradient of 1°C.min⁻¹ from 20°C to 95°C was subsequently carried out and the signal was collected.

2.6.3. Matrix-assisted laser desorption/ionisation-time of flight (MALDI-TOF) mass spectroscopy

MALDI-TOF was performed at EMBL, Hamburg. An hXOR stock solution of 6.5 µM was mixed with sinapinic acid matrix (10 mg.mL⁻¹ sinapinic acid, 30% (v/v) acetonitrile and 0.1% (v/v) trifluoroacetic acid) in different ratios (1:1, 1:2, 2:1, protein:matrix) and spotted on a SCOUT 384 MALDI plate (AnchorChip). The plate was left at room temperature until the spots were dry and crystals formed. Data was acquired on a CovalX HM4 High-Mass MALDI-TOF system (CovalX) immediately after crystallisation. The instrument was set in linear and positive modes at an accelerating voltage of 20 kV.

2.6.4. In-gel trypsin digest mass spectrometry

Protein samples were denatured and separated on a 4-20% Mini-PROTEAN[®] TGX[™] precast protein gel (Bio-Rad). The gel was stained using a Coomassie colloidal staining solution (0.08% (w/v) Coomassie Brilliant Blue G250, 10% (w/v) citric acid, 8% (w/v) ammonium sulfate, 20% (v/v) methanol) overnight at room temperature. The gel was destained using several changes of filtered distilled water. The gel was then sealed in plastic foil (VWR) and sent to EMBL (Heidelberg) for in-gel trypsin digest mass spectrometry.

2.6.5. Estimation of FAD content of purified hXOR

Known concentrations of hXOR were buffer exchanged to 50 mM potassium phosphate pH 7.4, 5% (w/v) trichloroacetic acid and incubated for 30 minutes at 4°C. The samples were centrifuged at 13,000 x g for 10 minutes at 4°C. The fluorescence of the supernatant at 535 nm was measured in a SPARK microtitre plate reader (TECAN) with an excitation at 430 nm. Standard solutions of FAD were measured and used to quantify the FAD content of the XOR samples using absorbance spectra with a molar coefficient of 11,300 M⁻¹.cm⁻¹ (Beaucamp, Bergmeyer and Beutler, 1974).

2.6.6. Element analysis

Element content analysis (S, F, Mo) was conducted by ALS Scandinavia AB (Sweden) using inductively coupled plasma sector field mass spectroscopy (ICP-SFMS).

2.7. Protein Crystallisation

Crystallisation conditions were determined using vapour diffusion and microbatch methods. The XOR protein solution was pre-incubated for 1 h with 10 mM DTT to ensure complete reduction of the protein to the XDH form. The reduced protein was then centrifuged at 16,000 x g for 10 minutes at 4°C to remove any precipitation. For the hanging drop vapour diffusion method, 2 µL of the protein solution was pipetted on a siliconised glass cover slide (Hampton Research) and mixed in different ratios with the precipitant solution (1:1, 1:2, 2:1, protein:precipitant). The cover slide was then sealed in a 24-well VDX plate with sealant (Hampton Research) and incubated at 18°C. For the sitting drop vapour diffusion method, 50 µL of the precipitant solution was pipetted into the reservoir of a Swissci crystallisation plate (Molecular Dimensions). The precipitant solution was mixed with 1 µL of the protein solution in different ratios and pipetted into the well of the plate. The plate was sealed using a ClearVue sheet (Molecular Dimensions) and incubated at 18°C. For the microbatch method, 15 µL paraffin oil was pipetted to each well of a Terasaki crystallisation plate (Griener Bio-One). The protein and precipitant solutions were carefully pipetted on the bottom of the wells. The Terasaki plate was incubated at 18°C. The crystals that formed were fished and flash cooled in liquid nitrogen using the precipitation solution with 10% glycerol as the cryoprotectant.

Crystals were diffracted at MASSIF-3 at the European Synchrotron Radiation Facility (ESRF) in Grenoble, France and at P14 at the Positron-Elektron-Tandem-Ring-Anlage III (PETRA III) in Hamburg, Germany.

Data analysis was performed using the CCP4i2 programme suite. Molecular modelling was carried out using Swiss-PDBviewer. Docking experiments were conducted using AutoDock tools and AutoDock Vina.

2.8. Electron Microscopy

2.8.1. Negative staining

Preliminary negative staining was carried out at the Consejo Superior de Investigaciones Científicas (CSIC), Spain under an iNEXT EM H2020 Grant # 653706. From the results obtained, further negative staining experiments were decided to be carried out at the Astbury Centre for Structural Molecular Biology, University of Leeds. Formvar/carbon on 300 mesh copper grids (Agar Scientific Ltd.) were placed on a microscope slide wrapped in paraffin with the shiny surface facing up. The microscope slide was then placed in a PELCO easiGlow™ glow discharge cleaning system (Ted Pella Inc.) at 0.39 mBar and 10 mA for 30 s to clean the grids and to introduce a negatively charged surface thereby allowing aqueous solutions to adhere and spread on the grids. The grids were removed and 5 μL of 1 $\text{mg}\cdot\text{mL}^{-1}$ hXOR was incubated on the shiny surface for 1 minute. A filter paper was used to blot the excess liquid and 5 μL of water was pipetted and incubated for a few seconds to remove excess buffer. The grids were blotted and immediately 5 μL of 1% (w/v) uranyl acetate (Agar Scientific Ltd) was pipetted and incubated for 2 s. The uranyl acetate was blotted and another 5 μL of 1% (w/v) uranyl acetate was pipetted and left for 10 s. Any excess uranyl acetate was blotted and the grids were dried under a lamp for a few seconds and stored at room temperature until use. To determine the optimum protein concentration, different dilutions (1:10, 1:25, 1:50, and 1:100) were then prepared and tested. The optimum dilution was determined and used to test further different pH conditions. The grids were visualised using a FEI Tecnai G2-Spirit microscope with Ultrascan 4000 CCD camera (ThermoFisher Scientific) operating at 120 keV with a tungsten filament.

2.8.2. Grid preparation for cryoEM

Grid preparation was performed at the Astbury Centre for Structural Molecular Biology, University of Leeds. Quantifoil® R1.2/1.3 on 300 mesh copper grids (Agar Scientific Ltd) were placed on a microscope slide wrapped in paraffin with the shiny part facing up. The microscope slide was placed in a Quorum GloQube® glow discharge system (Quorum Technologies Ltd.) at 40 mA and 0.07 mBar for 60 s to clean and

hydrophilise the grids. A polystyrene bucket with a metal ethane bucket in the middle was filled with liquid nitrogen, making sure that nitrogen did not seep in the ethane bucket. The ethane bucket was then filled with liquid ethane and the polystyrene bucket was placed in a Vitrobot Mark IV system (ThermoFisher Scientific). The grids were picked up with tweezers and placed in the Vitrobot. The sample was pipetted on the shiny side of the grid and the blotting was started (blot force of 6 for 6 s). Whatman® grade 1 qualitative filter papers (GE healthcare Bio-Sciences) were used for blotting the grid. The system was kept at 4°C and 100% humidity to avoid evaporation of the sample. After blotting, the grid was vitrified in liquid ethane and stored in a puck cooled by liquid nitrogen. The pucks were stored in punctured Falcon™ tubes in liquid nitrogen until required.

The grids were clipped and transferred to a cassette under liquid nitrogen. The cassette was put and analysed in a Titan Krios 1 (ThermoFisher Scientific) operating at 300 keV with an X-FEG electron source and a Falcon II direct electron detector.

2.9. Synthesis of XOR inhibitors

The synthesis of the first inhibitor, 4-[(Z)-(6-hydroxy-3-oxo-1-benzofuran-2(3H)-ylidene)methyl]benzoic acid (from now on, this compound will be referred to as inhibitor A) is described (Muzychka *et al.*, 2017). Inhibitor A is a carboxylated aurone derivative from sulfuretin, a natural aurone which showed inhibitory XO activity. From their studies, it was shown that inhibitor A was a potent XO inhibitor. From the docking experiments performed on bovine XOR, it was observed that inhibitor A binds to the Arg880 (bovine amino acid numbering) present in the catalytic Moco site of XO through hydrogen bonding and hydrophobic contacts.

The synthesis of the second inhibitor, (2E)-1-(2,4-dihydroxyphenyl)-3-(4-hydroxyphenyl)prop-2-en-1-one (from now on, this compound will be referred to as inhibitor B) is described (Xie *et al.*, 2017). Inhibitor B is a hydroxychalcone derivative from chalcones, a group of compounds which are used in various pharmacological applications such as free radical scavenging. From docking experiments, it was observed that inhibitor B binds to the Moco site of XO via 5 hydrogen bonds to Thr¹⁰⁸³, Gln¹¹⁹⁴, Arg⁹¹², Ser¹⁰⁸⁰ and Gln¹¹² (bovine amino acid numbering).

2.9.1. Synthesis of inhibitor A

The synthesis of inhibitor A was conducted as described by Muzychka, O. *et al.* (Muzychka *et al.*, 2017) The general scheme of the reaction is shown in Figure 2.1.

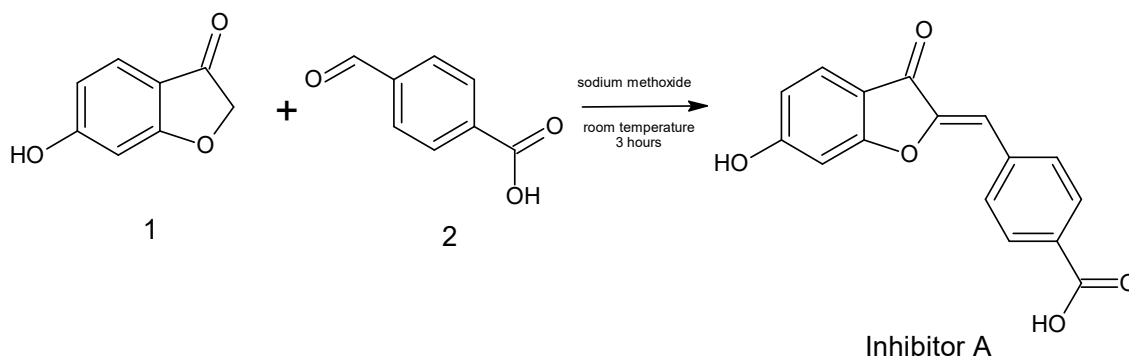


Figure 2.1: Aldol condensation of 6-hydroxy-1-benzofuran-3(2H)-one (1) with 4-formylbenzoic acid (2) to produce 4-[(Z)-(6-hydroxy-3-oxo-1-benzofuran-2(3H)-ylidene)methyl]benzoic acid (Inhibitor A) (Muzychka *et al.*, 2017). Structures drawn using ACD/Chemsketch (version 2018.1).

To a stirred solution of sodium methoxide (8 mM sodium in 494 mM anhydrous methanol), 2 mmol of 6-hydroxy-1-benzofuran-3(2H)-one (1) and 2 mmol of 4-formylbenzoic acid (2) were added. The mixture was left to stir for 3 hours at room temperature. The mixture was subsequently neutralized to pH 2 by dropwise addition of concentrated hydrochloric acid and quenched with water. The residue was filtered using a fritted vacuum Buchner filter funnel and washed with water. The yellow solid (inhibitor A) was left in a desiccator overnight with phosphorous pentoxide to dry. A sample of inhibitor A was sent for proton nuclear magnetic resonance ($^1\text{H-NMR}$). This experimentation was conducted at the Fachbereich Chemie, Universität Hamburg, Germany.

2.9.2. Synthesis of inhibitor B

The synthesis of inhibitor B was performed as described by Xie, Z. *et al.* (Xie *et al.*, 2017) The general scheme of the reaction is shown in Figure 2.2.

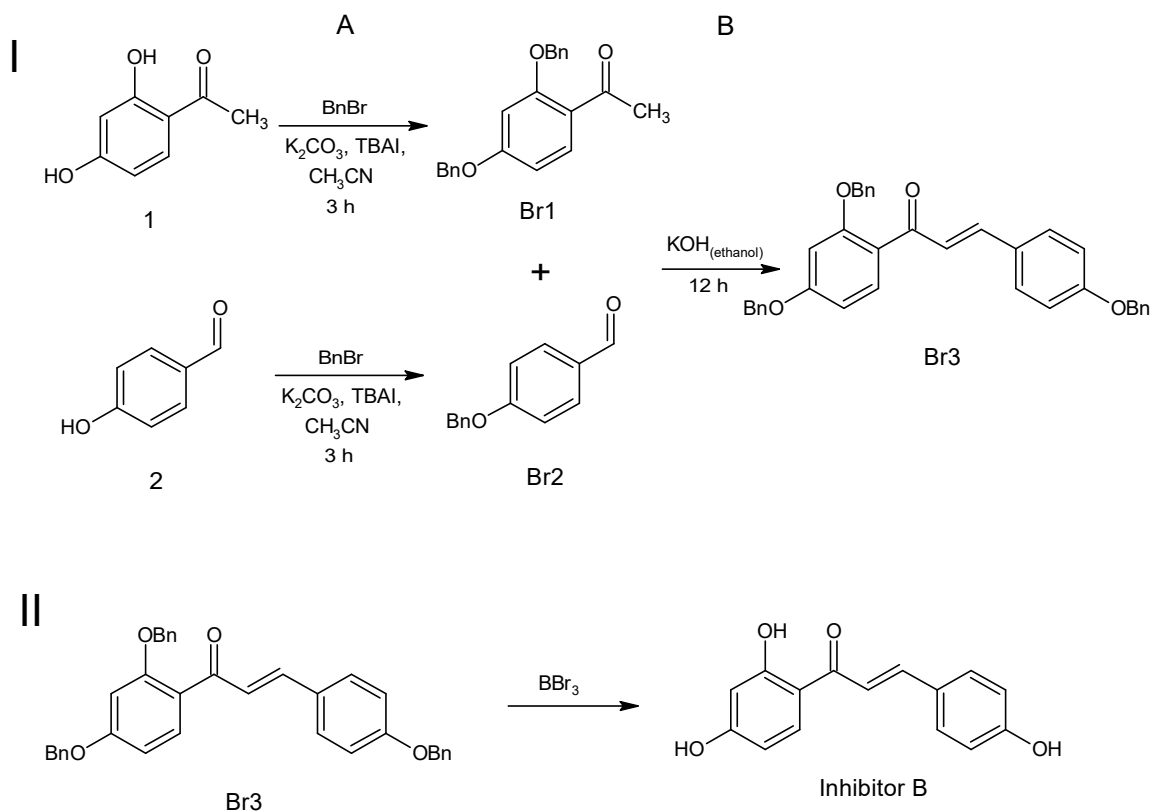


Figure 2.2: General reaction scheme of inhibitor B synthesis. I.A – Protection of the hydroxyl groups of 1-(2,4-dihydroxyphenyl)ethanone (1) and 4-hydroxybenzaldehyde (2) to form 1-(2,4-diphenoxyphenyl)ethanone (Br1) and 4-phenoxybenzaldehyde (Br2) respectively. I.B. – Aldol condensation reaction between Br1 and Br2 to form (2E)-1-(2,4-diphenoxyphenyl)-3-(4-phenoxyphenyl)prop-2-en-1-one (Br3). II – Removal of benzyl protecting groups from Br3 to form (2E)-1-(2,4-dihydroxyphenyl)-3-(4-hydroxyphenyl)prop-2-en-1-one (Inhibitor B) (Xie *et al.*, 2017). Structures drawn using ACD/Chemsketch (version 2018.1).

2.9.2.1. Synthesis of Br1 and Br2

To 766 mM of anhydrous acetonitrile, 3.55 mmol 1-(2,4-dihydroxyphenyl)ethanone (1), 1.35 mmol tetrabutylammonium iodide (TBAI) and 7.15 mmol anhydrous potassium carbonate were added and dissolved at 50°C. Benzyl bromide (BnBr, 4 mmol) was added dropwise to the solution and left stirring for 3 h. The same procedure was performed for 4-phenoxybenzaldehyde (2) but using 4.13 mmol instead. The procedure that follows was done for both Br1 and Br2 separately.

A thin layer chromatography (TLC) in hexane:ethyl acetate mixture in a 4:1 ratio was performed to analyse the completion of the reaction and the products. Once the

reaction was completed, the work-up was done by quenching the reaction with water. The reaction mixture was poured into a separating funnel and washed by using 3 x 30 mL ethylacetate. The organic layer was dried from water using a spatula-full of anhydrous magnesium sulfate. The magnesium sulfate was removed by filtration with glass wool. A single neck round-bottomed flask was then used to evaporate the solvent in a rotavapor using a water bath at 40°C. After evaporation, the product was dissolved in the minimum amount of ethylacetate.

A silica chromatography column was prepared using a mobile phase of hexane:ethylacetate in a 4:1 ratio. The sample was loaded on the column and fractions were collected. The fractions were analysed using TLC and the fractions with the appropriate product were combined. The solvent was evaporated using a rotavapor. The remaining solvent was extracted using vacuum pump, obtaining Br1 or Br2 (depending on the starting material).

2.9.2.2. Synthesis of Br3

Approximately 1.6 mmol of Br1 was dissolved in a solution of 16 mL ethanol with 2% (w/v) potassium hydroxide. An equimolar amount of Br2 (1.6 mmol) was added dropwise to the mixture. After 30 min, a sample was taken from the mixture for TLC analysis. The solution was left stirring overnight. The mixture was quenched by adding water and adjusted to pH 5. The solution was extracted with 3 x 30 mL of ethylacetate. Anhydrous magnesium sulfate was added to remove any residual water and the solution was filtered through glass wool. The solvent was removed using a rotavapor yielding a yellow oil. A TLC analysis was done to check which ratio of hexane:ethylacetate could be used. To the yellow oil, silica was added and the mixture was further evaporated to yield a solid. The solid was loaded to a silica column chromatography (dry loading). A gradient of 6:1, 5:1, 4:1 (hexane:ethylacetate) was performed on a silica column chromatography. The fractions were analysed using TLC, the fractions with the appropriate product were pooled and the solvent was evaporated using a rotavapor. The remaining solvent was extracted using vacuum pump, yielding the yellow oil, Br3. The mass of the product was weighed and yield was calculated.

2.9.2.3. Synthesis of Inhibitor B

Br3 was dissolved in dichloromethane. Boron tribromide was added dropwise to the solution which was left stirring for 3 hours or until the reaction was completed

(checked via TLC) at 0°C. The reaction was quenched with methanol and the solvents were evaporated. The product obtained was loaded on a silica chromatography column using hexane:ethylacetate with a ratio of 5:1. The fractions were analysed via TLC and the fractions containing the product were combined. The solvent was evaporated using a rotavapor and a vacuum pump, yielding inhibitor B. A sample of inhibitor B as well as samples of all of the intermediates were analysed by ¹H-NMR. This experimentation was conducted at the Fachbereich Chemie, Universität Hamburg, Germany.

2.10. Enzymatic Assays

2.10.1. Uric acid activity assay

The determination of the activity of xanthine oxidase was achieved by monitoring the rate of oxidation of xanthine to uric acid at 295 nm using an Olis spectrophotometer (Olis) and a molar extinction coefficient (ϵ) of 9.6 mM⁻¹.cm⁻¹ (Avis, Bergel and Bray, 1956). The assay was performed in a temperature-controlled environment of 25°C in 50 mM sodium phosphate buffer pH 7.4 containing 150 μ M xanthine (a stock solution of xanthine was prepared by dissolving xanthine with sodium hydroxide and adjusting the pH to 7.4 before use). The concentration of the enzyme used was less than 1/100 of the substrate to minimize as much as possible the effect of inactive enzyme on the substrate. The change in absorbance due to the production of uric acid was monitored over a period of 1 minute. The activity of both the oxidase and the dehydrogenase forms of the enzyme was determined by using the same set up as above with the addition of 0.5 mM NAD⁺. Xanthine dehydrogenase activity was then resolved from the ratio of xanthine oxidase and the total activity. This activity assay was also used to determine the optimum pH of the reaction, the effect of inhibitors on the activity of the enzyme and the effect of the mutations on the enzyme.

2.10.2. Thermal inactivation analysis using zymography

The enzyme was incubated for 10 min at different temperatures (25, 40, 50, 60°C). The uric acid activity assay was then performed to determine the total activity. A temperature ramp at three different temperatures (25, 37, 50 °C) was also conducted to determine the activity of the enzyme over 90 s at different temperatures.

Chapter 3 Results

3.1. pTrc-hXOR

3.1.1. Plasmid Map

The pTrc99a harbouring the hXOR cDNA (4017 bp) was kindly provided by Dr Claire Lane (Astbury Centre, University of Leeds). The pTrc-hXOR is 8162 bp in size and has an IPTG-inducible *trc* promoter. The *trc* promoter is a hybrid promoter of *trpB* and *lacUV5* and is used for high-level fusion protein expression (Amann, Brosius and Ptaslme, 1983). Moreover, the plasmid codes for beta-lactamase that confers ampicillin resistance to the cells transformed with this plasmid.

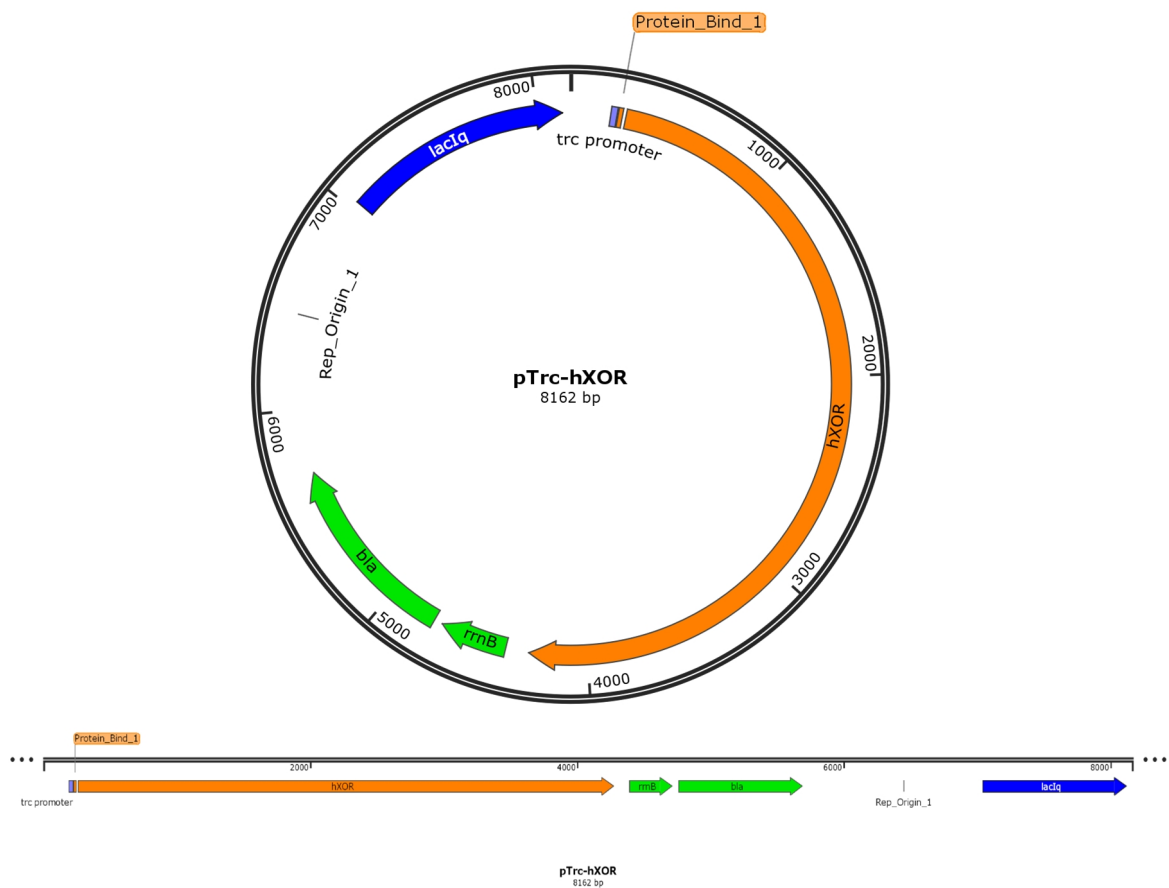


Figure 3.1: pTrc-hXOR plasmid map. In the pTrc99a, XOR cDNA is under the control of the IPTG inducible *trc* promoter. The *rrnB* gene represents the gene coding for the ribosomal RNA, the *bla* gene represents the beta-lactamase gene, and the *lacI^q* gene represents the Lac repressor gene. The plasmid map was reproduced using SnapGene® software (from GSL Biotech; available at snapgene.com)

The pTrc-hXOR plasmid DNA was linearised by NcoI restriction digestion and analysed by agarose gel electrophoresis to confirm size. From the agarose gel (Figure 3.2) it was confirmed that pTrc-hXOR was approximately 8000 bp.

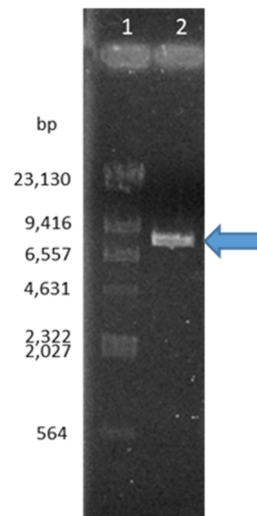


Figure 3.2: Agarose gel (0.7% w/v) of linearised pTrc-hXOR DNA. Lane 1: HindIII λ DNA ladder (1 μ g); lane 2: NcoI digested pTrc-hXOR (200 ng)

3.1.2. Sanger sequencing of pTrc-hXOR

The pTrc-hXOR clone was sequenced by employing the sequencing strategy in shown Figure 3.3 using the primers described in Section 2.2.6. The purpose of this step was to ensure the integrity of the cDNA and to determine the manner in which the hXOR cDNA was originally cloned into the pTrc-99a vector as this information was not readily available. The cDNA was sequenced in one direction with the exception of the 3' end that was sequenced in both directions. The sequencing primers pk-PRO and pk-TERM primers were designed to bind to the promoter and terminator regions of the vector

All the sequencing results were assembled with the pTrc-hXOR construct designed in SnapGene® and the hXOR sequence from NCBI (Reference sequence: NM_000379.4) using the DNASTAR Lasergene suite (Appendix) (DNASTAR version 7.1, 2006). The hXOR in pTrc-hXOR aligned correctly with the hXOR sequence accessed from NCBI. However, the second codon showed a conservative change in the threonine codon from ACA to ACC. Moreover, there was an insertion of 15 nucleotides (GAATTCGAGCTCGGT) after the first codon of the cDNA. On analysing this insertion, it was identified that this sequence is part of the multiple cloning site of the pTrc99a vector, implying that the inserted nucleotides were the result of the hXOR cloning into

pTrc99a. On further investigating the sequence, the cDNA was also found to be upstream of an XbaI restriction site. These findings confirmed that hXOR was cloned via sticky-end cloning using Acc65I (which cleaves at G[↓]GTACC, hence why the ACA codon was mutated to ACC) and XbaI restriction enzymes as shown in Figure 3.4. As the AUG start codon was from the vector, the inserted nucleotides led to the introduction of five amino acids (EFELG) to the N-terminal.

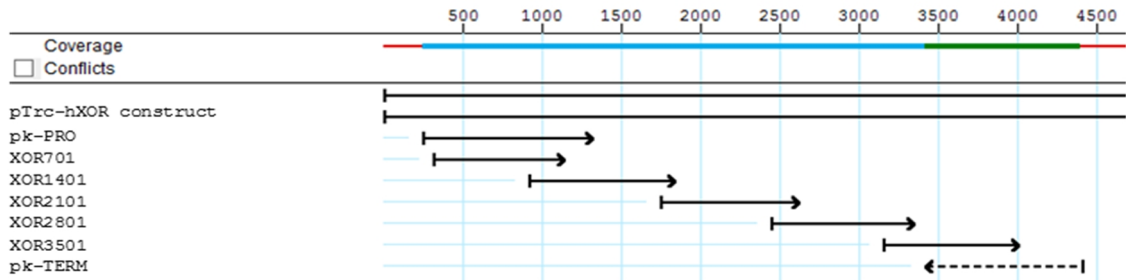


Figure 3.3: Sequencing strategy for pTrc-hXOR. The sequence strategy was visualised using the DNASTAR Lasergene suite (DNASTAR version 7.1, 2006).

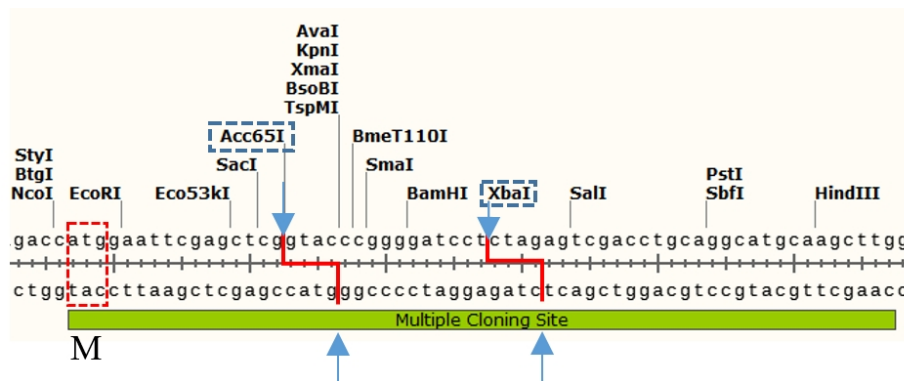


Figure 3.4: The multiple cloning site of pTrc99a vector. The red box represents the start codon. The blue box represents the restriction enzymes used and the arrows denote the cleavage site.

3.2. pTrcHis-hXOR

3.2.1. Plasmid Map

The pTrcHis-hXOR plasmid was designed *in silico* using the pTrc-hXOR vector map as a template and inserting a 6xHis-tag (CACCACCACCACCACCAC) with a Factor Xa cleavage site (GTGATCGAAGGTAGG) at the N-terminus of hXOR while

removing the fifteen nucleotides from the multiple cloning site (Section 3.1.2) introduced during the original cloning experiment of pTrc-hXOR.

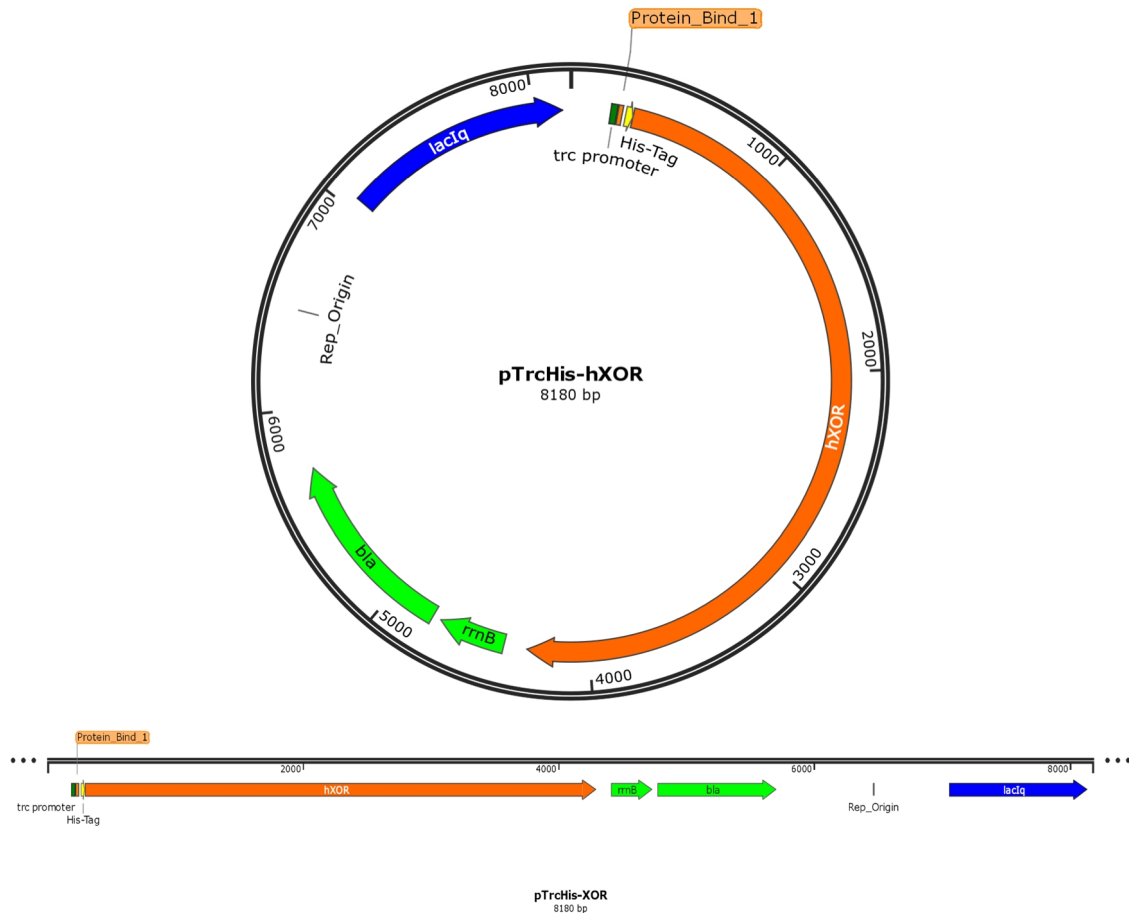


Figure 3.5: pTrcHis-hXOR plasmid map. The hXOR cDNA is under the control of the IPTG-inducible *trc* promoter. The *rrnB* gene represents the gene coding for the ribosomal RNA, the *bla* gene represents the beta-lactamase gene, and the *lacI^q* gene represents the Lac repressor gene. The plasmid map was reproduced using SnapGene® software (from GSL Biotech; available at snapgene.com).

3.2.2. Generation of the pTrcHis-hXOR clone

The primers were designed as described in Section 2.2.6. Parts of the primers contain a sequence that is homologous to the hXOR (for the forward primer, hisXOR-F) or to the vector (for the reverse primer, hisXOR-R) while having a flanking region coding for the 6xHis-tag and the Factor Xa cleavage site as shown in Figure 3.6. The PCR was carried out as described in Section 2.2.7. In the first ten cycles of the amplification step,

the annealing temperature was only calculated using the homologous part of the primers. After ten cycles, it was assumed that the amplified DNA has the flanking part of the primers incorporated into its sequence and thus, for the rest of the cycles, the annealing temperature was calculated using the whole primer sequence. For the second segment of the amplification step, a gradient PCR, with temperatures ranging between 66°C and 72°C, was performed to determine the optimum temperature of the annealing temperature. However, all temperatures produced the same amount of amplified PCR product as assessed by agarose gel electrophoresis.

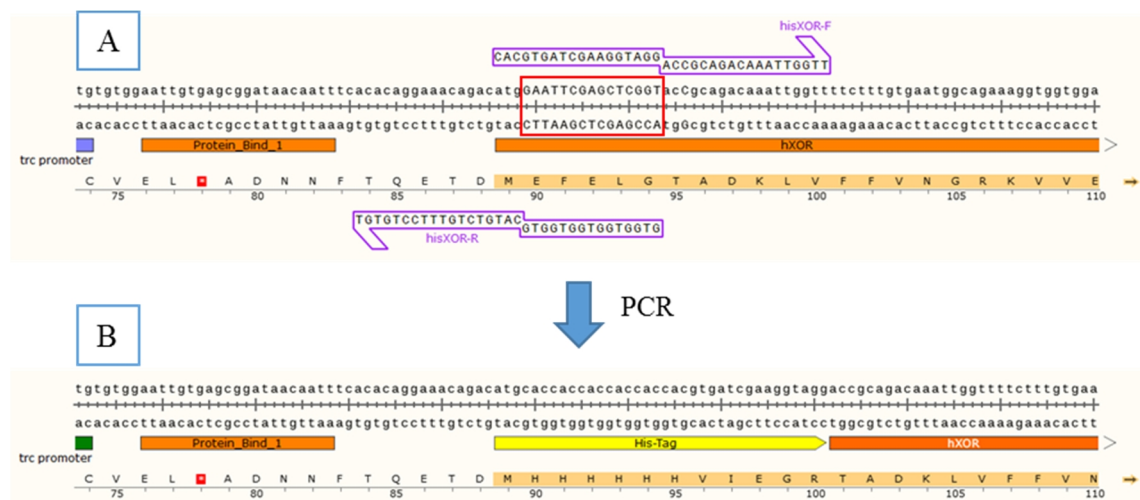


Figure 3.6: PCR of pTrc-hXOR to introduce a 6xHis-tag. A – Nucleotide sequence of the pTrc-hXOR. The nucleotides marked in red are the nucleotides from the multiple cloning site which were omitted from the primer design (thus removing them from the sequence). The nucleotide sequences in the purple arrow represent the primer sequence. B – Sequence of the pTrcHis-hXOR. After PCR, the 6xHis-tag was introduced at the N-terminus of hXOR. The plasmid maps were constructed using SnapGene® software (from GSL Biotech; available at snapgene.com).

The DNA was successfully amplified as shown in Figure 3.7. The PCR product was excised, gel-purified, ethanol precipitated and analysed by agarose gel electrophoresis (Section 2.2.7) (Figure 3.7). *In vitro* circularisation of the purified linear PCR product was carried out using T4 DNA ligase followed by transformation of NEB5α competent cells. This was done as circular plasmids transform more efficiently than linear forms (Dower, Miller and Ragsdale, 1988).

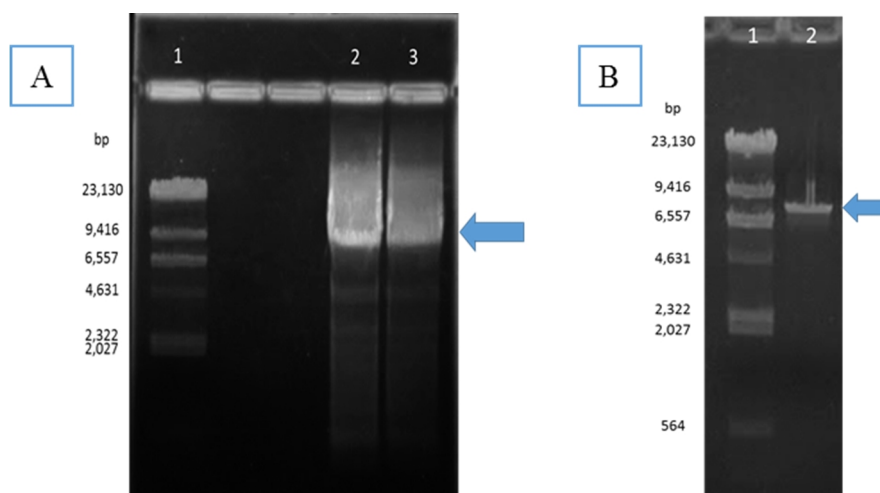


Figure 3.7: Agarose gel (0.7%, w/v) of the PCR product. A – After PCR. Lane 1: HindIII λ DNA ladder (1 μ g); lane 2 and 3: 50 μ L pTrcHis-hXOR PCR product. B – After gel purification. Lane 1: HindIII λ DNA ladder (1 μ g); lane 2: gel purified pTrcHis-hXOR PCR product (130 ng). The blue arrow indicates the pTrcHis-hXOR linear plasmid (size: 8180 bp).

3.2.3. Sanger DNA sequencing of pTrcHis-hXOR

Sanger DNA sequencing confirmed the insertion of a His-tag at the 5'-end of cDNA in the pTrc-hXOR DNA. However, as shown in Figure 3.8, two codons were absent in the inserted sequence producing a protein product with two missing amino acids, a histidine (CAC) and a valine (GTG). The CAC is part of the 6xHis-tag and as a result, its absence resulted in a 5xHis-tag. The GTG is a linker codon between the 6xHis-tag and the Factor Xa cleavage site and thus, the absence of the GTG codon does not affect the Factor Xa cleavage site. Both codons were present in the hisXOR-F primer suggesting that the codons were absent in the PCR product due to some aberration in the PCR. In view of the size of the template, one plausible explanation may be that the DNA was not amplified to completion, resulting into two missing codons. Nonetheless, since two codons were missing, the resulting cDNA sequence was in frame with the start codon and consequently, the pTrcHis-hXOR was still used for further experiments.

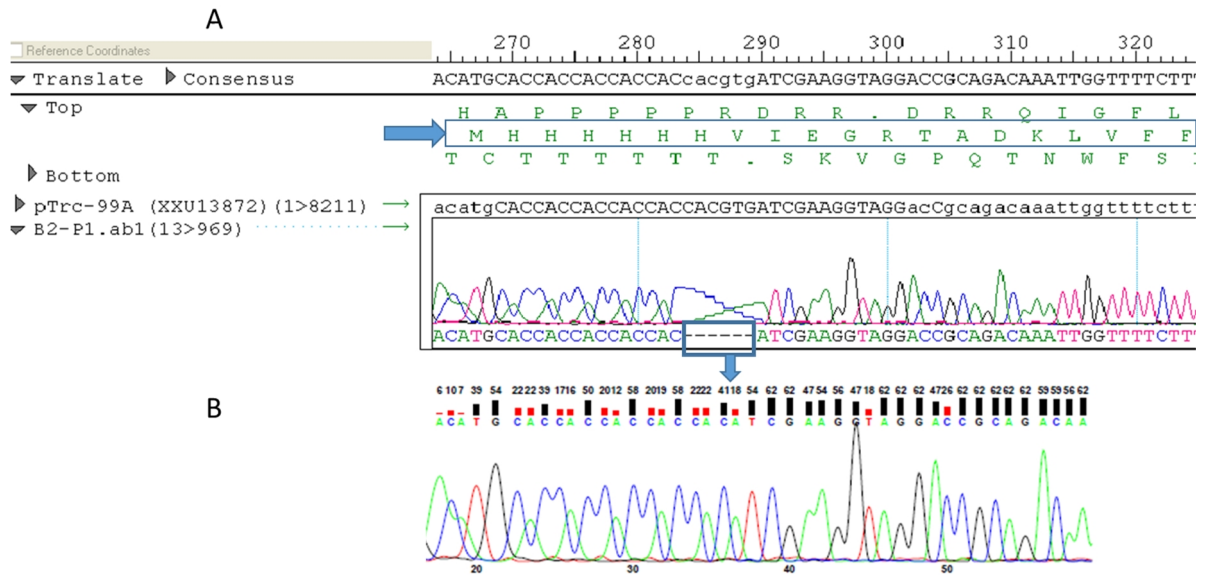


Figure 3.8: Sequencing results of pTrc99a-His-hXOR DNA A – Chromatogram of the pTrc99a-His-hXOR clone visualised using the DNASTAR Lasergene suite (DNASTAR version 7.1, 2006). The amino acid sequence marked with an arrow indicates what the sequence should be. The blue box shows the missing nucleotides. B – Chromatogram visualisation obtained from Bioneer (South Korea) showing that there were no mistakes in the sequencing results. The arrow indicates the position where the missing nucleotides should be.

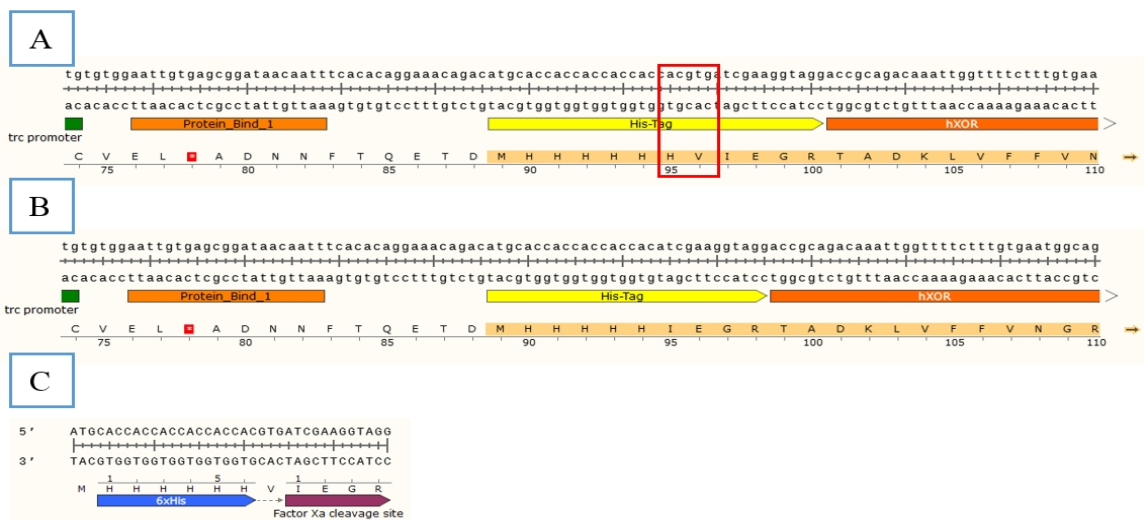


Figure 3.9: Plasmid maps indicating the position of the His-tag. A – The expected map of pTrcHis-hXOR. The nucleotides in the red box show were not inserted into the plasmid. B – The actual map of pTrcHis-hXOR with missing CACGTG (HV). C – The 6xHis-tag map with the Factor Xa cleavage site. From the map, it can be observed that the V residue is not part of the cleavage site. The plasmid maps were visualised using SnapGene® software (from GSL Biotech; available at snapgene.com).

3.3. *In-vitro* site-directed mutagenesis

The nucleotide and amino acid positions where the *in-vitro* site-directed mutagenesis (Section 2.2.8) was performed using primers hXOR_G172R-F and hXOR_G172R-R for the G172R mutation, hXOR_A932T-F and hXOR_A932T-R for the A932T mutation and hXOR_N1109T-F and hXOR_N1109T-R for the N1109T mutation (Table 2.1). The sites of the mutations are illustrated in Figure 3.10. The success of these reactions was assessed by DNA sequencing in the region of the mutation of the hXOR. Four colonies from each mutagenesis reaction were picked and their plasmid DNA was extracted for sequencing. At least one colony from each reaction harboured the mutated clone. Sequencing results are presented in Figure 3.11.

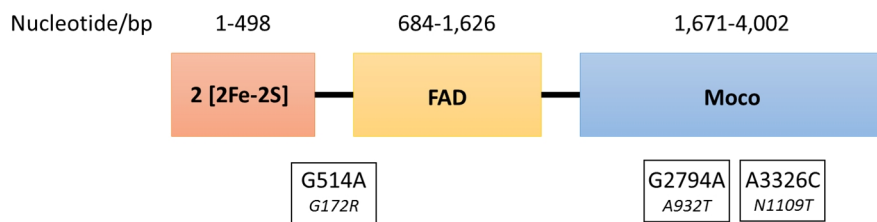


Figure 3.10: Sites for *in-vitro* mutagenesis. The bottom boxes represent the generated mutations. Each box represents a different reaction. The three one-point mutation were G172R, A932T and N1109T

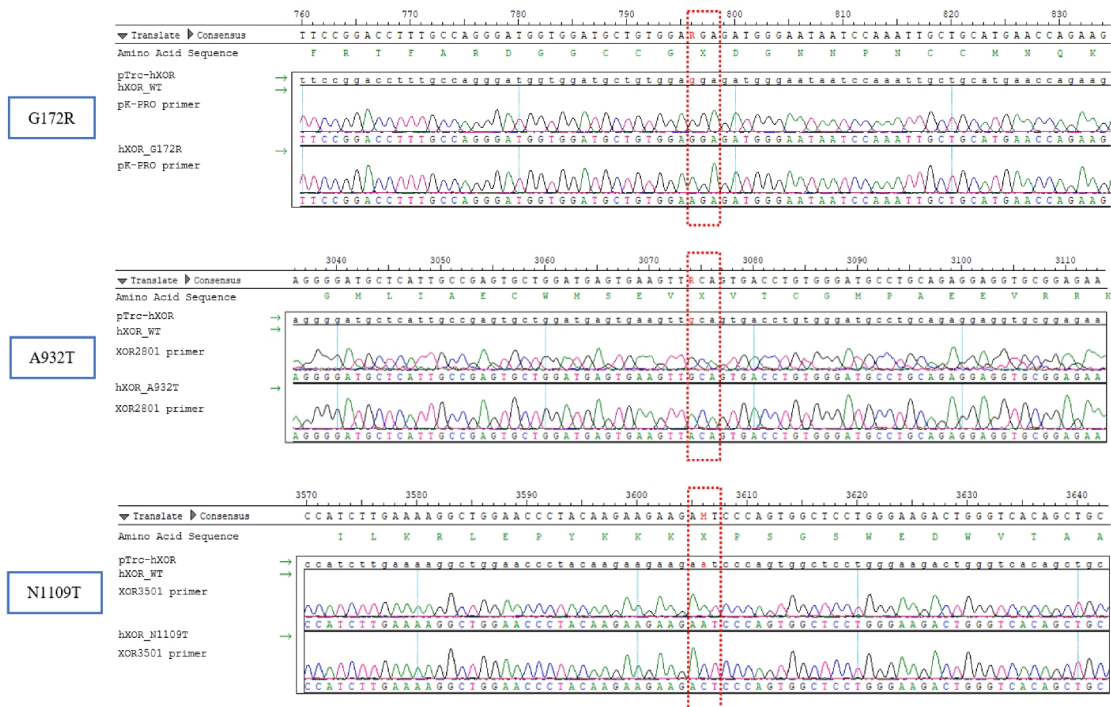


Figure 3.11: Sequencing results confirming the mutations in the pTrc-hXOR clone. The nucleotide in red represents the nucleotide that was mutated. The boxed nucleotides represent the codons where the nucleotide resides.

3.4. Expression of hXOR

The optimisation expression experiments were conducted using TP1000 cells. TP1000 cells have a mutation in the *mobA* and *mobB* genes where they are replaced by a gene conferring kanamycin resistance. The lack of these genes is essential in eukaryotic molybdoenzymes as the conversion of MPT to guanine dinucleotide is halted, thus accumulating MPT in TP1000 cells (Palmer *et al.*, 1996). Several optimisation experiments were performed to establish the best conditions for hXOR expression (Table 3-1). All expression cultures were supplemented with 1 mM sodium molybdate to ensure that there is sufficient molybdenum for the over-expressed hXOR Moco.

Table 3.1: Expression conditions tested for hXOR.

Condition number	Temperature/ °C	[IPTG]/ μM	Time of harvest/ h	OD ₆₀₀ for induction	Media
1	30	100	20	0.4	2xTY
2	37	100	20	0.4	2xTY
3	37	100	20	0.5	2xTY
4	37	100	20	0.6	2xTY
5	37	100	20	0.8	2xTY
6	37	100	20	1.0	2xTY
7	30	100	20	0.6	2xTY
8	37	100	20	0.6	2xTY + 1% Glu
9	30	100	20	0.6	TB
10	30	100	20	0.6	TB + 1% Glu
11	20	100	20	0.6	2xTY
12	20	20	20	0.6	2xTY
13	37	20	20	0.6	2xTY
14	20	20	0	0.6	2xTY
15	20	20	2	0.6	2xTY
16	20	20	4	0.6	2xTY
17	20	20	6	0.6	2xTY
18	20	20	20	0.6	2xTY
19	20	20	22	0.6	2xTY
20	20	20	24	0.6	2xTY
21	20	20	26	0.6	2xTY

Glu – Glucose. TB – Terrific broth. 2xTY – two times tryptone, yeast extract.

Conditions 1 to 6 were first tested to identify the optimum OD₆₀₀ for IPTG induction. From these conditions, OD₆₀₀ of 0.6 (condition 4) gave the best expression as shown in Figure 3.12A. As the pTrc-hXOR was found to have a leaky expression, the effect of glucose on the expression was tested. Glucose inhibits the expression of cDNA by binding to the *lacUV5* promoter present in the *trc* promoter (Wanner, Kodaira and Neidhardt, 1978). As glucose is metabolised during cell growth, the expression of the cDNA can be initiated stringently by the addition of IPTG. Consequently, conditions 8 and 10 were supplemented with 1% (w/v) glucose before at the time of inoculation. However, glucose inhibited the expression of hXOR in both cases (condition 8 and 10, Figure 3.12B,) and thus it was not used for further experiments (Figure 3.12, B). Terrific broth (TB) media was also tested (condition 9) but no increase in protein expression was observed and hence, TB was not used further (Figure 3.12, B).

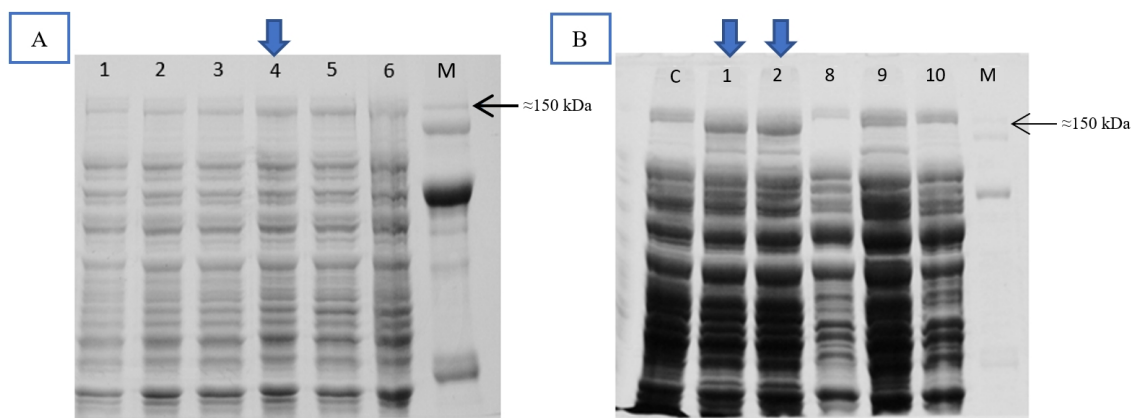


Figure 3.12: SDS-PAGE gel (8%) of the optimisation conditions 1-10. The lane number represents the condition tested from Table 3.1. All conditions were standardised to 10 μ g protein. Lane M represents bovine XOR used as a molecular weight marker while lane C represents TP1000 competent cells. The blue arrow represents the sample grown under the most favourable condition while the black arrow represents the XOR position.

The effect of a lower temperature on expression and protein solubility (20°C, condition 11) was subsequently tested. Previous research showed that lower temperatures increase the amount of soluble protein (Schein, 1989). All of the three different temperatures (37°C, 30°C, 20°C), however yielded poor solubility of the recombinant protein (Figure 3.13) indicating that the expressed protein was not being folded correctly

in the cells even at lower temperatures, resulting into the protein in inclusion bodies after lysis.

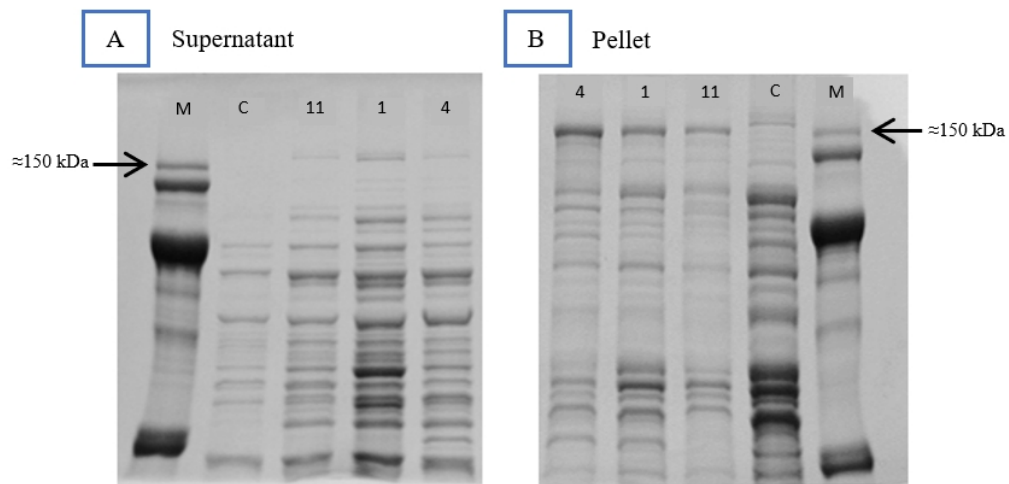


Figure 3.13: SDS-PAGE gel (8%) after lysis and clarification. The lane number represents the condition tested from Table 3.1. Gel A: Protein present in the supernatant after clarification. Gel B: Protein present in the pellet after clarification. All conditions were standardised to 10 μg protein. Lane M represents bovine XOR used as a molecular weight marker while lane C represents TP1000 competent cells. The black arrow represents the XOR position.

Another strategy to increase the yield of soluble recombinant protein is to lower the IPTG concentration. At low IPTG concentrations, the rate at which the protein is being produced is decreased, thus allowing the protein to fold properly and not aggregate (Sawyer, Schlom and Kashmiri, 1994). Consequently, the protein was expressed with a lower IPTG concentration of 20 μM (conditions 12 and 13). Lowering the IPTG concentration showed no difference in protein expression after 20 h (Figure 3.14, A). To determine the expression of hXOR over time, induced cells were left to express at 20°C for a set amount of time (conditions 14 to 20). The expression of hXOR increased during the time course experiment up to 20 h, after which, no increase in expression was observed. Growing the cells further did not result into an increased amount of expressed protein (Figure 3.14, B). Expressing hXOR using lower IPTG concentration at lower temperatures yielded soluble protein (Figure 3.15).

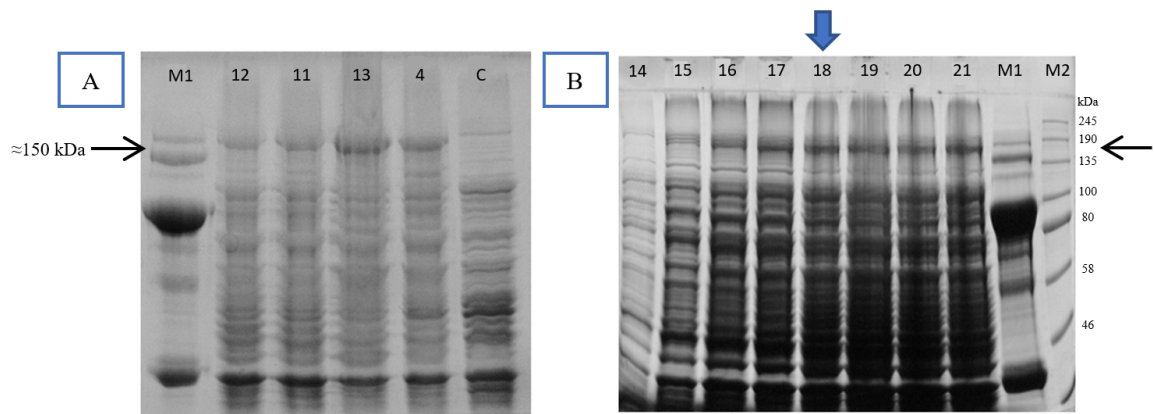


Figure 3.14: SDS-PAGE gel (8%) of the optimisation conditions 12-21. The lane number represents the condition tested from Table 3.1. Gel A: Testing different IPTG concentrations. Gel B: Testing different times of harvesting after induction. All conditions were standardised to 10 μg protein. Lane M1 represents bovine XOR used as a molecular weight marker, lane M2 represents BioLabs broad range protein standard markers (3 μL) while lane C represents TP1000 competent cells. The blue arrow represents the sample grown under the most favourable condition while the black arrow represents the XOR position.

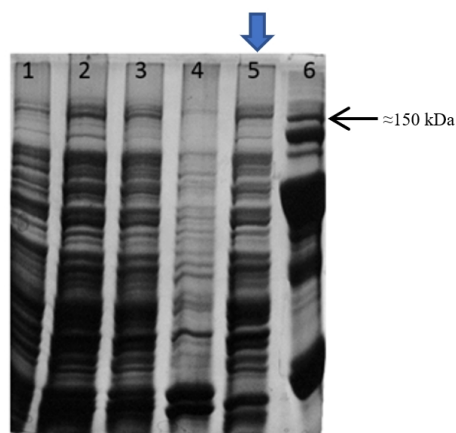


Figure 3.15: SDS-PAGE gel (8%) after lysis. Lane 1 – uninduced TP1000 cells; lane 2: Whole cells before lysis; lane 3: Whole cell lysates; lane 4: Pellet after clarification; lane 5: Supernatant after clarification; lane 6: 10 μg bovine XOR. Lanes 1-5 contained 15 μg protein. The blue arrow represents the protein supernatant while the black arrow represents the XOR position.

Thus, the condition chosen to express hXOR was: TP1000 cells induced at an OD_{600} of 0.6 with 20 μM IPTG for 20 h at 20°C in 2xTY media supplemented with 1 mM

sodium molybdate and 200 µg/mL ampicillin sodium salt. This condition resulted into the highest yield of soluble hXOR.

3.5. Purification of hXOR

Various purification techniques were tested as described in Section 2.4.3. These included: polyethylene glycol 4000 (PEG 4000) precipitation, salting out with ammonium sulfate, heparin affinity chromatography, ion exchange chromatography and size exclusion chromatography.

After PEG 4000 precipitation, the pellet containing hXOR did not resuspend. This method did not yield any soluble hXOR and as a result, it was not adopted. Optimisation of ammonium sulfate precipitation was carried out by testing various concentrations of ammonium sulfate (20, 30, 40, 50, 60, 70 % saturation) as described in Section 2.4.3.2. From this experiment it was determined that the protein was present in the pellet at 40% ammonium sulfate saturation (Figure 3.16).

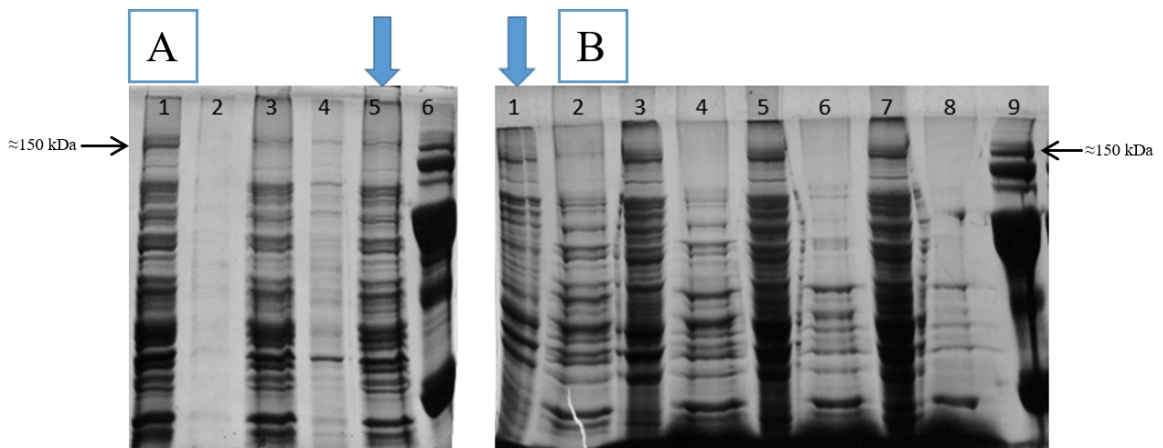
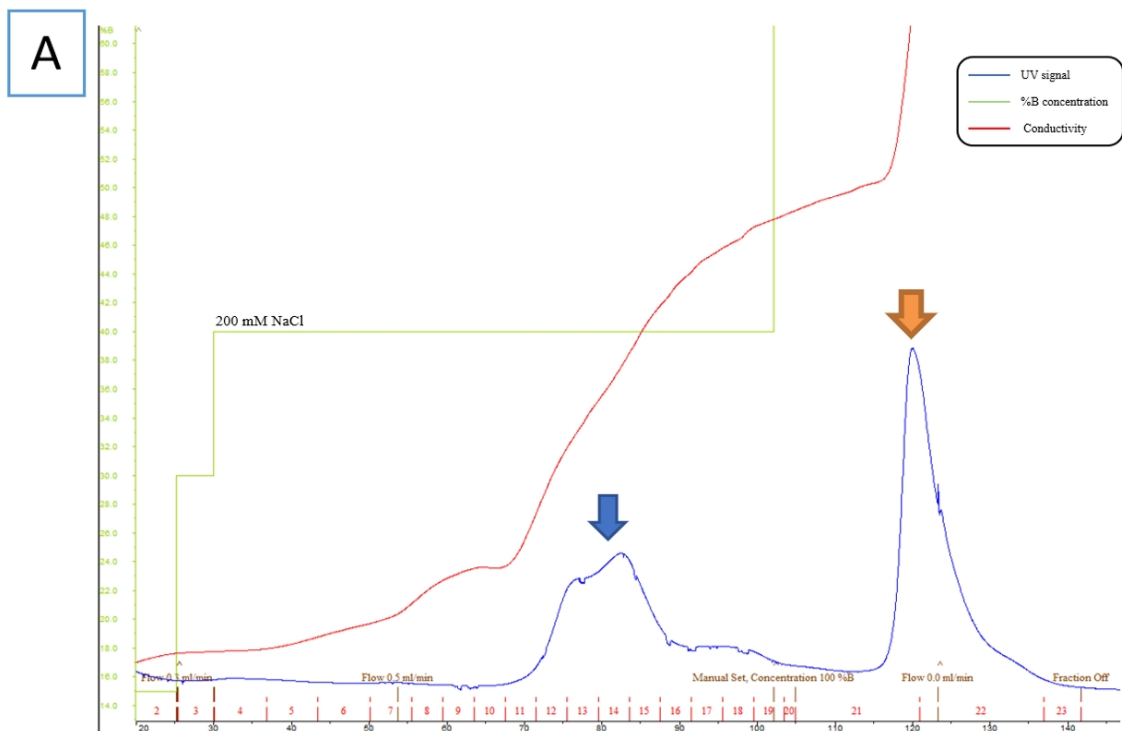


Figure 3.16: SDS-PAGE gel (8%) of the ammonium sulfate precipitation optimisations. Gel A: Lane 1 – 15 µg cell lysate; lane 2 – 20% ammonium sulfate pellet; lane 3 – 20% ammonium sulfate supernatant; lane 4 – 30% ammonium sulfate pellet; lane 5 – 30% ammonium sulfate supernatant; lane 6 – 10 µg bovine XOR. The blue arrow indicates the sample in which the hXOR is present in the ammonium sulphate supernatant. Gel B: Lane 1 – 40% ammonium sulfate pellet; lane 2 – 40% ammonium sulfate supernatant; lane 3 – 50% ammonium sulfate pellet; lane 4 – 50% ammonium sulfate supernatant; lane 5 – 60% ammonium sulfate pellet; lane 6 – 60% ammonium sulfate supernatant; lane 7 – 70% ammonium sulfate pellet; lane 8 – 70% ammonium sulfate

supernatant; lane 9 – 10 μg bovine XOR. The blue arrow represents the concentration at which the hXOR is present in the pellet.

Since XOR has a natural affinity to heparin (Fukushima, Adachi and Hirano, 1995), prepacked heparin affinity columns were used after the ammonium sulfate precipitation as described in Section 2.4.3.4. The 40% ammonium sulfate pellet was resuspended in two-times volume of sodium phosphate buffer pH 7.4 with 10 mM DTT. Desalting was subsequently carried out to remove excess ammonium sulfate using an Amicon® Ultra-15 Centrifugal Filter with a molecular cut-off of 100 kDa.

A step gradient (50, 100, 150, 200, 500 mM NaCl) was performed to determine the concentration of NaCl at which the protein elutes. It was determined that XOR eluted at 200 mM NaCl in sodium phosphate buffer pH 7.4 as shown in Figure 3.17.



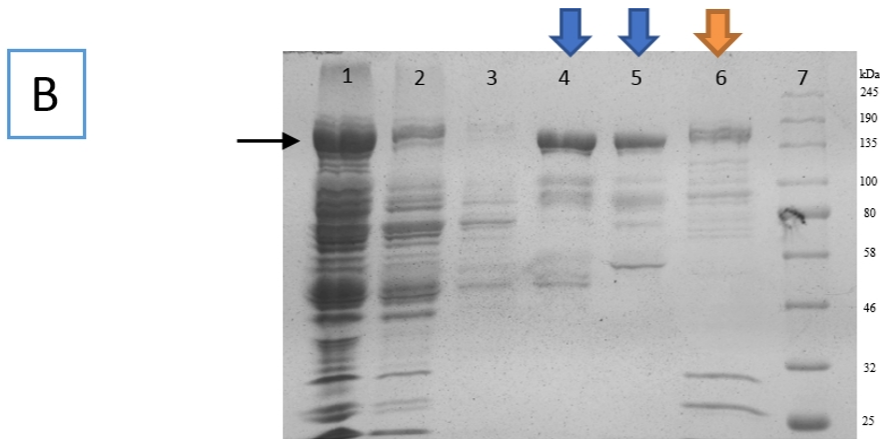


Figure 3.17: Heparin affinity chromatography purification. A – Chromatogram of the purification. Two peaks marked with an arrow were eluted with 200 mM NaCl. B – SDS-PAGE gel (8%) of the purification. Lane 1 –Lysate (5 µg) after ammonium sulfate cut; lane 2 – 10 µg flow-through of heparin column; lane 3 – 2 µg wash with 150 mM NaCl; lane 4 –Eluate (5 µg) from fractions 12 and 13; lane 5 – Eluate (5 µg) from fractions 14 and 15; lane 6 – 5 µg elution with 500 mM NaCl from fraction 22 (marked with an orange arrow); lane 7 – BioLabs broad range protein standard markers (3 µL). The blue arrows indicate the eluates which were used for further purifications while the black arrow indicates the position of hXOR.

After partially purifying the protein by heparin affinity chromatography, the hXOR fraction (fraction 12 to 15 in Figure 3.17A; lanes 4 and 5 in Figure 3.17B) was loaded on a size exclusion column. Various size exclusion resins were tested, including Sephacryl S-200, Sephacryl S-300 and Superose 6b (GE Healthcare Life Sciences). None of the resins tested improved the purity of hXOR to any degree. After size exclusion chromatography, the protein yield was very low and appeared less pure. This may be explained by the tendency of hXOR to degrade which may have occurred during the flow of the protein through the column. During the size exclusion chromatography, different additives were added to the protein and the buffer system, including 2 mM EDTA, 1 mM sodium salicylate, 5% (v/v) beta-mercaptoethanol and 1 mM TCEP, however, none improved the yield of pure protein.

An anion exchange chromatography using a prepacked HiTrap Q column was attempted after heparin affinity chromatography as described in Section 2.4.3.5. The eluate from the heparin affinity chromatography was first buffer exchanged to 50 mM HEPES pH 8.0 with 10 mM DTT using an Amicon® Ultra-15 Centrifugal Filter with a molecular cut-off of 100 kDa. A continuous NaCl gradient (0 – 500 mM) was tested and it was determined that hXOR elutes completely at 200 mM NaCl in 50 mM HEPES buffer pH 8.0, yielding purer protein. HEPES was the buffer of choice as later experiments showed increased stability of the protein in this buffer (Section 3.9.2.1). As a result, further purifications were performed via a step gradient with a wash at 100 mM NaCl and an elution at 200 mM NaCl as shown in Figure 3.18. At 200 mM NaCl, two peaks were eluted, both containing hXOR. As the second peak (marked with an orange arrow in Figure 3.18) contained less pure hXOR, this was not combined with the first peak elution.

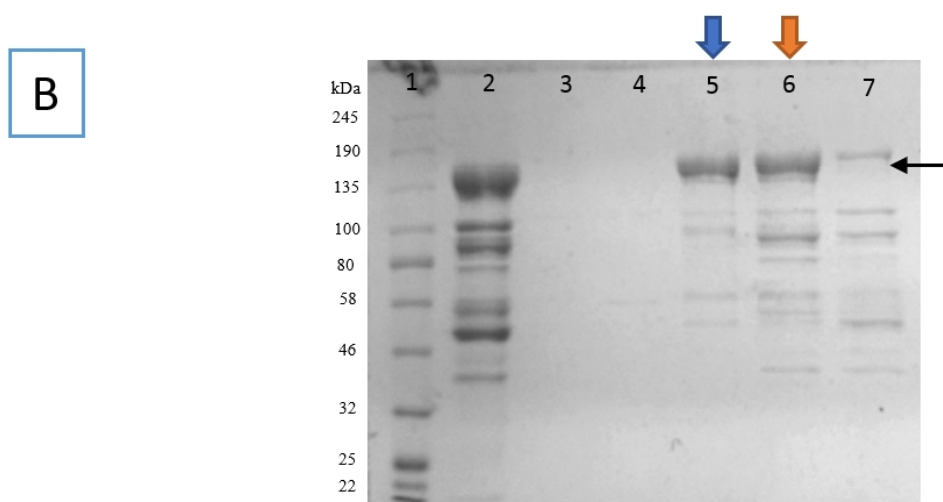
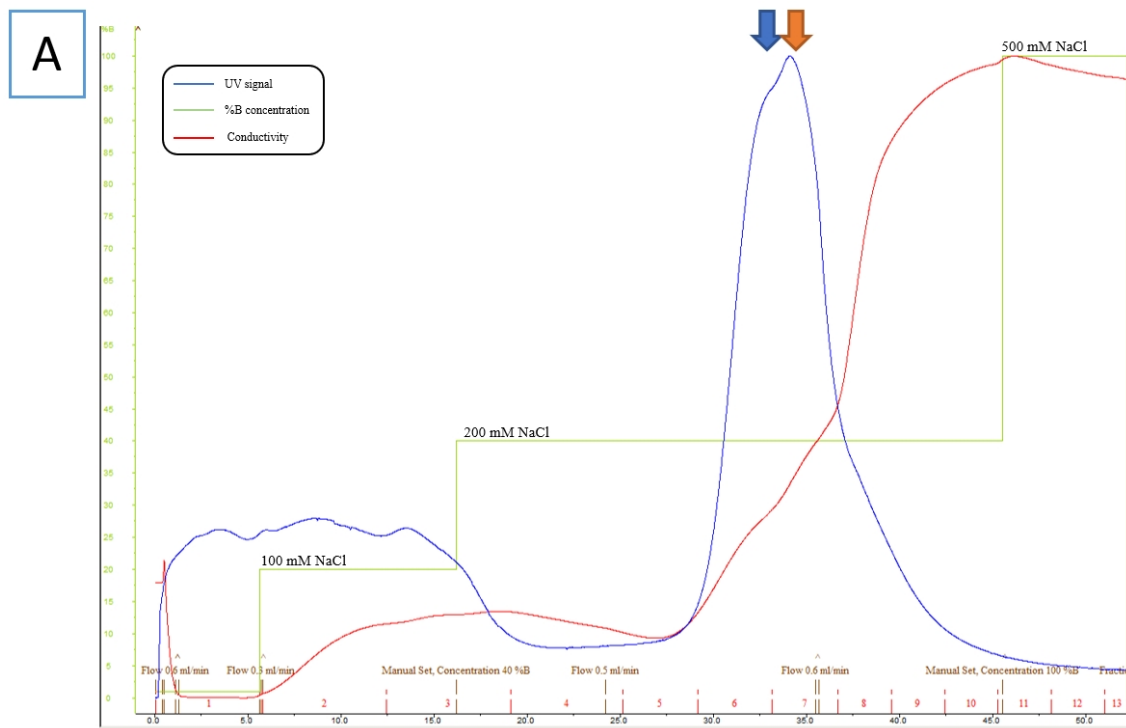


Figure 3.18: Anion exchange chromatography purification. A – Chromatogram of the purification. Two peaks marked with arrows were eluted with 200 mM NaCl. B – SDS-PAGE gel (8%) of the purification. Lane 1 – BioLabs broad range protein standard markers (3 μ L); lane 2 – 15 μ g heparin purified protein; lane 3 – 2 μ g flow-through of Q-column; lane 4 – 2 μ g wash with 100 mM NaCl; lane 5 – Eluate (5 μ g) from fraction 6; lane 6 – Eluate (5 μ g) from fraction 7; lane 7 – 3 μ g wash with 500 mM NaCl. The blue arrow indicates the eluate which was used while the black arrow indicates the position of hXOR.

After the purification, a western blot was carried out (Section 2.3.4) to ensure that the purified protein was hXOR. From the western blot (Figure 3.19), limited proteolysis products were observed. These were attributed to the proteolytical xanthine oxidase form (approximately 135 kDa), the Moco domain (approximately 90 kDa) and the combined FAD and iron-sulfur clusters (approximately 60 kDa).

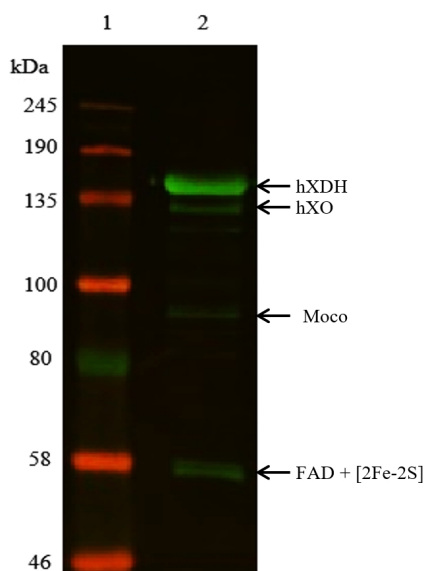


Figure 3.19: Western blot of purified hXOR. Lane 1: BioLabs broad range protein standard markers (3 μ L); lane 2: 2.5 μ g hXOR. Four distinctive bands can be observed: hXDH monomer at 150 kDa, hXO monomer at 135 kDa, Moco at 80 kDa and FAD with [2Fe-2S] cluster at 60 kDa.

The purified hXOR was electrophoresed through a 4% native-PAGE gel as described in 2.3.2. The protein was present as a single band and in the same region as the bovine XOR (Figure 3.20), implying that the purified hXOR was not aggregated and had similar electrostatic charges as bovine XOR. An in-gel NBT activity assay (Section 2.3.2) was also performed and the hXOR was shown to be active. However, the activity of hXOR was observed to be less when compared to the same concentration of bovine XOR (not shown in gel).

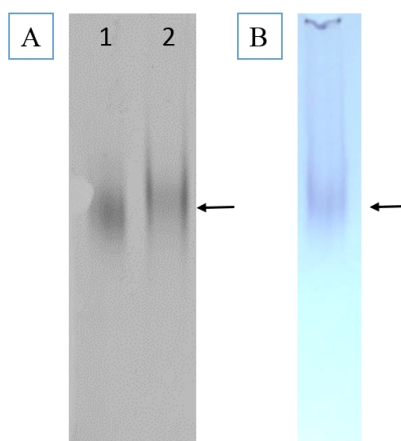


Figure 3.20: Native-PAGE gel (4%) of hXOR. Gel A: Coomassie stained gel. Lane 1 – 5 µg bovine XOR; lane 2 – 5 µg hXOR. Gel B: NBT activity stained gel with 5 µg hXOR. The purple colour is due to the formazan formation from the reaction of NBT with superoxides generated from the reaction of XOR with oxygen and xanthine. The black arrow indicates the position of XOR.

Figure 3.21 shows the consecutive purification steps. A purity of 82% was achieved at the end of the purification. The amount of protein per litre of cell culture was 1.2 mg of protein/litre of cell culture. The A280/450 ratio ranged between 6.0 – 8.0. A decrease in the A280/A450 ratio represents an increase in purity, with a value of around 5.0 representing pure XOR (Bray, 1977) During the purification process, there was considerable loss in yield due to protein aggregation.

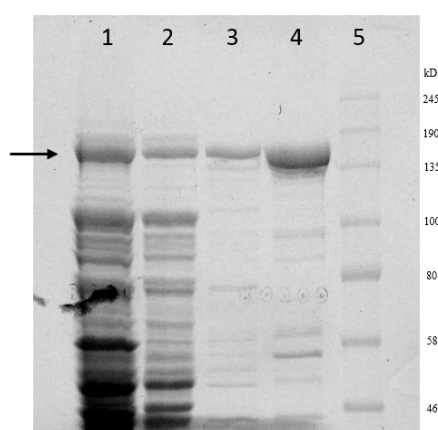


Figure 3.21: SDS-PAGE gel (8%) of the hXOR purification. Lane 1 – 15 µg lysate; lane 2 – after ammonium sulfate cut (10 µg); lane 3 – heparin purified (5 µg); lane 4 – anion exchange purified (10 µg); lane 5 – BioLabs broad range protein standard markers (3 µL). The black arrow indicates the position of XOR.

Table 3.2: Purification table of the hXOR purification.

Purification Stage	Volume/mL	Total Protein/mg per litre of cell culture	%Purity
Crude cellular extract	40	1502.6	6
Ammonium sulfate precipitation	15	178.4	11
Heparin affinity chromatography	10	15.5	42
Anion exchange chromatography	5	1.2	82

3.6. Expression of His-hXOR

As the both the purity (82%) and the yield (1.2 mg per L of cell culture) required an improvement, it was decided to introduce a His-tag to facilitate the purification protocol and increase both purity and yield. Optimisations for His-hXOR expression were carried out as described in Table 3.3. The optimum expression condition for hXOR (TP1000 cells induced at an OD₆₀₀ of 0.6 with 20 μ M IPTG for 20 h at 20°C in 2xTY media supplemented with 1 mM sodium molybdate and 200 μ g/mL ampicillin sodium salt) was used as the starting condition for the design the optimisation experiments. Conditions that were previously not successful (Section 3.4, Table 3.1) were not repeated.

Table 3.3: Expression conditions tested for hXOR.

Condition number	Temperature/ °C	[IPTG]/ μ M	Time of harvest/ h	OD ₆₀₀ for induction	Media
1	20	20	20	0.6	2xTY
2	30	20	20	0.6	2xTY
3	37	20	20	0.6	2xTY
4	20	100	20	0.6	2xTY
5	20	1000	20	0.6	2xTY
6	20	20	20	0.6	TB
7	20	20	20	0.4	2xTY
8	20	20	20	0.8	2xTY
9	20	20	20	1.0	2xTY
10	20	20	4	0.6	2xTY
11	20	20	20	0.6	2xTY + 10mM BA
12	20	/	20	/	2xTY

BA – benzyl alcohol.

A new condition was the addition of 1% benzyl alcohol (BA) before induction with IPTG. This was performed as BA was shown to, in some cases, increase the expression of recombinant protein via the induction of endogenous chaperones (Marco *et al.*, 2005). However, BA did not increase the yield of soluble His-hXOR. In conclusion, the optimal condition that produced the highest yield of soluble His-hXOR was: TP1000 cells induced at an OD₆₀₀ of 0.6 with 20 μ M IPTG for 20 h at 30°C in 2xTY media supplemented with 1 mM sodium molybdate and 200 μ g/mL ampicillin sodium salt (Figure 3.22).

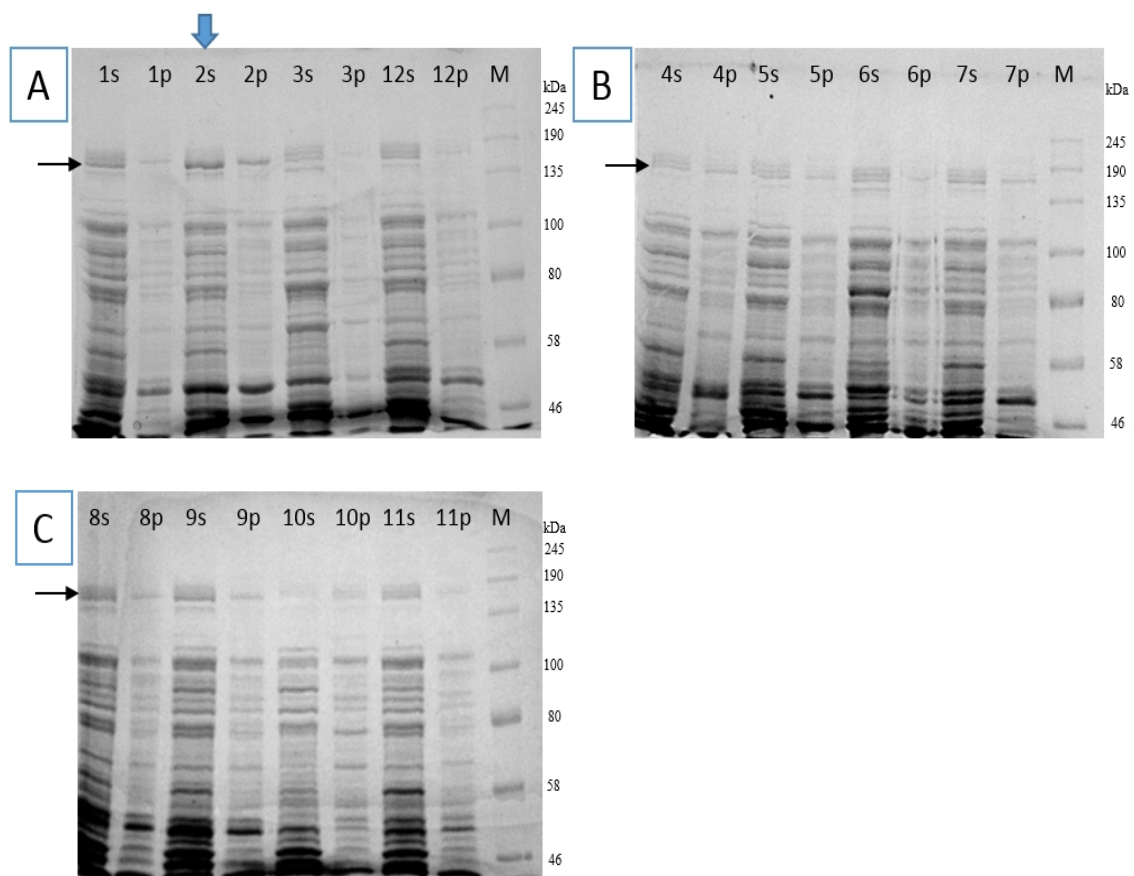


Figure 3.22: SDS-PAGE gel (8%) of the expression optimisation conditions. The lane number represents the condition tested from Table 3.3 while s and p represent supernatant and pellet respectively. M represents the BioLabs broad range protein standard markers (3 μ L). All conditions were standardised to 10 μ g protein. The blue arrow represents the sample grown under the most favourable condition while the black arrow represents the XOR position.

3.7. Purification of His-hXOR

His-hXOR was purified by IMAC column chromatography as described in section 2.4.3.6. A step gradient was performed to determine the concentration of imidazole (25, 50, 75, 200, 500 mM imidazole) at which the protein elutes. It was determined that His-hXOR eluted at 200 mM imidazole in 50 mM HEPES pH 8.0 as shown in Figure 3.23.

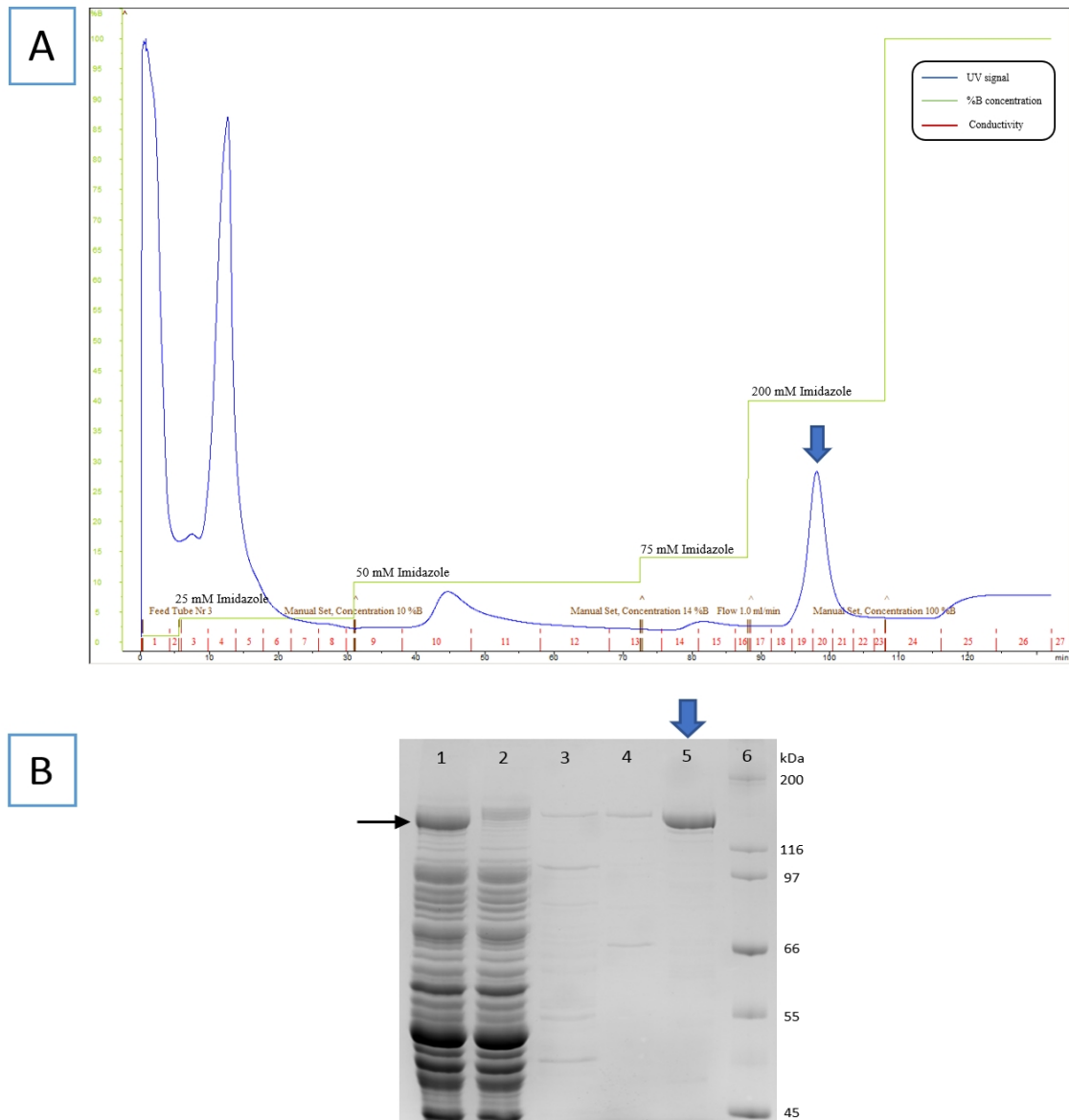


Figure 3.23: IMAC chromatography purification. A – Chromatogram of the purification. Peak marked with an arrow was eluted with 200 mM imidazole. B – SDS-PAGE gel (8%) of the purification. Lane 1 – 15 µg lysate; lane 2 – 10 µg flow-through; lane 3 – 2 µg wash with 50 mM imidazole; lane 4 – 2 µg wash with 75 mM imidazole; lane 5 – 5 µg His-hXOR elution with 200 mM imidazole from fractions 19 to 21; lane 6 – SigmaMarker™ wide range SDS markers (3 µL). The blue arrow indicates the eluate while the black arrow indicates the position of hXOR.

After the purification, a western blot was carried out (Section 2.3.4) to ensure that the purified protein was His-hXOR. From the western blot (Figure 3.24), no limited proteolysis products were observed.

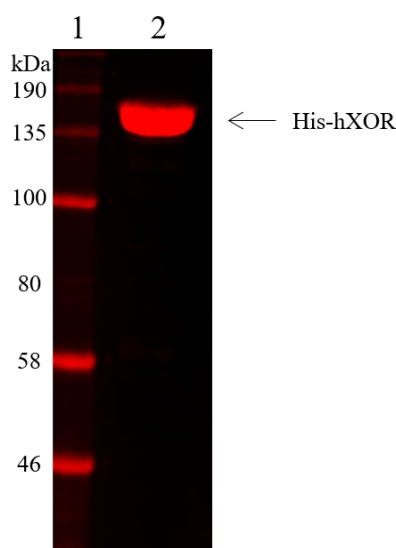


Figure 3.24: Western blot of purified His-hXOR. Lane 1: BioLabs broad range protein standard markers (3 μ L); lane 2: 5 μ g hXOR. No proteolysis was observed.

Blue Native PAGE (BN-PAGE) was used to resolve proteins in their native conformation by mass. In BN-PAGE, the protein under investigation is first solubilised using a mild detergent to preserve the native structure. Subsequently, Coomassie Blue-G250 is added to coat the protein with negative charges so that the sample can migrate to the anode. Due to this, the sample migrates only according to size and not to charge (Schagger and von Jagow, 1991).

Pure His-hXOR was electrophoresed in a blue-native-PAGE to determine the multimeric state of the purified protein and the approximate size. Most of the His-hXOR was present in a dimeric state as shown in Figure 3.25. A very faint band (marked with a red arrow in Figure 3.25) was present above the dimeric state band, indicating that a small portion of the protein had a mass of two dimers.

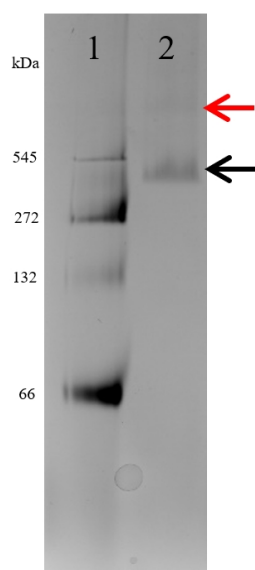


Figure 3.25: Blue-native-PAGE 4-16% gradient gel. Lane 1 – 5 μ g molecular weight markers: urease from Jack Bean and 2.5 μ g albumin from bovine serum (Sigma-Aldrich); lane 2 – 5 μ g His-hXOR. The black arrow represents the dimer band while the red arrow represents the size of two dimers band.

His-hXOR was purified to 96% purity after IMAC. The A280/A450 ratio was between 5.0-5.5. The amount of protein per litre of cell culture was 42 mg of protein/litre of cell culture. On comparing the yield of the His-hXOR purification against the yield of the hXOR purification, a 35-times increase in yield was achieved, while the purity of the protein was also increased. The higher yield could be explained by the fact that no aggregation was observed on the column and that only one purification step was carried out in contrast to the hXOR purification that had three purification steps. The protein was buffer exchanged in 50 mM HEPES pH 8.0 with 100 mM NaCl, 1 mM sodium salicylate, 1 mM EDTA and 1 mM TCEP using an Amicon® Ultra-15 Centrifugal Filter with a molecular cut-off of 100 kDa. The protein was stored at -80°C until required.

Table 3.4: Purification table of the His-hXOR purification.

Purification Stage	Volume/mL	Total Protein/mg per litre of cell culture	%Purity
Crude cellular extract	40	1923	8
Immobilised metal affinity chromatography	30	42	96

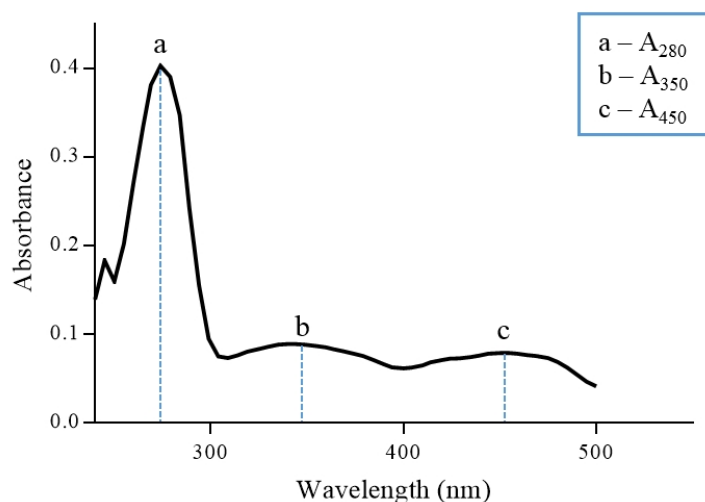


Figure 3.26: Typical plot of hXOR. Peak a has a maximum at A_{280} due to the UV absorptions from tryptophan and tyrosine residues. Peak b has a maximum at A_{350} due to the absorption of the [2Fe-2S] clusters. Peak c has a maximum at A_{450} due to the absorption of the FAD domain.

3.8. Extraction of ovine XOR from milk

Ovine XOR was purified as described in Section 2.5. DTT was added at each step to ensure that the protein remains reduced. EDTA was first added to the ovine milk as this chelates with divalent metals thereby inactivating any metalloproteases present (Scopes, 1987). The milk was first centrifuged to separate the cream from the whey. As XOR is present in association with lipoprotein membranes around milk-fat globules (REF), the cream part was kept for further purifications. The cream was dissolved in a 0.2 M K_2HPO_4 solution and left stirring at 4°C for 2 h to degrade the lipoprotein membranes, releasing XOR without denaturation of the protein. After another centrifugation, a fat layer and a liquid buttermilk layer were formed. XOR was present in the liquid buttermilk layer and as a result, this layer was collected (Dixon and Thurlow, 1924). Butanol was then added to the buttermilk layer to further dissociate XOR from fat globule membranes (Nishino *et al.*, 2005). Butanol extraction was followed by an ammonium sulfate precipitation (15% - 20% w/v ammonium sulfate cut), which formed a golden skin layer containing ovine XOR. This skin layer was collected, solubilised in sodium phosphate buffer containing 10 mM DTT and dialysed once for 1 h and twice for 2 h at 4°C in sodium phosphate buffer containing 1 mM DTT. The short dialysis steps were done to limit the oxidation of ovine XOR. The dialysed sample was further diluted

in sodium phosphate buffer with 10 mM DTT to ensure that the concentration of ammonium sulfate does not interfere with further purification steps.

The dialysed sample was then loaded on a HiTrap Heparin column using a 50 mM NaCl wash and a 300 mM NaCl elution. Ovine XOR was present in both the flow-through and in the 50 mM NaCl wash, showing that ovine XOR has a weak affinity with Heparin as reported previously (Vella *et al.*, 2014). Even though these steps represented losses in protein yield, they were still essential to purify ovine XOR. The eluted ovine XOR from the 300 mM fraction was concentrated in a 100 kDa-cut off Amicon® Ultra-15 Centrifugal Filter and desalted to 25 mM sodium phosphate pH 7.4 with 50 mM NaCl and 10 mM DTT. The desalted fraction was then passed through a HiTrap Q column and the flow-through containing the unbound ovine XOR was collected. This last step increased the purity of ovine XOR as shown by the A280/A450 ratio (Table 3.5).

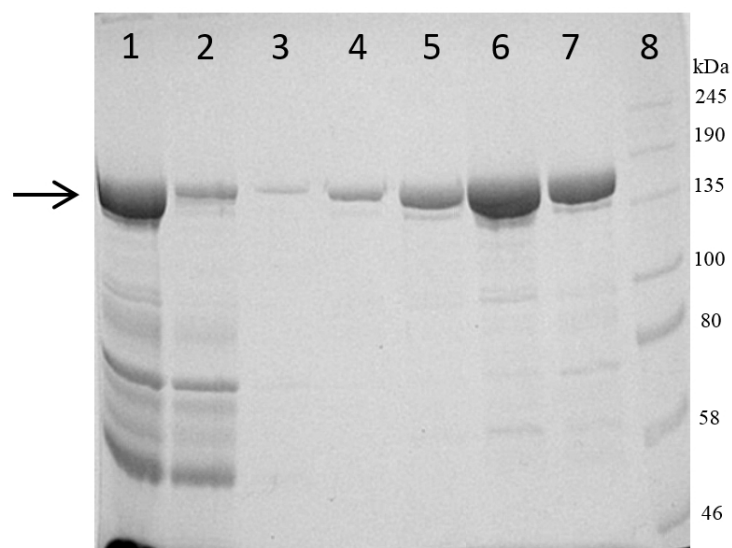


Figure 3.27: SDS-PAGE gel (8%) of the ovine XOR purification. Lane 1 - after ammonium sulfate cut (10 μ g); lane 2 - heparin affinity flow-through (5 μ g); lane 3 - start buffer wash (1 μ g); lane 4 - 50 mM NaCl wash (2 μ g); lane 5 - 300 mM NaCl elution (5 μ g); lane 6 - concentrated heparin elution (12 μ g); lane 7 - anion exchange flow-through (7 μ g); lane 8 - BioLabs broad range protein standard markers (3 μ L). The black arrow represents the ovine XOR position.

Table 3.5: Absorbances after purification steps

Purification Step	A280	A450	A280/A450 ratio
Heparin affinity	1.39	0.127	10.9
Anion exchange	0.548	0.097	5.6

Ovine XOR was then concentrated to $1 \text{ mg}\cdot\text{mL}^{-1}$ in 25 mM sodium phosphate pH 7.4 with 100 mM NaCl, 10 mM DTT, 1 mM EDTA and 1 mM sodium salicylate and stored at -80°C until required.

After the purification, a western blot was carried out (Section 2.3.4) to ensure that the purified protein was XOR. From the western blot (Figure 3.27), limited proteolysis products were observed. These were attributed to the proteolysed xanthine oxidase form (approximately 135 kDa), the Moco domain (approximately 90 kDa) and the combined FAD and iron-sulfur clusters (approximately 60 kDa).

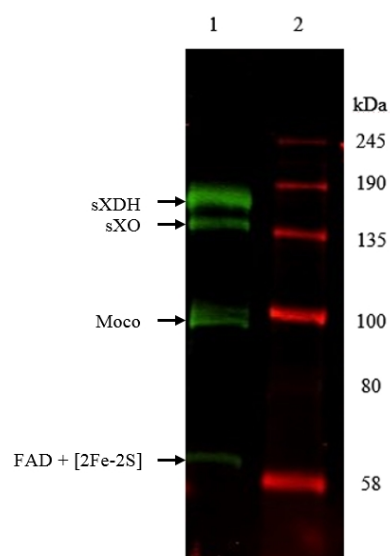


Figure 3.28: Western blot of purified ovine XOR. Lane 1: BioLabs broad range protein standard marker; lane 2: 2.5 µg ovine XOR. Four distinctive bands can be observed: ovine XDH (sXDH) monomer at 150 kDa, ovine XO (sXO) monomer at 135 kDa, Moco at 80 kDa and FAD with [2Fe-2S] cluster at 60 kDa.

The purified ovine XOR was electrophoresed through a 4% native-PAGE gel as described in Section 2.3.2. The protein was present as a single band and migrated further than the bovine XOR (Figure 3.28), implying that the purified ovine XOR was not

aggregated and was more positively charged than bovine XOR. An in-gel NBT activity assay (Section 2.3.2) was also performed and the ovine XOR was shown to be active.

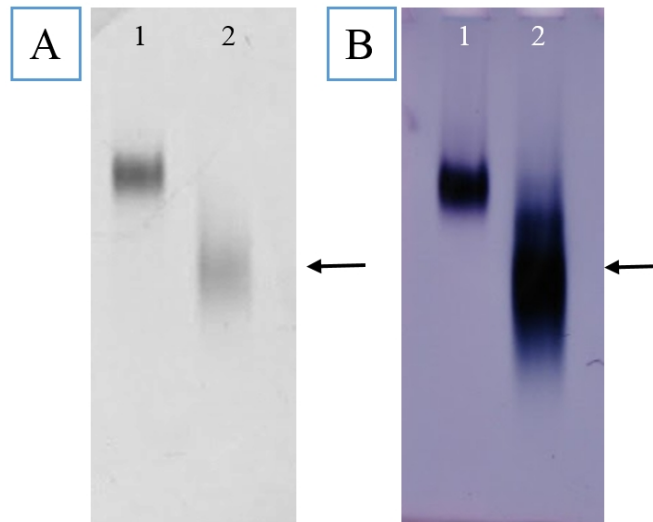


Figure 3.29: Native-PAGE gel (4%) of sXOR. Gel A: Coomassie stained gel. Lane 1 – 5 µg bovine XOR; lane 2 – 5 µg sXOR. Gel B: NBT activity stained gel. Lane 1 – 5 µg bovine XOR; lane 2 – 5 µg sXOR. The purple colour is due to the formazan formation from the reaction of NBT with superoxide anions generated from the reaction of XOR with oxygen and xanthine. The black arrow indicates the position of sXOR.

3.9. Protein characterisation

3.9.1. Circular dichroism

Far-UV circular dichroism (CD) was carried out as described in section 2.6.1. Far-UV CD was used to make sure that the secondary structure of the protein was retained after purification and to estimate the secondary structure content.

A variable selection method applying the CDSSTR version was used to analyse the CD spectra where a database of standard spectra from eight proteins of known secondary structures is first created. Nodes from these standard spectra are then randomly selected to construct a large number of spectrum combinations (Gliickner and Johnson, 1987). The experimental CD spectrum is then compared to this database and the protein structure is determined using a singular value decomposition (SVD) method. In SVD, basis curves are extracted from the known protein structures and used to analyse the unknown protein conformation (Hennessey and Johnson, 1981). The combination of these two methods deliver superior conformation fit to globular proteins. However, even though these methods provide the best α -helical content estimation, they assign poor β -sheet and turns content estimation if data are not collected up to 184 nm (Hennessey and Johnson, 1981).

The protein secondary structure content estimation was calculated using DichroWeb (Whitmore and Wallace, 2007). For the His-hXOR, a reference set optimised for 185 – 240 nm (set 3) was used while for the ovine XOR, a reference set optimised for 190 – 240 nm (set 4) was used. The choice of reference set was dictated by how far the CD spectrum was collected. Figures 3.30 and 3.31 show fitting of the experimental data with the reconstructed data from the reference set.

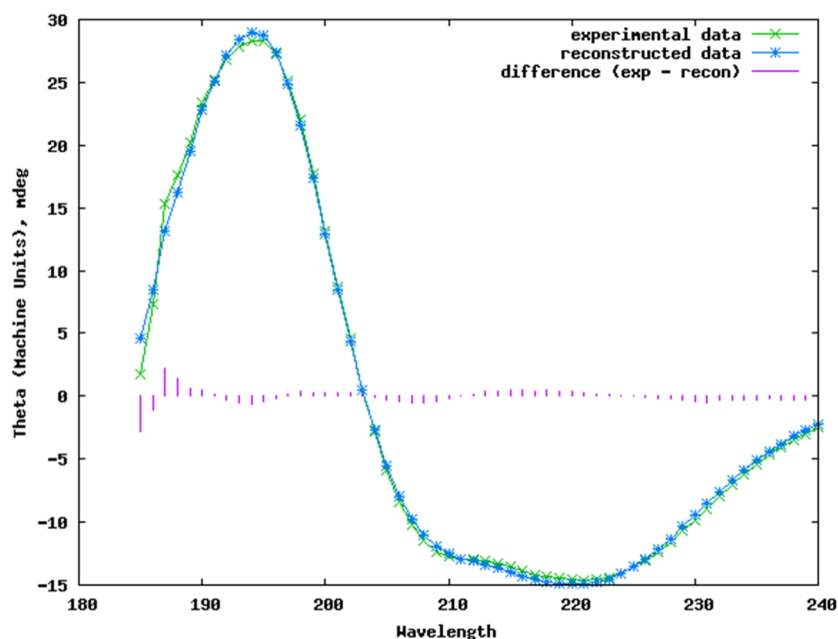


Figure 3.30: Far-UV CD spectrum of 0.2 mg.mL⁻¹ His-hXOR. Reference set 3 (185 – 240 nm) was used to construct the spectrum and to estimate the secondary structure content. The experimental data (green) shows good fit with the reconstructed data (blue) up to 188 nm. From 185 to 187 nm, some small deviations between the two data set can be observed (Whitmore and Wallace, 2007).

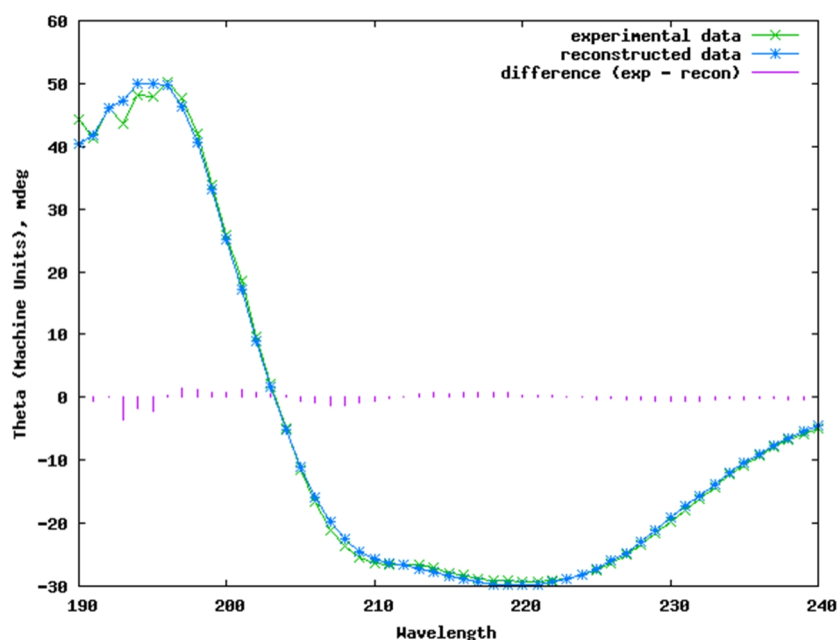


Figure 3.31: Far-UV CD spectrum of 0.88 mg.mL⁻¹ ovine XOR. Reference set 4 (190 – 240 nm) was used to construct the spectrum and to estimate the secondary structure content. The experimental data (green) shows good fit with the reconstructed data (blue). Small deviations between 193 – 195 nm can be observed (Whitmore and Wallace, 2007).

When comparing the secondary structure content estimation of both proteins (Table 3.6), it can be observed that the His-hXOR has higher α -helix content (24%) and lower β -strand content (27%) than the ovine XOR (α -helix – 7%, β -strand – 37%). This finding indicates that His-hXOR has a higher α -helix character than ovine XOR. The β -strand estimation of the ovine XOR cannot be considered accurate as the data were collected up to 190 nm and thus the β -strand estimation was poor. Both the turns and the unordered secondary structure characters were similar in both proteins.

The crystal secondary structure of bovine XOR (Table 3.7) was obtained using the Dictionary of Secondary Structure of Proteins (DSSP) method (Kabsch and Sander, 1983) via the Secondary Structure Server (2Struc) (Klose, Wallace and Janes, 2010). The α -helix character of bovine XOR was higher (32.2%) than both His-hXOR and ovine XOR whereas the β -strand character was lower (21.1%) than both proteins. The ‘other’ secondary structure of bovine XOR (which is composed of the turns and the unordered structures) was almost equivalent to that of His-hXOR (46.6% for bovine XOR versus 48% of His-hXOR). These findings indicate that the bovine XOR is closer in the secondary structure to His-hXOR than to ovine XOR.

Table 3.6: Secondary structure estimation from CD data using the CDSSTR method

Protein	Regular α -helix	Distorted α -helix	Regular β -strand	Distorted β -strand	Turns	Unordered	Total
His-hXOR	13%	11%	17%	10%	21%	27%	99%
	24%		27%				
Ovine XOR	3%	4%	25%	12%	22%	32%	98%
	7%		37%				

Table 3.7: Secondary structure content from PDB using the DSSP method.

Protein	PDB code	Method	α -helix	β -strand	Other
Bovine XOR	3UNC	DSSP*	32.2%	21.1%	46.6%

* (Kabsch and Sander, 1983)

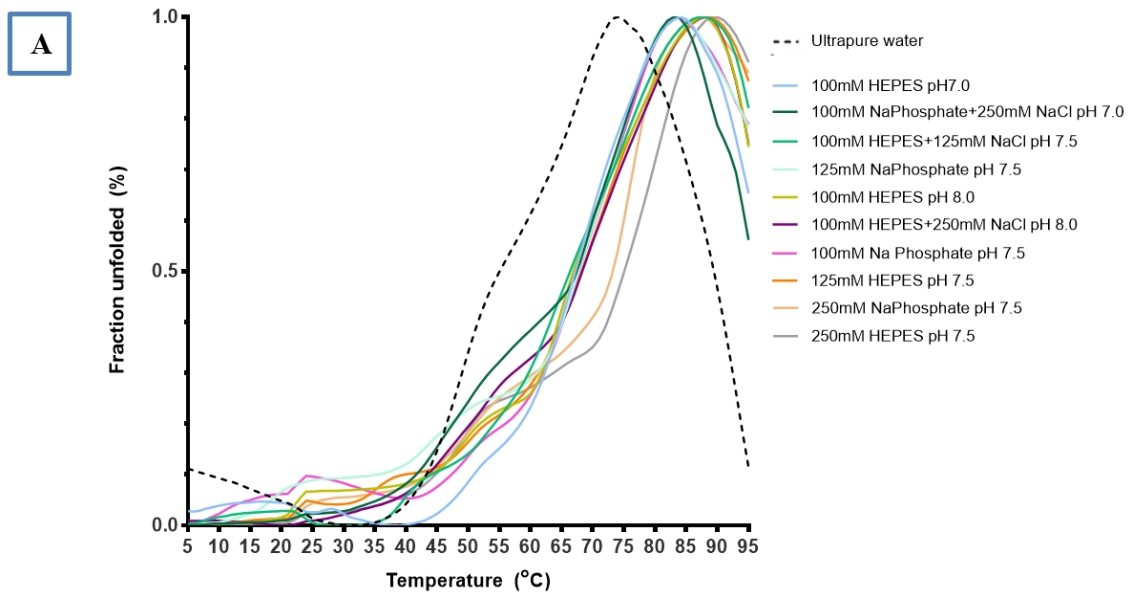
3.9.2. Thermal shift assays

The ThermoFluor method and nano-differential scanning fluorometry (nano-DSF) methods were employed for hXOR and ovine XOR respectively as described in Section 2.6.2. Both these methods were used to determine the melting temperature (T_M) and the most favourable buffer conditions for the proteins. The choice of method used depended on the amount of protein available for analysis. The ThermoFluor method requires more protein but is less expensive than the nano-DSF method and consequently the latter was preferred technique for the ovine XOR.

3.9.2.1. ThermoFluor Method

In the ThermoFluor method (Pantoliano *et al.*, 2001), a non-specific protein dye, in this case, SYPRO Orange, is used to monitor the thermal unfolding of the proteins. The fluorescence of the dye is quenched by the aqueous environment of the buffer tested. As the temperature gradually increases, the protein starts unfolding, exposing hydrophobic regions. The aromatic regions of the dye interact with the exposed hydrophobic environment of the partially unfolded protein. Due to this interaction, the dye is no longer quenched and fluorescence is observed. As the protein continues to unfold, the dye-protein interaction increases, increasing the fluorescence. As the protein completely unfolds, the dye becomes exposed to the aqueous environment and is quenched again (Pantoliano *et al.*, 2001; Rosa *et al.*, 2015).

The fluorescence emission was monitored at 569 nm with an excitation at 470 nm with a temperature gradient of $1^{\circ}\text{C}\cdot\text{min}^{-1}$ from 5°C to 95°C . A total of 96 buffers were tested. The signal of each data set was normalised using GraphPad Prism to obtain a Boltzmann distribution with the highest signal representing the 100% fraction unfolded while the lowest signal representing the 0% fraction unfolded. The T_M was determined by using a non-linear regression Boltzmann sigmoidal equation (GraphPad Prism). Figures 3.32 and 3.33 show the plots with the buffers yielding the highest T_M and lowest T_M respectively. Two buffer systems, HEPES pH 7.0 – 8.0 and sodium phosphate pH 7.0 – 7.5, were in the top ten buffers. As a result, these buffers were used for protein purifications and as storage buffers. The least favourable buffer systems (with the exception of imidazole buffers) were either acidic (pH 4.0 – 5.0) or alkaline (pH 8.5 – 9.0) indicating that hXOR is not stable under these conditions of pH.



Most Stable Buffers

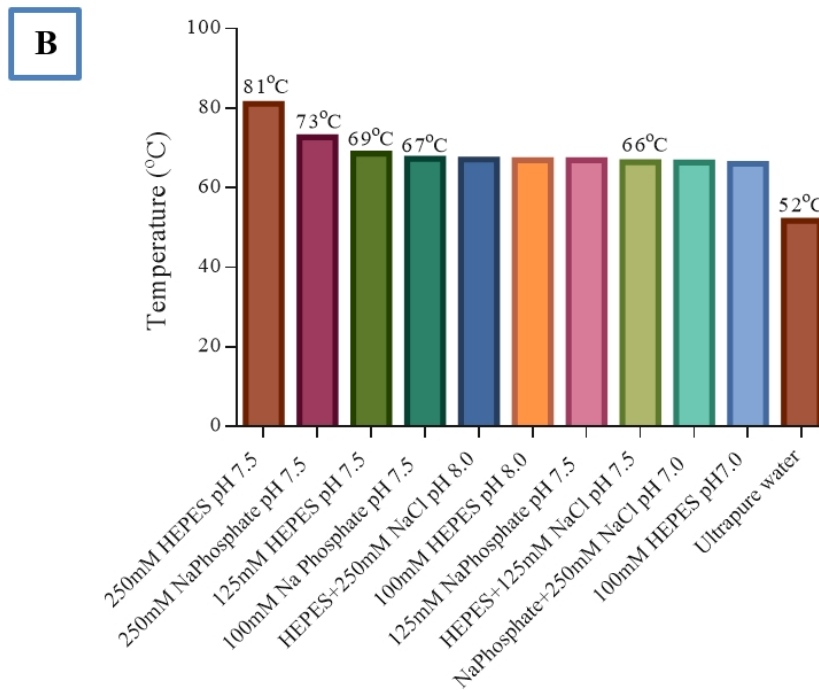


Figure 3.32: Top ten buffers which yielded the highest T_M . A – Normalised plot of the ThermoFluor experiment. The T_M can be extrapolated using a Boltzmann sigmoidal non-linear regression to find the temperature at which 50% of the protein was unfolded. B – The best buffers with T_M values. From all the buffers tested, 250 mM HEPES pH 7.5 yielded the highest T_M .

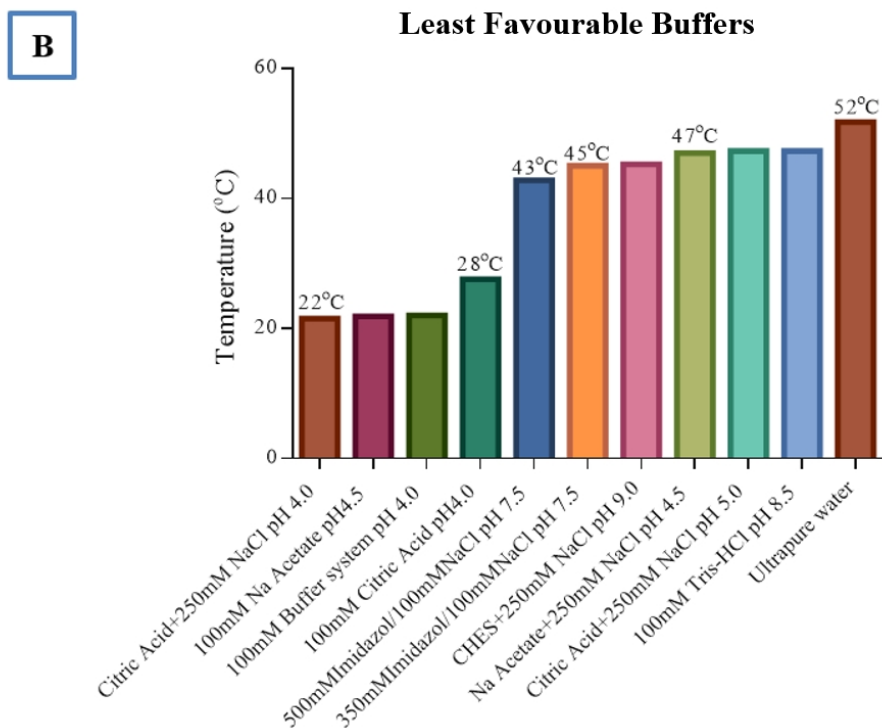
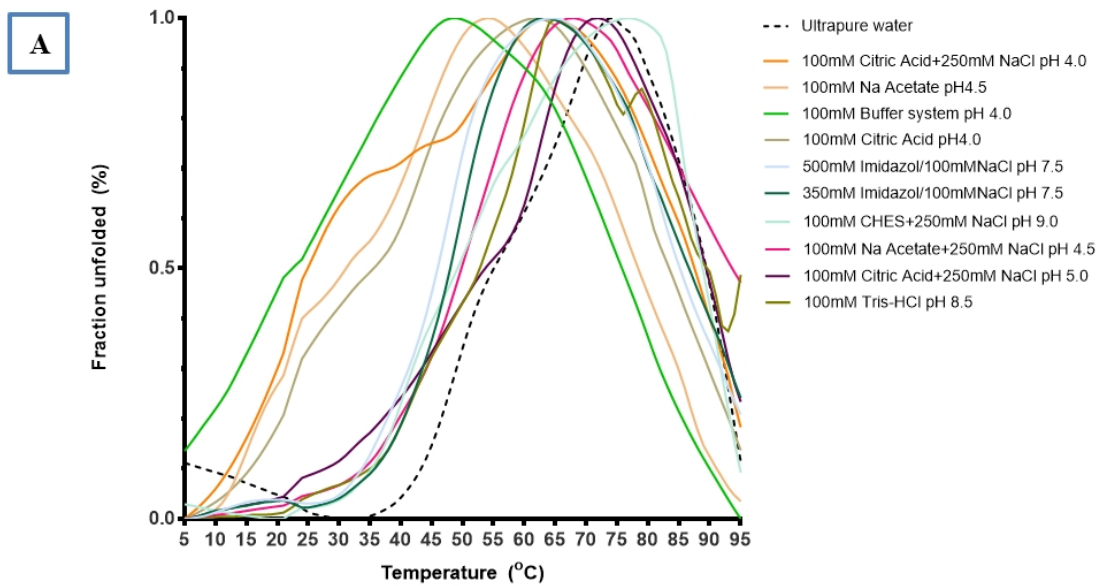


Figure 3.33: Least favourable buffers which yielded the lowest T_M . A – Normalised plot of the ThermoFluor experiment. The T_M can be extrapolated using a Boltzmann sigmoidal non-linear regression to find the temperature at which 50% of the protein was unfolded. B – The least favourable buffers with T_M values. From all the buffers tested, 100 mM citric acid with 250 mM NaCl pH 4.0 yielded the lowest T_M .

3.9.2.2. Nano-DSF Method

In the nano-DSF method, the fluorescence signals at 330 nm and 350 nm are monitored without the use of dyes. The temperature is increased gradually inducing protein denaturation. As the protein is unfolding, the tryptophan residues which are present in the hydrophobic part of the protein, become exposed to the aqueous hydrophilic environment causing a red-shift (bathochromic shift) from 330 nm. During unfolding, the fluorescence at 350 nm experiences little change while the fluorescence at 330 nm decreases drastically due to the shift. Thus, the ratio of the 350 nm signal to the 330 nm signal increases as the temperature increases. The ratio is then plotted and the first derivative of the ratio is calculated and plotted. The maximum peak of the first derivative corresponds to the melting temperature of the protein at that particular condition (Gihaz *et al.*, 2016).

A temperature gradient of $1^{\circ}\text{C}\cdot\text{min}^{-1}$ from 20°C to 95°C was employed on ovine XOR and a total of 48 buffers were tested. The signals from the 350 nm and 330 nm were divided to obtain the ratio. A first derivation of the ratio was then carried out to produce a classical peak shape. The two peaks observed in the first derivative plot correspond to different domains in the protein, in this case the unfolding of each monomer in the dimer (Figure 3.34). The T_M was calculated using a non-linear regression Boltzmann sigmoidal equation on the ratio signal and by reading the maxima of the first derivatives of the ratio. Only the maximum of the first peak was considered when calculating the T_M .

The buffers that gave the highest T_M in the ovine XOR were in the pH range of 6.0 – 8.0 with the exception of bicine pH 8.5. Since phosphate buffer was present in four out of the best ten buffers, phosphate buffer was used for subsequent purifications and as a storage buffer (Figure 3.35).

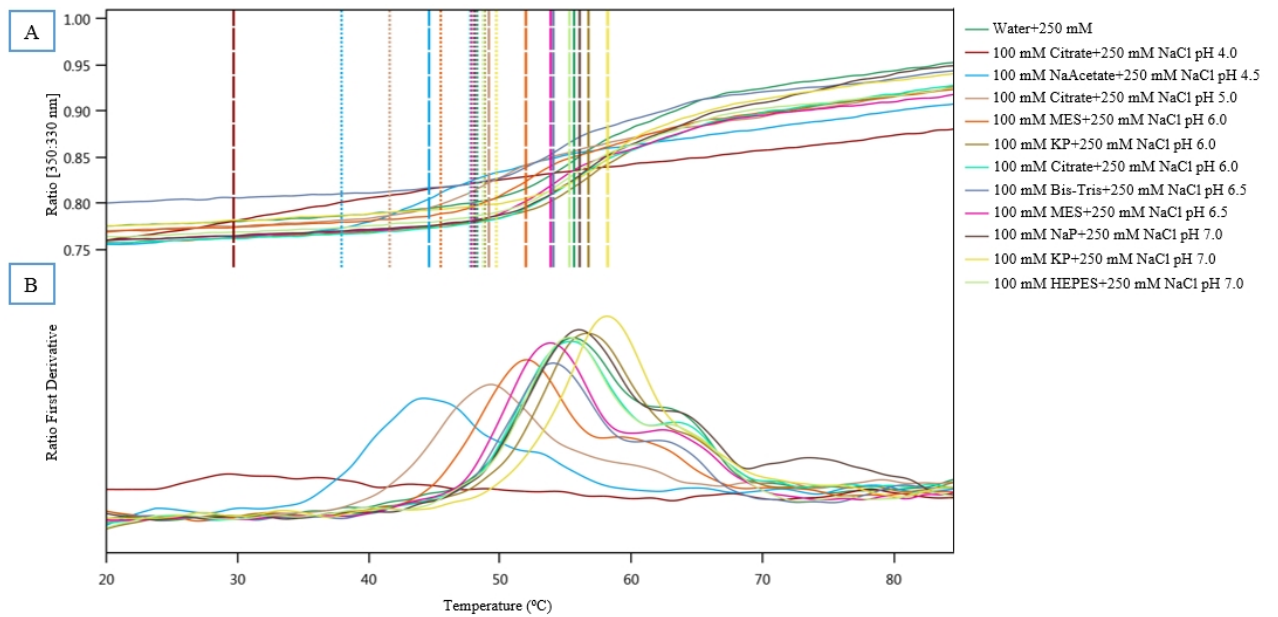


Figure 3.34: Nano-DSF plots of ovine XOR. A – Plot of the ratio of the 350 nm to the 330 nm signal. The dotted lines represent the T_M values. B – The first derivative of the ratio. Each graph gave two peaks representing the unfolding of each individual monomer.

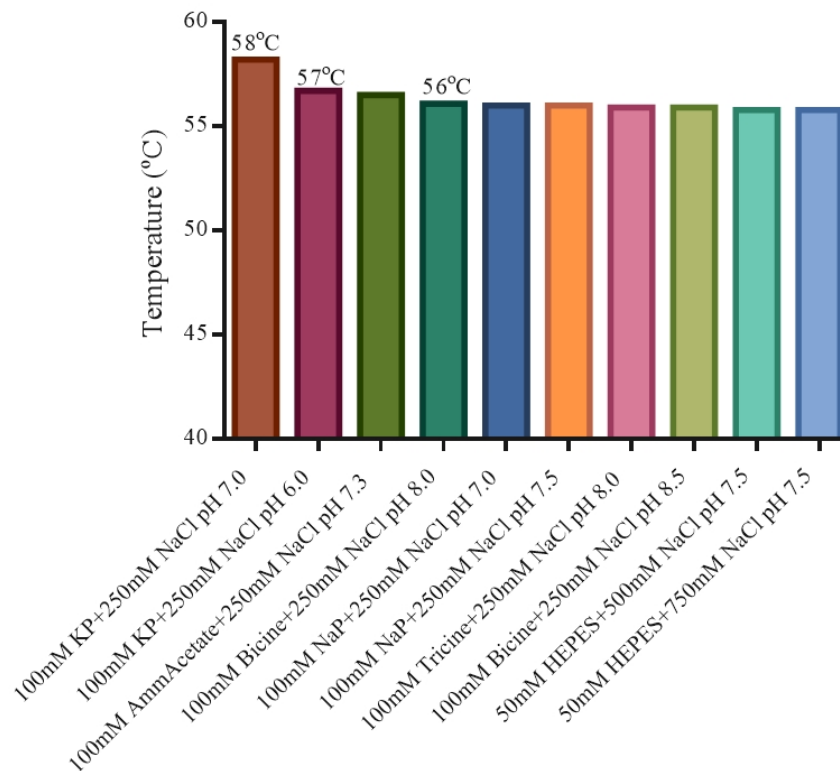


Figure 3.35: Top ten buffers which yielded the highest T_M. From all the buffers tested, 100 mM KP with 250 mM NaCl pH 7.0 yielded the highest T_M.

3.9.3. MALDI-TOF mass spectroscopy

MALDI-TOF was carried out as described in Section 2.6.3. The MALDI-TOF mass spectrometer was not calibrated for high molecular mass proteins (above 44.6 kDa) and as a result, the mass spectrum obtained (Figure 3.36) was used to approximately confirm the structure. A small peak at around 297 kDa confirmed the presence of the dimer. Due to the ionisation energy of the mass spectrometer, the dimer was split to the monomer as observed in the mass spectrum at approximately 149 kDa. The other two peaks at lower m/z were attributed to the monomer with a charge of +2 (74 kDa) and a charge of +3 (50 kDa). The difference in mass between the theoretical and the measured mass was due to discrepancy in instrument calibration (Table 3.8) (S. Niebling, personal communication, 2019).

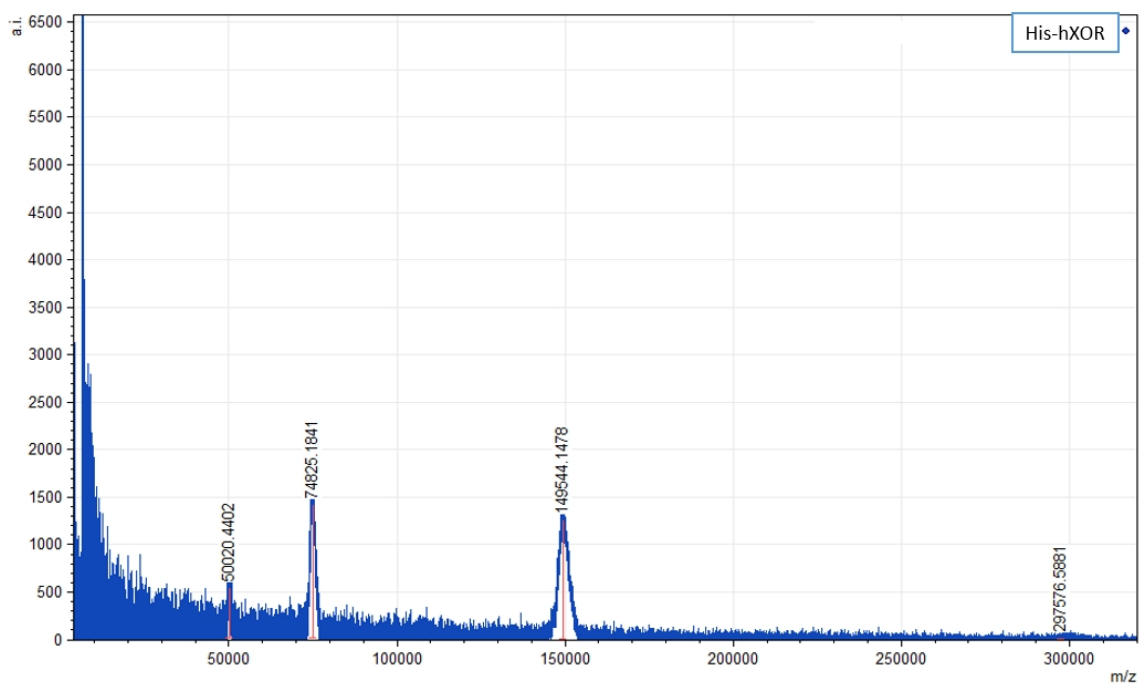


Figure 3.36: MALDI-TOF spectrum of His-hXOR. Spectrum plotted and annotated using mMass software (Niedermeier and Strohaln, 2012)

Table 3.8: Experimental and theoretical molecular mass

Experimental mass determined from MALDI-TOF (Da)	Theoretical molecular mass determined by Protean (Protean version 7.1, 2006) (Da)	Difference (Da)	Peak contribution
297576.5881	299128.0594	1551.4713	Dimer protein
149544.1478	149564.0297	19.8819	Monomer protein
74825.1841	74782.01485	43.1693	+2 charge of monomer
50020.4402	49854.6766	165.7636	+3 charge of monomer

3.9.4. In-gel trypsin digest

An in-gel trypsin digest was performed on His-hXOR as described in Section 2.6.4. For this analysis, the protein sample was first denatured and loaded on an 8% SDS-PAGE gel (Figure 3.37). Particular care was taken when preparing the buffers for electrophoresis as any contamination may affect the analysis. The 8% SDS-PAGE gel was sent to EMBL (Hiedelberg) where the band of interest (marked with an arrow in Figure 3.37) was excised and an in-gel trypsin digestion was carried out. The sample was then cleaned up and liquid chromatography-mass spectroscopy (LC-MS) was performed on the cleaved sample. The mass of the peptides obtained from LC-MS was then compared to the expected peptides from trypsin digestion and the number of peptides, unique peptides, and % sequence coverage were obtained. All the proteins that may contribute to both the expected peptides and unique peptides were listed. The peptides were scored by an ion score which represents the probability that the experimental mass obtained matches the database sequence. The higher the ion score, the more probable that the peptide comes from the database sequence. The ion scores were then summed up and the protein containing the highest ion score was the most probable protein present in the denatured sample sent.

From the data analysis obtained, the band of interest was concluded to be hXOR, having a total score (8154) which was approximately ten times higher than the second-best protein candidate (nitrate reductase, 855). Moreover, hXOR had the highest sequence coverage of 72.6% against 19.6% of nitrate reductase. Nitrate reductase was considered a possible candidate since it has similar mass to hXOR (140489 Da and 147816 Da respectively) and shares a 19.17% amino acid identity to hXOR. The sequence coverage

was not 100% as LC-MS has a threshold of detection. In fact, when the sequence of hXOR was analysed using PeptideMass (Wilkins *et al.*, 1997) a peptide mass cut-off of 1000 Da (meaning that peptides with lower mass will not be detected), the sequence coverage simulated was 70.5%, which was similar to that obtained experimentally. The other proteins listed in the analysis (pig trypsin and human keratin) were experimental contaminants.

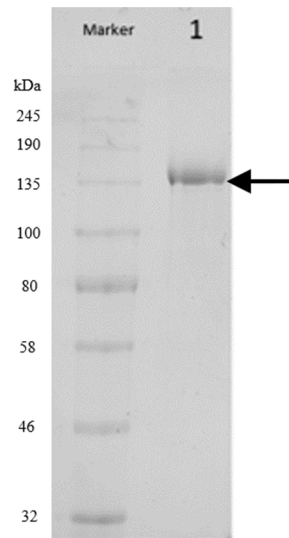


Figure 3.37: SDS-PAGE gel (8%) sent to EMBL (Heidelberg) for in-gel trypsin digestion. Lane 1: 4 μ g His-hXOR; Marker: BioLabs broad range protein standard marker. The black arrow represents the XOR position.

Table 3.9: In-gel trypsin digest analysis

UniProt Protein ID	Protein name	Molecular weight (Da)	Sequence spectral matches	Unique Peptide matches	Total Score	Sequence coverage (%)
P47989	Human xanthine oxidoreductase	147815.681	404	143	8154	72.6
P09152	Respiratory nitrate reductase 1 alpha chain	140489.391	23	19	855	19.6
/	Pig trypsin	24409.4758	15	5	317	25
/	Human Keratin, type 1 cytoskeletal 9	62064.3245	7	6	398	12.7
/	Human Keratin, type II cytoskeletal 1	66038.7298	4	3	168	5.6

3.9.5. Element analysis

Element analysis by ICP-SFMS was conducted as described in Section 2.6.6 using 2.04 μM of His-hXOR. Element analysis was only carried out on the His-hXOR as there was insufficient amounts of ovine XOR for the analysis. The results of the analysis are presented in Table 3.10. To determine the abundance of each element, the amount of each element in a dimer was first calculated. This yielded into 156 atoms of sulfur, 8 atoms of iron and 2 atoms of molybdenum per dimer of protein. From the corresponding number of atoms, the abundance was calculated. The protein was completely sulfurated ($99.49 \pm 3.93\%$). However, both metal sites had a low abundance. Iron was only present as $23.25 \pm 3.51\%$ while molybdenum was present as $19.90 \pm 0.66\%$. As a result, a mixture of non-metallated, partially metallated and metallated enzymes was present in the purified sample (Table 3.11). This indicates that more supplements are required in the growth media to increase the metal abundance in the enzyme. Previous work reported that recombinant molybdoenzymes expressed with low to moderate molybdenum content (Yamaguchi *et al.*, 2007; Foti *et al.*, 2016).

Table 3.10: Element analysis of His-hXOR.

Element	Amount (mg.L^{-1})	Abundance (%)
S	10.132	99.49 ± 3.93
Fe	0.212	23.25 ± 3.51
Mo	0.0779	19.90 ± 0.66

Table 3.11: Proposed different metallation combinations of His-hXOR.

Combination	Fe in 1 st [2Fe-2S]	Fe in 2 nd [2Fe-2S]	Mo in Moco
Fully metallated	✓	✓	✓
Partially metallated	✓	✗	✗
Partially metallated	✗	✓	✗
Partially metallated	✓	✓	✗
Partially metallated	✓	✗	✓
Partially metallated	✗	✓	✓
Non-metallated	✗	✗	✗

✓ - Present

✗ - Absent

3.9.6. Estimation of FAD content of purified hXOR

The estimation of FAD content was carried out as described in Section 2.6.5. The concentration of hXOR was calculated from the A_{280} as determination of the concentration from A_{450} would bias the results. The concentration of hXOR tested was $0.5 \mu\text{M}$ (dimer concentration) and the FAD content of hXOR was determined to be $1.0 \mu\text{M}$. As hXOR is a dimer and contains one FAD per monomer, the expected amount of FAD for $0.5 \mu\text{M}$ of protein is $1.0 \mu\text{M}$, meaning that the FAD content was 100%.

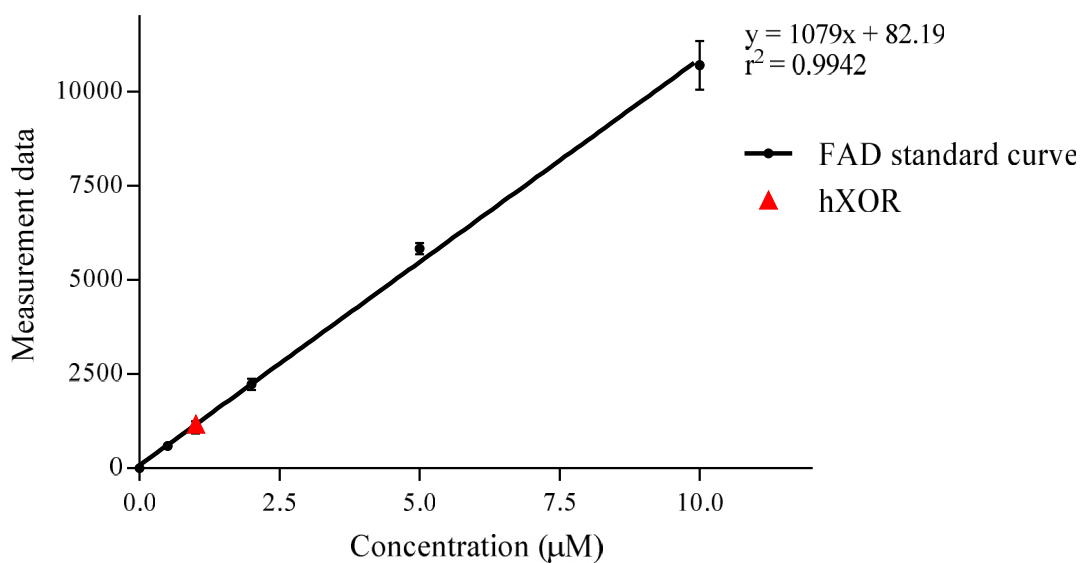


Figure 3.38: FAD standard curve. Standard concentrations of FAD were prepared at 0.5, 1.0, 2.0, 5.0 and 10.0 μM . Error bars represent the standard deviation ($n=3$). The concentration of FAD in hXOR was found to be $1.0 \mu\text{M}$.

3.10. Inhibitor synthesis

3.10.1. Inhibitor A

The synthesis of inhibitor A (4-[(Z)-(6-hydroxy-3-oxo-1-benzofuran-2(3H)-ylidene)methyl]benzoic acid) was carried out as described in Section 2.9.1 via an aldol condensation. To a stirred solution of sodium methoxide, 2 mmol of 6-hydroxy-1-benzofuran-3(2H)-one (a) and 2 mmol of 4-formylbenzoic acid (b) were dissolved. Due to the electronegative pull of the two oxygens in (a), the β -hydrogen had a partial positive charge and thus was subject to a nucleophilic attack by the methoxide anion. This resulted into the β -deprotonation of (a) and the subsequent formation of an enolate ion (Figure 3.38, 1). The enolate ion tautomerised back to the keto form and the β -carbon (which was now negative) acted as the nucleophile and attacks the carbonyl in (b), resulting into a nucleophilic addition of compound (a) to (b) (Figure 3.38, 2 and 3). The formed species was protonated to form a hydroxyl group (Figure 3.38, 4) and the β -hydrogen was attacked again by a nucleophile (OH^-) to produce the enolate (Figure 3.38, 5). The enolate tautomerised back to the keto form, and by doing so the hydroxyl ion was eliminated to form an α,β unsaturated ketone (inhibitor A) (Figure 3.38, 6). As the aldol condensation was carried out under basic conditions, the acidic groups of inhibitor A were deprotonated. Consequently, concentrated hydrochloric acid was added to protonate inhibitor A (Figure 3.38, 7). Inhibitor A was then filtered and left in a desiccator to dry overnight. The full mechanism of the aldol condensation is outlined in Figure 3.38.

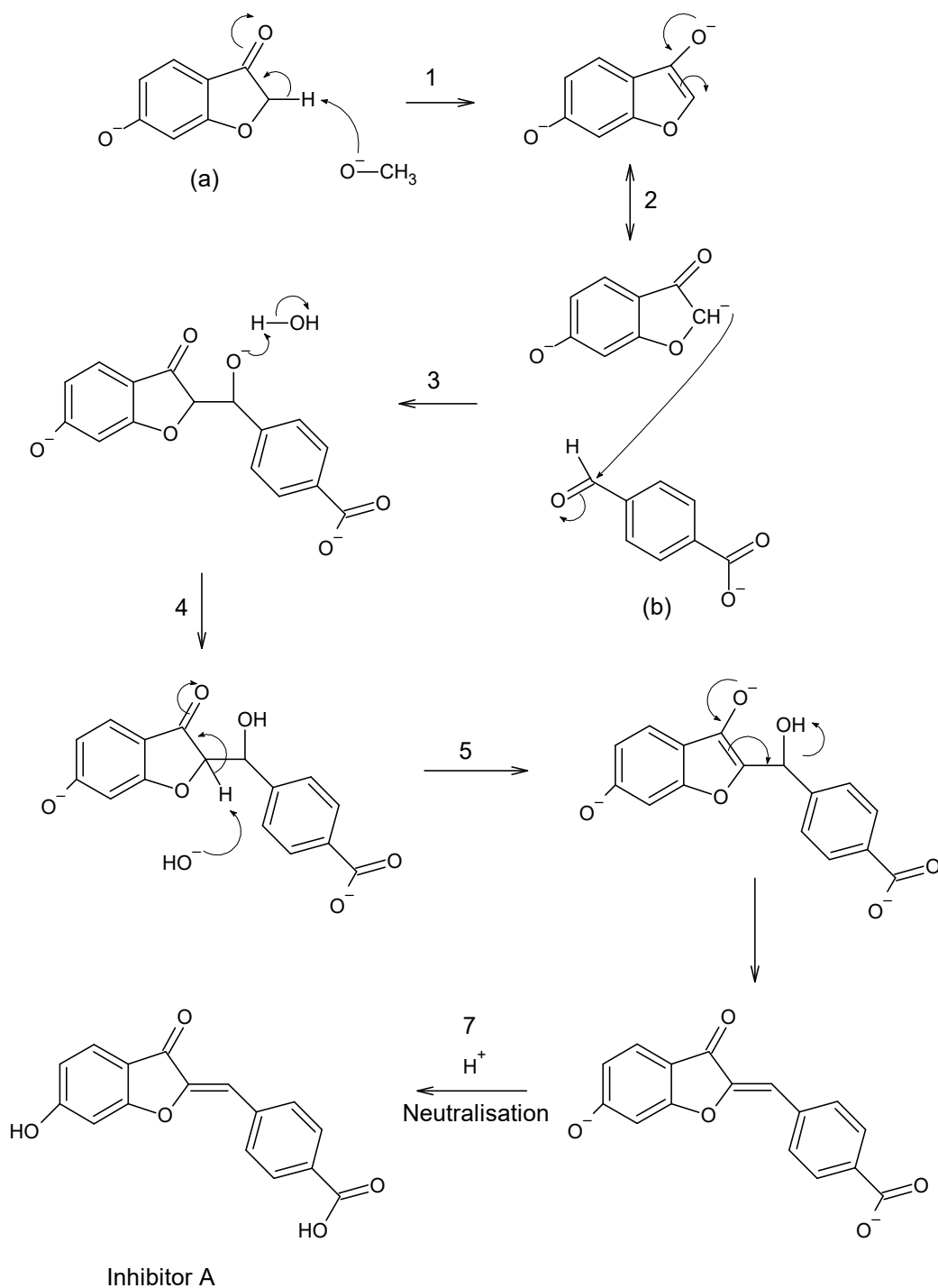


Figure 3.39: Mechanism of the aldol condensation between 6-hydroxy-1-benzofuran-3(2*H*)-one (a) and 4-formylbenzoic acid (b) to form inhibitor A. Structures drawn by ACD/Chemsketch (Advanced Chemistry Development, Inc. version 2018.1).

3.10.1.1. NMR spectra of Inhibitor A

Proton (^1H) and carbon-13 (^{13}C) NMR were conducted at the Fachbereich Chemie, Universität Hamburg, Germany. In NMR, the resulting peaks are due to different chemical shifts (δ) caused by the local magnetic environment of the compound. In general, more electronegative groups increase the shift. As different carbons and protons have different electrostatic environments, different chemical shifts will be present, thus helping to elucidate the structure under investigation. Both ^1H and ^{13}C -NMR were used to confirm the structure of inhibitor A.

The ^1H -NMR of inhibitor A (Figure 3.39) integrates to a total of nine hydrogens. However, inhibitor A has ten hydrogens. The chemical shift of the missing hydrogen was masked by the DMSO solvent used to dissolve the compound during the experimental preparation. The chemical shifts pertained to the hydrogens of inhibitor A are described in Figure 3.40.

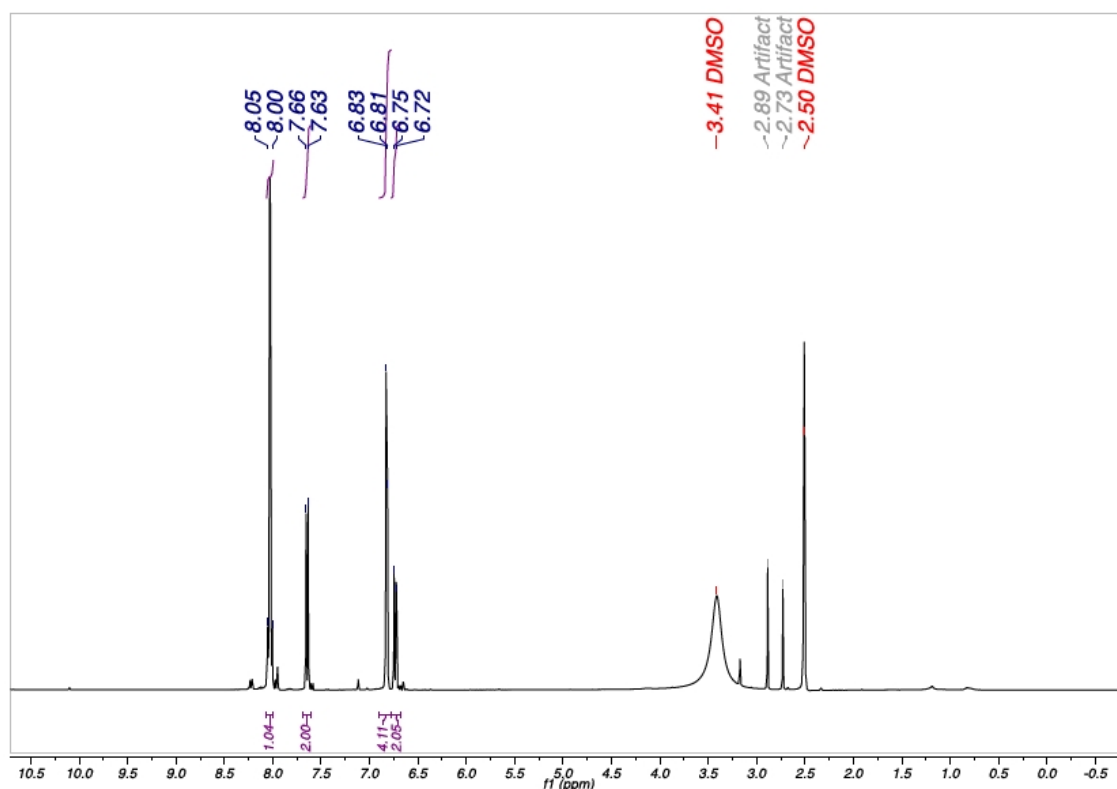


Figure 3.40: ^1H NMR (400 MHz, DMSO) of inhibitor A. δ 8.05-8.00 (d, $J=8.03$ Hz, 4H), 7.66 (d, $J=7.64$ Hz, 1H), 6.83 (s, 2H), 6.81 (d, $J=6.82$ Hz, 1H), 6.75-6.72 (d, $J=6.63$ Hz, 1H).

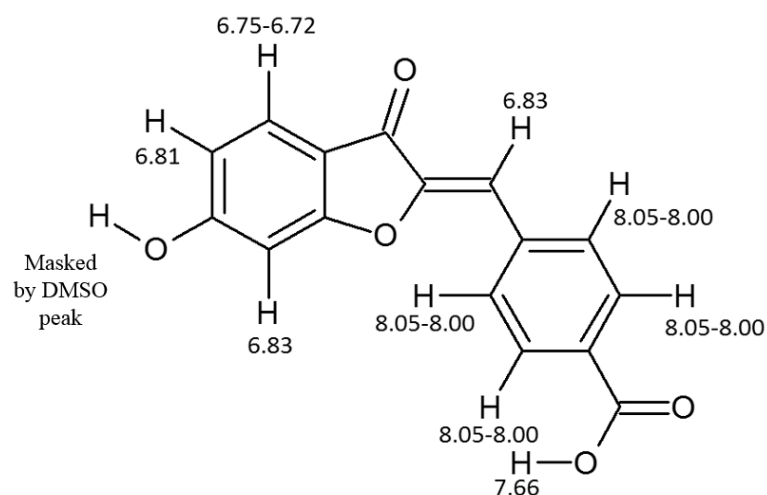


Figure 3.41: Inhibitor A with ^1H chemical shift annotations. All values are in ppm.

Figure 3.41 shows the presence of the different carbons (CO, COOH, C, CH) in the ^{13}C -NMR that account for inhibitor A. The different chemical shifts pertaining to the carbons of inhibitor A are described in Figure 3.42.

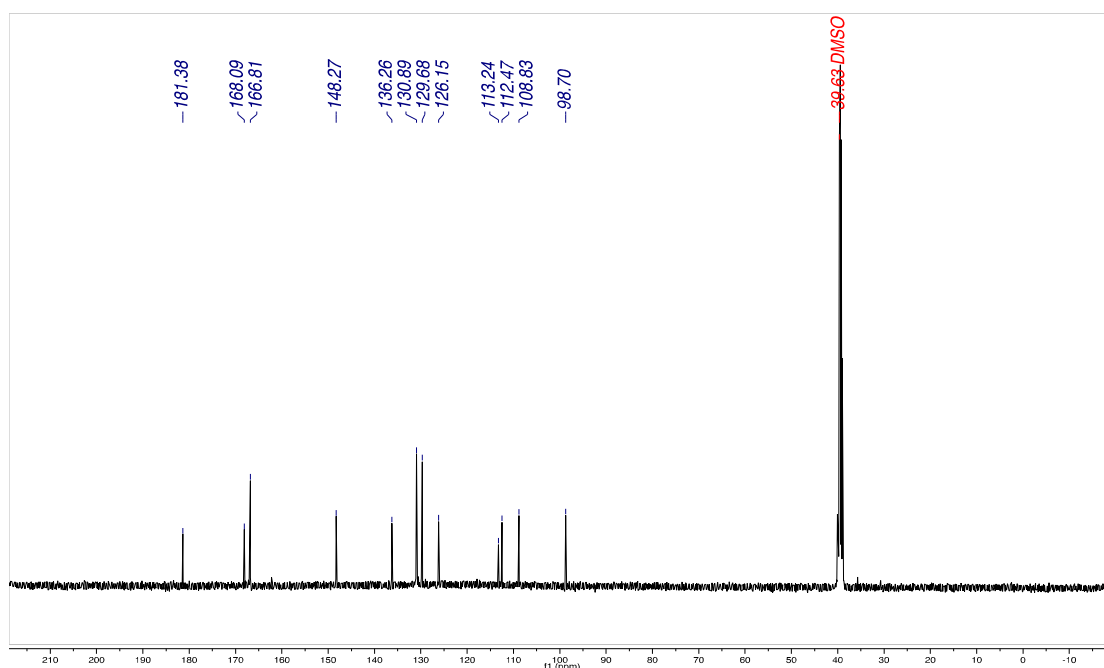


Figure 3.42: ^{13}C NMR (100 MHz, DMSO) of inhibitor A. δ 181.38 (CO), 168.09 (COOH), 166.81 (C), 148.27 (C), 136.26 (C), 130.89 (CH), 129.68 (C), 126.15 (CH), 113.24 (CH), 112.47 (CH), 108.83 (CH), 98.70 (CH).

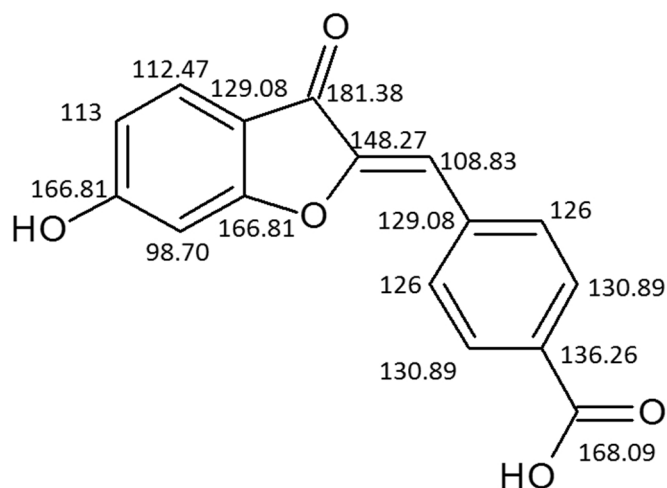


Figure 3.43: Inhibitor A with ^{13}C chemical shift annotations. All values are in ppm. Structures drawn by ACD/Chemsketch (Advanced Chemistry Development, Inc. version 2018.1).

Both the ^1H -NMR and the ^{13}C -NMR confirmed that this synthesised compound (Section 2.9.1) had the correct structure of inhibitor A (4-[(Z)-(6-hydroxy-3-oxo-1-benzofuran-2(3H)-ylidene)methyl]benzoic acid).

3.10.2. Inhibitor B

3.10.2.1. Synthesis of Br1 and Br2

The synthesis of Br1 and Br2 was carried out as described in Section 2.9.2.1. The first step of the synthesis was to protect the hydroxyl groups in 1-(2,4-dihydroxyphenyl)ethanoate and 4-hydroxybenzaldehyde to form Br1 and Br2 respectively. This was done to prevent the formation of side products of possible reactions of the hydroxyl groups with the potassium hydroxide present in the next step of the synthesis. The hydroxyl groups were therefore benzylated by the addition of benzyl bromide. The general mechanism of hydroxyl group benzylation is described in Figure 3.43.

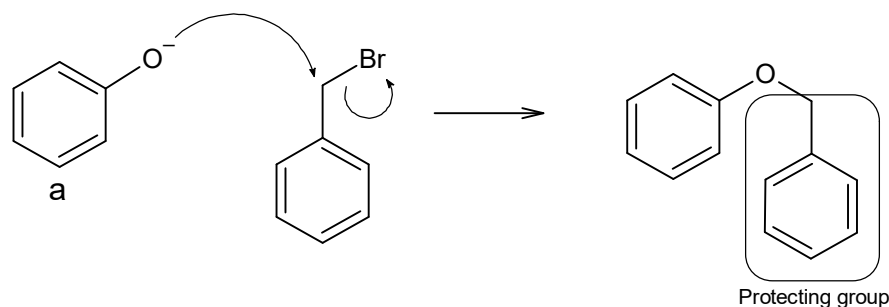


Figure 3.44: Protection of the hydroxyl group by the addition of a benzyl group. Compound a represents both starting materials. Structures drawn by ACD/Chemsketch (Advanced Chemistry Development, Inc. version 2018.1).

The synthetic reactions and the column chromatography were monitored using thin-layer chromatography (TLC). When analysing the products of Br1 synthesis by TLC (Figure 3.45, (A)) 4 main bands were observed. As the silica TLC plates used were polar, the more polar substances migrated least on a TLC plate due to the high degree of interactions with the silica phase. As the starting material, 1-(2,4-dihydroxyphenyl)ethenone (1), is very polar due to the hydroxyl groups, it migrated the least. On the other hand, the excess reagent (benzyl bromide) that is not polar, migrated the furthest. Since the protection step involved benzenating the hydroxyl groups of (1), the polarity of Br1 is less than that of (1), resulting in less migration in the silica phase. The bands in the middle were identified as impurities such as mono-benzenated samples.

After three hours, the product and side-reactions were loaded on a silica column chromatography and the fractions were evaluated by TLC (Figure 3.46, B and C). The tubes containing Br1 (fraction 12 to 18 in Figure 3.46C) were identified and pooled together. The solvent in the pooled sample was evaporated and a sample was taken for $^1\text{H-NMR}$ and $^{13}\text{C-NMR}$ (Appendix).

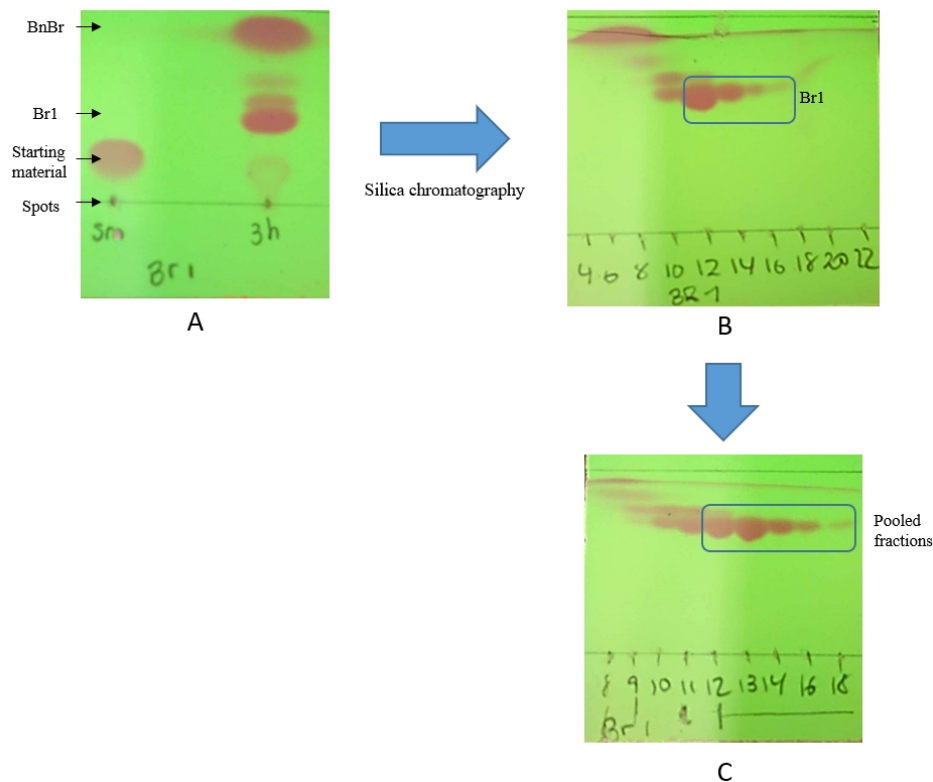


Figure 3.45: TLC for Br1 using 4:1, hexane:ethyl acetate. A - SM: starting material; 3h - after 3h reaction. The multiple bands were identified to be excess reagents (BnBr, top), impurities (middle bands), fully benzenated Br1 (bottom band). B – After a silica column chromatography. C – Detail of the silica column chromatography. Fractions 12 – 18 were pooled together.

The same procedure was done for Br2. When analysing the TLC plate of Br2 synthesis (Figure 3.46, A), two bands were observed after 3 hours of reaction. These two bands were identified as excess benzyl bromide (top band) and the product Br2 (bottom band). Silica column chromatography was performed and the Br2 was successfully isolated and purified (Figure 3.46 B, C). The solvent in the pooled sample was evaporated and a sample was taken for $^1\text{H-NMR}$ and $^{13}\text{C-NMR}$ (Appendix). The intermediates were weighed and the yield was calculated as shown in Table 3.12.

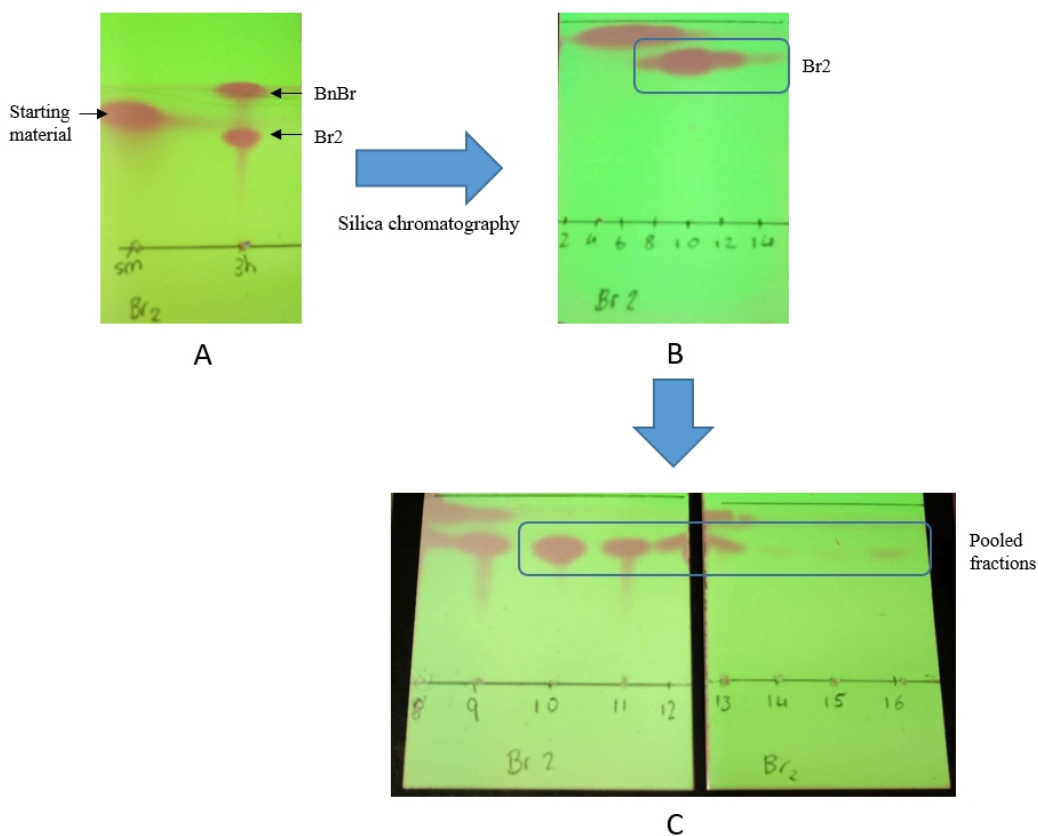


Figure 3.46: TLC for Br₂ using 4:1, hexane:ethyl acetate. A - SM: starting material; 3h - after 3h reaction. The multiple bands were identified to be excess reagents (BnBr, top), benzenated Br₂ (bottom band). B – After a silica column chromatography. C – Detail of the silica column chromatography. Fractions 10 – 16 were pooled together.

Table 3.12: Amount and yield of intermediates Br1 and Br2

Sample	Mass of product/mg	RMM/g.mol ⁻¹	Amount/mmol	Yield/%
Br1	920	304	3.29	85.2
Br2	630	198	3.18	77

3.10.2.2. Synthesis of Br3

The synthesis of Br3 was conducted as described in Section 2.9.2.2. Br1 and Br2 were combined in the presence of potassium hydroxide to perform an aldol condensation reaction. The mechanism of the aldol condensation between Br1 and Br2 is the same as described in Section 3.12.1. In this reaction, Br1 was first β -deprotonated and acted as the nucleophile on Br2 (Figure 3.44, 1). The subsequent product was then β -deprotonated again, forming the enolate which goes back to the keto form, thereby eliminating the hydroxyl group and forming the α,β -unsaturated ketone, Br3 (Figure 3.44,2).

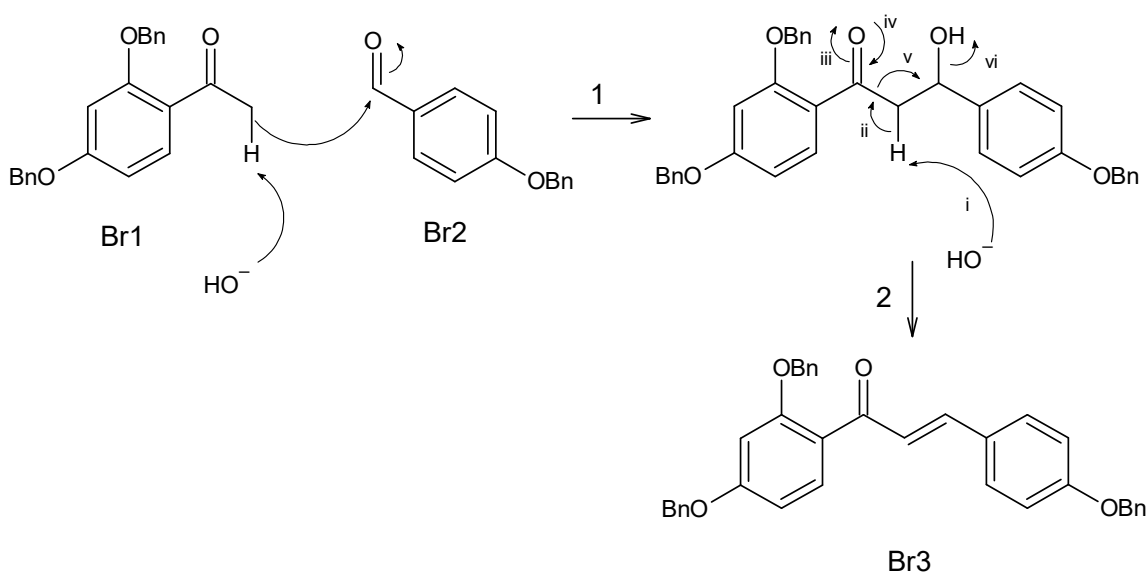


Figure 3.47: Mechanism (summarised) of the aldol condensation between Br1 and Br2 to form Br3. Structures drawn by ACD/Chemsketch (Advanced Chemistry Development, Inc. version 2018.1).

After 30 minutes an aliquot was taken to analyse the reaction mixture on a TLC plate. The reaction was then left stirring overnight and adjusted to pH 5.0 by adding hydrochloric acid so that hydroxide ions were removed from the mixture, thus stopping the reaction. An aliquot for TLC was taken after addition of the acid (Figure 3.47 A,B). When analysing the TLC of the Br3 synthesis (Figure 3.47), four distinctive bands can be observed at the starting material lane (A, lane SM). After an overnight incubation, the third band from top in the SM lane increased in intensity. This band was identified as the product Br3. Since with a mobile phase of 4:1, hexane:ethyl acetate (A), the bands did not have a good resolution, a more apolar mobile phase was tested (B). With a mobile phase of 6:1, hexane:ethyl acetate, the bands were not resolved at all. As a result, a

gradient of mobile phases of 4:1, 5:1, and 6:1, hexane:ethyl acetate, was carried out on a silica column chromatography (C). Br3 was isolated and purified from this gradient purification. The solvent in the pooled sample was evaporated and a sample was taken for $^1\text{H-NMR}$ and $^{13}\text{C-NMR}$ (Appendix). The intermediate was weighed and the yield was calculated as shown in Table 3.13.

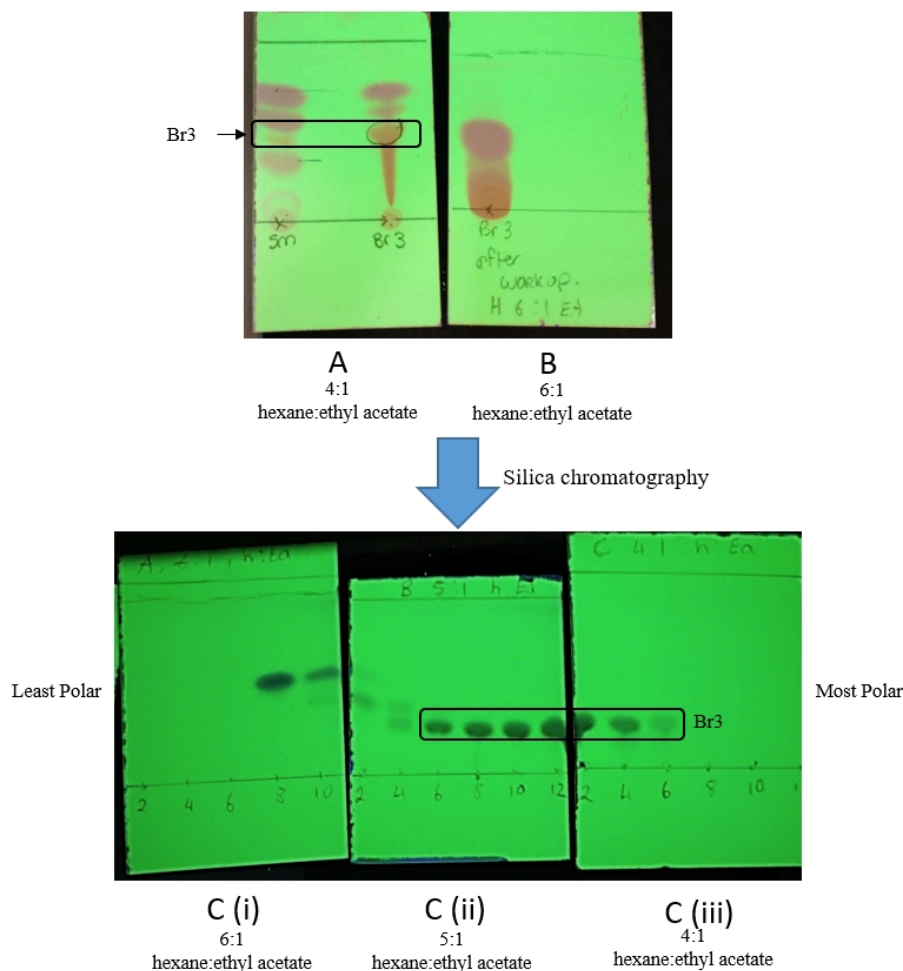


Figure 3.48: TLC for Br3. A – Mobile phase: 4:1, hexane:ethyl acetate. SM: starting material after 30 minutes; Br3 - after overnight reaction. B – Mobile phase: 6:1, hexane:ethyl acetate. C – After a silica column chromatography. C (i) – Mobile phase 6:1, hexane:ethyl acetate. C (ii) – Mobile phase 5:1, hexane:ethyl acetate. C (iii) – Mobile phase 4:1, hexane:ethyl acetate. Tubes 6 – 12 from C (ii) and tubes 1 – 6 from C (iii) were combined.

Table 3.13: Amount and yield of intermediate Br3.

Sample	Mass of product/mg	RMM/g.mol ⁻¹	Amount/mmol	Yield/%
Br3	540	484	1.12	69.7

3.10.2.3. Synthesis of Inhibitor B

The synthesis of inhibitor B was carried out as described in Section 2.9.2.3. The last step of the synthesis was to deprotect the hydroxyl groups to produce inhibitor B. This was done by the addition of boron tribromide. In this reaction, the benzylated oxygen attacked nucleophilically boron tribromide, eliminating a bromide ion in the process (Figure 3.48, 1). The eliminated bromide attacked the benzyl group, which subsequently donated its electrons to the oxy cation (Figure 3.48, 2). The boron group attached donated its electrons to the oxygen that in turn took up a proton in the reaction mixture to form the hydroxyl ion (Figure 3.48, 3). The mechanism of the general reaction is described in Figure 3.48.

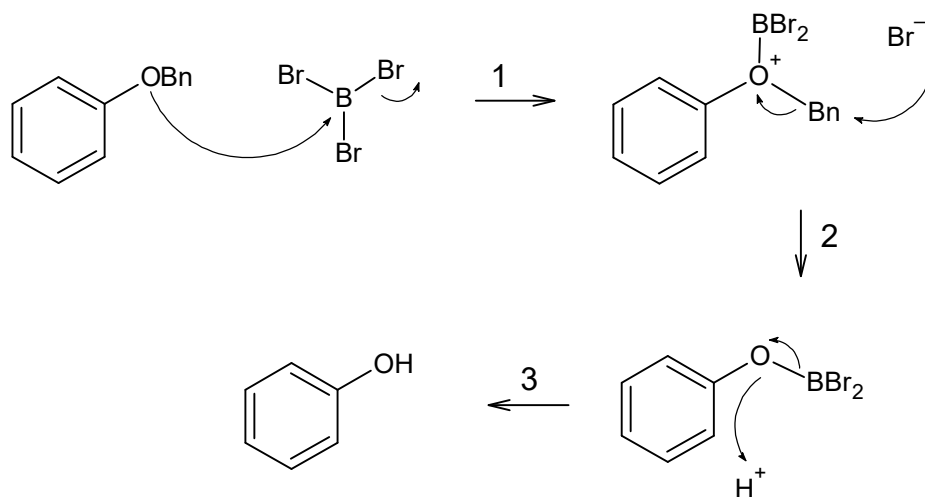


Figure 3.49: Removal of the benzyl group by boron tribromide. Structures drawn by ACD/Chemsketch (Advanced Chemistry Development, Inc. version 2018.1).

When analysing the TLC after the reaction work-up (Figure 3.49A), three distinctive bands can be observed. During the production of inhibitor B, the apolar benzyl bromide was produced as a side product, accounting for the top band in the TLC. The other two bands were identified as unreacted Br₃ (middle band) and inhibitor B (lower band). Inhibitor B was identified as the lower band as it has a higher polarity than unreacted Br₃. This indicated that the reaction did not go to completion and therefore, more reaction time and a larger excess of BBr₃ may be used in future experiments to ensure reaction completion.

The reaction mixture was then purified via silica column chromatography (plates B and C in Figure 3.49 B,C) using a 2:1, hexane:ethyl acetate solution as the mobile

phase. Inhibitor B was isolated to purity (Figure 3.49, fraction 24 – 30) and the solvent was evaporated and a sample was taken for $^1\text{H-NMR}$ and $^{13}\text{C-NMR}$. The product was weighed and the yield was calculated as shown in Table 3.14.

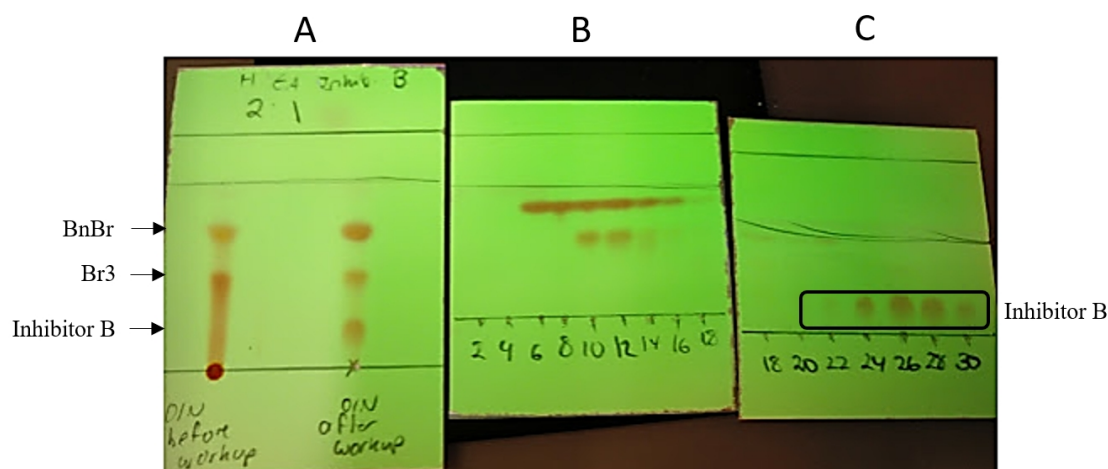


Figure 3.50: TLC for inhibitor B. A – TLC before and after reaction workup showing three distinctive bands. B and C – TLC after a silica column chromatography.

Table 3.14: Amount and yield of intermediate Br3.

Sample	Mass of product/mg	RMM/g.mol ⁻¹	Amount/mmol	Yield/%
Inhibitor B	100	256	0.39	39

3.10.2.4. NMR spectra of Inhibitor B

Both $^1\text{H-NMR}$ and $^{13}\text{C-NMR}$ (Figure 3.50, 3.52) confirmed that the product obtained was Inhibitor B ((2E)-1-(2,4-dihydroxyphenyl)-3-(4-hydroxyphenyl)prop-2-en-1-one). The most notable confirmation in the NMR spectra is the presence of the three different hydroxyl (-OH) groups in the product ($^1\text{H-NMR}$: δ 13.47 (s, 1H), 10.44 (s, 2H); $^{13}\text{C-NMR}$: 165.77 (COH), 165.08 (COH), 157.24 (COH)), showing that the deprotection step of Br3 was successful. The chemical shifts pertained to the different protons and carbons are shown in Figures 3.51, 3.52 respectively.

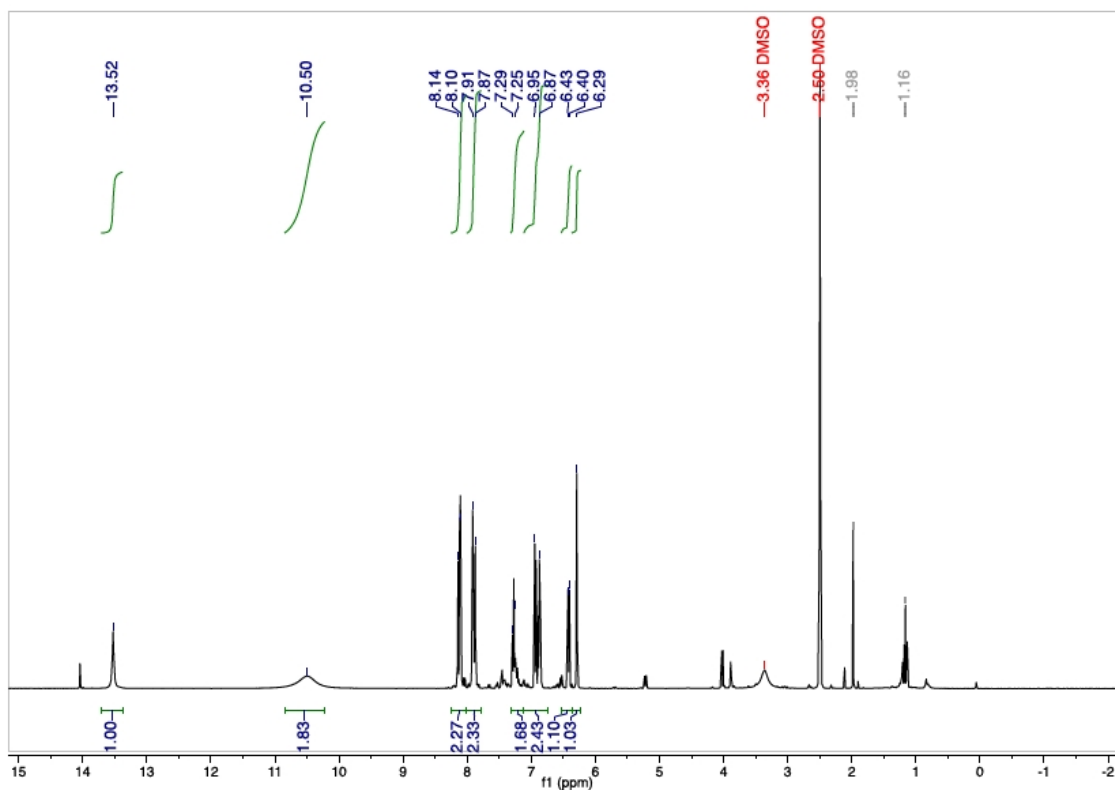


Figure 3.51: ^1H NMR (400 MHz, DMSO) of inhibitor B. δ 13.47 (s, 1H), 10.44 (s, 2H), 8.09-8.04 (d, $J=8.06$, 2H), 7.85-7.82 (d, $J=7.84$, 2H), 7.24-7.17 (m, 1H), 6.89-6.81 (m, 2H), 6.37 (d, $J=6.36$, 1H), 6.35 (d, $J=6.23$, 1H).

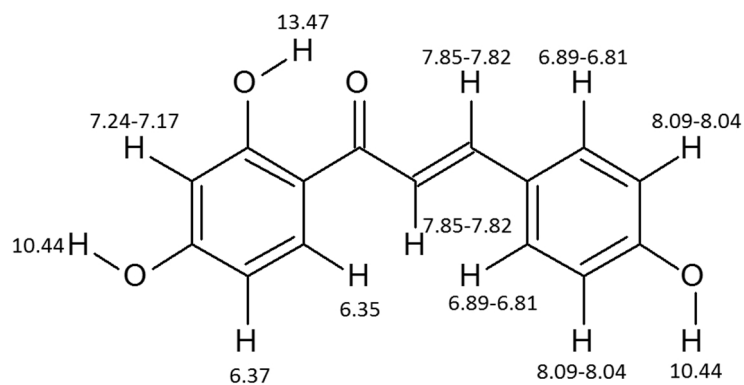


Figure 3.52: Inhibitor B with ^1H chemical shifts. All values are in ppm. Structures drawn by ACD/Chemsketch (Advanced Chemistry Development, Inc. version 2018.1).

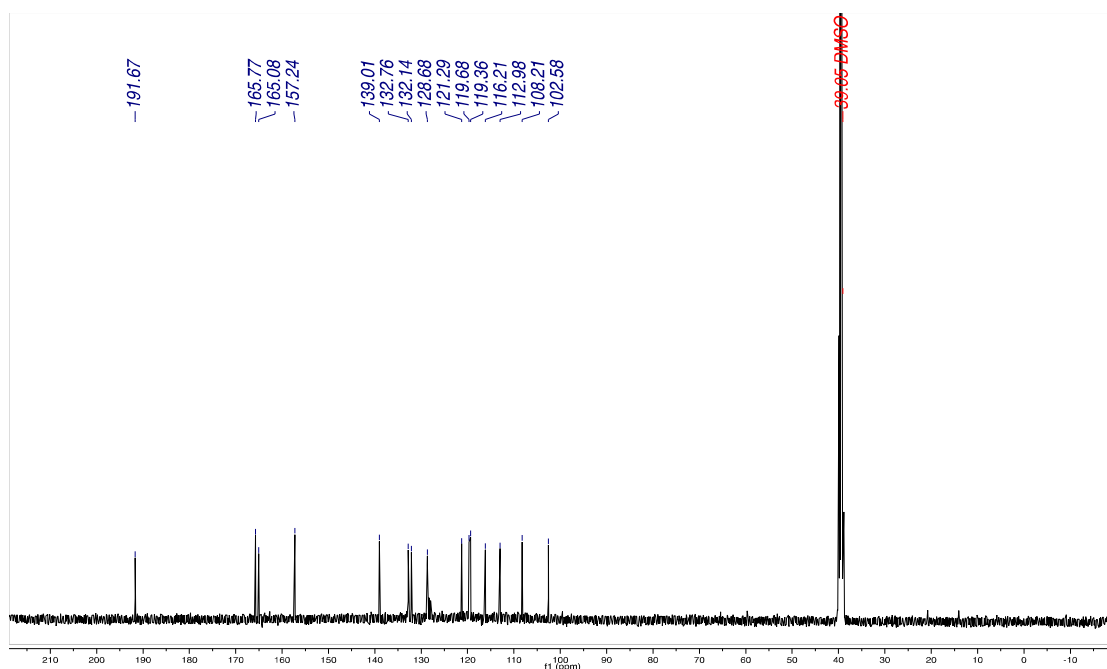


Figure 3.53: ^{13}C NMR (101 MHz, DMSO) of inhibitor B. δ 191.67 (CO), 165.77 (COH), 165.08 (COH), 157.24 (COH), 139.01 (CH), 132.76 (CH), 132.14 (CH), 128.68 (CH), 121.29 (C), 119.68 (CH), 119.36 (CH), 116.21 (CH), 112.98 (C), 108.21 (CH), 102.58 (CH).

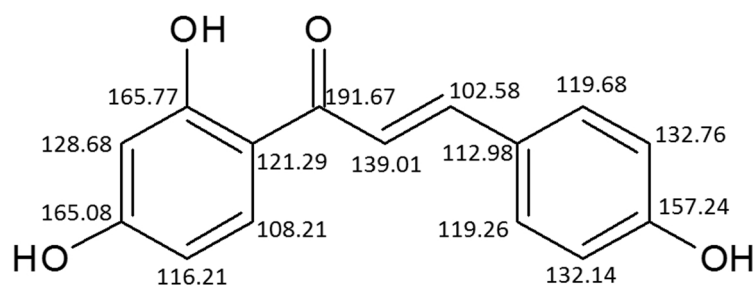


Figure 3.54: Inhibitor B with ^{13}C chemical shifts. All values are in ppm. Structures drawn by ACD/Chemsketch (Advanced Chemistry Development, Inc. version 2018.1).

3.11. Protein Crystallisation and Crystallography

3.11.1. Crystallisation and X-ray data collection

Crystallisation conditions were tested on the reduced protein as the oxidised form was found to be more difficult to crystallise and diffracts at a lower resolution (Enroth *et al.*, 2000). To this effect, hXOR was supplemented with 10 mM DTT and left at room temperature for 1 hour to ensure that the protein was reduced. Different crystallisation techniques were tested. The first crystallisation technique tested was microbatch under oil. This technique prevented to a certain extent the mixture of atmospheric oxygen with the reduced protein by covering the crystallisation drops with paraffin oil. Screening of various pre-set crystallisation conditions was done using sitting drop crystallisation on 96-well plates. Hanging drop crystallisation was also tested after a number of crystallisation conditions were determined from the previous techniques. Both hXOR (Section 3.5) and His-hXOR (Section 3.7) were tested. As hXOR did not produce reproducible crystals whilst His-hXOR did, His-hXOR was used for the following crystallisation trials.

As previous crystallisation conditions of XDH produced crystals with PEG4000, the first screening was performed by using different PEG4000 concentrations with ammonium sulfate as a salt in a range of pH (7.0 – 8.0) using a concentration of 2 mg.mL⁻¹ protein (PDB: 2CKJ; Pearson *et al.*, unpublished). The crystals formed after two to seven days. From the first screening, 0.2 M bicine pH 7.5 with 30 % PEG4000 and 0.350 M ammonium sulfate gave the first crystals. These crystals needles were approximately 20 µm in size and had a yellow tinge, the characteristic colour of hXOR (Figure 3.55). However, due to their size, the crystals formed were unsuitable for data collection.

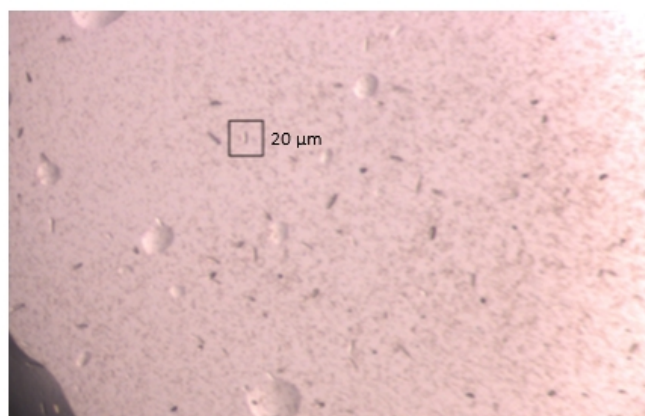


Figure 3.55: Drop with yellow crystal needles formed. Precipitation solution contained 0.2 M bicine pH 7.5, 30% (w/v) PEG4000, 0.350 M ammonium sulfate, 10 mM DTT, 2

μg hXOR. Several crystals (approximate 20 microns) with a yellow tinge were observed. An example is shown inside the black box.

Consequently, further optimisation trials were done to obtain larger crystals. The next screening was carried out using PEG4000 at lower pH ranges (6.0 – 7.0). Two different salts were tested, ammonium sulfate and ammonium acetate, to check which salt produced better crystals. From the 296 conditions tested, 0.1 M sodium acetate pH 6.0 with 30% PEG4000 and 0.40 M ammonium acetate gave the largest crystal needles ranging from 110 μm to 169 μm (Figure 3.56)

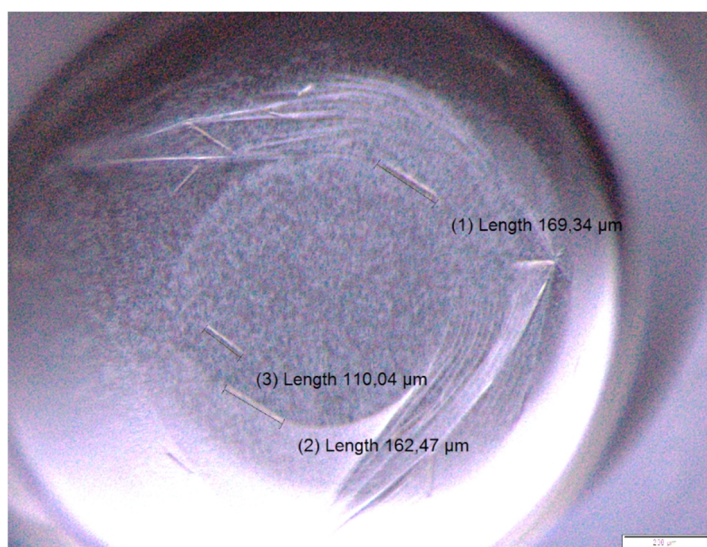


Figure 3.56: Drop with yellow crystal needles. Formed with 0.1 M sodium acetate pH 6.0, 30% PEG4000, 0.40 M ammonium acetate, 10 mM DTT, 2 μg hXOR.

These crystals were collected, cooled in liquid nitrogen using 10% glycerol as the cryoprotectant and sent for beamtime at ESRF, Grenoble. The crystals diffracted at a low resolution of around 6 \AA and thus, further optimisations were required. Different buffers with a pH range from 4.0 to 6.0 were tested. These included sodium acetate, sodium citrate, Bis-Tris and MES. Out of the buffers screened, 0.1 M sodium acetate and 0.1 M Bis-Tris buffer at a pH range of 5.4 – 6.0 produced the best crystals. The quality of crystals was evaluated by how big the crystals were, both in length and thickness. Different additive screens were done, including HR Additive Screen and HR Silver Bullets (Hampton Research, USA). However, none of the additives tested resulted in larger crystals. In fact, some of the additives of the HR Silver Bullets produced salt crystals and oligopeptide crystals. As a result, crystals that formed in 0.1 M sodium acetate and 0.1 M Bis-Tris pH 5.4 – 6.0 were collected, cryo-cooled in 10% glycerol and analysed at P14 at

the Positron-Elektron-Tandem-Ring-Anlage III (PETRA III) in Hamburg, Germany. The crystals diffracted to 3.95 Å. The condition that produced these crystals was 0.1 M sodium acetate pH 5.5 with 0.375 M ammonium acetate and 28% (w/v) PEG 4000 (Figure 3.57).

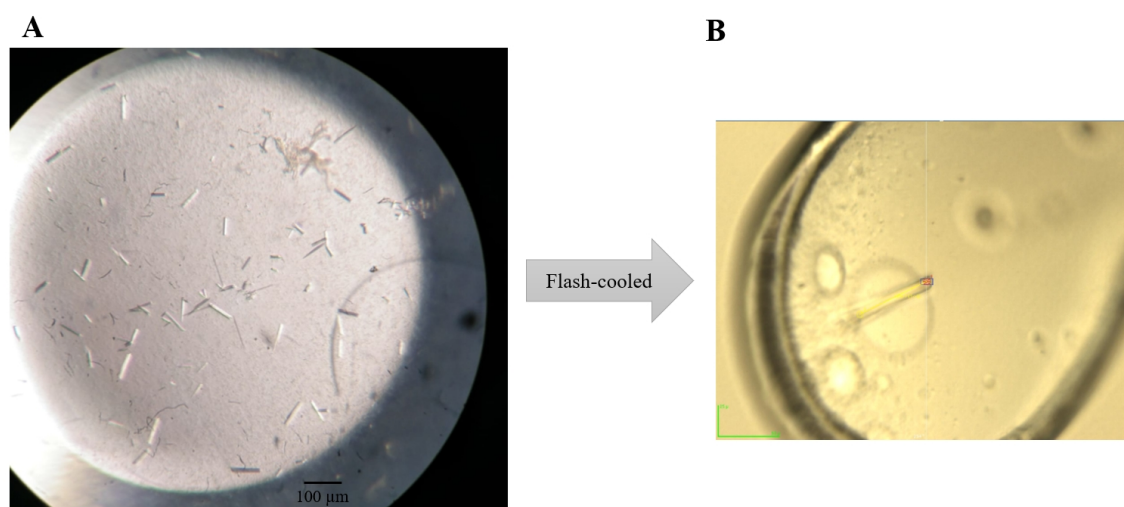


Figure 3.57: Collected crystals for analysis. A – Crystals formed in 0.1 M sodium acetate pH 5.5 with 0.375 M ammonium acetate and 28% (w/v) PEG4000. B – Cryo-cooled hXDH crystal which diffracted at 3.95 Å.

Different pre-set crystallisation screens were tested to obtain better diffraction quality crystals. These included ShotGun (Molecular Dimensions), JCSG+ (Molecular Dimensions), Morpheus III (Molecular Dimensions), and Crystal Screen (Hampton Research). Several crystallisation conditions were established, however, even after optimisation of these conditions, none produced larger crystals or produced better diffraction than the previous condition. Interestingly, most of the crystallisation conditions that gave positive results were at acidic conditions, inferring that the crystallisation of hXDH is encouraged at lower pH.

Some conditions were also tested at 4°C. However, none of these conditions produced crystals. The acetate condition (0.1 M sodium acetate pH 5.5 with ammonium acetate and PEG 4000) was repeated on a hanging drop crystallisation setup with a different range of ammonium acetate (0.3 – 0.4 M), PEG4000 (25 – 35% w/v), and pH (5.0 – 6.0). Crystals were produced albeit they had similar size as before. Different concentrations of hXDH (2, 3, 6, 12 mg.mL⁻¹) were also tested by hanging drop method with the acetate condition and the Crystal Screen by Hampton Research. A large amount of precipitation was observed with both screens at higher concentrations (6 and 12 mg.mL⁻¹). As a result, for the acetate condition, the PEG4000 and ammonium acetate

concentrations were decreased to 6-12% (w/v) and 0.200–0.300 M respectively. The crystals formed at these conditions were similar as before but had a higher degree of precipitation (Figure 3.58).

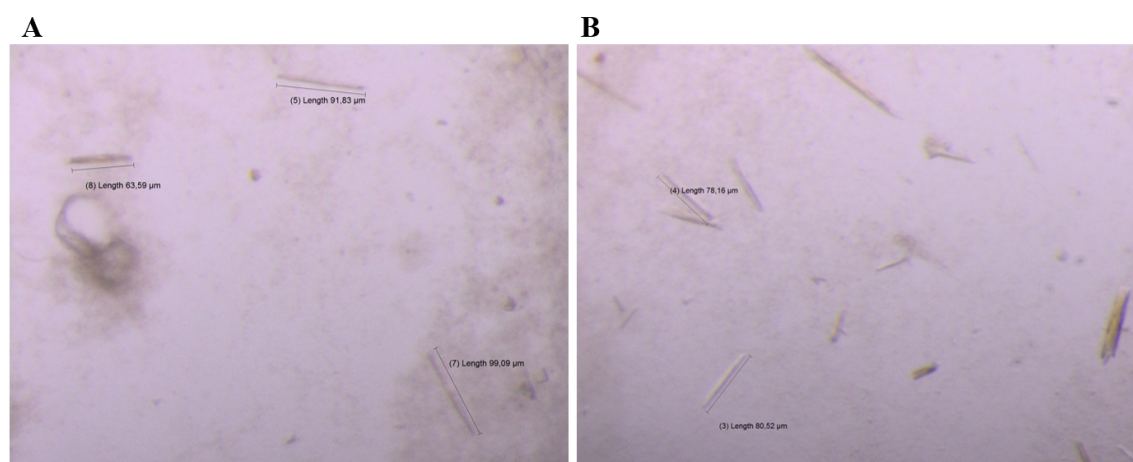


Figure 3.58: Crystals formed at 12 mg.mL⁻¹. A – 0.1 M Sodium acetate pH 5.5, 10% PEG4000, 0.200 M ammonium acetate. B – 0.1 M Sodium acetate pH 5.5, 8% PEG4000, 0.250 M ammonium acetate.

Crystal seeding was also tested on the acetate condition. Seeding was done using a horse hair to transfer microcrystalline material and crushed crystals with a seed bead. This procedure did produce crystals, however, the quality of the crystals did not improve. Crystals formed from the pre-set crystallisation screens, from the hanging-drop experiments and seeding experiments were diffracted at P14 at PETRA. Nonetheless, none of the crystals diffracted better than the previous set of crystals. As a result, crystals that diffracted to a maximum useful resolution of 3.95 Å were used for crystallographic analysis.

3.11.2. Crystallographic analysis of hXOR

3.11.2.1. Data processing

The collected data from Section 3.11.2 were processed using the CCP4i2 programme suite (Potterton *et al.*, 2018). The first step was to conduct autoindex and integrate the diffraction data. This was performed using DIALS (Winter *et al.*, 2018). In indexing, the images were analysed and the diffraction spots were located. The coordinates were then converted to vectors that provided the 3D reciprocal lattice coordinates that were later used to determine the Bravais lattice. After indexing, the intensity

of the spots was measured using a process called integration. The symmetry of the cell was subsequently determined using Pointless and the reflections were scaled and merged (data reduction) using Aimless. Aimless initially estimated the scales, refined the data to the standard deviation estimates, rejected outliers and refined the data again after outlier rejection. This generated a weighted mean of observations used for the next steps of analyses. Aimless was followed by Ctruncate that converted the intensities into amplitude structure factors. Moreover, Ctruncate was applied to generate statistical data to check the possibility of twinning and evaluate data quality.

From the analysis performed, it was determined that the space group is P 31 2 1 (solution probability: 0.864, confidence: 0.816). The unit cell parameters are: $a = 194.164 \text{ \AA}$, $b = 194.164 \text{ \AA}$, and $c = 282.250 \text{ \AA}$ with $\alpha = 90^\circ$, $\beta = 90^\circ$ and $\gamma = 120^\circ$. The crystal resolved to 3.95 \AA with an overall completeness of 96.6% and an overall $CC_{1/2}$ of 0.971 (inner shell = 0.986, outer shell = 0.325). No evidence of twinning and anisotropy was found. A free-R set was created using 5% of the data.

The crystal cell content was then estimated using the amino acid sequence of hXOR, the unit cell parameters and the space group via the 'Estimate cell content' programme in CCP4. Matthew's coefficient was calculated which indicated the expected number of molecules in the asymmetric unit based on solvent content. The number of molecules that gave approximately 50% of solvent content was determined to be the amount present in the asymmetric unit. The probability of having four molecules in the asymmetric unit was 46% while that of having five molecules was 45% while the solvent content was 53.13% and 41.41% respectively. As four molecules in the asymmetric unit resulted into a structure solution when using molecular replacement while five molecules did not, the former for subsequent analyses.

3.11.2.2. Molecular replacement and refinement

Molecular replacement was carried out using MOLREP (Vagin and Teplyakov, 1997) with 3UNC (Ishikita *et al.*, 2012) with an identity of 0.9 as the atomic model. In molecular replacement, phases from previously solved structures are used to overcome the phase problem and solve the unknown structure. The structure was solved as four molecules in the asymmetric unit. The solution obtained was refined using Refmac5 (Vagin *et al.*, 2004) and the structure was visualised using Coot (Emsley *et al.*, 2010). Coot was used to make sure that the main chain fitted the electron density, to introduce and fit ligands (FAD, [2Fe-2S], Mo) and to fix Ramachandran outliers. After Coot,

another set of refinement was performed, and the process was repeated until the R-value and R-free values were determined to be adequate. The R-value (0-1) determined the quality of the atomic model, with a value close to 0 representing a perfect fit to the electron density while a value higher than 0.6 representing a random set of atoms. The typical R-value for a high-resolution data set is 0.20. The R-free value determined how well the 5% of the experimental observations fit to the model generated. Typically, the value of R-free is 0.05 higher than that of the R-value.

The final model was refined to an R-value of 0.23 and an R-free value of 0.32. The average B-factor was 108.8 Å². The B-factor (or temperature factor) evaluates the mobility of a macromolecule, with values lower than 30 Å² showing confidence in the position of the atom while values higher than 60 Å² showing disorder. The higher than usual R-free value and B-factor were attributed to the low-resolution data set collected.

All four chains present were found to contain the FAD ligand and the two [2Fe-2S] clusters. As from previous experiments (Section 3.9.5) it was determined that only 23.25% of the protein contained iron, the presence of iron in all four chains may indicate that iron must be present for the protein to crystallise. Molybdenum was present in one chain only while the molybdopterin was not present at all. Since molybdenum has to be coordinated with the molybdopterin inside the protein, it was deduced that the lack of molybdopterin in the crystal was due to the low-resolution data.

Ramachandran plots were analysed using the MolProbity server (Williams *et al.*, 2018). Ramachandran plots evaluate the phi (φ) and the psi (ψ) torsion angles of the residues and provide regions of allowed and disallowed angles (Ramachandran, Ramakrishnan and Sasisekharan, 1963). It was determined that 81.44% of residues were Ramachandran favoured while 2.97% were Ramachandran outliers. Due to the low resolution of the structure, some outliers were very difficult to correct as the side chains were not well defined. Ramachandran plots are described in Figure 3.59.

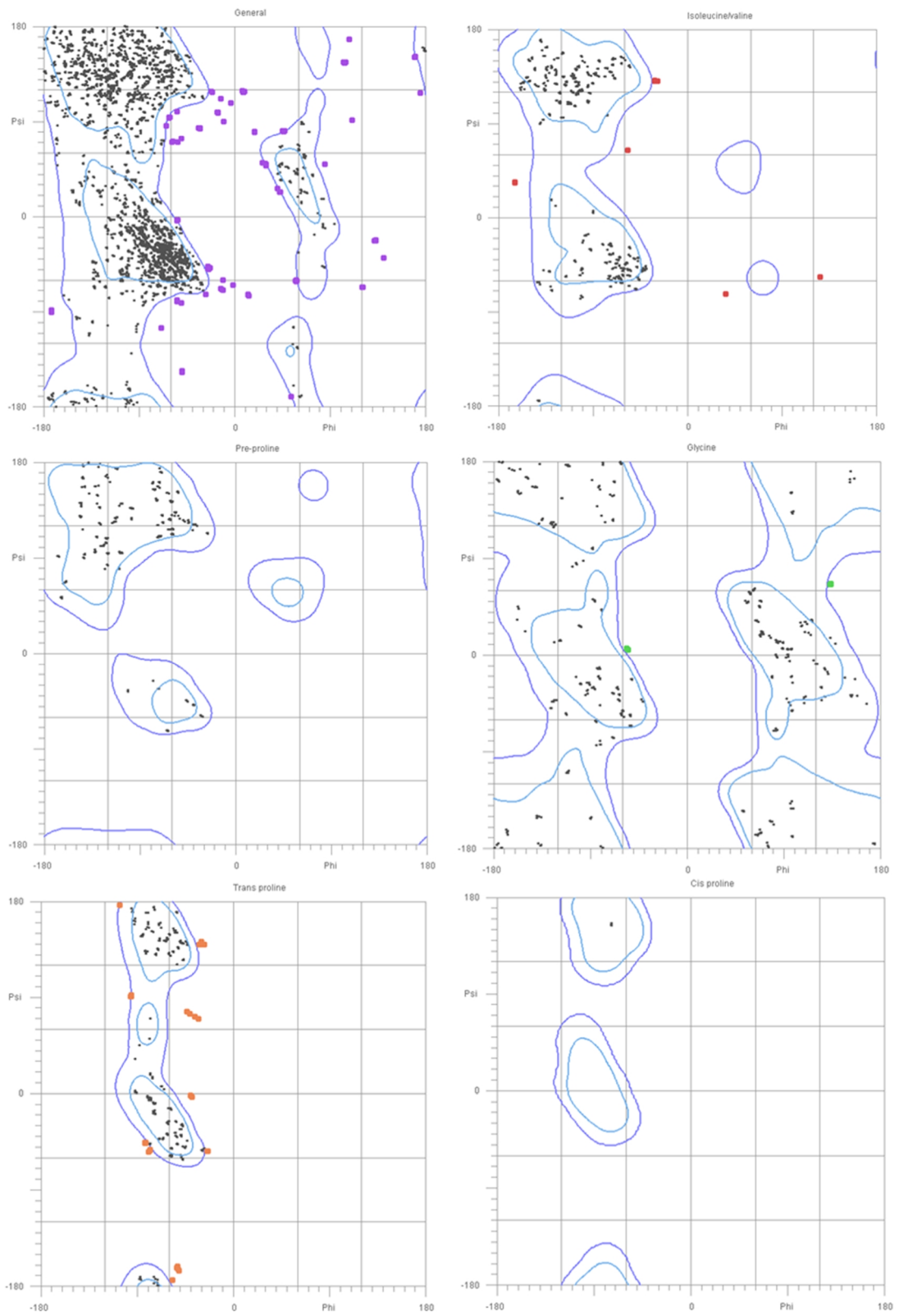


Figure 3.59: Ramachandran plots of hXDH.

Table 3.15: Statistics for data collection and refinement

Statistics	Overall
Low resolution limit (Å)	282.25
High resolution limit (Å)	3.95
Space Group	P 31 2 1
Wavelength (Å)	0.9793
Number of observations	255330
Number unique	52535
Mean((I)/sd(I))	3.8
Half-set correlation $CC_{1/2}$	0.971
Completeness (%)	96.6
R-value	0.23
R-free	0.32
Deviations in bond lengths (Å)	0.0049
Deviations in bond angles (°)	1.478
Average B-value (Å ²)	108.8
Number of non-hydrogen atoms	39882
Residues in favoured regions (%)	81.44
Residues in outlier regions (%)	2.97

3.11.2.3. Overall Structure

Structure visualisation and analysis was done using The PyMol Molecular Graphics System (Schrodinger, 2019) unless otherwise stated. The asymmetric unit (Figure 3.60) contained four monomers. No protein-protein interface interactions were present in the asymmetric unit meaning that the biological dimer did not form in the asymmetric unit. However, when the asymmetric unit was repeated, the biological dimer (Figure 3.61) was observed. Three different domains and two loops were present in each monomer corresponding to residues 1-166 for the [2Fe2S] clusters, 228-542 for the FAD domain, 557-1333 for the Moco domain, and 167-227 and 543-556 to the linking loops (as shown in Figure 3.61). The distances between the cofactors were similar to that found in bovine XOR (PDB: 3UNC) (Figure 3.61). The overall vacuum electrostatics of the dimer (Figure 3.62) was generated using a quasi-Coulombic-shaped convolution function and calculating the local charge density.

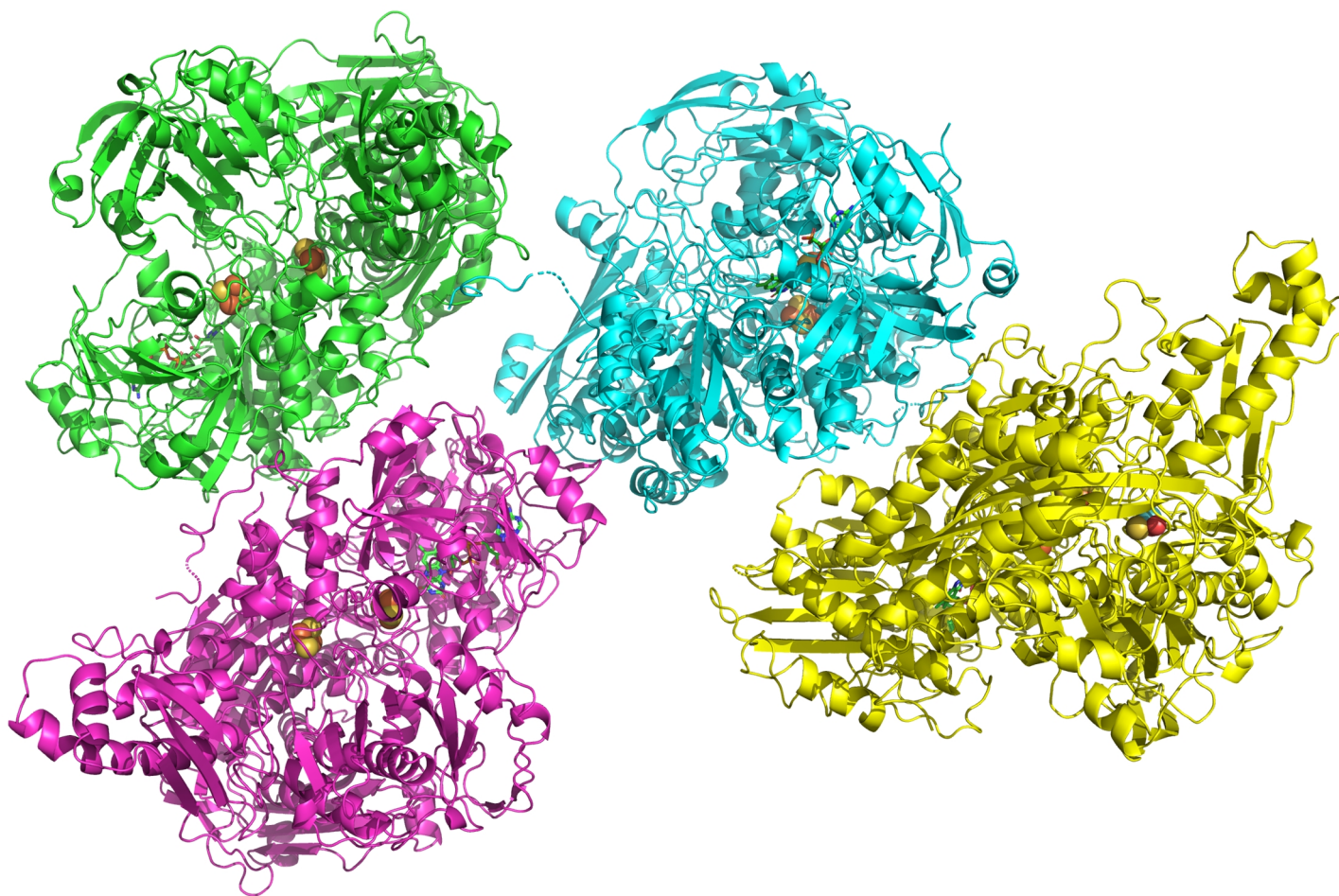


Figure 3.60: hXDH asymmetric unit. The asymmetric unit of hXDH contained four molecules. The biological dimer was not present in the asymmetric unit. Different colours represent different chains. The figure was generated by PyMOL Molecular Graphics System (Schrodinger, 2019)

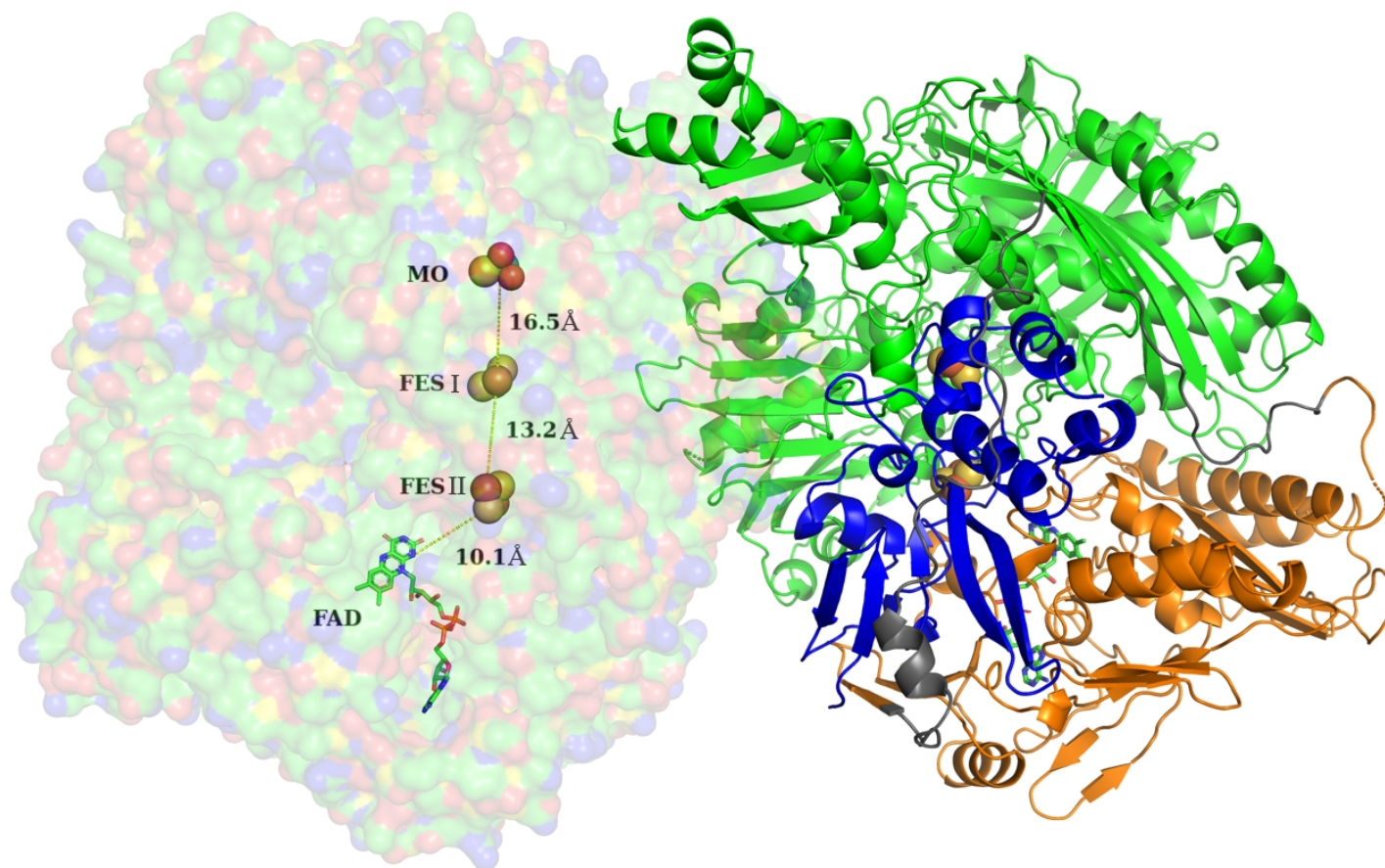


Figure 3.61: Biological hXDH dimeric unit. Left: Cofactors and the distance between them. Right: Structure is divided into three domains and two loops. Green represents the Moco domain, blue represents the [2Fe-2S] domain, orange represents the FAD domain, and grey represents the connecting loops. The figure was generated by PyMOL Molecular Graphics System (Schrodinger, 2019)

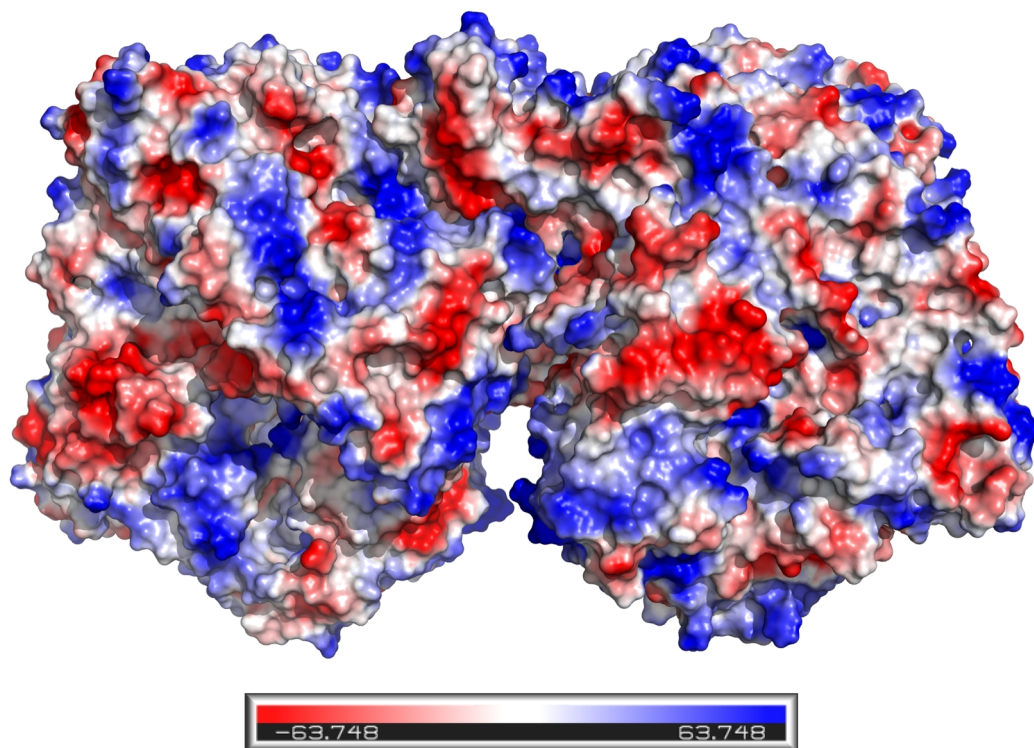


Figure 3.62: Vacuum electrostatics of the dimer unit. Electrostatic surface coloured blue represents positive regions while electrostatic surface coloured red represents negative regions. The figure was generated by PyMOL Molecular Graphics System (Schrodinger, 2019)

The overall dimensions of the dimer unit are 148.8 x 85.7 x 65 Å (Figure 3.63). The dimer has a butterfly shape and the closest distance between the cofactors from the two monomers is approximately 55 Å. To that end, it was previously suggested that the two monomers act independent of each other and that no electron transfer between the two monomers takes place (Enroth *et al.*, 2000)

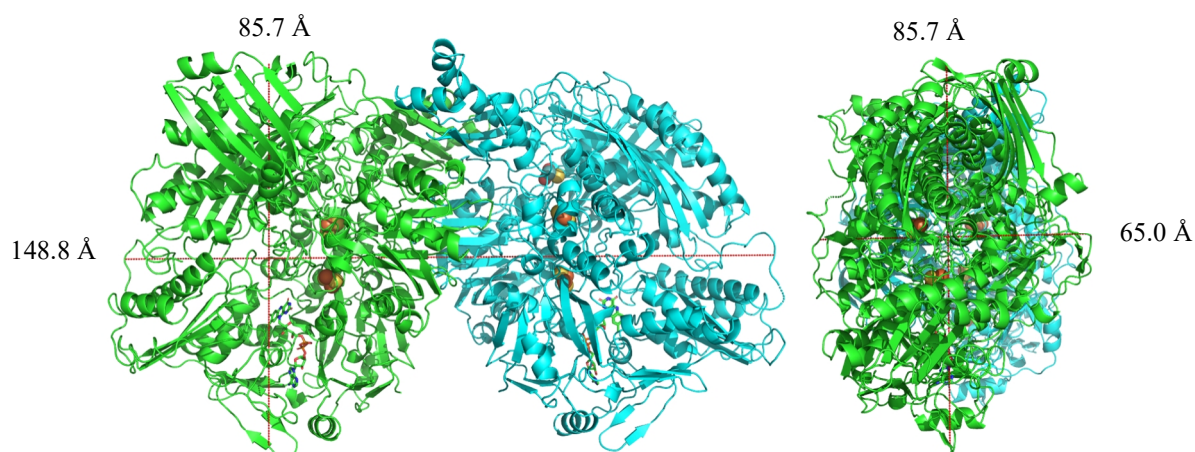


Figure 3.63: Dimer unit with measurements. The dimer measures to 148.8 x 85.7 x 65 Å. The figure was generated by PyMOL Molecular Graphics System (Schrodinger, 2019)

The protein-protein interaction interface of the dimer unit was calculated using the SPPIDER server (Porollo and Meller, 2007). SPPIDER uses solvent accessibility to determine if proteins are interacting. A decrease in the accessible surface area (ASA) (according to set cut-offs) or in the residue solvent accessibility (RSA) demonstrates interaction. The criteria selected for the interaction evaluation were a loss in RSA and ASA by at least 4% and 5 Å² respectively. The residues participate in the dimer interface interaction are shown in Table 3.16 and in Figure 3.64

Table 3.16: Dimer interface interaction residues according to the SPPIDER server.

Chain	Interacting with chain	Residues in the interaction	ISA* (Å ²)	HPI**
A	B	R32 L34 K95 M585 E590 V592 P598 R599 Y600 E601 N602 K755 G756 E757 A758 E760 E762 M771 Q774 S775 P784 A785 N786 R787 V789 R791 K793 Y818 G821 P823 P1013 F1014 Q1017 L1021 H1023 Y1025 T1026 D1027 S1029 L1031 S1060 K1061 Y1063 S1065 E1066 T1069 N1070 T1071 P1073 N1074 R1101 Y1122 M1123 D1124 T1125 S1127 L1128 S1129 A1130 T1131 F1133 R1135	2913	0.82 ± 0.71
B	A	R32 K95 M585 E590 V592 P598 R599 Y600 E601 N602 K755 G756 E757 A758 E760 E762 M771 Q774 S775 P784 A785 N786 R787 V789 R791 K793 Y818 R822 F1014 Q1017 L1021 H1023 Y1025 T1026 D1027 S1029 L1031 S1060 K1061 Y1063 S1065 T1069 N1070 T1071 P1073 N1074 R1101 Y1122 M1123 D1124 T1125 V1126 S1127 L1128 S1129 A1130 T1131 F1133 R1135	2901	0.79 ± 0.68

* - Total change in the interface surface area calculated using DSSP

** - Mean hydrophobicity index calculated using ARGP820101

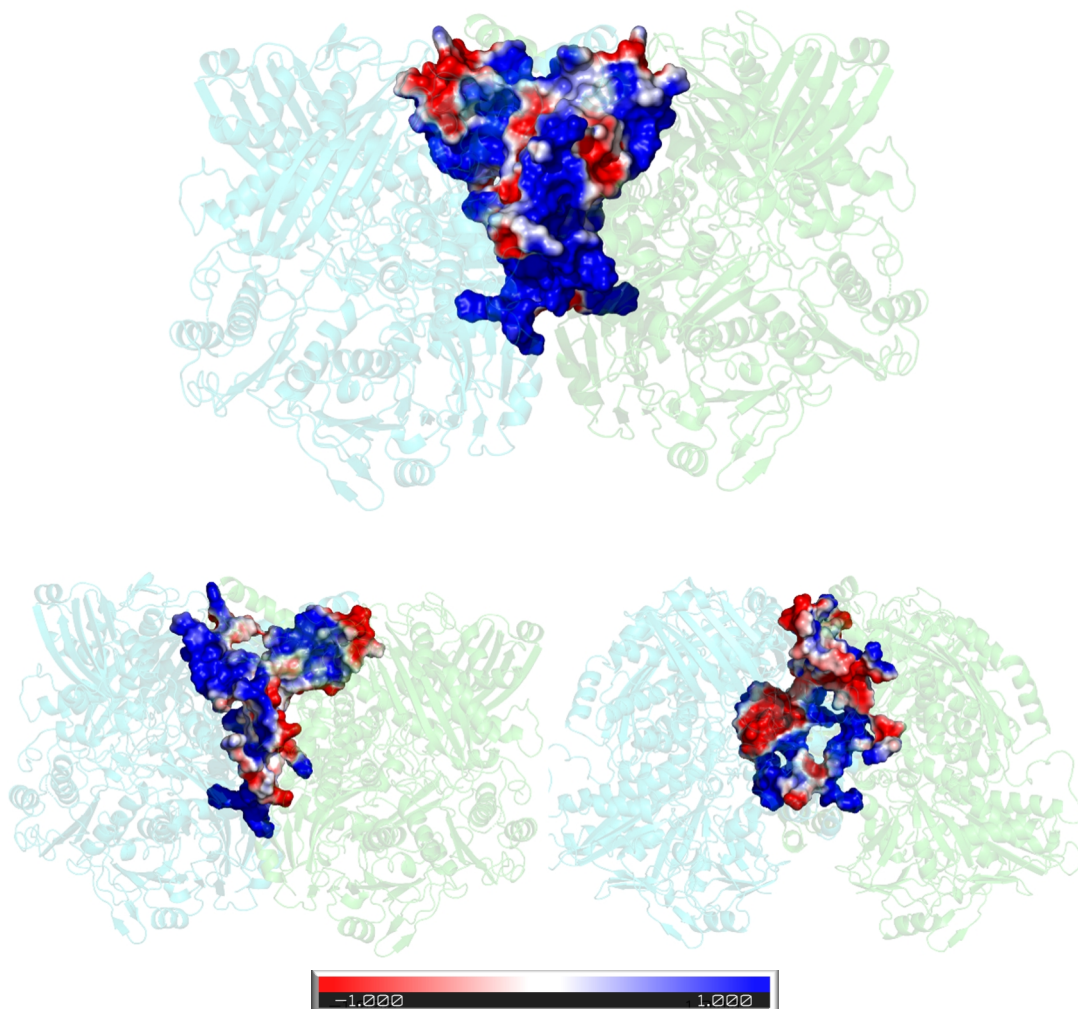


Figure 3.64: Electrostatic protein-protein interface interaction representation of the dimeric unit. Top – all interfacing residues from both chains. Bottom – interfacing residues from each monomer. Red and blue area represent negative and positive moieties in the residues respectively.

The interface was also analysed using the Protein Interfaces, Surfaces and Assemblies (PISA) server (Krissinel and Henrick, 2007). PISA established more interfacing residues than SPPIDER. Interfacing residues are listed in Table 3.17. Hydrogen bonds and salt bridges between the interfacing residues are listed in Table 3.18 and 3.19 respectively.

Parts of the electron density were not well defined or completely missing. Figure 3.65 shows the overall B-factor distribution. The B-factors values increase from blue to green to red, meaning that blue-coloured areas have lower B-factors than green-coloured areas that have lower B-factors than red-coloured areas. The representation in Figure 3.65

was only used to demonstrate areas where the B-factors were high, which in turn indicates that the electron density was not well defined. The B-factors in this representation were taken to be relative to each other, so the blue regions in the image (due to low B-factor), are only so with respect to other regions in the molecule. From Figure 3.65, it could be observed that the non-well-defined regions were present at the molecular surface of the protein. These regions were also found to be not well defined in the bovine XOR which was solved at higher resolution indicating that these regions were present in flexible regions which were difficult to diffract. In fact, regions which had their electron density missing or not well-defined were in the linker regions or close to the linker regions (residues 165-192, 528-537, 545-557), in loops (residues 425-434) and at the C-terminus (residues 1315-1333).

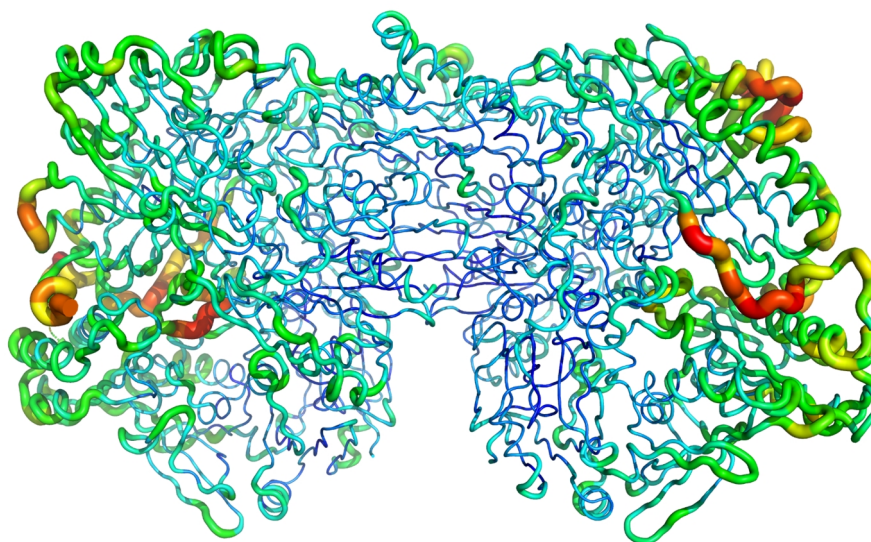


Figure 3.65: Relative overall B-factors of the dimeric unit. Blue represents areas with lower B-factors, followed by green that is followed by red. The lower the B-factors, the better defined the electron density. The regions with non-well-defined electron density regions were present at the molecular surface and in loops. The figure was generated by PyMOL Molecular Graphics System (Schrodinger, 2019).

Human XDH was aligned with bovine XDH (3UNC) using TM-align (Zhang and Skolnick, 2005). TM-align optimises residue-residue alignment derived from structural similarity. The algorithm generates a TM-score and the root-mean-square deviation (RMSD). Values of the TM-score span from 0 to 1 with values between 0 to 0.3 indicating random structural similarity and values higher than 0.5 showing same structural fold. The alignment of hXDH with bXDH had an RMSD of 0.78 based on 1281 aligned residues

and a TM-score of 0.99560, demonstrating that the structure of hXDH and bXDH have the same structural fold. The alignment is shown in Figure 3.66.

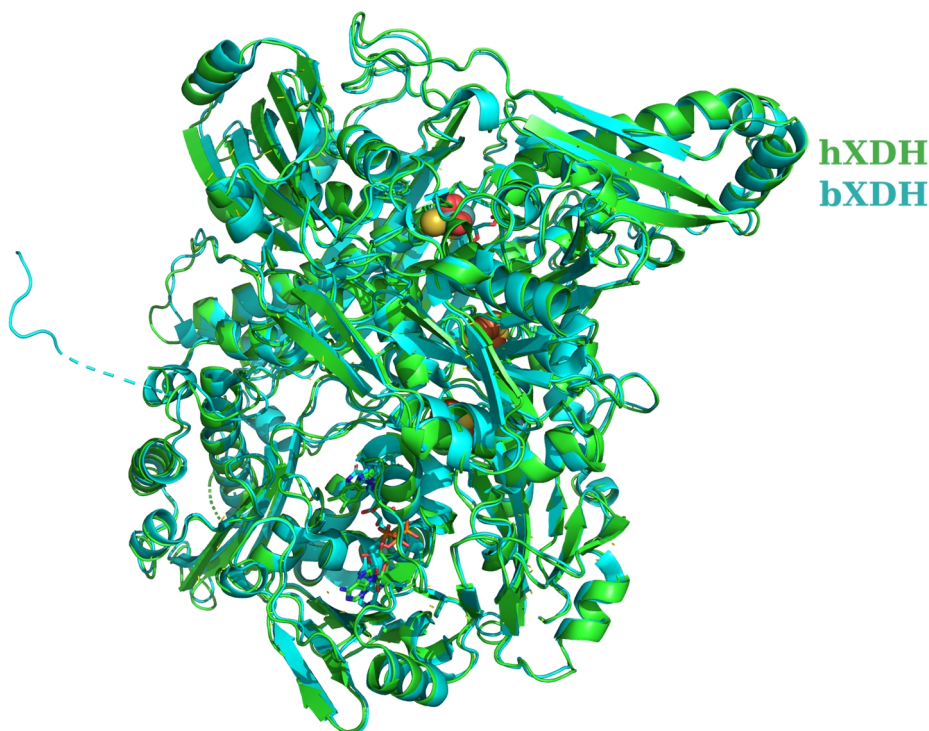


Figure 3.66: Structural based alignment of hXDH (green) with bovine XDH (cyan). The figure was generated by PyMOL Molecular Graphics System (Schrodinger, 2019)

3.11.2.4. The Moco domain

Out of four chains in the asymmetric unit, only one contained a molybdenum ion. None of the chains contained a positive electron density for the molybdopterin ion. The molybdenum ion in the structure was identified based on its position in the bovine XOR, where the molybdenum ion is covalently bonded with a sulfur atom (σ and π bonds) and with two oxygen atoms (one has σ bond while the other one has both σ and π bonds) (Enroth *et al.*, 2000). From previous studies, it was established that the active site residues at the Moco centre, Glu⁸⁰³, Arg⁸⁸¹, Thr¹⁰¹¹, and Glu¹²⁶², interact with both the Moco and the substrate. The Moco centre acts as the electron acceptor to the xanthine substrate and is the site where catalysis starts. The electron accepted by the Moco centre is then subsequently transferred to the [2Fe-2S] clusters to transport the electron to the FAD centre (Enroth *et al.*, 2000). When a vacuum electrostatic surface was applied to the protein, a small solvent funnel was exposed (Figure 3.67B). This funnel acts as the entry to solvent and substrates for the catalytic reaction to initiate.

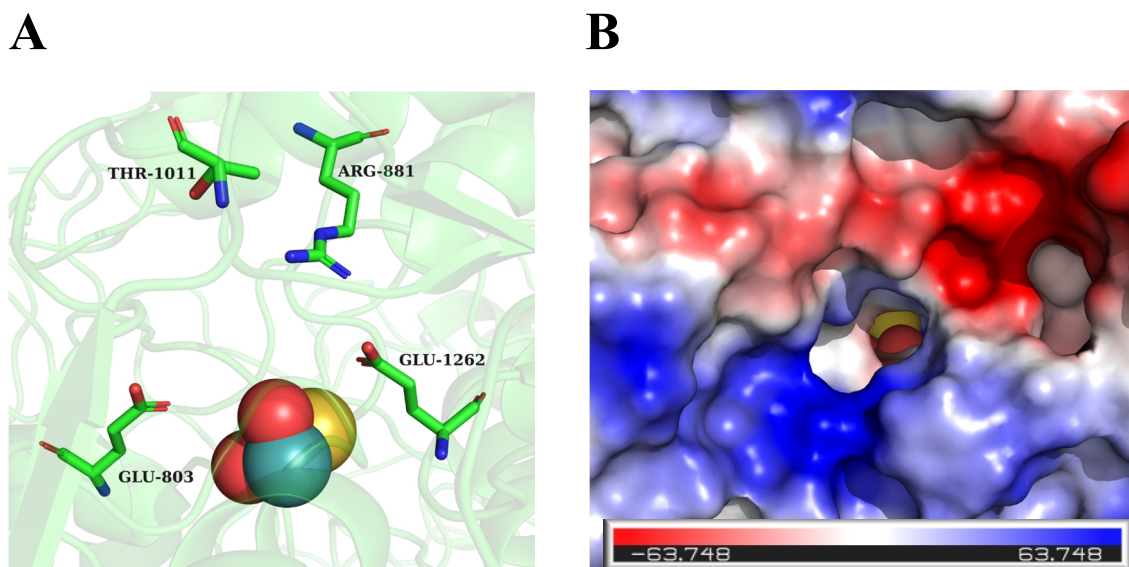


Figure 3.67: The Moco centre. A – Residues around the Mo centre which interact with the molybdopterin, the Mo centre and the substrate. B - Vacuum electrostatics around the Mo molecule. Electrostatic surface coloured blue represents positive regions while electrostatic surface coloured red represents negative regions. A small solvent funnel where the substrate can enter the active site was recognized. The figure was generated by PyMOL Molecular Graphics System (Schrodinger, 2019)

The bovine XDH and hXDH were structurally aligned as described in Section 3.11.3.4. The molybdenum centre of both bovine and hXDH holds a similar position. The bovine XDH molybdopterin does not clash with any hXDH residue side chains, supporting the position of the molybdopterin in the hXDH structure (Figure 3.68).

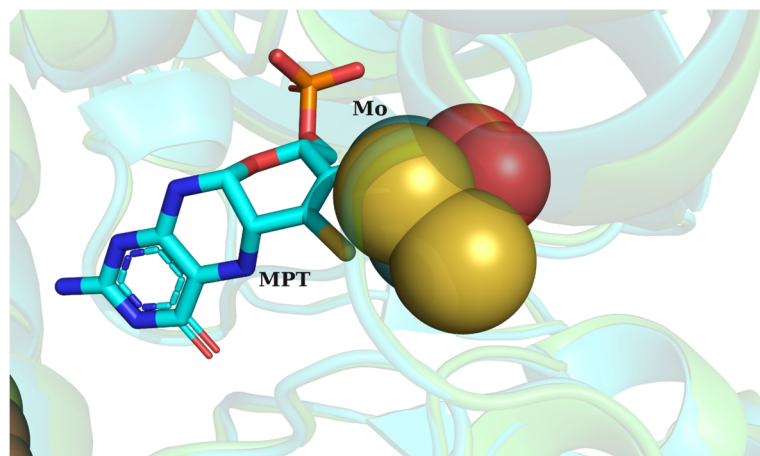


Figure 3.68: Alignment of bovine XDH (3UNC) and hXDH at the Moco. The molybdenum centre aligned well in both species. No clashes between the hXDH residues and the bovine XDH molybdopterin were observed. Cyan – bovine XDH, green – hXDH. The figure was generated by PyMOL Molecular Graphics System (Schrodinger, 2019)

3.11.2.5. The [2Fe-2S] domain

The first [2Fe-2S] domain is coordinated with Cys⁴³, Cys⁴⁸, Cys⁵¹ and Cys⁷³ and is close to the FAD molecule (10.1 Å). The second [2Fe-2S] domain is coordinated with Cys¹¹⁶, Cys¹¹³, Cys¹⁴⁸, Cys¹⁵⁰ and is 16.5 Å away from the Mo atom. As the molybdopterin was not visible in the structure, the actual distance between the second [2Fe-2S] domain and the Mo domain could not be calculated. The distance between the two domains is 13.2 Å. The short distance between the sulfur of the cysteines and the iron in the domain (2.3 Å) indicates that the mode of interaction is covalent. The two [2Fe-2S] domains act as electron transporters from the Mo domain to the FAD domain. Due to the distance between the two [2Fe-2S] and the other domains, the mechanism of electron transfer was proposed to be via tunnelling (Enroth *et al.*, 2000).

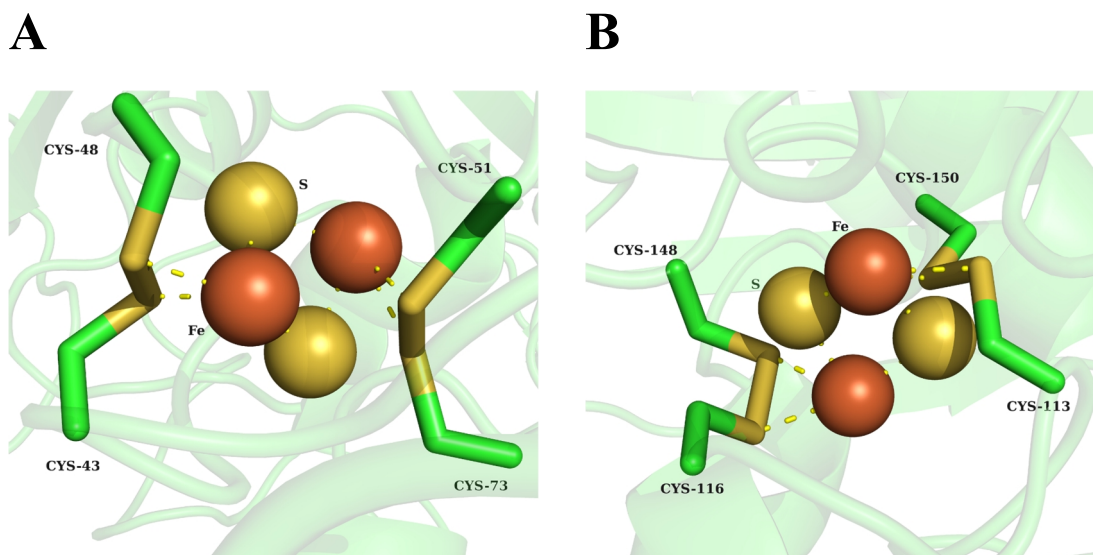


Figure 3.69: The two [2Fe-2S] domains in hXDH. A – The first [2Fe-2S] cluster present close to the FAD domain. B – The second [2Fe-2S] cluster present close to the Moco domain. The two clusters act as electron transporters between the Moco domain and the FAD domain. The figure was generated by PyMOL Molecular Graphics System (Schrodinger, 2019).

3.11.2.6. The FAD domain

The FAD domain, which spans from residue 228 to 542, contains an FAD molecule that is responsible for the electron donation to an electron acceptor in the last step of catalysis. The molecule that acts as the electron acceptor depends on the oxidation state of XOR, with XDH preferring NAD^+ while XO uses exclusively oxygen. The preference of the electron acceptor is dependent on the electrostatic environment and size of the cleft around the tricyclic isoalloxazine ring of the FAD. The XDH has a wide enough cleft for an NAD^+ ion to access to the FAD. In XDH, the loop between Gln⁴²³ and Lys⁴³³ is held by a π -cation interaction between the amino acid cluster composed of Phe⁵⁵⁰, Arg³³⁵, Trp³³⁶, and Arg⁴²⁷. In XO, the disulfide bridge formation between Cys⁵³⁶ and Cys⁹⁹² disrupts the π -cation interaction, displacing the Gln⁴²³ and Lys⁴³³ loop that in turn masks part of the FAD tricyclic isoalloxazine ring. Consequently, the cleft through which electron acceptor gains entry to FAD site decreases in size and blocks the entry of the NAD^+ , allowing oxygen to be the sole electron acceptor in XO (Enroth *et al.*, 2000).

When analysing the electrostatic environment and cleft size at the FAD centre (Figure 3.70), it was observed that the isoalloxazine ring is exposed to the solvent. This indicates that the protein that was crystallised and solved was XDH form not XO.

Moreover, the Gln⁴²³ - Lys⁴³³ loop (Figure 3.71A) appears not to mask the FAD ring. The interaction between the Arg⁴²⁷ of this loop and the residues Arg³³⁵, Trp³³⁶ and Phe⁵⁵⁰ was analysed using Discovery Studio Visualizer (Dassault Systèmes BIOVIA, 2018) (Figure 3.71B). This showed that a π - π interaction was established between the aforementioned residues, further confirming that the protein solved was the reduced XDH form of the enzyme.

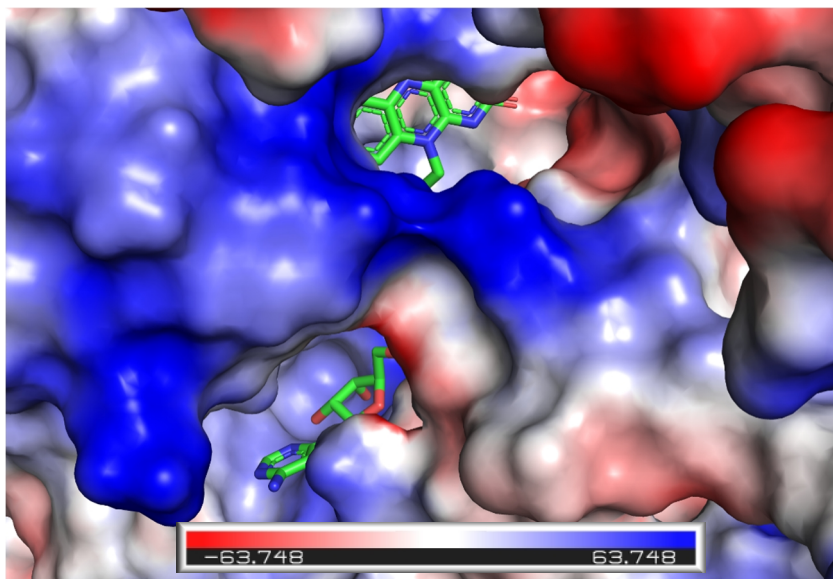


Figure 3.70: Vacuum electrostatics around the FAD molecule. Electrostatic surface coloured blue represents positive regions while electrostatic surface coloured red represents negative regions. The tricyclic isoalloxane ring is exposed to the surrounding solvent indicating that the protein was XDH. The figure was generated by PyMOL Molecular Graphics System (Schrodinger, 2019).

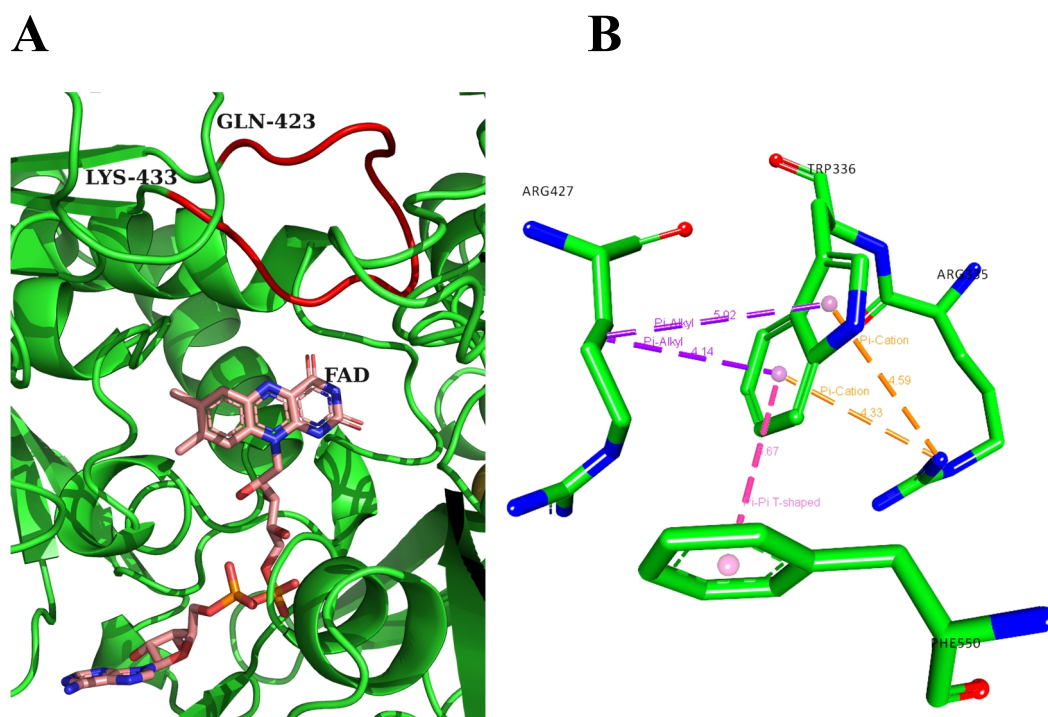


Figure 3.71: Interactions of the Gln⁴²³-Lys⁴³³ loop. A – The loop (in red) does not mask the isoalloxazine fraction of FAD. A was generated by PyMOL Molecular Graphics System (Schrodinger, 2019). B – The loop was established to have a series of π - π interactions between Trp³³⁶, Arg³³⁵, Arg⁴²⁷ and Phe⁵⁵⁰. These findings confirm that the crystal was that of XDH. B was generated by Discovery Studio Visualizer (Dassault Systèmes BIOVIA, 2018).

From the crystal structure it was established that the FAD molecule forms a number of hydrogen bonds with the neighbouring amino acids. These include: Gly²⁶⁰, Asn²⁶¹, Thr²⁶², Glu²⁶³, Ser³⁴⁷, Asn³⁵¹, Thr³⁵⁴, Asp³⁶⁰, and Leu⁴⁰⁴. Most hydrogen bonds were between 2.5 to 3.4 Å, indicating that the hydrogen bonds were moderate and mostly electrostatic. The positions and the bond lengths of the hydrogen bonds are shown in Figure 3.72. The Phe³³⁷ was also previously reported to form a π - π interaction with the isoalloxazine ring of FAD. However, in the solved crystal structure of hXOR, no interaction is apparent. As the resolution was low, the electron density of most rotamers was missing, and so the rotamer for Phe³³⁷ might have not been the real rotamer.

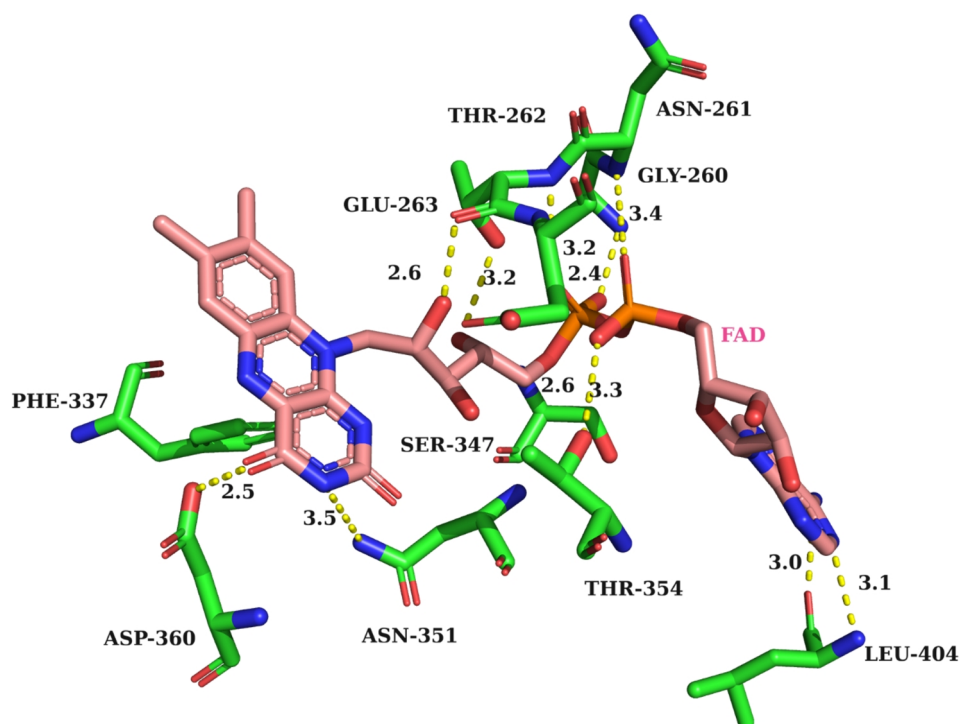


Figure 3.72: Interactions of the FAD molecule with the surrounding residues. Hydrogen bonds were mostly moderate and electrostatic. No interaction was found between Phe³³⁷ and the tricyclic isoalloxazine ring of FAD (pink) that was most probably due to an incorrect rotamer of Phe³³⁷. The figure was generated by PyMOL Molecular Graphics System (Schrodinger, 2019).

3.11.3. Molecular modelling of the hXOR mutants

The mutants described in Section 2.2.8 and 3.3 were analysed using the structure solved in Section 3.11.3. The G172R mutant was omitted from the analysis as residue 172 was not resolved in the structure. Chain D from the asymmetric unit was used for the analysis. The ligands were first removed using PyMol and the structure with no ligands was opened in Swiss-PDBviewer (Guex and Peitsch, 1997). The polar hydrogen bonds were computed and the site directed mutagenesis was performed for each mutant. The mutated residue was selected and each mutant was energy minimised using 100 steps of steepest descent with the non-selected residues locked. The energy minimised structure was saved and transferred to PyMol for analyses.

3.11.3.1. The A932T mutant

The wild type protein and the A932T mutant were aligned and the mutated residue was analysed (Figure 3.73). The mutation, present in the Moco domain, changed an alanine residue, a non-polar amino acid, with a threonine residue, a polar amino acid. No change in the conformation of the neighbouring residues was observed after mutation. A vacuum electrostatic surface analysis shown no (Figure 3.74) observable change in electrostatics due to this mutation

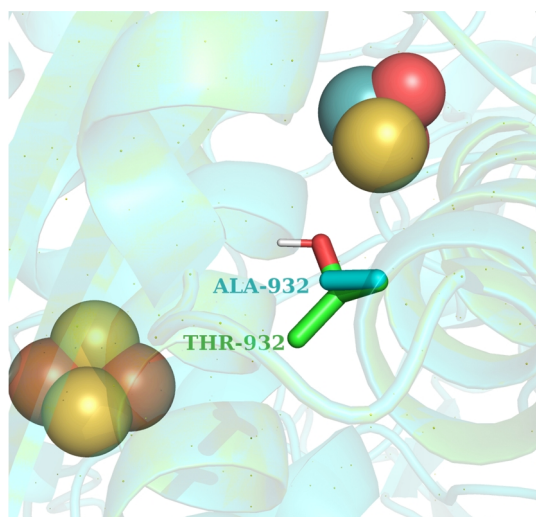


Figure 3.73: Wild type and A932T mutant hXDH aligned. Cyan – wild type XDH, Green – A932T mutant. The figure was generated by PyMOL Molecular Graphics System (Schrodinger, 2019).

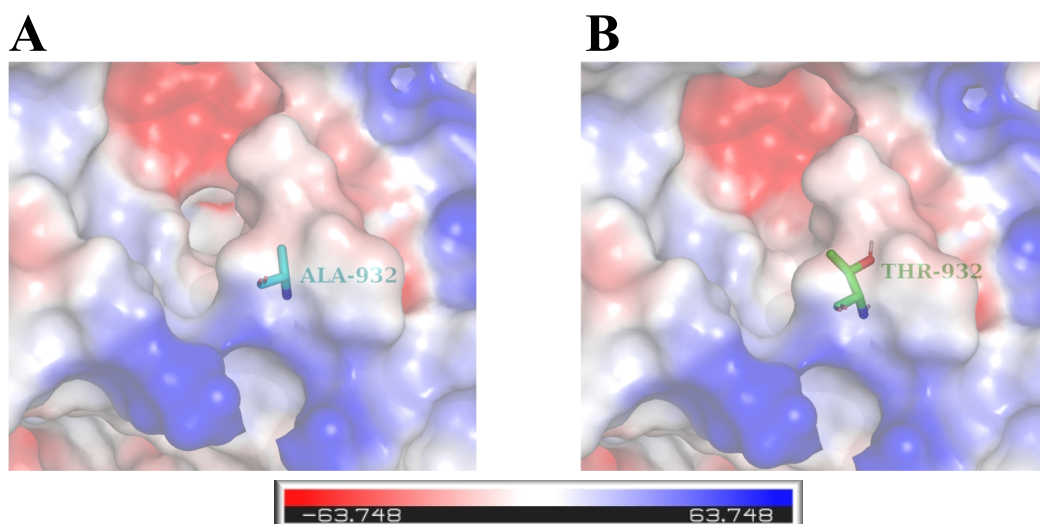


Figure 3.74: Vacuum electrostatics around the residue 932. Electrostatic surface coloured blue represents positive regions while electrostatic surface coloured red represents negative regions. A – wild type. B – A932T mutant. The figure was generated by PyMOL Molecular Graphics System (Schrodinger, 2019).

In the wild type, a weak electrostatic hydrogen bond of 3.6 Å forms between Ala⁹³² and Met⁹²⁸ (Figure 3.75A) while in the A932T mutant, the Thr⁹³² residue forms a moderate hydrogen bond with Ala⁹³⁹ (3.1 Å) and moderate to weak hydrogen bonds with Gly⁹³⁶ and Cys⁹³⁵ (2.6 and 3.2 Å respectively) (Figure 3.75B). Threonine has an extra hydroxide ion which can hydrogen bond with adjacent residues.

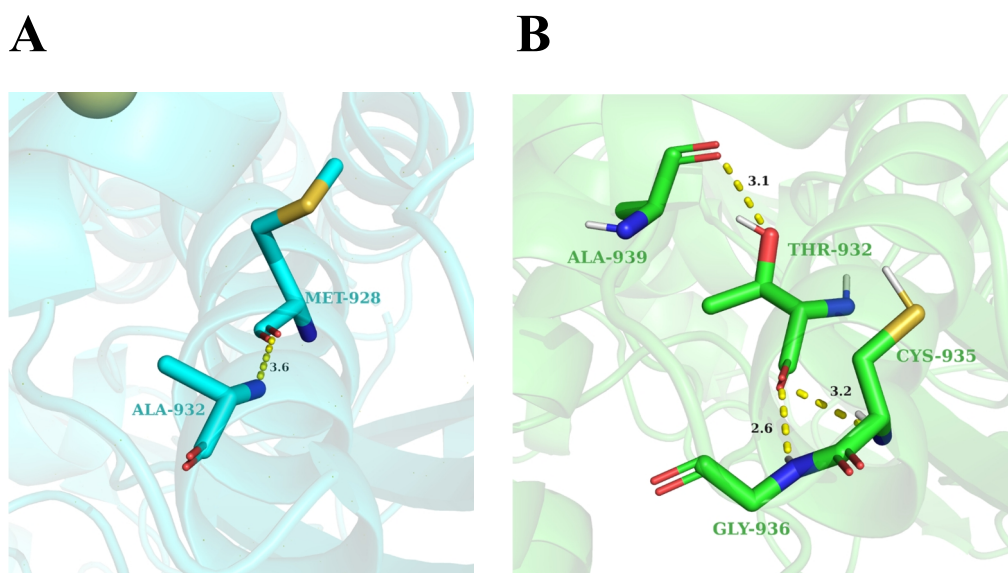


Figure 3.75: Interactions of the residue 932 with the surrounding residues. A – Wild type residue. B – A932T residue. The figure was generated by PyMOL Molecular Graphics System (Schrodinger, 2019).

3.11.3.2. The N1109T mutant

The N1109T mutation caused no change in the overall alignment of wild type with mutant (Figure 3.76). The mutation changed a polar asparagine residue, having an amide group in the side chain, with a polar threonine residue having a hydroxide group. When vacuum electrostatic surfaces were applied (Figure 3.77), a slight decrease in negative electrostatic charge around mutated residue was observed.

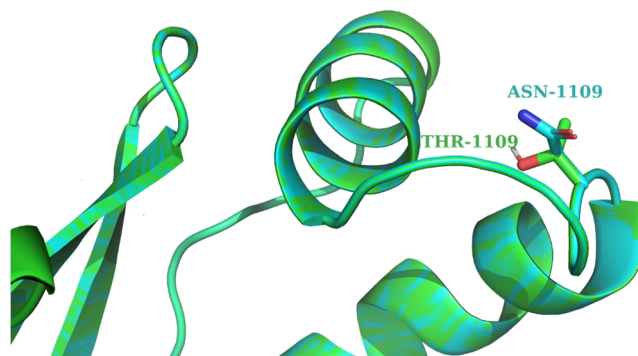


Figure 3.76: Wild type and mutant N1109T hXDH aligned. Cyan – wild type XDH, Green – N1109T mutant. The figure was generated by PyMOL Molecular Graphics System (Schrodinger, 2019).

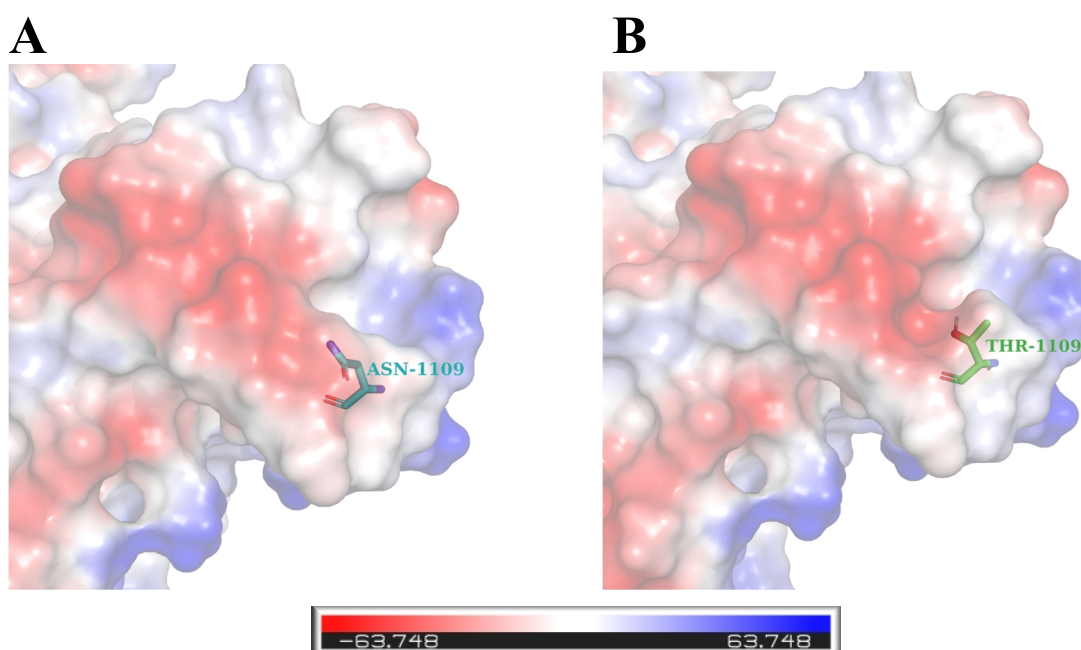


Figure 3.77: Vacuum electrostatics around the residue 1109. Electrostatic surface coloured blue represents positive regions while electrostatic surface coloured red represents negative regions. A – wild type. B – N1109T mutant. The figure was generated by PyMOL Molecular Graphics System (Schrodinger, 2019).

The hydrogen bonds between the residues under investigation and the adjacent residues remained the same with both Asn¹¹⁰⁹ or Thr¹¹⁰⁹ capable of forming a weak 3.3 Å hydrogen bond with Trp¹¹¹⁷ (Figure 3.78). As a result, no difference in stability was expected between the wild type protein and the mutant.

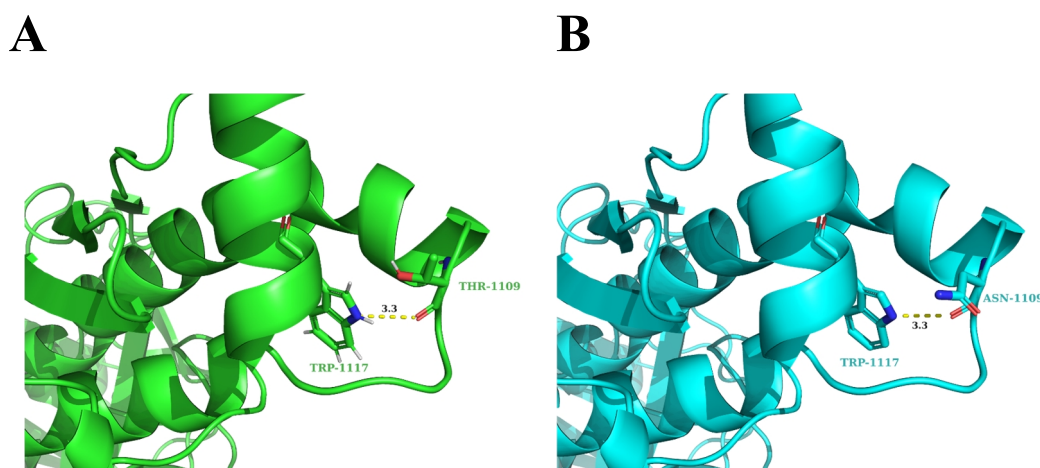


Figure 3.78: Interactions of the residue 1109 with the surrounding residues. A – Wild type residue. B – N1109T residue.

3.11.4. Molecular docking

The structure of the inhibitors described in Section 2.9 and 3.10 were used for docking experiments. First, the inhibitors were built using PyMol Builder and saved as pdb files. The chain without ligands constructed in Section 3.11.4 was used for docking experiments. Polar hydrogens were added to both the protein and the ligand by using AutoDock tools (Morris *et al.*, 2009). The coordinates of the molybdenum active site were noted and both the ligand and protein were converted to pdbqt files by using AutoDock tools. Docking was performed on AutoDock Vina with an exhaustiveness of 20. The generated states were then opened in PyMol and the most favourable state (i.e. the state that had the highest affinity and the most favourable orientation to the active site) was chosen.

3.11.4.1. Oxypurinol

Oxypurinol (the metabolised form of allopurinol, a commercial inhibitor) was used as control for preliminary docking experiments. Oxypurinol was chosen instead of allopurinol as the structure of bovine XOR with oxypurinol was previously determined

via crystallography (3BDJ, Okamoto *et al.*, 2008). As a result, by comparing the docking experiments with the crystallography experiments, the reliability of the docking experiment can be established. From the docking experiment with oxypurinol (Figure 3.79) it could be observed that the docked oxypurinol is in the same moiety as the crystallographic oxypurinol. However, it should be taken into consideration that due to this slight mismatch in location, the bonding of the docked inhibitor is not exactly the same as the crystallographic one. Consequently, the docked experiments performed were used only to indicate where the possible location of the inhibitor inside the enzyme is and to which residues the inhibitors might bind.

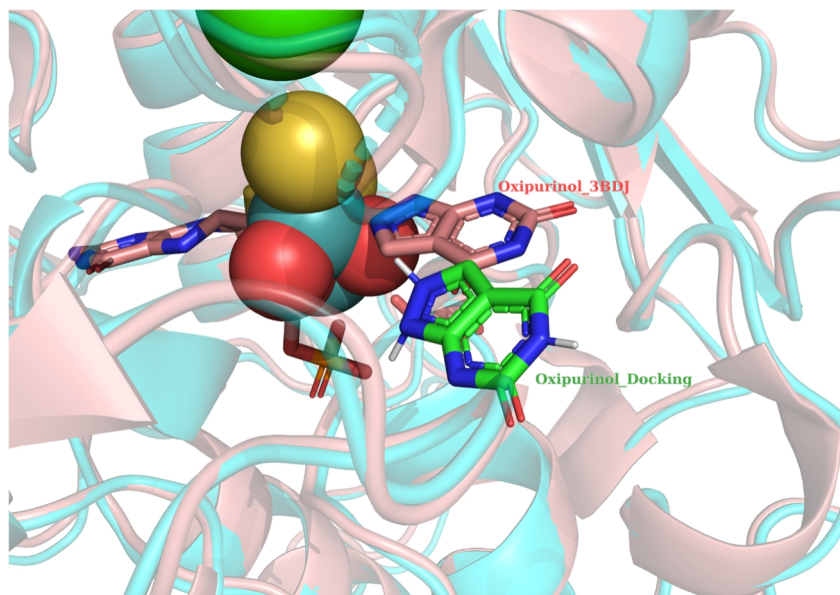


Figure 3.79: Docking experiment against crystallographic experiment. Pink – Bovine XOR crystal structure with oxypurinol (PDB: 3BDJ). Cyan – Human XOR crystal structure. Green – Docked oxypurinol.

3.11.4.2. Inhibitor A

A total of nine states were generated with AutoDock Vina. The state with the best orientation had an affinity of -6.6 kcal/mol. The inhibitor bound successfully to the Mo active site by hydrogen bonding to Glu⁸⁰³ (residue which takes part in catalysis), Glu⁸⁸⁰ and Ser⁸⁷⁷ (Figure 3.80A). Inhibitor A was reported to be a mixed inhibitor (Muzychka *et al.*, 2017). To that end, the fact that the inhibitor binds to both Glu⁸⁰³ and the other residues might indicate this mixed inhibitor effect. Inhibitor A was observed to bind on the surface of the protein just outside the active site (Figure 3.80B). This suggests that

prior to its addition, the substrate might already be inside the active site but due to the interaction of the Glu⁸⁰³ with the inhibitor, the catalysis of the substrate is slowed down.

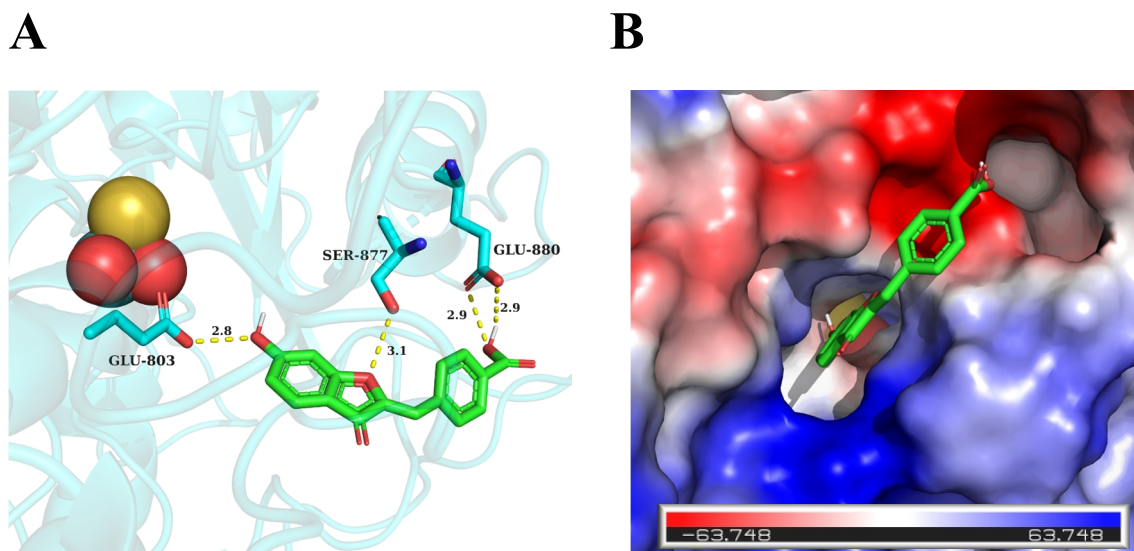


Figure 3.80: Interactions of Inhibitor A with hXDH. A – Hydrogen bonds between inhibitor A and residues Glu⁸⁰³, Ser⁸⁷⁷ and Glu⁸⁸⁰. B – Vacuum electrostatics of inhibitor A showing that it binds to the surface of the protein with only part of it at the active site. The figure was generated by PyMOL Molecular Graphics System (Schrodinger, 2019).

3.11.4.3. Inhibitor B

A total of nine states were generated with AutoDock Vina. The state with the best orientation had an affinity of -6.2 kcal/mol. The inhibitor bound successfully to the Mo active site by hydrogen bonding to Glu⁸⁰³, Gl⁸⁷⁶ and Ser⁸⁷⁷ (Figure 3.81A). The mode of binding of inhibitor was observed to be very similar to that of inhibitor A (Figure 3.81B). In fact, inhibitor B was also reported to be a mixed inhibitor (Xie *et al.*, 2017) and the same rationale of inhibitor A can be used to describe inhibitor B's mode of inhibition.

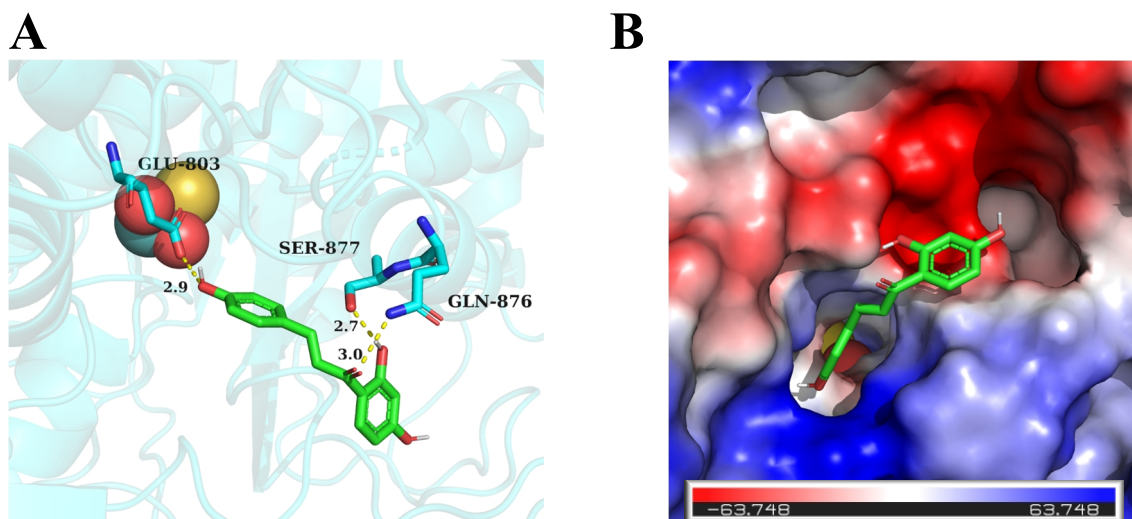


Figure 3.81: Interactions of Inhibitor B with hXDH. A – Hydrogen bonds between inhibitor A and residues Glu⁸⁰³, Ser⁸⁷⁷ and Gln⁸⁷⁶. B – Vacuum electrostatics of inhibitor B showing that it binds to the surface of the protein with only part of it at the active site. The figure was generated by PyMOL Molecular Graphics System (Schrodinger, 2019).

3.12. Electron microscopy

3.12.1. Preliminary negative staining: transmission electron microscopy

During negative staining, proteins are adsorbed to an EM grid and subsequently enveloped by an electron dense stain. This results into a high relative contrast between the protein of interest and the background, with the background being more electron dense (and thus darker) than the protein of interest. Negative staining is one of the best methods used for rapid assessment of the overall structure topography of a protein sample as it provides subnatural details due to the ability of the stain to penetrate into any crevice present (Carlo and Harris, 2011).

Approximately 0.5 mg.mL⁻¹ of hXOR and ovine XOR were sent to the Consejo Superior de Investigaciones Científicas (CSIC, Spain), for preliminary negative staining under an iNEXT EM H2020 Grant # 653706. From the results obtained (Figure 3.82, 3.84) it was observed that both human and ovine XOR form filaments that are homogenous in shape and size. Both proteins produced similar structures, confirming that the hXOR chain structure was not an artefact resulting from its synthesis in a bacterial expression system. The TEM grid of ovine XOR (Figure 3.84) showed that the protein sample needed to be more dilute to acquire better visualisation. The hXOR (Figure 3.82) was predominantly present as filaments composed of two dimers linked together (53.3%, n=510). HEPES buffer, 50 mM pH 8.0, was the buffer of choice as phosphate buffers react with uranyl acetate to produce uranyl acetate crystal. The distribution of hXOR dimers is shown in Figure 3.83 and Table 3.17.

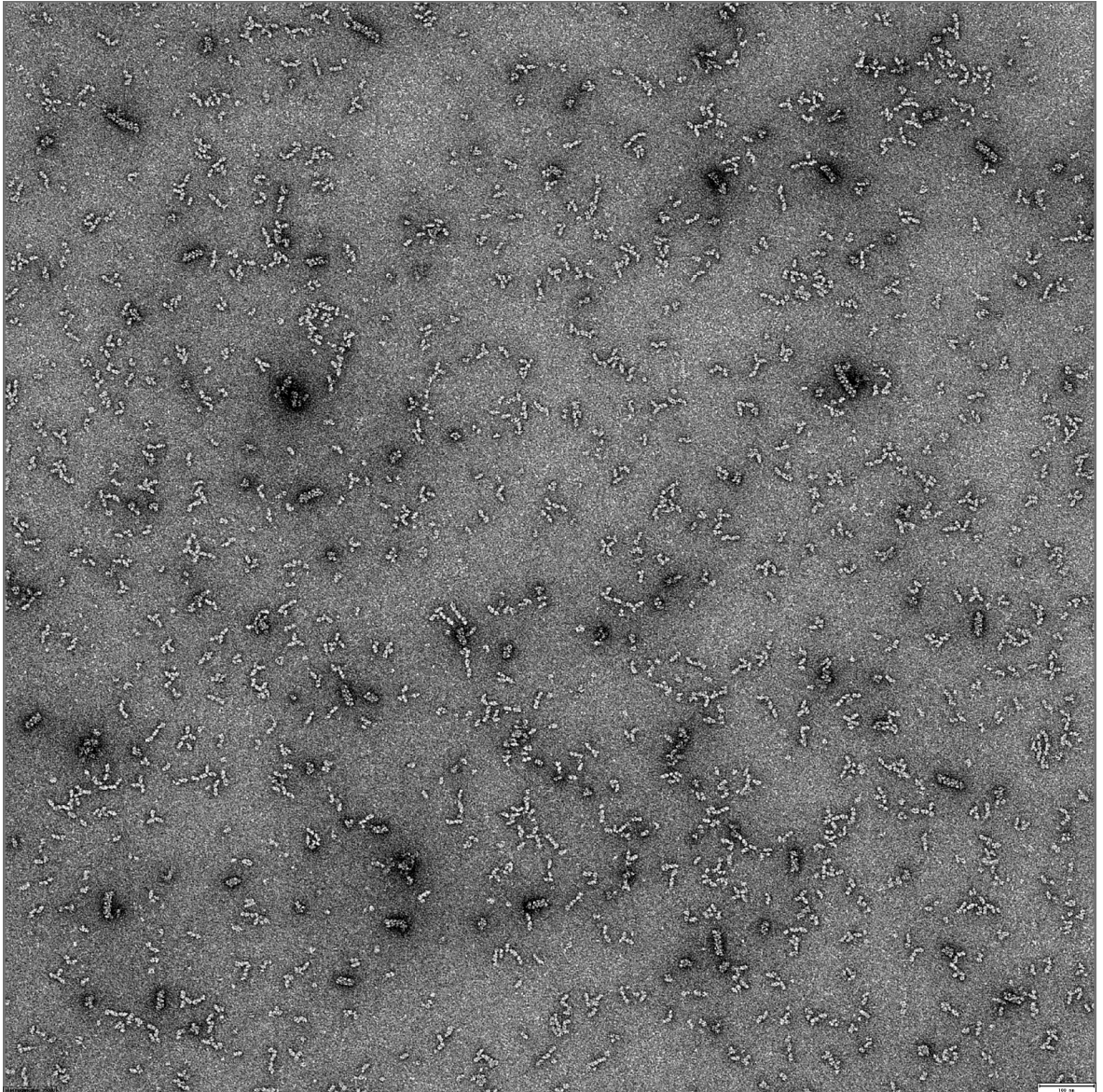


Figure 3.82: Transmission electron microscopy (TEM) images of 1:100 hXOR in 50 mM HEPES buffer pH 8.0. The protein was blotted on a TedPella carbon grid with 2% (w/v) uranyl acetate as an electron dense stain. The grid shows homogeneous distribution of filaments.

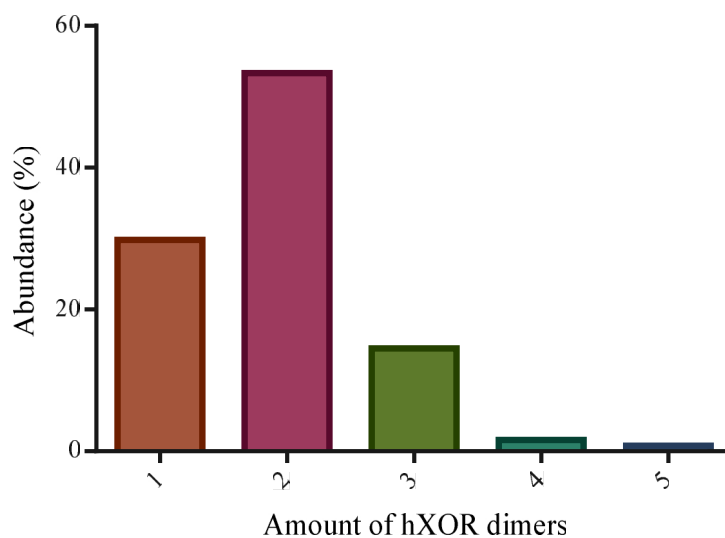


Figure 3.83: Distribution of hXOR dimers in 50 mM HEPES pH 8.0. The x-axis represents the number of dimers present where 1 representing unbound dimer, 2 representing two dimers connected to each other and so on. (n=510).

Table 3.17: Abundance of hXOR dimers in 50 mM HEPES pH 8.0

hXOR dimers	Amount	Abundance (%)
1	152	29.8
2	272	53.3
3	74	14.5
4	8	1.6
5	4	0.8

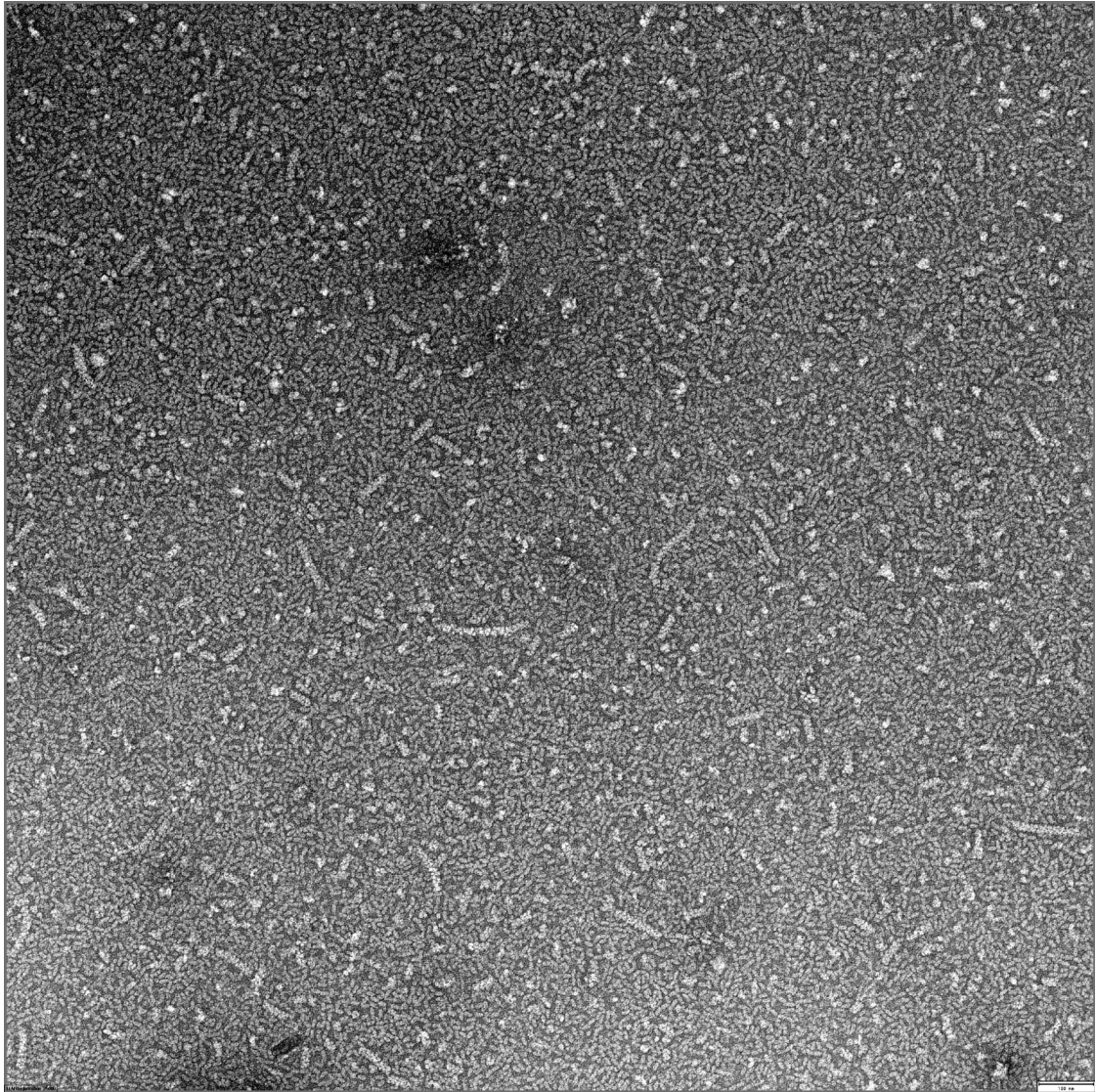


Figure 3.84: Transmission electron microscopy (TEM) images of 1:100 ovine XOR in 50 mM HEPES buffer pH 8.0. The protein was blotted on a TedPella carbon grid with 2% (w/v) uranyl acetate as an electron dense stain. The grid shows that the protein sample might need to be diluted more to get a better visualisation. Several filaments can be observed throughout the grid.

3.12.2. Negative staining at different conditions

The experiment was repeated under different conditions to further ensure that the XOR filaments were not experimental artifacts, and to validate the reproducibility of the filament formation. These negative staining experiments were performed at the Astbury Centre for Structural Molecular Biology, University of Leeds as described in Section 2.8.1. Explorative TEM images were obtained for a range a of hXOR concentrations (1:10, 1:25, 1:50, 1:100 dilutions of a 1 mg.mL⁻¹ of hXOR in 50 mM HEPES pH 8.0 with 100 mM NaCl). From these TEM images, it was determined that concentrations between 1:50 and 1:100 resulted in optimal visualisation of the filaments (Figure 3.85). As a result, a 1:75 dilution was chosen for all the different buffers tested. Filament formed at all the XOR concentrations tested, with the number of filaments increasing with increasing protein concentration. The protein did not aggregate at the higher concentrations. In fact, XOR formed filaments with a similar assembly at all the concentrations tested

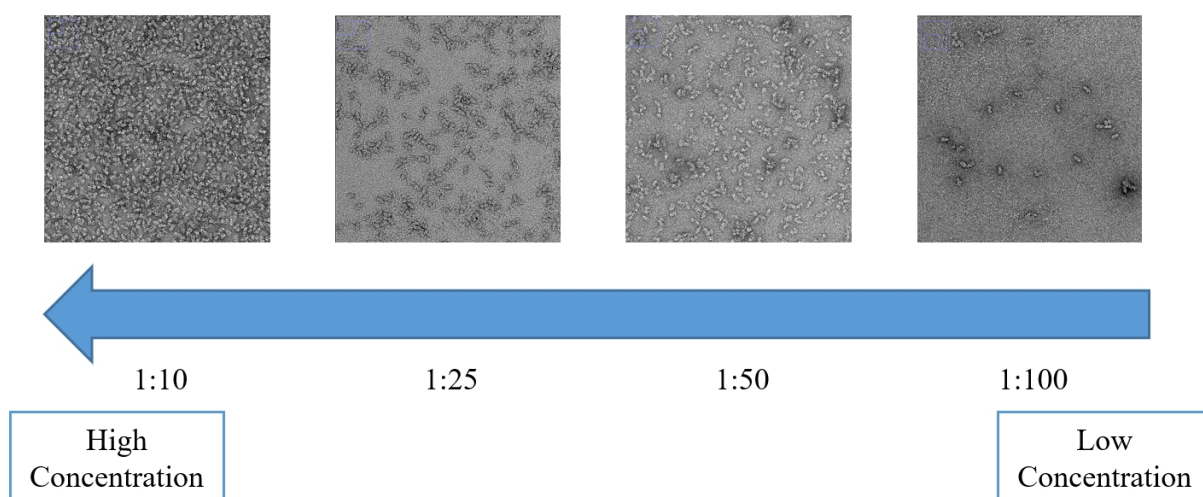
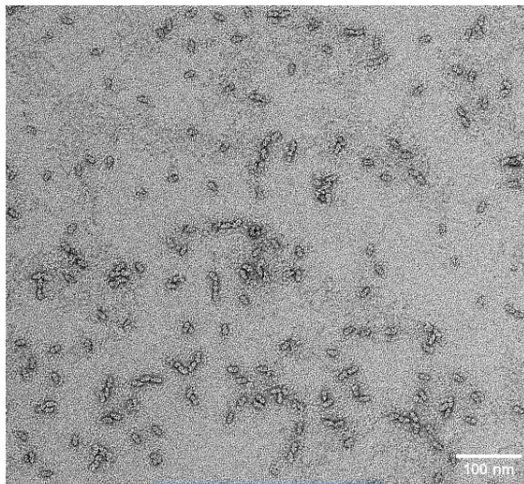


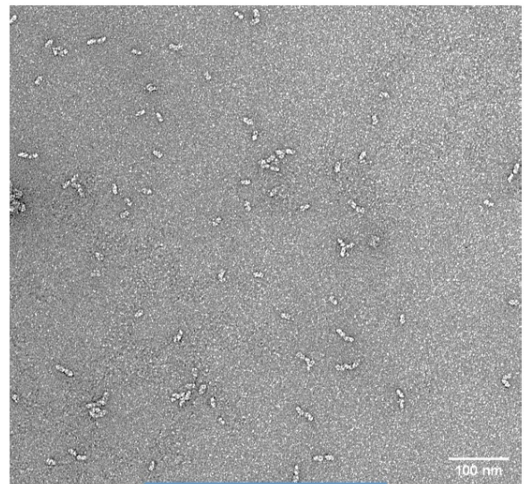
Figure 3.85: TEM images of hXOR in 50 mM HEPES pH 8.0 at different concentrations.

A 1 mg.mL⁻¹ of hXOR solution was diluted (1:75 ratio) in the each of the buffers tested, applied onto a Formvar/carbon grid and stained for analysis (Figure 3.86). In general, the number of filaments decreased with decreasing pH of the buffer. Large aggregates of hXOR formed in citric acid at pH 3.5. The highest number of filaments were observed in 50 mM HEPES pH 8.0 and in 50 mM sodium acetate pH 5.6, hXOR was present mostly as dimers (95%).

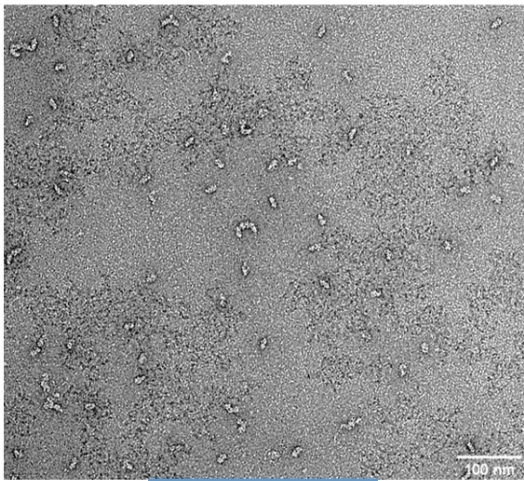
The majority of the filaments assembled as two dimers attached together (Figure 3.87, Table 3.21). Interestingly, as described in Section 3.11.1, most hXOR protein crystals formed at pH 5.5, when the protein was only present as a homodimer. This may indicate that for crystallisation to occur, the protein must be in a dimeric state with as little filaments as possible.



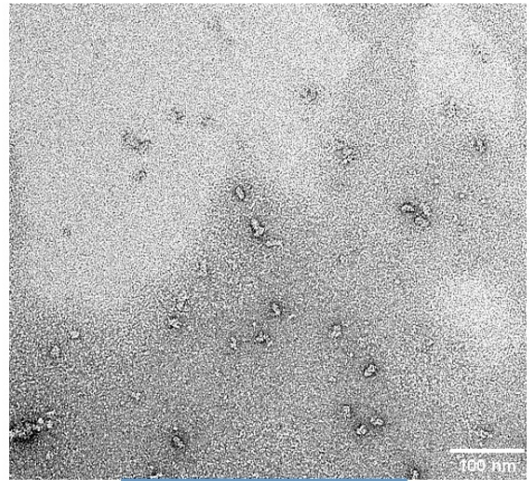
Bicine pH 9.0



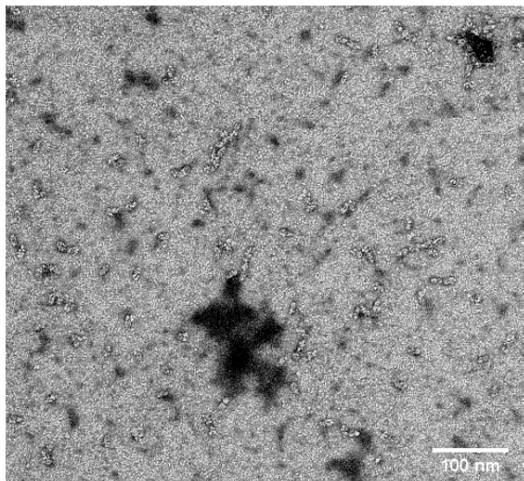
HEPES pH 8.0



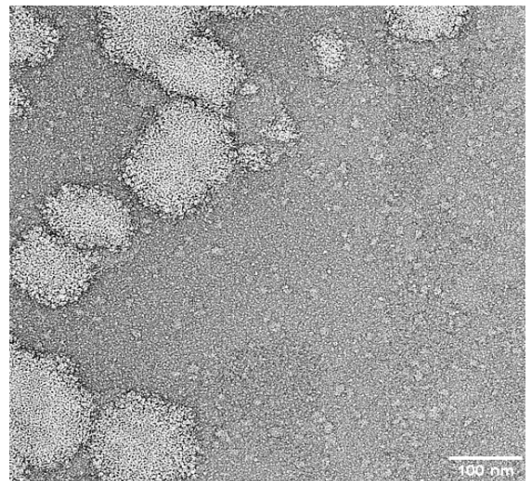
MOPS pH 7.0



Na Acetate pH 5.6



Na Acetate pH 4.6



Citric Acid pH 3.5

Figure 3.86: TEM images of hXOR in different buffers. In general, the number of filaments increased with pH. In citric acid pH 3.5, hXOR aggregated, probably due to denaturation.

When comparing the preliminary TEM negative staining conducted at CSIC (in 50mM HEPES pH 8.0) with that at the Astbury Centre (also in 50mM HEPES pH 8.0), it was observed that the proportion of two-dimer filaments was similar, with the former experiment having a 53.3% abundance of two-dimer filaments and the latter experiment having a 46.4% abundance. However, it was observed that the CSIC experiment also produced a greater proportion of longer filaments (three-dimer (14.5%), four-dimer (1.6%), and five-dimer (0.8%) filaments) probably due to the higher concentration of hXOR on the grid. On the other hand, the two-dimer filaments were the longest filaments obtained from the Astbury experiment. Therefore, at pH 8.0 the XOR protein did not aggregate and formed filaments of increasing length with increasing protein concentration.

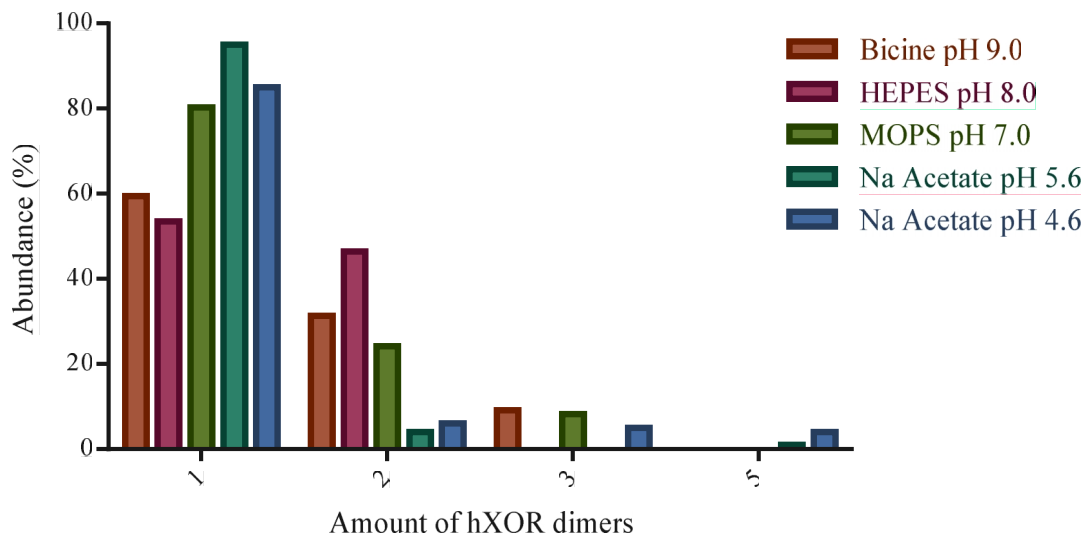


Figure 3.87: Distribution of hXOR filaments across different pH.

Table 3.18: Abundance of hXOR across different pH.

hXOR dimers	Abundance (%)				
	Bicine pH 9.0	HEPES pH 8.0	MOPS pH 7.0	Na Acetate pH 5.6	Na Acetate pH 4.6
1	59.5	53.6	71.1	95.0	85.0
2	31.4	46.4	21.5	4.0	6.0
3	9.1	0	7.4	0	5.0
5	0	0	0	1.0	4.0
	<i>n</i> = 153	<i>n</i> = 112	<i>n</i> = 149	<i>n</i> = 100	<i>n</i> = 100

The different morphologies of the dimers and other filaments can be observed in Figure 3.88, with A showing the hXOR dimer, B showing two-dimer filaments and C showing the interaction between two two-dimer filaments.

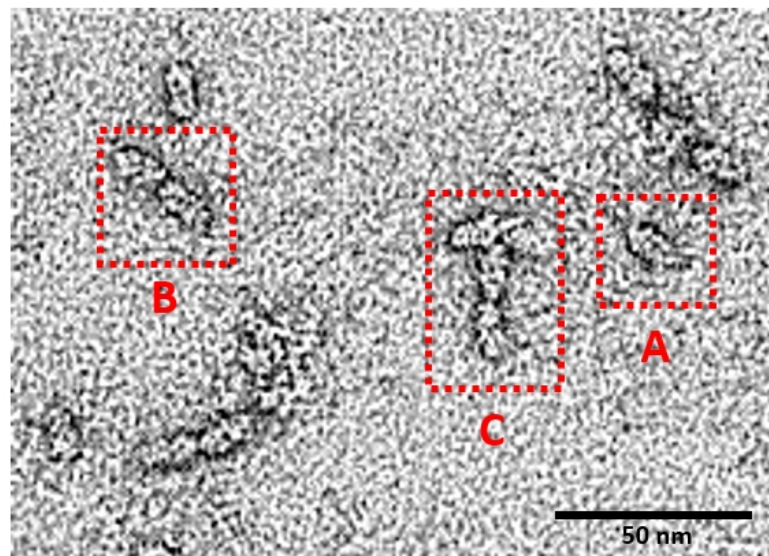


Figure 3.88: Different morphologies hXOR dimers and filaments. A – hXOR dimer. B – hXOR two-dimer filament. C – hXOR two two-dimer filaments.

3.12.3. Grid preparation for cryoEM

Grid preparation was carried out as described in Section 2.8.2. The grids (Quantifoil® R1.2/1.3 on 300 mesh copper grids) were analysed using a Titan Krios 1 (ThermoFisher Scientific) and hydrated images were taken at different concentrations. From the images taken, it was observed that there was a local concentration of protein through the grid, meaning that the protein was aggregating (as shown in Figure 3.89 and 3.90). However, a number of filament structures were observed on the grid, indicating that the filament structures were not an artefact of negative staining. Several factors may influence aggregation, including collision of molecules with the air-water interface that may cause denaturation, and different support films that might affect the thickness of the layer of ice formed during preparation (Drulyte *et al.*, 2018). As a result, 0.01% (w/v) n-Dodecyl β -D-maltoside (DDM, a detergent used to prevent denaturation at the air-water interface by forming a thin layer above the ice layer, thus shielding the protein from the air-water interface) (Glaeser and Han, 2017) and different support films such as gold grids and lacey carbon grids were tested. However, none of these conditions reduced aggregation. Other conditions that might be tested in the future include increasing both the concentration of detergent and salt.

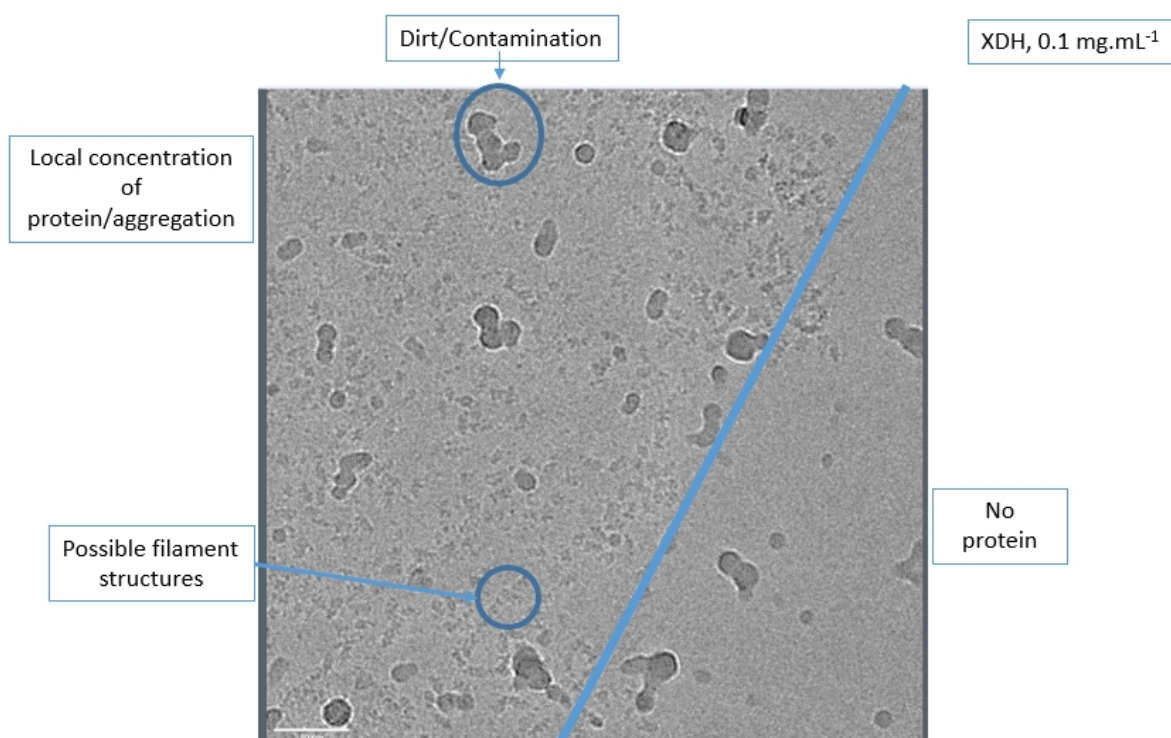


Figure 3.89: Hydrated cryoEM image of 0.1 mg.mL⁻¹ hXOR. The protein was shown to form localised aggregation. Possible filament structures could be observed.

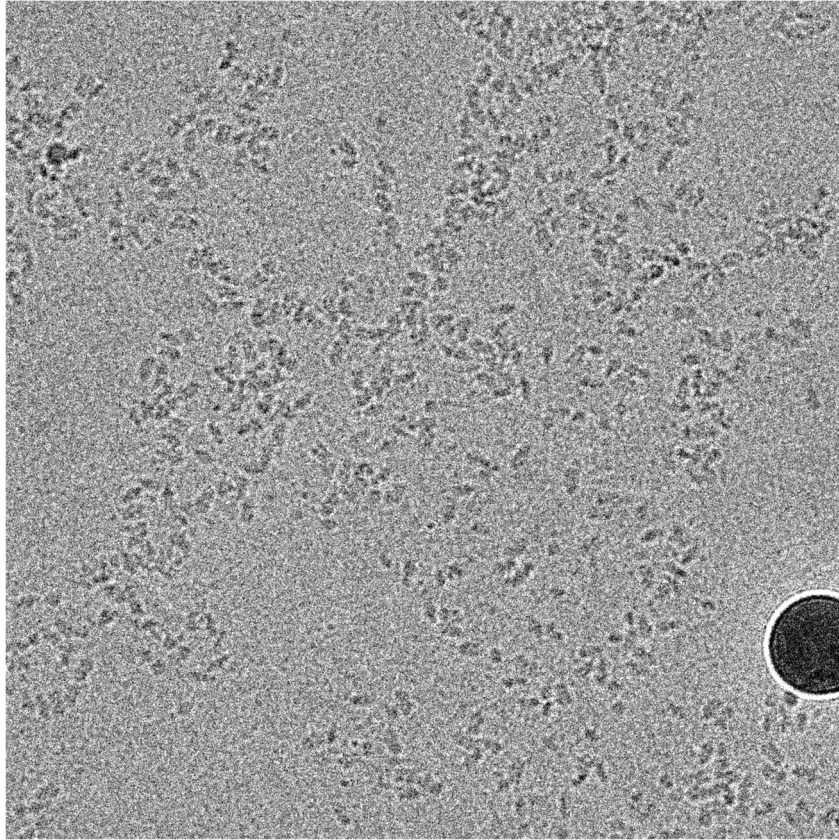


Figure 3.90: Hydrated cryoEM image of 0.5 mg.mL^{-1} hXOR. Localised concentration of protein was observed with possible filament structures.

3.13. Enzymatic assays

3.13.1. Specific activity of hXOR

In order to determine the specific activity of hXOR, a spectrophotometric assay monitoring the rate of oxidation of xanthine to uric acid at 295 nm was used (Avis, Bergel and Bray, 1956). Both the activities of the oxidase form and the dehydrogenase form were determined as described in Section 2.10. The definition of one unit of hXOR is the amount of XOR that will convert 1.0 μ mole of xanthine to uric acid per minute at pH 7.5 at 25°C (Avis, Bergel and Bray, 1956). The unit per mg of protein was calculated as described in Equation 3 below.

$$\text{Units per mg enzyme} = \frac{(\Delta A_{295/\text{min}} \text{Test} - \Delta A_{295/\text{min}} \text{Blank}) \times df}{9.6 \times [W]} \quad \text{Eq. 3}$$

Where:

df is the dilution factor of the enzyme

9.6 $\text{mM}^{-1}\text{cm}^{-1}$ is the extinction coefficient of uric acid at A_{295}

[W] is the concentration in $\text{mg}\cdot\text{mL}^{-1}$ of the enzyme used

The total activity of hXOR (hXDH + hXO) was determined to be 0.231 $\text{U}\cdot\text{mg}^{-1}$ (Figure 3.92) whereas the activity of hXO was determined to be 0.125 $\text{U}\cdot\text{mg}^{-1}$ (Figure 3.91). The percentage hXDH was resolved as described in Equation 4 (Nakamura and Yamazaki, 1982).

$$\%hXDH = \frac{U_{hXOR}}{(U_{hXO} \times \frac{350}{452}) + U_{hXOR}} \times 100 \quad \text{Eq. 4}$$

Where:

U_{hXOR} is the total activity of hXOR

U_{hXO} is the activity of hXO

350 and 452 are the assumed activities of typical reduced and oxidised XOR respectively.

The % hXDH at 25°C for the standard assay was established to be 79.8% whereas the % hXO was 20.2%.

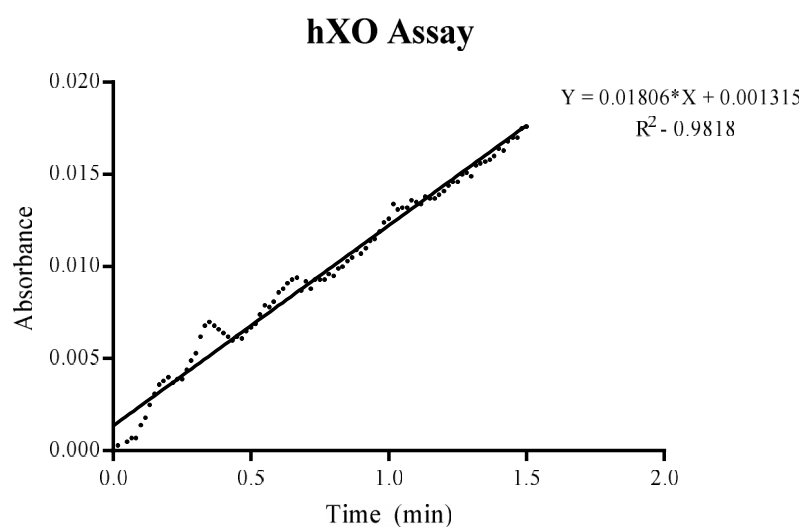


Figure 3.91: hXO activity assay. The gradient of the graph represents the amount of uric acid formed over time by hXO which gives 0.0018 U. The amount of protein in the cuvette was $15 \mu\text{g}\cdot\text{mL}^{-1}$, meaning that the activity was $0.125 \text{ U}\cdot\text{mg}^{-1}$.

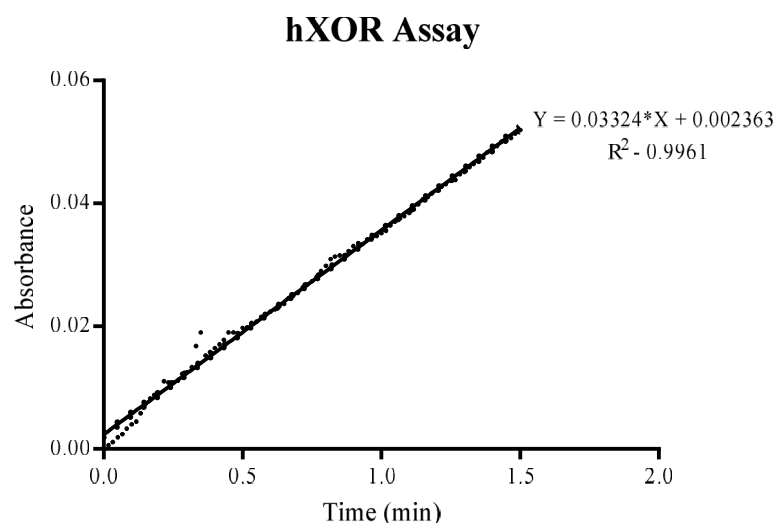


Figure 3.92: hXOR activity assay. The gradient of the graph represents the amount of uric acid formed over time by hXO and hXDH combined which gives 0.00346 U. The amount of protein in the cuvette was $15 \mu\text{g}\cdot\text{mL}^{-1}$, meaning that the total activity was $0.231 \text{ U}\cdot\text{mg}^{-1}$.

3.13.2. Activity of hXOR at different temperatures

The activity of hXOR was also tested at 30°C and at 37°C. As expected, the activity increased as the temperature increased with the assay at 30°C exhibiting an activity of 0.3113 U.mg⁻¹ while at 37°C exhibiting an activity of 0.5056 U.mg⁻¹. The amount of hXDH present decreased marginally as the temperature increased with 77.9% hXDH activity at 30°C while 75.7% hXDH activity at 37°C. This appears to indicate that on increasing the temperature, the rate of oxidation of hXDH to hXO increases. Plots of the activities are shown in Figure 3.93 while the values of activities and % hXDH activity are shown in Table 3.19.

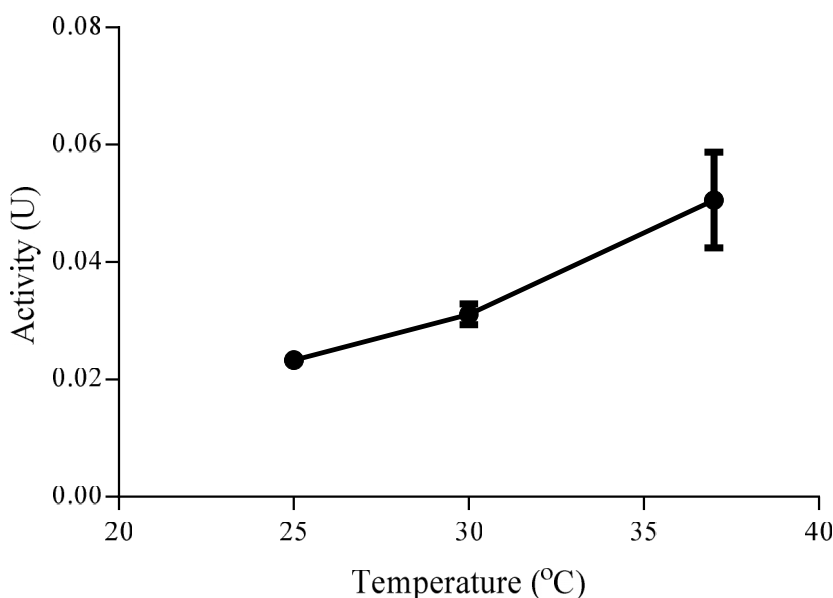


Figure 3.93: Activity of hXOR at 25, 30 and 37°C. The activity shown represents the total activity of hXOR (hXDH + hXO). Error bars represent the standard deviation ($n=3$).

Table 3.19: Activities of hXOR at different temperatures. The error presented is the standard deviation ($n=3$)

Temperature (°C)	Activity (U.mg ⁻¹)	XDH (%)
25	0.23300 ± 0.00061	79.8
30	0.31130 ± 0.00175	77.9
37	0.50595 ± 0.00819	75.7

3.13.3. Thermal inactivation analysis of hXOR

The enzyme was incubated for 10 min at 25, 40, 50, 60°C and the activity was determined as described in Section 2.10.2. From the results obtained (Figure 3.94), it was observed that the activity decreased slightly from 25°C to 40 and 50°C by approximately 20% which continued to decrease to 10% (ten-time decrease) at 60°C. In fact, at 60°C, the enzyme was observed to precipitate and thus, before taking any readings, the sample was centrifuged at 16k x g for a few seconds to remove any particles which might affect the assay.

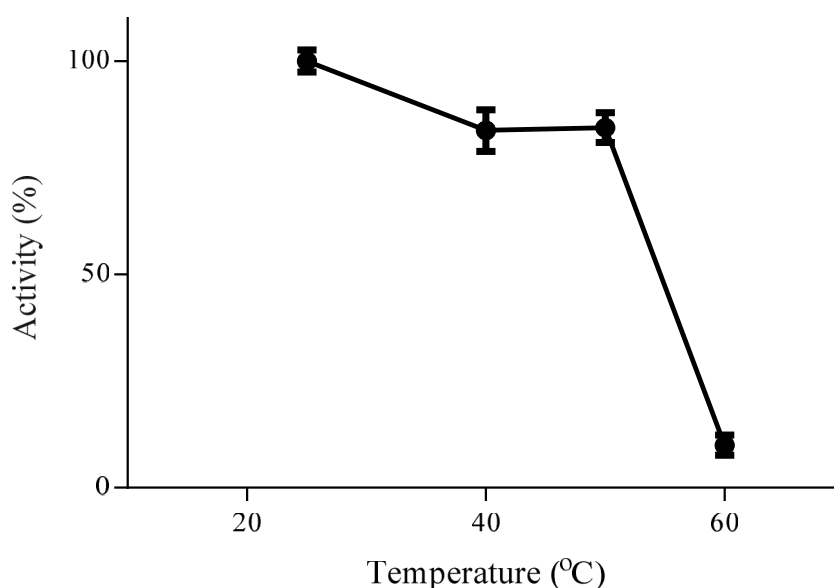


Figure 3.94: Activity of hXOR after incubation for 10 minutes at different temperatures. The activity was determined at 25°C. Error bars represent the standard deviation ($n = 2$).

A temperature ramp at 25, 37 and 50°C was conducted for 60 minutes at 0, 10, 20, 40, 60 min time intervals. At 25°C, the activity only decreased by 13% after 60 min incubation. At 37°C, the activity decreased steadily until 40 min by 33% but remained constant thereafter. At 50°C, the activity decreased linearly up to 20 min by 40%, which remained constant for the next 20 min but further decreased by 47% after 60 min of incubation (Figure 3.95).

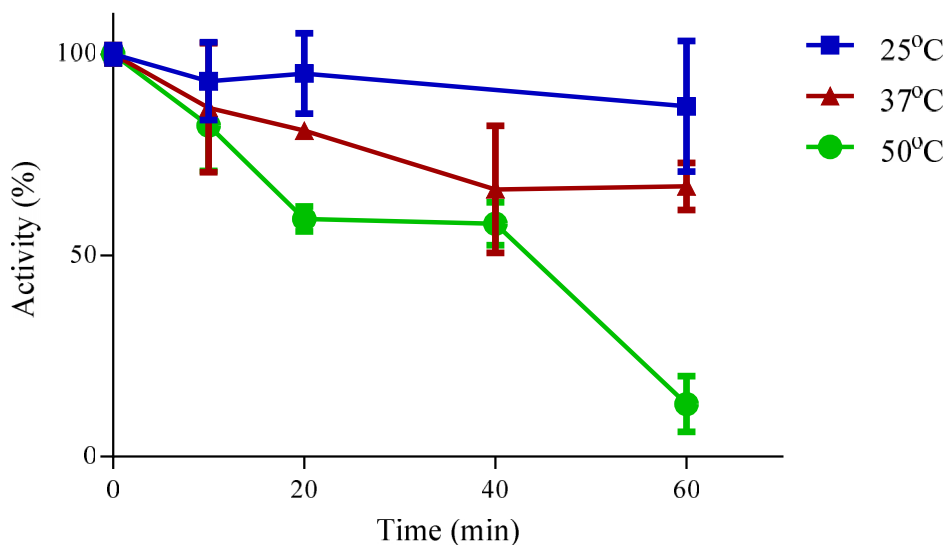


Figure 3.95: Thermal inactivation of hXOR. The activity was determined at 25°C. Error bars represent the standard deviation ($n = 4$).

First-order thermal inactivation was determined by plotting the natural logarithm of the activity against time. Both the first order thermal inactivation rate constant, K_d , and the thermal inactivation half-time, T_i were calculated from the linear regression of the plots. For the 25°C ramp, the whole 60 min was used for the calculation, whereas for the 37°C and the 50°C only the first 40 min and 20 min respectively were used. The values of the rate constant and the half-time are shown in Table 3.20.

Table 3.20: Thermal Inactivation constant and half-time of hXOR

Temperature (°C)	K_d (min^{-1})	T_i (min)
25	-0.002241 ± 0.0006017	300.6
37	-0.006852 ± 0.001646	92.2
50	-0.03210 ± 0.008534	27.1

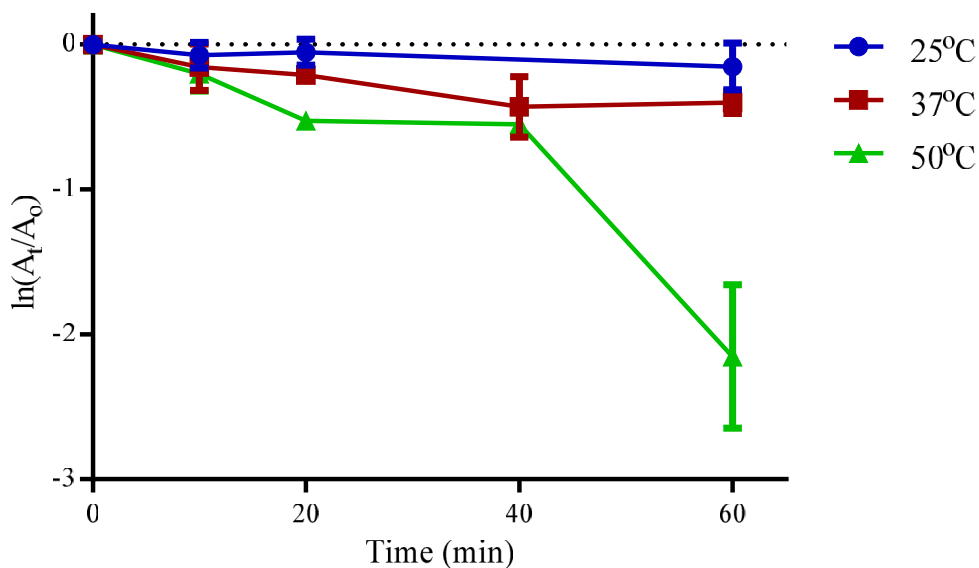


Figure 3.96: First-order thermal inactivation of hXOR. A_t is the activity at time t while A_0 is the activity at time 0 min. Error bars represent the standard deviation ($n = 4$).

3.13.4. Activity of hXOR in different buffers

Different buffers at different pH were tested to determine the optimum buffer of the enzyme. The buffers tested were: bicine pH 9.0, HEPES pH 8.0, sodium phosphate pH 7.4, sodium phosphate pH 6.0, sodium citrate pH 5.0, and sodium citrate pH 3.5. All buffers tested had a concentration of 50 mM. The buffer in which the enzyme exhibited the highest activity was assigned a value of 100% and the activity of the enzyme in the other buffers were compared to this value to obtain a % activity. This was carried out to facilitate comparisons amongst the buffers. The buffer with the highest activity was HEPES pH 8.0 followed by sodium phosphate pH 6.0 and sodium phosphate pH 7.4. At higher pH, the activity decreased by approximately 40% while at pH 5.0 and 3.5, the activity decreased by 60% and 97% respectively (Figure 3.97).

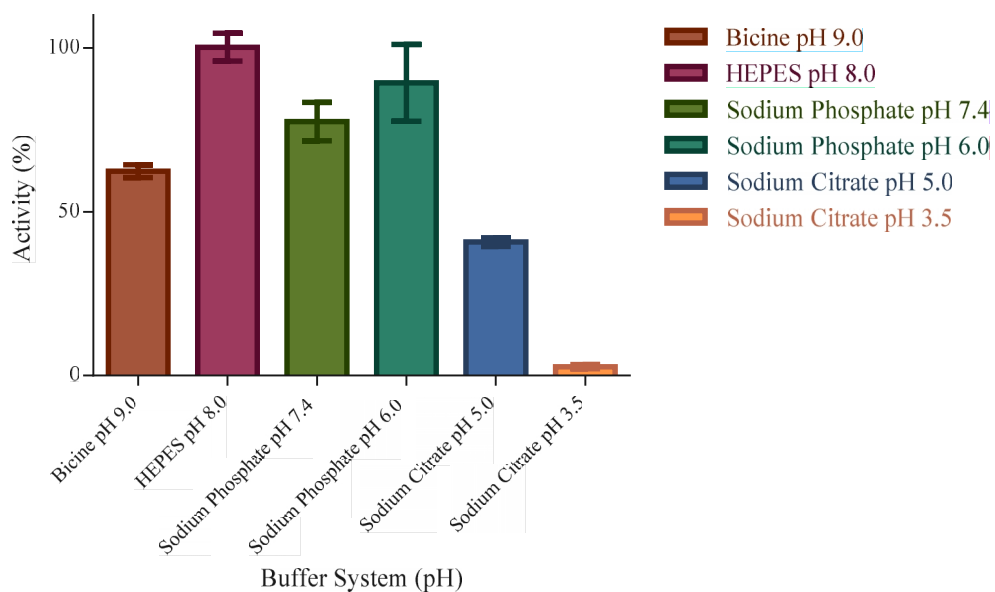


Figure 3.97: Activity of hXOR in different buffer systems. All buffers were at a concentration of 50 mM. HEPES pH 8.0 was determined to be the optimum buffer. Error bars represent the standard deviation ($n = 3$).

The enzyme activity was also measured in 50 mM sodium acetate pH 5.6 and pH 4.6. The activity determined was observed to be very high. To check whether this activity was due to the formation of uric acid or due to another compound, the spectrum from 210 nm up to 200 nm was monitored. A peak at A_{230} formed during the reaction, implying that the compound being formed was not uric acid. A number of control experiments were performed, including: removing the enzyme that resulted in the disappearance of A_{230} peak formation, removing xanthine and using commercial bovine XO instead of hXOR. Removing xanthine did not alter the A_{230} peak formation, inferring that the peak formation was not from the reaction of hXOR with xanthine. Using bovine XO instead of hXOR resulted into no peak formation. This suggested that the product being formed was exclusive to hXOR and was due to the reaction of hXOR with acetate. To make sure that the reaction was not due to improper preparation of sodium acetate, sodium acetate was prepared again and filtered using a 0.2 μm filter. Still, the result was reproducible. Different possible products were scanned to determine which compound was being formed. These included ethanol (the reduced form of acetate), acetaldehyde (reduced form of acetate) and acetic anhydride but neither produced a peak at A_{230} .

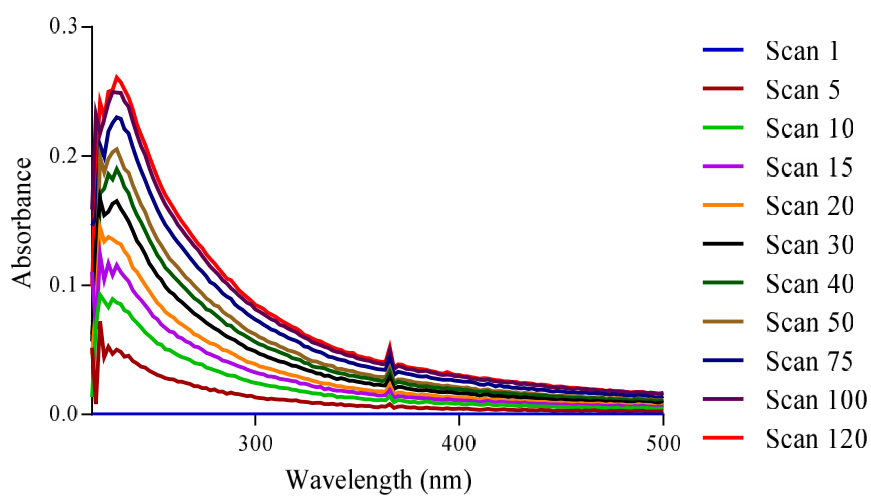


Figure 3.98: Peak formation at A_{230} produced by hXOR with sodium acetate. The duration of one scan was about 0.5 to 1 s. The peak at around 370 nm was due to change of the deuterium lamp to the tungsten lamp in the spectrophotometer.

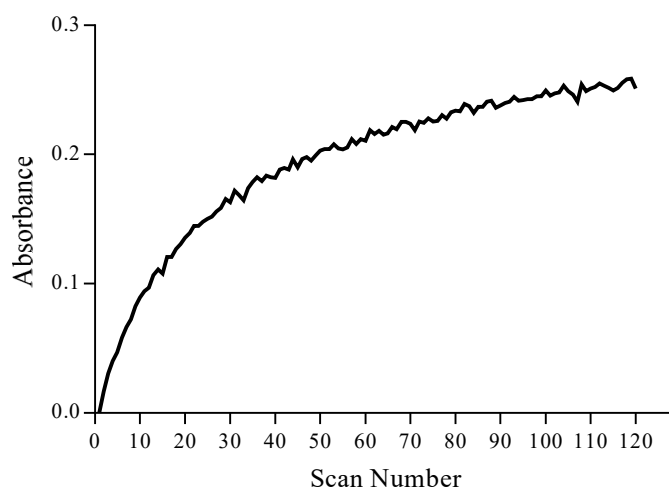


Figure 3.99: Absorbance increase over time at 230 nm.

3.13.5. Inhibition studies of hXOR

The effectiveness of Inhibitor A was tested on both hXOR and bovine XOR while that of inhibitor B was only tested on hXOR. Allopurinol was used as a control inhibitor (Figure 3.100). A range of concentrations was used for both inhibitors to determine the IC_{50} . The IC_{50} was determined by fitting a non-linear regression of $\log(\text{inhibitor})$ against response using GraphPad Prism. For inhibitor A (Figure 3.101), the IC_{50} for hXOR was $0.648 \mu\text{M}$ while for bovine XOR was $0.667 \mu\text{M}$, both of which were ten times higher than the reported value of $0.068 \mu\text{M}$ (Muzychka *et al.*, 2017). For inhibitor B (Figure 3.102), the IC_{50} for hXOR was $45.5 \mu\text{M}$ while for bovine XOR the value of IC_{50} was not determined. The value for the IC_{50} of hXOR with inhibitor B matched that of the bovine XOR ($47.3 \mu\text{M}$) described in literature (Xie *et al.*, 2017). Thus, inhibitor A was established to have better inhibition properties as lower concentrations of inhibitor A were required to decrease the activity of hXOR by 50%. This difference in inhibition could be due to the structure homology of inhibitor A with purines such as xanthine.

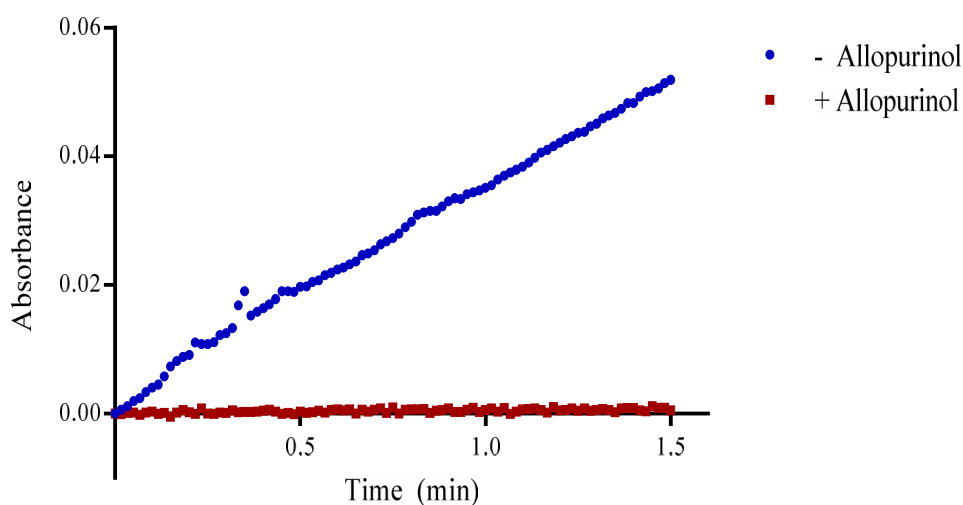


Figure 3.100: Enzymatic activity with (red) and without (blue) allopurinol. The concentration of allopurinol used was $10 \mu\text{M}$.

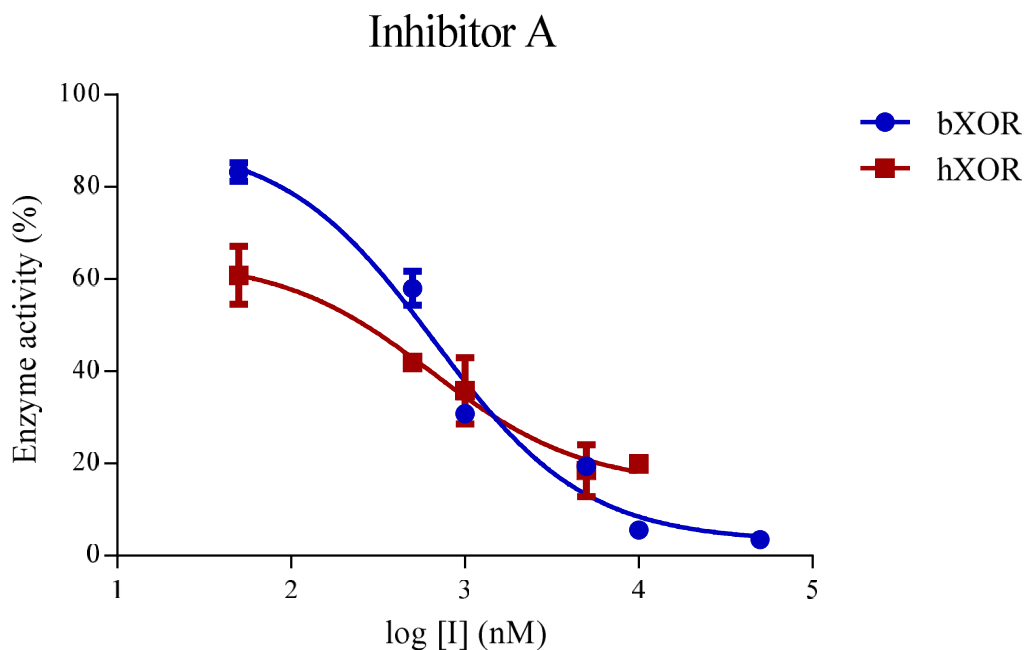


Figure 3.101: Enzyme activity against the logarithm of the concentration of inhibitor A. The IC_{50} of hXOR was $0.648 \mu\text{M}$ while that of bXOR was $0.667 \mu\text{M}$. Error bars represent the standard deviation ($n = 3$).

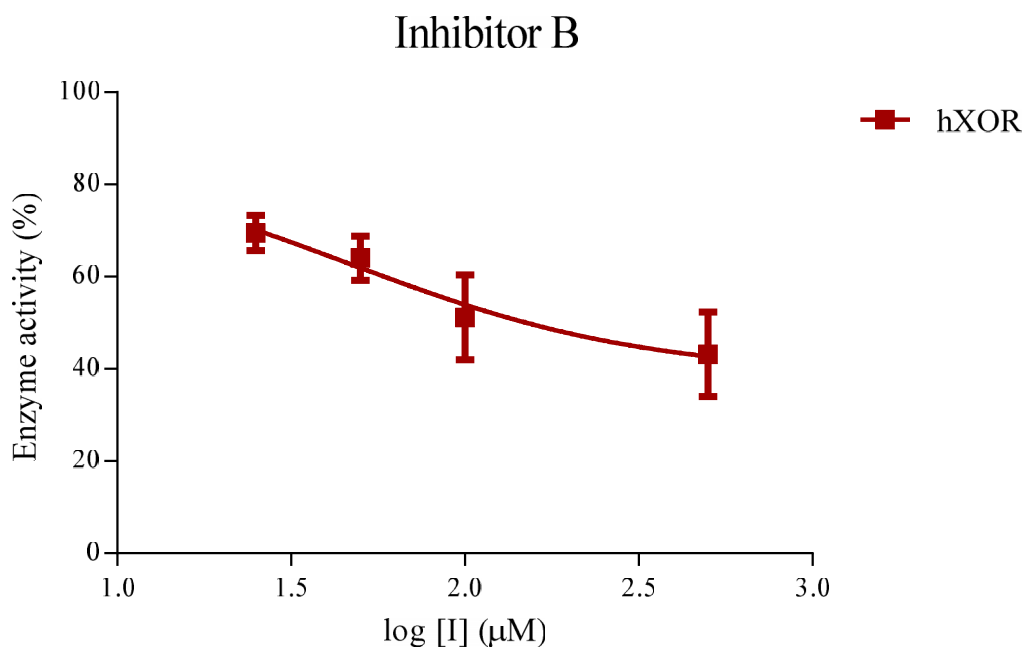


Figure 3.102: Enzyme activity against the logarithm of the concentration of inhibitor B. The IC_{50} of hXOR was $45.5 \mu\text{M}$ while that of bXOR was not determined. Error bars represent the standard deviation ($n = 3$).

3.13.6. Activity assays of hXOR mutants

Mutants of hXOR (G172R, A932T, N1109T, Section 2.2.8) were purified to the same degree of purity using heparin affinity chromatography as described in Section 2.4.3.4. The total activity of hXOR was determined for the wild type and mutants. The G172R and N1109T mutants had similar activities to that of the wild type, indicating that these mutations did not affect the activity. However, the A932T mutation increased the activity by almost three-fold.

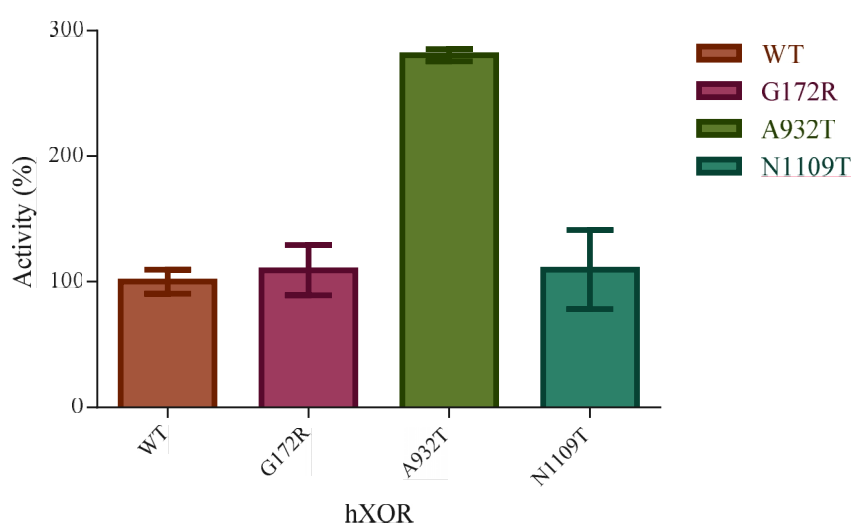


Figure 3.103: Activities of hXOR and mutants. The G172R and N1109T mutants had similar activities to that of the wild type whilst the A932T mutant exhibited a three-fold increase in activity. Error bars represent the standard deviation (n = 3).

3.13.7. Specific activity of ovine XOR

Both the activities of the oxidase form and the dehydrogenase form were determined as described in Section 2.10. The total activity of ovine XOR was determined to be 0.395 U.mg^{-1} (Figure 3.105) whereas the activity of ovine XO was determined to be 0.046 U.mg^{-1} (Figure 3.104). The percentage ovine XDH was resolved as described in Equation 4. The % ovine XDH at 25°C for the standard assay was established to be 91.6% whereas the % ovine XO was 8.4%.

Ovine XO assay

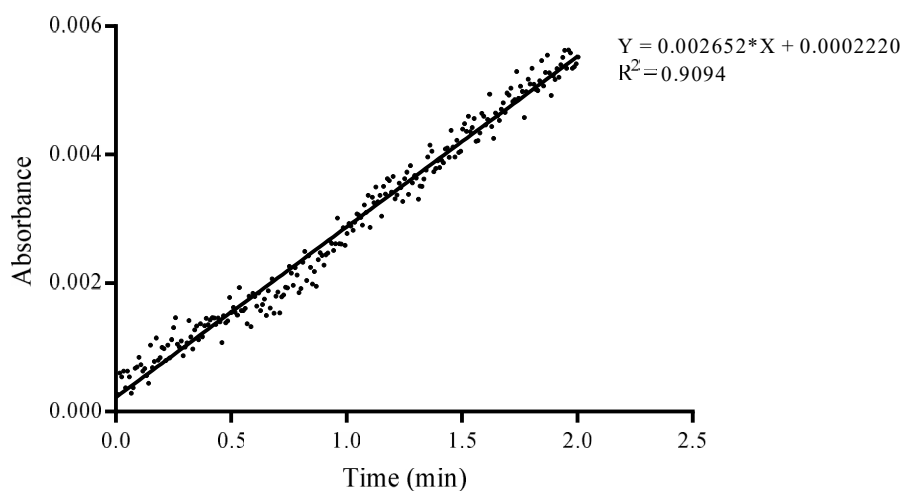


Figure 3.104: Ovine XO activity assay. The gradient of the graph represents the amount of uric acid formed over time by ovine XO which gives 2.76×10^{-4} U. The amount of protein in the cuvette was $6 \mu\text{g.mL}^{-1}$, meaning that the activity was 0.046 U.mg^{-1} .

Ovine XOR assay

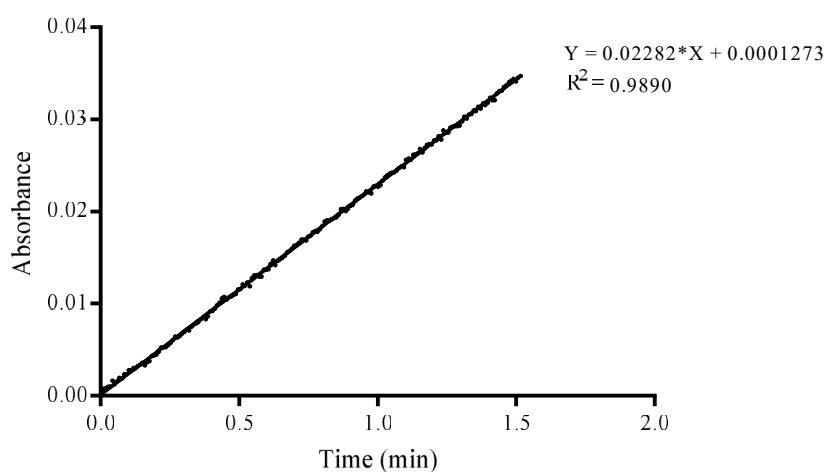


Figure 3.105: Ovine XOR activity assay. The gradient of the graph represents the amount of uric acid formed over time by ovine XO and ovine XDH combined which gives 2.37×10^{-3} U. The amount of protein in the cuvette was $6 \mu\text{g.mL}^{-1}$, meaning that the total activity was 0.395 U.mg^{-1} .

3.13.8. Thermal inactivation analysis of ovine XOR

The enzyme was incubated for 10 min at 25, 40, 50, 60°C and the activity was determined as described in Section 2.10.2. From the results obtained (Figure 3.106), it was observed that the activity remained constant from 25 to 40°C while it decreased by 12% at 50°C. The activity continued to decrease at 60°C to 35% activity, approximately three-fold less than that at 25°C.

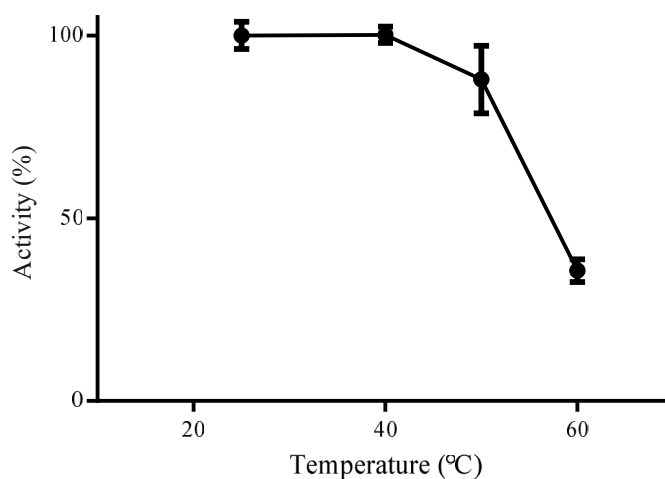


Figure 3.106: Activity of ovine XOR after incubation for 10 minutes at different temperatures. The activity was determined at 25°C. Error bars represent the standard deviation (n = 3).

Chapter 4 Discussion

Apart from catalysing the oxidation of hypoxanthine and xanthine, XOR can catalyse other aromatic heterocycles, nitrites and can activate carcinogenic substances (Bray, 1977, Battelli *et al.*, 2016). In humans, XOR is transcribed as XDH but it can be oxidised to XO. In humans, both XOR specific activity and molybdenum content were found to be low when compared to other mammals such as *Bos taurus* (Jarasch *et al.*, 1981). In humans, deficiency of XOR activity might result in xanthinuria while increased activity of XOR might result in hyperuricemia that can lead to gout (Schwarz and Belaidi, 2013). XOR was shown to be a source of reactive oxygen species (ROS) and reactive nitrogen species (RNS) in vasculature and digestive tract and may provide protection against infection (Martin *et al.*, 2004). Conversion of hXDH to hXO was noted to occur during ischaemia-reperfusion injury. This leads to an increased production of ROS which might lead to inflammation, oncogenesis, brain injury and stroke (Shah and Keenan, 2010, Abramov, Scorziello and Duchon, 2007). Formation of RNS may lead to hypertension, atherosclerosis and coronary artery disease (Murad, 2006). XOR is also involved tumour lysis syndrome in chemotherapy patients. Consequently, the level of XO in blood can be used as an indication of disease and can act as a biomarker for a number of conditions including oxidative stress that is attributed to neurodegenerative diseases (Phillips *et al.*, 2004). Currently, only two XO inhibitors are FDA and EMA approved and XOR is now considered as an important drug target (Diaz-Torné, Perez-Herrero and Perez-Ruiz, 2015; Sattui and Gaffo, 2016).

4.1. Protein Purification

Purification of human XOR from source is impractical. This is due to the limited availability of human liver tissue and human milk and due to the high percentage of inactive XOR in these sources. As a result, the first step of studying hXOR was to establish a reproducible and straight forward purification protocol of recombinant hXOR from *E. coli*. Two cDNA constructs were used to overexpress hXOR: pTrc-hXOR and pTrcHis-hXOR. TP1000 cells, cells that are routinely used to express eukaryotic molybdoenzymes (Palmer *et al.*, 1996), were transformed with these constructs.

Expression and purification experiments from pTrc-hXOR proved to be inefficient and yielded only 1.2 mg of pure protein per litre of cell culture. Sequencing of this construct revealed the presence of five extra amino acids (EFELG) that were

introduced after the first AUG codon during cloning. The effect these extra amino acids may have on expression of the cDNA is unknown and may be a contributing factor to the low yield. Since this hXOR did not have any affinity tags, a number of purification steps were required which resulted in a loss of yield especially during the ammonium sulfate cut which, however, was a necessary step in the purification. The purity of the hXOR by this purification was 82%. The hXOR did not produce reproducible crystals. This inability may be due to the presence of protein contaminants as a purity above 90% is generally recommended for successful crystallisation.

In view of this, another method for the purification of recombinant hXOR was designed. A His-tag with a Factor Xa cleavage site was introduced at the N-terminal of the hXOR cDNA to produce the pTrcHis-XOR. This design ensured that no extra amino acids between Factor Xa cleavage site and the start of the protein were present (Section 3.1.2). The His-tag was added via PCR and ligated using T4 DNA ligase. During this process, two codons were absent in the inserted sequence. This resulted into two missing amino acid residues, a valine (GTG) and a histidine (CAC). The missing GTG was a linker codon between the tag and the cleavage site and its loss did affect either the tag or the cleavage site. The missing CAC resulted in one less histidine residue in the His-tag (i.e. 5xHis-tag instead of 6xHis-tag). As two codons were missing, the resulting cDNA sequence was still in frame with the start codon. Both missing codons were present in the hisXOR-F primer suggesting that some aberration in the PCR occurred. One plausible explanation may be that the DNA was not amplified to completion due to the size of the plasmid (8180 bp), resulting into the two missing codons. Nonetheless, since the cleavage site was unaffected and the His-tag was still present (albeit might have less affinity due to the missing histidine), the pTrcHis-hXOR was still used for further experiments.

Purification of the His-hXOR yielded approximately 42 mg of protein per litre of cell culture, a 35-fold increase in yield compared to the amount recovered from the non-tagged procedure. Following affinity chromatography, the purity of the His-tagged protein was 96%, thus showing a significant improvement over the non-tagged hXOR. Another advantage of this procedure is that this was a one-step protocol that considerably reduced the time required to complete the purification, a factor that may influence the quality of the protein. In fact, when comparing the western-blots of hXOR (Section 3.5, Figure 3.19) and His-hXOR (Section 3.7, Figure 3.24), it could be observed that hXOR (untagged) experienced limited proteolysis while His-hXOR appeared as a single band without any proteolytic product. (Section 3.7, Figures 3.23, 3.24). Recombinant hXOR

was previously purified by Yamaguchi and co-workers (Yamaguchi et al., 2007). However, there is no information regarding the yield of the purified protein. Moreover, the published SDS-PAGE gel showed partial proteolysis.

Ovine XOR was purified from milk with a slight modification to the method described by Benboubetra and co-workers (Benboubetra et al., 2004) that resulted into an increase in purity. The change in protocol was the addition of an anion exchange column after the heparin-affinity column. Ovine XOR was also analysed via western blot to confirm that the purified protein was in fact XOR. Ovine XOR gave a prominent signal (approximately 150 kDa) when probed with a xanthine oxidase primary antibody. The bands for the proteolytic products were weak and included the Moco domain (approximately 90 kDa) and the combined FAD and iron-sulfur clusters (approximately 60 kDa).

The A280/A450 ratio of XOR was calculated. A280/A450 ratio represents the absorbance contribution from the total protein present in the sample, represented by the A280, to the absorbance contribution from the FAD domain, represented by the A450. The smaller the value, the purer the protein, with a value close to 5 indicating pure XOR (Bray, 1977). For the human protein, the A280/A450 ratio ranged from 6.0 to 8.0 for the non-tagged hXOR and 5.0 – 5.5 for the tagged His-hXOR. This further indicated that the His-hXOR was of superior quality. The collected ovine XOR had a A280/A450 of 5.6 after the anion exchange, indicating that it was significantly pure.

Both in-gel trypsin digest and MALDI-TOF confirmed the purity and identity of hXOR. Furthermore, far-UV CD confirmed that all purified proteins (hXOR, His-hXOR, ovine XOR) retained their secondary structure.

4.2. Thermal shift assays

Thermal shift assays revealed that hXOR and ovine XOR were more stable in buffers close to physiological pH. Buffer optimisation is important to ensure both the quality and stability of the proteins as buffer composition is known to influence protein structural homogeneity and this may be pivotal for successful protein crystallisation (Reinhard *et al.*, 2013). The determined optimal buffer conditions for both hXOR and ovine XOR were used for subsequent purifications and as storage buffers. For hXOR, two buffer systems, HEPES pH 7.0 – 8.0 and sodium phosphate pH 7.0 – 7.5, were the most favourable buffers. In fact, hXOR exhibited the highest specific activity in both HEPES

and sodium phosphate (Figure 3.97). The least favourable buffer systems were either acidic (pH 4.0 – 5.0) or alkaline (pH 8.5 – 9.0) indicating that hXOR is not stable under these conditions of pH. In fact, the activity of hXOR was lower at such pH conditions. Ovine XOR was the most stable in phosphate buffers pH 6.0 – 7.5. The optimum pH of ovine XOR described in literature was that of pH 7.5 which correlates with the increased in stability of the enzyme at such pH (Zaahkouk *et al.*, 2019).

4.3. Specific Activity of XOR

Specific activity experiments for the human XOR were carried out on the tagged His-hXOR due to the abundance and purity of the protein. The hXO activity determined in this study was 0.125 U.mg^{-1} while the total hXOR activity was 0.231 U.mg^{-1} . The abundance of the oxidase was 20%. This means that the activity of 0.125 U.mg^{-1} determined for the hXO was due to the contribution of this 20% hXO. If the abundance of hXO is adjusted to 100% (i.e. assuming that there was 100% hXO), the activity of hXO would equate to 0.625 U.mg^{-1} . The reported activity of hXO from human milk is 0.06 U.mg^{-1} (Sanders, Eisenthal and Harrison, 1997). However, the Mo content in human milk was reported to be only 3% while the Mo content of the recombinant His-hXOR in this study was 20%. Adjusting the activity to per Mo molecule, the activity of hXO works out to be 3 and $2 \text{ U.mg}^{-1}.\text{Mo}^{-1}$ for the recombinant hXO and hXO from milk respectively. The ovine XO activity was determined to be 0.046 U.mg^{-1} while that of the total ovine XOR activity was 0.395 U.mg^{-1} . The proportion of ovine XOR present as XO was 8.4%. This infers that for 100% ovine XO, the activity would be 0.548 U.mg^{-1} which is similar to previous reported values of 0.69 U.mg^{-1} (Benboubetra *et al.*, 2004). The hXOR and ovine XOR showed similar stability when heated at 50°C for 10 min and exhibited a 20% and 12% decrease in activity respectively. However, the activity of each of the enzymes decreased drastically when heated for 10 min at 60°C . The hXOR appears to be less thermostable at the higher temperature compared to the ovine protein.

4.4. Protein Crystallisation and Crystallography

The maximum resolution obtained from hXOR crystals was 3.95 \AA with a space group of P 31 2 1. The space group matched that of the deposited xanthine dehydrogenase from human milk (2CKJ, Pearson *et al.*, unpublished). The low resolution may be due to

several reasons. For instance, even though the crystallisation trials were done in the presence of DTT, oxygen could react with the DTT, depleting it and leaving hXDH exposed to oxygen attack. This would result into a mixture of hXDH and hXO that may hinder crystallisation. Furthermore, during data collection, the hXDH crystal was exposed to oxygen leading to oxidation which might have also reduce crystal quality. Moreover, as the crystals were thin, they were susceptible to radiation damage.

From the data collected, it was established that the asymmetric unit contained four molecules. The dimer interface formed between monomers present in adjacent asymmetric units and not in the same asymmetric unit (Figure 3.61). All chains contained FAD and the iron-sulfur clusters. As the iron content in hXOR was only 24%, the presence of iron in all chains suggests that iron may have a stabilizing effect and its presence is required for crystallization. Only one chain in the asymmetric unit contained molybdenum at the Moco active site. However, molybdopterin was not visible in any of the chains. As molybdenum coordinates with the molybdopterin, the presence of molybdenum indicates that molybdopterin has to be present. This is most likely due to the low resolution of the data obtained. Three different domains and two loops were identified in each monomer corresponding to the [2Fe-2S] cluster, FAD domain, Moco domain, and two linking loops. The cofactors in the two monomers of the biological unit are too far apart to permit electron transfer between monomers, implying that each monomer acts independently of the other. Some regions on the surface of the protein have missing or poorly defined residues. These regions were in linker regions (residues 165-192, 528-537, 545-557), in loops (residues 425-434) and at the C-terminus (residues 1315-1333). These residues are most likely flexible and are in fact also not detectable in the bovine XDH (PDB: 3UNC) resolved at a higher resolution (1.65 Å).

Bovine XDH (PDB: 3UNC) and hXDH were structurally aligned and the position of the molybdenum and that of the molybdopterin were confirmed. A solvent funnel through which substrates enter and interact with the Moco active site was identified close to the molybdenum. When analysing the FAD centre, it was observed that the Gln⁴²³-Lys⁴³³ loop did not mask the tricyclic isoalloxane ring of the FAD. Furthermore, a π -to- π interaction was identified between Arg⁴²⁷ present in the loop and the residues Arg³³⁵, Trp³³⁶, Phe⁵⁵⁰. Both these observations confirm that the protein solved was in the reduced XDH form (Enroth *et al.*, 2000, Ishikita *et al.*, 2012).

The current work is the first report of X-ray crystallographic structural studies of the wild type recombinant hXDH. Previous structures of hXDH from human milk

(Pearson *et al.*, unpublished) lacked both molybdenum or molybdopterin in the Moco domain. This may be due to the low level of molybdenum in human milk, with approximately 97% of milk hXOR in the demolybdo form (Bray *et al.*, 1999). In the current study, the molybdenum content was 20% which is supported by the occurrence of molybdenum in one of the asymmetric chains. However, further work is required to obtain crystals that diffract at higher resolution. Currently, bovine XOR is mostly used for computer aided drug design and docking analysis due its high-resolution structure (3UNC, 1.65 Å, Ishikita *et al.*, 2012). Due to the specific activity difference in hXOR and bovine XOR and since these drugs are targeted for the human protein, it would be more sensible to perform these *in silico* experiments on the hXOR structure.

4.5. Inhibition studies

Two recently published inhibitors, inhibitor A (4-[(Z)-(6-hydroxy-3-oxo-1-benzofuran-2(3H)-ylidene)methyl]benzoic acid) (Muzychka *et al.*, 2017) and inhibitor B ((2E)-1-(2,4-dihydroxyphenyl)-3-(4-hydroxyphenyl)prop-2-en-1-one) (Xie *et al.*, 2017), were synthesised to test their efficacy on hXOR. Both ¹H-NMR and ¹³C-NMR (Section 3.10.1.1 and 3.10.2.4) confirmed the structure of the synthesised compounds. Allopurinol was used as a control inhibitor in activity assays (Figure 3.100). For inhibitor A (Figure 3.101), the IC₅₀ values were 0.648 μM and 0.667 μM for hXOR and bovine XOR respectively. These values were ten times higher than the reported value of 0.068 μM (Muzychka *et al.*, 2017) implying that in the current work, inhibitor A had less affinity than what was published. For inhibitor B (Figure 3.102), the IC₅₀ calculated (45.5 μM) matched that of the bovine XOR described in literature (Xie *et al.*, 2017). From the IC₅₀ of both inhibitors, it was established that inhibitor A had better inhibition properties due to a lower IC₅₀, which might be explained by the structure homology of inhibitor A with purines. However, it must be noted that due to slight differences in structures and activity between hXOR and bovine XOR, it would be best to measure the effects of inhibitors on the human protein to get more dependable results. To this end, this study shows that such experiments could be reliably done on the recombinant human protein.

Possible binding modes of both inhibitors to hXOR was established by docking on the structure of the His-hXDH obtained in the current study. Oxypurinol was used as control for preliminary docking experiments and compared well to that crystallographic structure of bovine XOR with oxypurinol that was previously determined via

crystallography (3BDJ, Okamoto *et al.*, 2008). This experiment showed that the oxypurinol in the docking experiment (Figure 3.79) was in the same position as the crystallographic oxypurinol with slight deviation of the bonding with the surrounding residues. Consequently, results obtained from the docking experiments were only used to indicate the possible location of the inhibitor within the enzyme and to determine any possible binding modes.

The affinities of inhibitor A and B were calculated to be $-6.6 \text{ kcal.mol}^{-1}$ and $-6.2 \text{ kcal.mol}^{-1}$ respectively. Even though inhibitor A showed higher affinity, the difference between the calculated affinities is minute and cannot be used to evaluate their inhibitory efficacy. Both inhibitors were reported to bind inside the Moco active site (Muzychka *et al.*, 2017; Xie *et al.*, 2017). When analysing the structure of hXOR and the specific amino acids that interact with the inhibitor molecules, it was clear that original study did not take into consideration the presence of Mo and MPT at the Moco active site. It was evident that during the docking experiments, the cofactors were eliminated and were not re-introduced when the results were analysed. The results from the docking experiments previously reported are not feasible due to classical steric hindrance of the inhibitors with the cofactors. Conversely, in the current study, cofactors were re-introduced. Both inhibitor A and B were now able to hydrogen bond to Glu⁸⁰³ outside the Moco substrate funnel and did not actually gain access to the Moco site as previously predicted. Moreover, both inhibitors formed hydrogen bonds to surface amino acids as indicated in Figure 3.80 and Figure 3.81. Thus, it is proposed that the compounds actually inhibit the enzyme by hindering the entry of possible substrates to the Moco site and by disrupting the interaction of Glu⁸⁰³ with any possible substrates.

Chemotherapy patients are susceptible to high levels of uric acid due to tumour lysis syndrome. In view of this, the XO level in these patients is tested, where allopurinol is administered if the level of XO is high. However, it was shown that XO is important for cell differentiation and low levels of XO may encourage proliferation of non-differentiated cells, encouraging tumour cells (Battelli *et al.*, 2016). As such, inhibition studies should not be only tested on enzymes having higher activity such as the bovine XOR as these inhibitors may lead to a complete depletion of the human enzyme. Ideally, drugs are designed using the specific protein that is to be targeted and not a relative. This provides further justification to use hXOR for inhibition assays and docking.

4.6. *In-vitro* site directed mutagenesis

Three mutations (G172R, N1109T, A932T) that were previously linked to hypertension in Japanese patients were introduced into hXOR (Yang *et al.*, 2008). G172R and N1109T had similar activities to that of the wild type, inferring that the mutations had no effect on the activity. On the other hand, A932T showed a three-fold increase in activity. Due to this higher activity, the A932T mutant XOR may be generating more superoxide than the wild type. This elevation in superoxide may increase the probability of hypertension due to the depletion of nitrites and production of peroxynitrite (Cai and Harrison, 2000). After energy minimisation of the A932T residue and alignment with the wild type hXOR, the interactions between the residue under investigation and neighbouring residues were analysed. The A932T mutation mutates an alanine residue, a non-polar amino acid, to a threonine residue, a polar amino acid at the Moco domain. The mutation did not alter the conformation of the neighbouring residues and no surface electrostatic change was observed. However, a new hydrogen bond established between Thr⁹³² and Ala⁹³⁹ present in a different helix may confer a structural change. This may also suggest that the mutant is slightly more stable than the wild type, which thus results into a higher activity. Even so, the increase of one hydrogen bond over a protein of 1333 residues might not have a significant result on the stability which indicates that other mechanisms that increase the enzyme activity might be in effect.

4.7. Electron Microscopy

Due to the low-resolution structure of hXOR obtained during this study and difficulty in crystallisation, tomography electron microscopy (negative staining TEM) and cryoEM were carried out to elucidate the tomography of the protein and to try to solve a better resolution structure.

Surprisingly, TEM of both the human and ovine XOR clearly showed that XOR present in 50 mM HEPES pH 8.0 formed filaments that are homogenous in both shape and size. The fact that these filaments formed by both proteins, appears that the hXOR chain structure is natural and not as a consequence of experimental artefact. In the hXOR sample (Figure 3.82), the predominant filaments were composed of two dimers (53.3%, $n=510$). These filaments form at both high and low concentration of hXOR and ovine XOR. Further negative staining experiments were repeated with and were again shown at pH close to the physiological pH. This formation of filaments may explain the increase in stability and higher T_M of the protein in HEPES. Moreover, the presence of filaments was also observed on the blue-native PAGE, where a band roughly twice the size of the homodimer was observed (Figure 3.25). The number of filaments was shown to decrease with decreasing pH with large aggregates of hXOR visible at pH 3.5. At pH 5.6, hXOR predominantly formed homodimers (95%). Interestingly, hXOR protein crystals tend to form at acidic pH, suggesting that the protein crystals were formed by homodimers. Furthermore, this may lend to the possibility that the filaments may in fact inhibit crystallisation. It would be interesting to determine whether the predominant enzyme species in the filaments is XO or XDH or a mixture.

An unexpected peak at A230 formed when conducting the hXOR assay in 50 mM sodium acetate pH 5.6. This peak was observed even in the absence of xanthine from the reaction mixture, implying that the acetate or pH was affecting hXOR. Previous reports state that the A230 peak is due to tryptophan and tyrosine residues that are exposed because of conformational changes (Glazer and Smith, 1961). To that end, it is proposed that the acidic pH causes a disruption in the filament interactions thus exposing tryptophan and tyrosine residues that may be normally buried at the dimer-dimer interface (Figure 4.1), giving rise to a peak at A230.

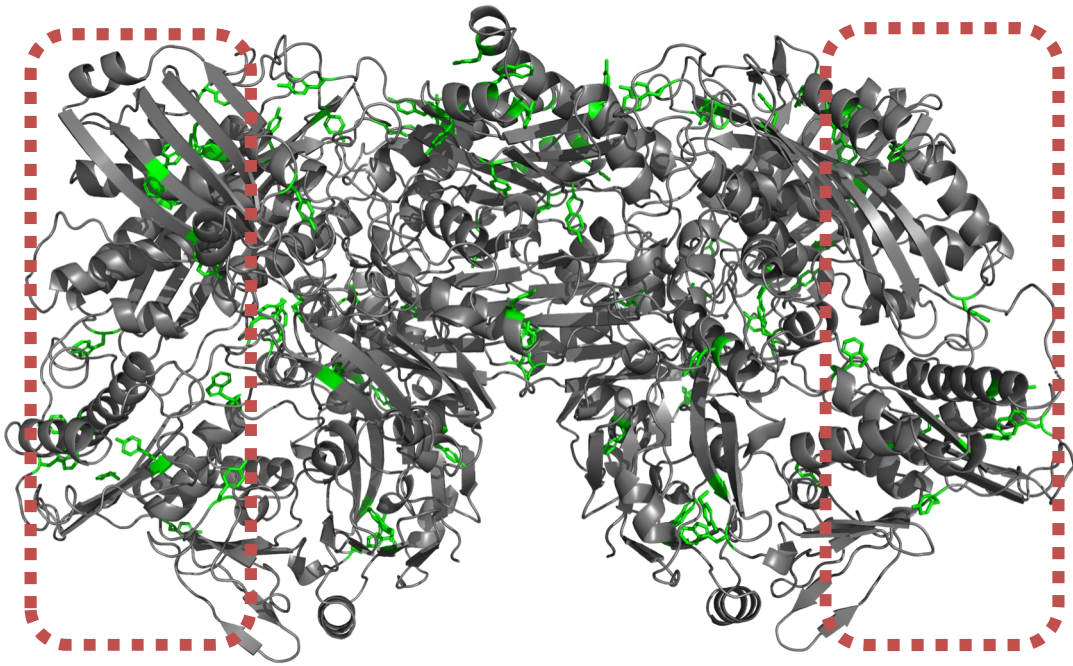


Figure 4.1: Tryptophan and tyrosine residues in hXOR and possible interaction. Tryptophan and tyrosine residues are coloured in green. The red dotted box represents the possible interactions between adjacent dimers. The figure was generated using PyMOL Molecular Graphics System (Schrodinger, 2019).

The advances in the technology of protein TEM and cryoEM have made the detection of protein filaments possible. In fact, similar filaments have been identified in phosphofructokinase-1 (Webb *et al.*, 2017) and bacterial CTP synthase (Barry *et al.*, 2014). Interestingly, phosphofructokinase-1 was expressed in MTLn3 cells and their filament formation was also observed using confocal microscopy using a time-lapse sequence (Webb *et al.*, 2017). This shows that these filaments occur naturally in cells and are not an EM artefact. This deduces that the ability of forming chains is not unique to XOR. It was suggested that the ability of proteins to form filaments can be attributed to regulation of activity, efficient transfer of substrate and scaffolding, however there is limited information about filaments up till now (Barry *et al.*, 2014; Webb *et al.*, 2017). The filament structures of hXOR at physiological pH would be an interesting avenue to explore as hXOR was shown to bind and concentrate on endothelial membranes, leading to an elevation of ROS levels in blood (Kelley, 2015).

The proposed dimer-dimer interaction is shown in Figure 4.2, with the area of interaction highlighted by a dashed line. Analysis of the charges at the surface of the

protein suggest that the two dimers are organised antiparallel to each other (i.e. one of the dimers is upside down). Due to this, the FAD domain is close to Moco domain of the next dimer and as a result, if the domains are close enough, electrons can theoretically propagate from the FAD of one dimer to the Moco of the next.

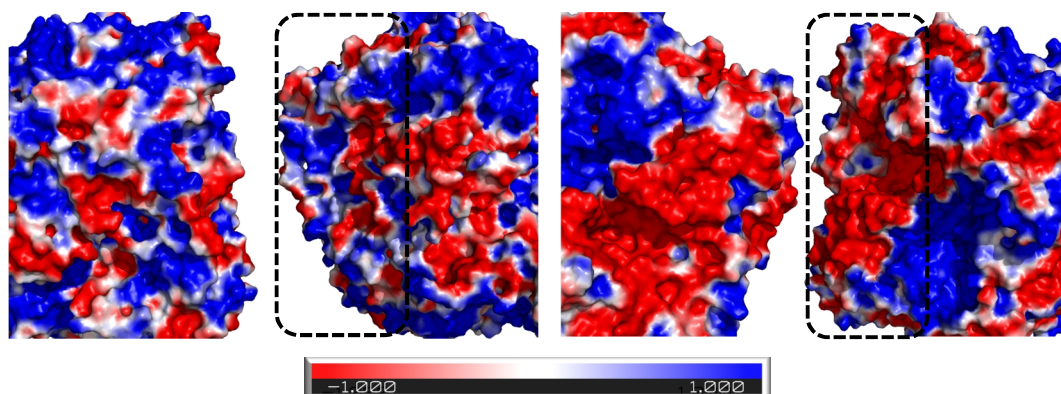


Figure 4.2: Proposed areas of interaction between the two hXOR dimers to form the filaments. Blue and red areas represent electropositive and electronegative regions respectively. The figures were generated using PyMOL Molecular Graphics System (Schrodinger, 2019).

Two hypotheses were formulated to explain the role these filaments may play. During catalysis, hypoxanthine or xanthine donates a pair of electrons at the Moco domain, which then propagates through the enzyme via two [2Fe-2S] clusters to the FAD domain, where the electrons are accepted by an electron acceptor, being either oxygen or NAD^+ . In the first hypothesis (Figure 4.3), an electron donor such as xanthine donates electrons to the Moco domain. The electrons propagate to the FAD domain via the two [2Fe-2S] clusters. If the interaction of the two dimers in a filament blocks the solvent funnel leading to the FAD domain of one dimer, and if the FAD domain is in close proximity to the Moco domain of the adjacent dimer, the electrons in the FAD domain can be transferred to the Moco domain of the next dimer. This pair of electrons can then continue to propagate to the FAD domain and accepted by an electron acceptor such as oxygen or NAD^+ . In this scenario, if the solvent funnel to one of the FAD cofactor is blocked, the dimers must be tilted or at an angle to each other. As a result, only the region with the blocked solvent funnel has the Moco and the FAD domains close enough for electron transfer.

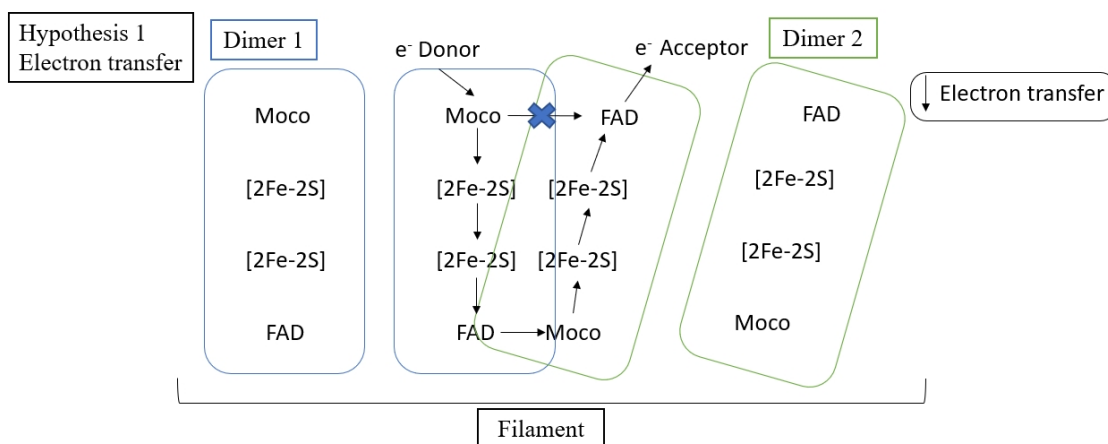


Figure 4.3: Hypothesis 1. The electrons are transferred from one dimer to another. The transfer of electron between the top Moco and FAD would not be possible due to distance.

In the second hypothesis (Figure 4.4), the overlap of the two adjacent monomers of the two interacting dimers is less. The electron donor donates its electrons to the Moco domain and transfers the electron directly to the FAD domain. The FAD molecule is favoured over the [2Fe-2S] clusters due to electron potentials. In this scenario, the solvent funnel of the FAD is not blocked and as a result, an NAD^+ or oxygen molecule can enter the FAD domain and accept the electrons. In this scenario, the [2Fe-2S] clusters are not involved in the electron transfer.

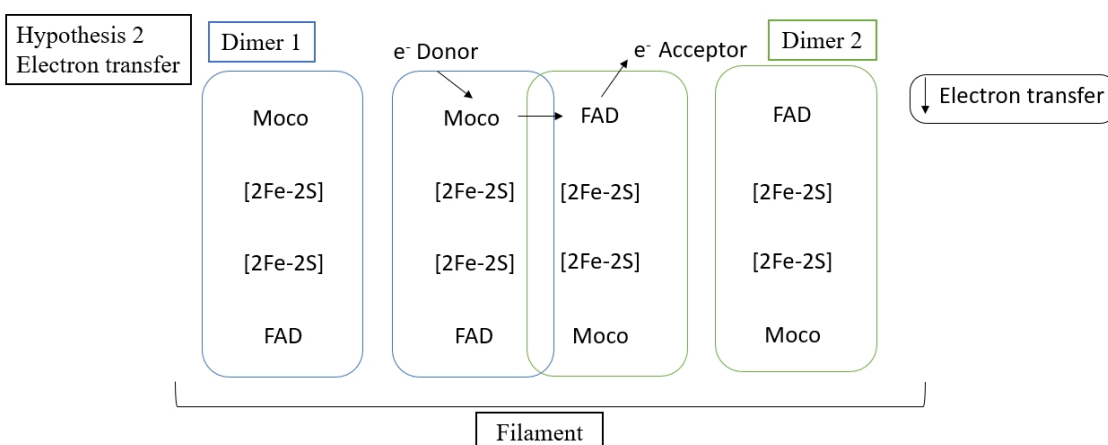


Figure 4.4: Hypothesis 2. The electrons are transferred from a Moco domain of one dimer to the FAD domain of the next dimer.

These two hypotheses suggest that the arrangement of the dimers in the filament may affect the rate of the reaction. This electron transport is reminiscent to the electron

transport chain where even though the proteins are not present in filaments, they are in close proximity and allow the transfer of electrons between each other. In the first hypothesis, as the interaction of the two dimers in the filament hinders the entry of substrates to one of the FAD domains and since this results into a longer electron pathway, the formation of the filament may slow down the rate of the reaction. In the second hypothesis, the electron is immediately transferred from the Moco to the FAD domain, thus bypassing the [2Fe-2S] clusters and decreasing the electron pathway thereby increasing the rate of the reaction. Structural organisation of the filaments will be elucidated from the cryoEM structure that is currently being analysed. This could give an insight into the mechanism of XOR in cells.

4.8. Conclusions

This study established an efficient and reproducible protocol for the synthesis and purification of human recombinant XOR using a bacterial host. Both hXOR and ovine XOR were purified to a high degree of purity, retained their secondary structure after purification and their activity was comparable to published data. The crystal structure of hXDH was solved to a resolution of 3.95 Å with a space group of P 31 2 1. Further experiments regarding the optimisation of the crystals of hXDH might lead to a better resolution structure that can be used for soaking and co-crystallisation experiments with ligands. Nonetheless, the structure was used in this study for *in silico* experiments on the possible docking of the synthesised inhibitors and assessment of the mutants.

This study demonstrates that the use of hXOR for inhibitory studies is possible and is facilitated by the fact that hXOR can be purified at a high yield. Moreover, in view of the difference between the specific activity of the human and the bovine protein, studying the effects of inhibitors on the target protein is more reliable than on a close relative protein. Docking experiments of both inhibitors showed flaws in the published results stressing the importance of re-introducing cofactors after docking. The availability of *in vitro* site-directed mutagenesis reactions on the recombinant human protein is also convenient when investigating mutants. Out of the three mutations tested (G172R, A932T, N1109T), only the A932T mutation had an effect on the activity by increasing it considerably.

The highlight of this study is the identification of XOR filaments that are homogenous in shape and size at pH 7 and 8. To date, only a few enzymes have been

detected to form filaments. To that end, this is a new area of study in the assembly and regulation of enzymes within cells. Moreover, cryoEM might provide more information on the non-resolved regions in X-ray crystallography. The structure obtained from the cryoEM data may be closer to the structure of hXOR at physiological conditions and may give further scope to do inhibitor docking experiments on the human structure. Currently, the cryoEM data is being analysed and it would be curious to determine what further factors would influence the formation of filaments.

4.9. Suggestions for future work

Additional optimisation expression experiments can be performed to increase the amount of iron and molybdenum in the enzyme. These might include supplementing the growth media with ferric ammonium citrate and other iron compounds and testing different molybdenum compounds.

As the crystals obtained only diffracted up to 3.95 Å, more optimisations are required. This low resolution might be due to the presence of hXO in the crystallisation drop. As a result, the crystallisation of hXO can be attempted by carrying out limited proteolysis on hXDH by trypsin digestion and purify the hXO through a size exclusion column. This would ensure an almost 100% hXO abundance which then can be used for crystallisation. Alternatively, crystallisation of hXDH can be done anaerobically in a glove box filled with nitrogen to ensure that the protein is not oxidised. If higher resolution crystal structures of hXOR are obtained, hXOR can be crystallised with ligands such as substrates and inhibitors to elucidate their effect on the human protein. Nitrites are of particular interest as XOR was shown to produce NO^{*}, a cardiovascular protective molecule, via a nitrite reductase activity (Godber *et al.*, 2000; Maia and Moura, 2011). Co-crystallisation of hXOR with nitrites might clarify the mechanism of this activity.

The A932T mutation demonstrated increased activity when compared to the wild type. As a result, further experiments on the A932T mutant can be carried out to determine the mechanism which increases such activity. Experiments might include thermal shift assays to determine the stability of the mutant and crystallisation to solve the mutant structure.

Currently, ligand-based drug design is being carried out on both inhibitor A and B to determine potential inhibitors and test their inhibitory efficacy. As this study showed that a considerable amount of protein can be synthesised from *E. coli*, inhibition assays

of potential inhibitors can be done on the hXOR directly. In addition, hXOR can be used to screen affimer proteins. Affimer proteins are molecules that are able to bind at high affinity and specificity (Tiede *et al.*, 2017). Screening of affimer proteins on hXOR can result into novel inhibitors which can then be tested via inhibition assays.

Further experiments involving negative staining using hXOR with inhibitors and substrates might elucidate whether the filamentous structures form when in the presence of a ligand. Moreover, cryoEM data collection of hXOR with ligands might clarify the presence of these filamentous structures. Currently, cryoEM data of hXOR is being analysed. Once analysis is finished, the structure obtained from cryoEM can be compared to the crystal structure to determine whether the crystal structure and the structure in solution are different or the same. Moreover, if the analysis of the cryoEM data of hXOR gives rise to a high-resolution structure, this structure can be used to model and dock potential inhibitors.

References

- Abramov, A. Y., Scorziello, A. and Duchen, M. R. (2007) Cellular/Molecular Three Distinct Mechanisms Generate Oxygen Free Radicals in Neurons and Contribute to Cell Death during Anoxia and Reoxygenation. *The Journal of Neuroscience* **27**(5), 1129–1138.
- ACD/ChemSketch, version 2018.1 (2019). Advanced Chemistry Development, Inc., Toronto, ON, Canada. Available at: www.acdlabs.com, 2019.
- Allawi, H. T. and Santalucia, J. (1997) Thermodynamics and NMR of Internal G , T Mismatches in DNA. *Biochemistry* **36**, 10581–10594.
- Amann, E., Brosius, J. and Ptaslme, M. (1983) Vectors bearing a hybrid trp-lac promoter useful for regulated expression of cloned genes in Escherichia coli. *Gene* **25**, 167–178.
- Arellano, F. and Sacristan, J. a (1993) Allopurinol hypersensitivity syndrome: a review. *Ann Pharmacother* **27**(3), 337–343.
- Atmani, D., Benboubetra, M. and Harrison, R. (2004) Goat's milk xanthine oxidoreductase is grossly deficient in molybdenum. *Journal of Dairy Research* **71**, 7–13.
- Avis, P. G., Bergel, F. and Bray, R. C. (1956) Cellular constituents. The chemistry of xanthine oxidase. Part III. Estimations of the cofactors and the catalytic function sof enzyme fractions of cows' milk. *J. Chem. Soc.*, 1219–1226.
- Barrera, G., Pizzimenti, S. and Dianzani, M. U. (2008) Lipid peroxidation : control of cell proliferation, cell differentiation and cell death. *Molecular aspects of medicine* **29**, pp. 1–8.
- Barry, R. M., Bitbol, A. F., Lorestani, A., Charles, E. J., Habrian, C. H., Hansen, J. M. ... Wingreen, N. S. (2014) Large-scale filament formation inhibits the activity of CTP synthetase. *eLife* **3**, 1–19.
- Barsotti, C. and Ipata, P. L. (2004) Metabolic regulation of ATP breakdown and of adenosine production in rat brain extracts. *International Journal of Biochemistry and Cell Biology* **36**(11), 2214–2225.
- Bartesaghi, S., Valez, V., Trujillo, M., Peluffo, G., Romero, N., Zhang, H. ... Radi, R. (2006) Mechanistic Studies of Peroxynitrite-Mediated Tyrosine Nitration in Membranes Using the Hydrophobic Probe N-t-BOC-L-tyrosine tert-Butyl Ester. *Biochemistry* **45**, 6813–6825.
- Battelli, M. G., Polito, L., Bortolotti, M. and Bolognesi, A. (2016) Xanthine

oxidoreductase in cancer: more than a differentiation marker. *Cancer Medicine* **5**(3), 546-557.

Beaucamp, K., Bergmeyer, H.-U. and Beutler, H.-O. (1974) Coenzymes, metabolites and other biochemical reagents. *Methods of Enzymatic Analysis*. New York: Verlag Chemie, Weinheim and Academic Press, 532.

Becker, M. A., Schumacher H.R., Wortmann, R.L., MacDonald, P.A., Eustace, D., Palo, W.A. ... Joseph-Ridge, N. (2005) Febuxostat Compared with Allopurinol in Patients with Hyperuricemia and Gout. *New England Journal of Medicine* **353**(23), 2450–2461.

Beedham, C. (1987) Molybdenum hydroxylases: Biological distribution and substrate-inhibitor specificity. *Progress in Medicinal Chemistry*. Amsterdam: Elsevier, 85–127.

Benboubetra, M., Baghiani, A., Atmani, D., Harrison, R. (2004) Physicochemical and Kinetic Properties of Purified Sheep's Milk Xanthine Oxidoreductase. *Journal of Dairy Science* **87**(6), 1580–1584.

Berman, M.H., Westbrook, J., Feng, Z., Gilliland G., Bhat, T.N., Weissig, H. ... Bourne, P.E. (2000) The Protein Data Bank. *Nucleic Acids Research* **28**, 235–242.

Bolli, R. (2001) Cardioprotective function of inducible nitric oxide synthase and role of nitric oxide in myocardial ischemia and preconditioning: an overview of a decade of research. *Journal of molecular and cellular cardiology* **33**(11), 1897–1918.

Bradshaw, W. H. and Barker, H. A. (1960) Purification and characterization of xanthine dehydrogenase from *Clostridium acidurici* and *Clostridium cylindrosporium*. *J. Biol. Chem* **235**, 3620–3629.

Bray, R. C. (1977) Molybdenum-containing enzymes. *Journal of The Less-Common Metals* **54**(2), 527–536.

Bray, R. C., Lowe, D., Godber, B., Harrison, R. and Eisenthal R. (1999) Properties of xanthine oxidase from human milk: The enzyme is grossly deficient in molybdenum and substantially deficient in iron-sulfur clusters. *Flavins and flavoproteins, Proceedings of the 13th international symposium*. Berlin, Germany: Agency for Scientific Publications, 775–778.

Breslauert, K. J., Frank R., Blocker, H. and Marky, L.A. (1986) Predicting DNA duplex stability from the base sequence. *Proc Natl Acad Sci USA*. **83**, 3746–3750.

Brondino, C.D., Romao, M.J., Moura, I. and Moura, J.J. (2006) Molybdenum and tungsten enzymes: The xanthine oxidase family. *Current Opinion in Chemical Biology* **10**(2), 109–114.

Cai, H. and Harrison, D. G. (2000) Endothelial Dysfunction in Cardiovascular Diseases: The Role of Oxidant Stress. *Circulation Research* **87**(10), 840–844.

Carlo, S. De and Harris, J. R. (2011) Negative staining and cryo-negative staining of macromolecules and viruses for TEM. *Micron* **42**(2), 117–131.

Chan, M., Mukund, S., Kletzin, A., Adams, M.W. and Rees, D.C. (1995) Structure of a hyperthermophilic tungstopterin enzyme, aldehyde ferredoxin oxidoreductase. *Science* **267**(5203), 1463–1469.

Choi, H. K., Mount, D. B. and Reginato, A. M. (2005) Pathogenesis of gout. *Annals of Internal Medicine* **143**(7), 499–516.

Corran, H. S., Dewan, J. G., Gordon, A. H. and Green, D. E. (1939) Xanthine oxidase and milk flavoprotein. *Biochemical Journal*, **33**(10), 1694–1708.

Crowt, J. P., Kerby, J. D. and Beckmantt, J. S. (1996) Nitration and inactivation of manganese superoxide dismutase in chronic rejection of human renal allografts. *Proc Natl Acad Sci USA* **93**, 11853–11858.

Dassault Systèmes BIOVIA (2018) Discovery Studio Visualizer. San Diego: Dassault Systèmes

Diaz-Torné, C., Perez-Herrero, N. and Perez-Ruiz, F. (2015) New medications in development for the treatment of hyperuricemia of gout. *Current Opinion in Rheumatology* **27**(2), 164–169.

Dix, T. A. and Aikens, J. (1993) Mechanisms and biological relevance of lipid peroxidation initiation. *Chem. Res. Toxicol* **6**(1), 2–18.

Dixon, M. and Thurlow, S. (1924) Studies on Xanthine Oxidase: The Dynamics of the Oxidase System. *The Biochemical Journal* **18**(5), 976–988.

DNASTAR version 7.1 (2006) DNASTAR Lasergene. Madison, WI.

Dobbek, H., Gremer, L., Kiefersauer, R., Huber, R. and Meyer, O. (2002) Catalysis at a dinuclear [CuSMo(=O)OH] cluster in a CO dehydrogenase resolved at 1.1 Å resolution. *Proc Natl Acad Sci USA* **99**(25), 15971–15976.

Dower, W. J., Miller, J. F. and Ragsdale, C. W. (1988) High efficiency transformation of *E. coli* by high voltage electroporation. *Nucleic Acids Research* **16**(13), 6127–6145.

Droge, W. (2002) Free radicals in the physiological control of cell function. *Physiological Reviews* **82**(1), 47–95.

Drulyte, I., Johnson, R. M., Hesketh, E. L., Hurdiss, D. L., Scarff, C. A., Porav, S. A. ... Thompson, R. F. (2018) Approaches to altering particle distributions in cryo-electron microscopy sample preparation research papers. *Acta Crystallographica* **D74**, 560–571.

Eger, B. T., Okamoto, K., Enroth, C., Sato, M., Nishino, T, Pai, E. F. and Nishino, T. (2000) Purification , crystallization and preliminary X-ray diffraction studies of xanthine dehydrogenase and xanthine oxidase isolated from bovine milk. *Acta Crystallographica* **D56**(12), 1656–1658.

Emsley, P., Lohkamp, B., Scott, W. G. and Cowtan K. (2010) Features and development of Coot. *Acta Crystallographica* **D66**, 486–501.

EnCor Biotechnology, Inc. (2019) *Ammonium Sulfate Calculator*. Florida, USA

Enroth, C., Eger, B. T., Okamoto, K., Nishino, T., Nishino T. and Pai E. F. (2000) Crystal structures of bovine milk xanthine dehydrogenase and xanthine oxidase: structure-based mechanism of conversion. *Proceedings of the National Academy of Sciences of the United States of America* **97**(20), 10723–10728.

Esterbauer, H., Schaur, R. J. and Zollner, H. (1991) Chemistry and biochemistry of 4-hydroxynonenal, malonaldehyde and related aldehydes. *Free Radical Biology and Medicine* **11**, 81–128.

Fang, F. C. (2004) Antimicrobial reactive oxygen and nitrogen species: concepts and controversies. *Nature Reviews Microbiology* **2**(10), 820–832.

Foti, A., Hartmann, T., Coelho, C., Santos-Silva, T, Romao, M. J. and Leimkuhler, S. (2016) Optimization of the expression of Human Aldehyde Oxidase for Investigations of Single Nucleotide Polymorphisms. *Drug Metabolism and Disposition* **44**(8), 1277–1285.

Franco, M. C., Ye, Y., Refakis, C. A., Feldman, J. L., Stokes, A. L., Basso, M. ... Estevez, A. G. (2013) Nitration of Hsp90 induces cell death. *Proceedings of the National Academy of Sciences* **110**(12), E1102–E1111.

Fried, R. (1966) Calorimetric Determination of Xanthine Dehydrogenase by Tetrazolium Reduction. *Analytical Biochemistry* **16**, 427–432.

Fukushima, T., Adachi, T. and Hirano, K. (1995) The Heparin-Binding Site of Human Xanthine Oxidase. *Biol. Pharm. Bull* **18**(1), 156–158.

Ghosh, S. M., Kapil, V., Fuentes-Calvo, I., Bubb, K. J., Pearl, V., Milsom, A. B. ... Ahluwalia, A. (2013) Enhanced vasodilator activity of nitrite in hypertension: Critical role for erythrocytic xanthine oxidoreductase and translational potential. *Hypertension* **61**(5), 1091–1102.

Gihaz, S., Weiser, D., Dror, A., Satorhelyi, P., Jerabek-Willemsen, M., Poppe, L. and Fishman, A. (2016) Creating an Efficient Methanol-Stable Biocatalyst by Protein and Immobilization Engineering Steps towards Efficient Biosynthesis of Biodiesel. *ChemSusChem* **9**, 1–11.

Glaeser, R. M. and Han, B. (2017) Opinion : hazards faced by macromolecules when confined to thin aqueous films. *Biophysics Reports* **3**(1), 1–7.

Gliickner, J. and Johnson, W. C. (1987) Variable Selection Method Improves the Prediction of Protein Secondary Structure from Circular Dichroism Spectra. *Analytical Biochemistry* **167**, 76–85.

Godber, B. L. J., Doel, J. J., Sapkota, G. P., Blake, D. R., Stevens, C. R., eisenhal, R. and Harrison, R. (2000) Reduction of nitrite to nitric oxide catalyzed by xanthine oxidoreductase. *Journal of Biological Chemistry* **275**(11), 7757–7763.

Godber, B. L. J., Schawrz, G., Mendel, R. R., Lowe, D. J., Bray, R. C., Eisenhal, R. and Harrison, R. (2005) Molecular characterization of human xanthine oxidoreductase : the enzyme is grossly deficient in molybdenum and substantially deficient in iron-sulphur centres. *Biochem J.* **508**, 501–508.

Guex, N. and Peitsch, M. C. (1997) SWISS-MODEL and the Swiss-PdbViewer: An environment for comparative protein modeling. *Electrophoresis* **18**, 2714–2723.

Hänsch, R., Lang, C., Rennenberg, H. and Mendel, R. R.(2007) Significance of plant sulfite oxidase. *Plant Biology* **9**(5), 589–595.

Harrison, R. (2002) Structure and function of xanthine oxidoreductase: Where are we now? *Free Radical Biology and Medicine* **33**(10), 774–797.

Harrison, R. (2006) Milk xanthine oxidase : Properties and physiological roles. *International Dairy Journal* **16**, 546–554.

Hausladen, A. and Fridovichs, I. (1994) Superoxide and Peroxynitrite Inactivate Aconitases, but Nitric Oxide Does Not. *Journal of Biological Chemistry* **47**, 29405–29408.

Hennessey, J. P. and Johnson, W. C. (1981) Information Content in the Circular Dichroism of Proteins. *Biochemistry* **2**, 1085–1094.

Hille, R. (1996) Structure and function of mononuclear molybdenum enzymes. *Journal of Biological Inorganic Chemistry* **1**(5), 397–404.

Hille, R., Hall, J. and Basu, P. (2014) The mononuclear molybdenum enzymes. *Chemical Reviews* **114**(7), 3963–4038.

Hille, R. and Nishino, T. (1995) Flavoprotein structure and mechanism. 4. Xanthine oxidase and xanthine dehydrogenase. *The FASEB Journal* **9**(11), 995–1003.

Hille, R. and Nishino, T. (1995) Xanthine oxidase and xanthine dehydrogenase. *The FASEB Journal* **9**(11), 995–1003.

Hille, R., Nishino, T. and Bittner, F. (2011) ‘Molybdenum enzymes in higher organisms’, *Coordination Chemistry Reviews* **255**(9-10), 1179–1205.

Ishikita, H., Eger, B. T., Okamoto, K., Nishino, T. and Pai E. F. (2012) Protein Conformational Gating of Enzymatic Activity in Xanthine Oxidoreductase. *J. Am. Chem. Soc.* **134**, 999–1009.

Jarasch, E. D., Grund, C., Bruder, G., Heid, H. W., Keenan, T. W. and Franke, W. W. (1981) Localization of xanthine oxidase in mammary-gland epithelium and capillary endothelium. *Cell* **25**(1), 67–82.

Johnson, J. L., Cohen, H. J. and Rajagopalan, K. V. (1974) Molecular Basis of the Biological Function of Molybdenum. *Journal of Biological Chemistry* **249**, 5056–5061.

Kabsch, W. and Sander, C. (1983) Dictionary of Protein Secondary Structure: Pattern Recognition of Hydrogen-Bonded and Geometrical Features. *Biophysics* **22**, 2577–2637.

Kanda, M., Brady, F. O., Rajagopalan, K. V. and Handler, P. (1972) Studies on the dissociation of flavin adenine dinucleotide from metalloflavoproteins. *Journal of Biological Chemistry* **247**(3), 765–770.

Kelley, E. E., Hock, T., Khoo, N. K., Richardson, G. R., Johnson, K. K., Powell, P. C. and Tarpey, M. M. (2006) Moderate hypoxia induces xanthine oxidoreductase activity in arterial endothelial cells. *Free Radical Biology and Medicine* **40**(6), 952–959.

Kelley, E. E. (2015) A new paradigm for XOR-catalyzed reactive species generation in the endothelium. *Pharmacological Reports* **67**(4), 669–674.

Kitamura, S., Sugihara, K. and Ohta, S. (2006) Drug-Metabolizing Ability of Molybdenum Hydroxylases. *Drug Metabolism and Pharmacokinetics* **21**(2), 83–98.

Klose, D. P., Wallace, B. A. and Janes, R. W. (2010) 2Struc : the secondary structure server. *Bioinformatics* **26**(20), 2624–2625.

Kovac, S., Dinkova-Kostova, A. T. and Abramov, A. Y. (2005) The Role of Reactive Oxygen Species in Epilepsy. *Reactive Oxygen Species* **15**(8), 273–277.

Krenitsky, T. A., Neil, S. M., Elion, G. B. and Hitchings, G. H. (1972) A comparison of the specificities of xanthine oxidase and aldehyde oxidase. *Archives of Biochemistry and*

Biophysics **150**(2), 585–599.

Krenitsky, T., Spector, T. and Hall, W. (1986) Xanthine Oxidase from Human Liver : Purification and Characterization. *Archives of Biochemistry and Biophysics* **247**(1), 108–119.

Krissinel, E. and Henrick, K. (2007) Inference of Macromolecular Assemblies from Crystalline State. *J. Mol. Biol.* **372**, 774–797.

Kuwabara, Y., Nishino, T., Okamoto, K., Matsumura, T., Eger, B. T., Pai, E. F. and Nishino, T. (2003) Unique amino acids cluster for switching from the dehydrogenase to oxidase form of xanthine oxidoreductase. *Proc Natl Acad Sci USA* **100**(14), 8170-8175.

Laemmli, U. K. (1970) Cleavage of Structural Proteins during the Assembly of the Head of Bacteriophage T4. *Nature* **227**, 680-685

Leimkühler, S., Wuebbens, M. M. and Rajagopalan, K. V. (2011) The history of the discovery of the molybdenum cofactor and novel aspects of its biosynthesis in bacteria. *Coordination Chemistry Reviews* **255**(9-10), 1129–1144.

Li, H., Samouilov, A., Liu, X. and Zweier, J. L. (2001) Characterization of the Magnitude and Kinetics of Xanthine Oxidase-catalyzed Nitrite Reduction. *Biochemistry* **276**(27), 24482–24489.

Li, H., Cui, H., Kundu, T. K., Alzawahram, W. and Zweier, J. L. (2008) Nitric oxide production from nitrite occurs primarily in tissues not in the blood: Critical role of xanthine oxidase and aldehyde oxidase. *Journal of Biological Chemistry* **283**(26), 17855–17863.

Maia, L. B. and Moura, J. J. G. (2011) Nitrite reduction by xanthine oxidase family enzymes: A new class of nitrite reductases. *Journal of Biological Inorganic Chemistry* **16**(3), 443–460.

De Marco, A., Vigh, L., Diamant, S. and Goloubinoff, P. (2005) Native folding of aggregation-prone recombinant proteins in *Escherichia coli* by osmolytes, plasmid- or benzyl alcohol – overexpressed molecular chaperones. *Cell Stress & Chaperones* **10**(4), 329–339.

Marla, S. S., Lee, J. and Groves, J. T. (1997) Peroxynitrite rapidly permeates phospholipid membranes. *Proc Natl Acad Sci USA* **94**(26), 14243–14248.

Martin, H. M., Hancock, J. T., Salisbury, V. and Harisson, R. (2004) Role of Xanthine Oxidoreductase as an Antimicrobial Agent', *Infection and Immunity* **72**(9), 4933–4939.

Matsumoto, K., Okamoto, K., Ashizawa, N. and Nishino, T. (2011) FYX-051 : A Novel

and Potent Hybrid-Type Inhibitor of Xanthine Oxidoreductase. *The Journal of Pharmacology and Experimental Therapeutics* **336**(1), 95–103.

McEwan, A. G., Ridge, J. P., McDevitt, C. A. and Hugenholtz, P. (2002) The DMSO reductase family of microbial molybdenum enzymes; molecular properties and role in the dissimilatory reduction of toxic elements. *Geomicrobiology Journal* **19**(1), 3–21.

Mcwhirter, R. B. and Hille, R. (1991) The Reductive Half-reaction of Xanthine Oxidase. *The Journal of biological chemistry* **266**(35), 23724–23731.

Montero-Moran, G. M., Li, M., Rendon-Huerta, E., Jourdan, F., Lowe, D. J., Stumpff-Kane, A. W., Feig, M. ... Hausinger, R. P. (2007) Purification and characterization of the FeII- and alpha-ketoglutarate-dependent xanthine hydroxylase from *Aspegillus nidulans*. *Biochemistry* **46**, 5293.

Morpeth, F. F. (1983) Studies of the specificity toward aldehyde substrates and steady-state kinetics of xanthine oxidase. *Biochemicaa et Biophysica Acta*, **744**, 328–334.

Morris, G. M. *et al.* (2009) AutoDock4 and AutoDockTools4 : Automated Docking with Selective Receptor Flexibility. *Journal of Computational Chemistry* **30**(16), 2785–2791.

Van Den Munckhof, R. J. M., Vreeling-Sindelarova, H., Schellens, J. P. M. and Van Noorden, C. J. F. (1995) Ultrastructural localization of xanthine oxidase activity in the digestive tract of the rat. *Histochemical Journal* **905**(27), 897–905.

Murad, F. (2006) Nitric Oxide and Cyclic GMP in Cell Signaling and Drug Development. *Nitric Oxide* **355**(19), 2003–2011.

Murray, K. N., Watson, G. and Chaykin, S. (1966) Catalysis of the Direct Transfer of Oxygen from Nicotinamide N-Oxide to Xanthine by Xanthine Oxidase. *J. Biol. Chem.*, **241**, 4798.

Muzychka, O. V., Kobzar, O. L., Popova, A. V., Fransinjuk, M. S. and Vovk, A. I. (2017) Carboxylated aurone derivatives as potent inhibitors of xanthine oxidase. *Bioorganic and Medicinal Chemistry* **25**(14), 3606–3613.

Nakamura, M. and Yamazaki, I. (1982) Preparation of Bovine Milk Xanthine Oxidase as a Dehydrogenase Form. *Journal of Biochemistry* **92**, 1279–1286.

Niedermeyer, T. and Strohal, M. (2012) mMass as a Software Tool for the Annotation of Cyclic Peptide Tandem Mass Spectra. *PLoS ONE*, **7**(9), e44913.

Nishino, T. (1994) The conversion of xanthine dehydrogenase to xanthine oxidase and the role of the enzyme in reperfusion injury. *Journal of biochemistry* **116**(1), 1–6.

Nishino, T., Okamoto, K., Kawaguchi, Y., Hori, H., Matsumura, T., Eger, B. T. ... Nishino, T. (2005) Mechanism of the conversion of xanthine dehydrogenase to xanthine oxidase: Identification of the two cysteine disulfide bonds and crystal structure of a non-convertible rat liver xanthine dehydrogenase mutant. *Journal of Biological Chemistry* **280**(26), 24888–24894.

Nishino, T., Nishino, T. and Tsushima, K. (1981) Purification of highly active milk xanthine oxidase by affinity chromatography on sepharose 4b/folate gel. *FEBS Letters* **131**(2), 369–372.

Okamoto, K., Eger, B. T., Nishino, T., Kondo, S., Pai, E. F. and Nishino, T. (2003) An Extremely Potent Inhibitor of Xanthine Oxidoreductase. *The Journal of biological chemistry* **278**(3), 1848–1855.

Okamoto, K., Eger, B. T., Nishino, T., Pai, E. F. and Nishino, T. (2008) Mechanism of inhibition of xanthine oxidoreductase by allopurinol: crystal structure of reduced bovine milk xanthine oxidoreductase bound with oxipurinol. *Nucleosides, nucleotides & nucleic acids* **27**(6), 888–893.

Omar, S. A. and Webb, A. J. (2014) Nitrite reduction and cardiovascular protection. *Journal of Molecular and Cellular Cardiology* **73**, 57–69.

Palmer, T., Santini, C. L., Iobbi-Nivol, C., Eaves, D. J., Boxer, D. H. and Giordano, G. (1996) Involvement of the narJ and mob gene products in distinct steps in the biosynthesis of the molybdoenzyme nitrate reductase in Escherichia coli. *Molecular Microbiology* **20**(4), 875–884.

Pantoliano, M., Petrella, E. C., Kwasnoski, J. D., Lobanov, V. S., Myslik, J., Graf, E. ... Salemme, F. R. (2001) High-Density Miniaturized Thermal Shift Assays as a General Strategy for Drug Discovery. *Journal of Biomolecular Screening* **6**(6), 429–440.

Pearson, A. R., Gosber, B. L. J., Eisenthal R., Taylor, G. L. and Harrison, R. (no date) Human Milk Xanthine Dehydrogenase is Incompletely Converted to the Oxidase Form in the Absence of Proteolysis. A Structural Explanation. *Not published*.

Phillips, M., Cataneo, R. N., Cheema, T. and Greenberg, J. (2004) Increased breath biomarkers of oxidative stress in diabetes mellitus. *Clinica Chimica Acta* **344**, 189–194.

Porollo, A. and Meller, J. (2007) Prediction-Based Fingerprints of Protein – Protein Interactions. *PROTEINS: Structure, Function and Bioinformatics* **66**, 630–645.

Potterton, L., Agirre, J., Ballard, C., Cowtan, K., Dodson, E., Evans, P. R. ... Wojdyr, M. (2018) CCP4i2 : the new graphical user interface to the CCP 4 program suite research papers. *Acta Crystallographica* **D74**, 68–84.

Pritsos, C. A. (2000) Cellular distribution, metabolism and regulation of the xanthine oxidoreductase enzyme system. *Chemico-Biological Interactions* **129**, 195–208.

Quijano, C., Alvarez, B., Gatti, R. M., Augusto, O. and Radi, R. (1997) Pathways of peroxynitrite oxidation of thiol groups. *Biochem J.*, **173**, 167–173.

Rajagopalan, K. V. and Handler, P. (1967) Purification and Properties of Chicken Liver Xanthine Dehydrogenase. *J. Biol. Chem.* **242**(18), 4097–4107.

Ramachandran, G. N., Ramakrishnan, C. and Sasisekharan, V. (1963) Stereochemistry of Polypeptide Chain Configurations. *J. Mol. Biol.* **7**, 95–99.

Reinhard, L., Mayerhofer, H., Geerlof, A., Mueller-Dieckmann, J. and Weiss, M. S. (2013) Optimization of protein buffer cocktails using Thermofluor laboratory communications. *Acta Crystallographica* **F69**, 209–214.

Robert, M. and Robert, L. (2014) Xanthine oxidoreductase, free radicals and cardiovascular disease. A critical review. *Pathology oncology research* **20**(1), 1–10.

Robert, X. and Gouet, P. (2014) Deciphering key features in protein structures with the new ENDscript server. *Nucleic Acids Research* **42**, 320–324.

Rosa, N., Ristic, N., Seabrook, S. A., Lovell, D., Lucent D. and Newman, J. (2015) Meltdown : A Tool to Help in the Interpretation of Thermal Melt Curves Acquired by Differential Scanning Fluorimetry. *Journal of Biomolecular Screening* **20**(7), 898–905.

Saito, T., Nishino, T. and Massey, V. (1989) Differences in environment of FAD between NAD-dependent and O₂-dependent types of rat liver xanthine dehydrogenase shown by active site probe study. *Journal of Biological Chemistry* **264**, 15930-15935.

Saksela, M., Lapatto, R. and Raivio, K. O. (1999) Irreversible conversion of xanthine dehydrogenase into xanthine oxidase by a mitochondrial protease. *FEBS Letters* **443**, 117–120.

Salgo, M. G., Bermudez, E., Squadrito, G. L. and Pryot, W. A. (1995) DNA damage and oxidation of thiols peroxynitrite causes in rat thymocytes. *Archives of Biochemistry and Biophysics* **322**(2), 500–505.

Sambrook, J. and Green, M. R. (2012) *Molecular Cloning: A Laboratory Manual*. 4th edn. Cold Spring Harbor Laboratory Press.

Sanders, S. A., Eisenthal, R. and Harrison, R. (1997) NADH oxidase activity of human xanthine oxidoreductase. Generation of superoxide anion. *Eur. J. Biochem* **245**, 541–548.

Santiago, B., Schubel, U., Egelseer, C. and Meyer, O. (1999) Sequence analysis,

characterization and CO-specific transcription of the cox gene cluster on the megaplasmid pHCG3 of *Oligotropha carboxidovorans*. *Gene* **236**(1), 115–124.

Sattui, S. E. and Gaffo, A. L. (2016) Treatment of hyperuricemia in gout: current therapeutic options, latest developments and clinical implications. *Therapeutic Advances in Musculoskeletal Disease* **8**(4), 145–159.

Sawyer, J. R., Schlom, J. and Kashmiri, S. V. (1994) The effects of induction conditions on production of a soluble anti-tumor sFc in *Escherichia coli*. *Protein Eng.* **7**, 1401–1406.

Schagger, H. and von Jagow, G. (1991) Blue Native Electrophoresis for Isolation of Membrane Protein Complexes in Enzymatically Active Form. *Analytical Biochemistry* **199**, 223–231.

Schein, C. H. (1989) Production of soluble recombinant proteins in bacteria. *Biotechnology* **7**, 1141–1148.

Schrodinger, L. (2019) ‘The PyMOL Molecular Graphics System’. LLC

Schwarz, G. and Belaidi, A. A. (2013) Molybdenum in Human Health and Disease. *Met Ions Life Sci* **13**, 415–450

Scopes, R. K. (1987) Separation by Precipitation. *Protein Purification: Principles and Practice*. 2nd edn. New York: Springer-Verlag, 41–64.

Semisotnov, G. V., Rodionova, N. A., Razgulyaev, O. I., Uversky, V. N., Gripas A. F. and Gilmanishin, R. I. (1991) Study of the “Molten Globule” Intermediate State in Protein Folding by a Hydrophobic Fluorescent Probe. *Biopolymers* **31**, 119–128.

Shah, A. and Keenan, R. T. (2010) Gout, hyperuricemia, and the risk of cardiovascular disease: Cause and effect? *Current Rheumatology Reports* **12**(2), 118–124.

Stiburkova, B., Krijt, J., Vyletal, P., Bartl, J., Gerhatova, E., Korinerk, M. and Sebesta, I. (2012) Novel mutations in xanthine dehydrogenase/oxidase cause severe hypouricemia: Biochemical and molecular genetic analysis in two Czech families with xanthinuria type I. *Clinica Chimica Acta* **413**(1), 93–99.

Stirpe, F. and Della Corte, E. (1969) The regulation of rat liver xanthine oxidase. Conversion in vitro of the enzyme activity from dehydrogenase (type D) to oxidase (type O). *Journal of Biological Chemistry* **244**(14), 3855–3863.

Szabó, C., Ischiropoulos, H. and Radi, R. (2007) Peroxynitrite: biochemistry, pathophysiology and development of therapeutics. *Nature reviews. Drug discovery*, **6**(8), 662–680.

Terao, M., Romao, M. J., Leimkuhler, S., Bolis, M., Fratelli, M., Coelho, C, Santos-Silva, T. and Garattini, E. (2016) Structure and function of mammalian aldehyde oxidases. *Archives of Toxicology* **90**(4), 753–780.

ThermoFisher Scientific (2019) *Tm Calculator*. Available at: www.thermofisher.com/tmcalculator.

Tiede, C., Bedford, R., Heseltine, S. J., Smith, G., Wijetunga, I., Ross, R. ... Tomlinson, D. C. (2017) Affimer proteins are versatile and renewable affinity reagents. *eLife* **6**, e24903

Vagin, A. A., Steiner, R. A., Lebedev, A. A., Potterton, L., McNicholas, S., Long, F. and Murshudov, G. N. (2004) REFMAC5 dictionary: organization of prior chemical knowledge and guidelines for its use. *Acta Crystallographica* **D60**, 2184–2195.

Vagin, A. and Teplyakov, A. (1997) MOLREP: an Automated Program for Molecular Replacement. *J. Appl. Cryst.* **30**, 1022–1025.

Vella, M., Hunter, T., Farrugia, C., Pearson, A. R., Hunter, G. (2014) Purification and Characterisation of Xanthine Oxidoreductases from Local Bovids in Malta. *Advances in Enzyme Research* **2**, 54–63.

Ventom, A. M., Deistung, J. and Bray, R. C. (1988) The isolation of demolybdo xanthine oxidase from bovine milk. *Biochemical Journal* **255**, 949–956.

Veskoukis, A. S., Kouretas, D. and Panoutsopoulos, G. I. (2006) Substrate specificity of guinea pig liver aldehyde oxidase and bovine milk xanthine oxidase for methyl- and nitrobenzaldehydes. *European Journal of Drug Metabolism and Pharmacokinetics* **31**(1), 11–16.

Walling, C. (1975) Fenton's Reagent Revisited. *Accounts of Chemical Research* **8**(4), 125–131.

Wang, C. H., Zhang, C. and Xing, X. H. (2016) Xanthine dehydrogenase: An old enzyme with new knowledge and prospects. *Bioengineered* **7**(6), 395–405.

Wanner, B. L., Kodaira, R. and Neidhardt, F. C. (1978) Regulation of lac Operon Expression : Reappraisal of the Theory of Catabolite Repression. *Journal of Bacteriology* **136**(3) 947–954.

Webb, B. A., Dosey, A. M., Wittmann, T., Kollman, J. M. and Barber D. L. (2017) The glycolytic enzyme phosphofructokinase-1 assembles into filaments. *J. Cell Biol.* **216**(8), 2305–2313.

Whitmore, L. and Wallace, B. A. (2007) Protein secondary structure analyses from

circular dichroism spectroscopy: methods and reference databases. *Biopolymers* **89**(5), 392–400.

Wilkins, M. R., Lindskog, I., Gasteiger, E., Bairoch, A., Sanchez, J. C., Hochstrasser, D. F. and Appel, R. D. (1997) Detailed peptide characterization using PEPTIDEMASS - a World-Wide-Web-accessible tool. *Electrophoresis* **18**, 403–408.

Williams, C. J., Headd, J. J., Moriarty, N. W., Prisant, M. G., Videau, L. L., Deis, L. N. ... Richardson, D. C. (2018) MolProbity : More and better reference data for improved all-atom structure validation. *Protein Science* **27**, 293–315.

Winter, G., Waterman, D. G., Parkhurst J. M., Brewster, A. S., Gildea, R. J., Gerstel, M. ... Evans, G. (2018) DIALS : implementation and evaluation of a new integration package. *Acta Crystallographica* **D74**, 85–97.

Xia, M., Dempski, R. and Hille, R. (1999) The reductive half-reaction of xanthine oxidase. Reaction with aldehyde substrates and identification of the catalytically labile oxygen. *Journal of Biological Chemistry* **274**(6), 3323–3330.

Xie, Z., Luo, X., Zou, Z., Zhang, X., Huang, F., Li, R. ... Liu, Y. (2017) Synthesis and evaluation of hydroxychalcones as multifunctional non-purine xanthine oxidase inhibitors for the treatment of hyperuricemia. *Bioorganic and Medicinal Chemistry Letters* **27**(15), 3602–3606.

Yamaguchi, Y., Matsumura, T., Ichida, K., Okamoto, K. and Nishino, T. (2007) Human Xanthine Oxidase Changes its Substrate Specificity to Aldehyde Oxidase Type upon Mutation of Amino Acid Residues in the Active Site : Roles of Active Site Residues in Binding and Activation of Purine Substrate. *J. Biochem.* **524**, 513–524.

Yang, J., Kamide, K., Kokubo, Y., Takiuchi S., Horio T., Matayoshi, T. ... Kawano, Y. (2008) Associations of Hypertension and Its Complications with Variations in the Xanthine Dehydrogenase Gene. *Hypertens. Res.* **31**(5), 931–940.

Zaahkouk, S. A. M., Darwish, D. A., Hassam, M. M. M., Abdel-Monsef, M. M., Helmy, M. S., Esa, S. S. ... Ibrahim, M. (2019) Purification and Characterization of Xanthine Oxidase from liver of the Sheep (*Ovis Aries*). *Journal of Antioxidant Activity* **1**(4), 8–18.

Zhang, Y. and Skolnick, J. (2005) TM-align : a protein structure alignment algorithm based on the TM-score. *Nucleic Acids Research* **33**(7), 2302–2309.

Zhou, L., Stanley, W. C., Saidel, G. M., Yu, X. and Cabrera, M. E. (2005) Regulation of lactate production at the onset of ischaemia is independent of mitochondrial NADH/NAD⁺: insights from *in silico* studies. *The Journal of physiology* **569**, 925–937.

Zweier, J. L., Samouilov, A. and Kuppusamy, P. (1999) Non-enzymatic nitric oxide

synthesis in biological systems. *Biochimica et Biophysica Acta* **1411**, 250–262.